2019

Hyperpolarized Carbon-13 Magnetic Resonance Imaging As A Tool For Assessing Lung Transplantation Outcomes

Sarmad Muneeb Siddiqui
University of Pennsylvania, sarmad@smsiddiqui.com

Recommended Citation

Siddiqui, Sarmad Muneeb, "Hyperpolarized Carbon-13 Magnetic Resonance Imaging As A Tool For Assessing Lung Transplantation Outcomes" (2019). *Publicly Accessible Penn Dissertations*. 3672.
https://repository.upenn.edu/edissertations/3672

Hyperpolarized Carbon-13 Magnetic Resonance Imaging As A Tool For Assessing Lung Transplantation Outcomes

Abstract

Lung transplantation is the established treatment for patients with chronic, end-stage lung diseases such as chronic obstructive pulmonary disease (COPD), idiopathic pulmonary fibrosis (IPF) and cystic fibrosis (CF). However, its utility remains limited by the chronic shortage of donor lungs, limited lung preservation strategies and post-transplant complications leading to graft failure. Although efforts have been made to expand the limited pool of viable donor lungs via novel preservation strategies such as ex vivo lung perfusion (EVLP), our limited understanding of the mechanism and progression of donor lung injury continues to inhibit our ability to fully exploit these advances to improve lung transplant outcomes. Furthermore, the clinical standard for post-transplant assessment is limited to whole lung measurement such as pulmonary functional tests (PFTs) and structural imaging via radiography or HRCT, both of which lack the necessary sensitivity to detect lung rejection early. Given these limitations of currently available pre- and post-transplant lung assessment tools, a novel metabolic biomarker may provide higher sensitivity for determining the viability of donated lungs, as well as for assessing the onset of rejection before permanent structural changes in the lungs become apparent. We proposed that hyperpolarized (HP) [1-13C]pyruvate magnetic resonance imaging (MRI)—which provides real-time metabolic assessment of tissue based on the conversion of [1-13C] pyruvate to [1-13C]lactate via glycolysis, or to 13C bicarbonate via oxidative phosphorylation—may be an effective tool for assessing the health of donated lungs and may also serve as an early biomarker for detecting pulmonary graft dysfunction (PGD)-associated inflammation or acute lung rejection. In a rat model, we demonstrated the feasibility of using HP [1-13C]pyruvate nuclear magnetic resonance (NMR) spectroscopy to assess the viability of ex vivo perfused lungs. We further showed that our technique can be used to measure the improved viability of those lungs after treatment with ascorbic acid. Finally, translating our previously developed technique to in vivo HP [1-13C]pyruvate imaging of an inflamed rat lung, we not only demonstrated its utility for detecting lung transplantation rejection, but found that the HP lactate-to-pyruvate ratio is a better predictor of acute lung rejection in a rat model than computed tomography.

Degree Type

Dissertation

Degree Name

Doctor of Philosophy (PhD)

Graduate Group

Bioengineering

First Advisor

Rahim Rizi

Keywords

hyperpolarized carbon-13, lactate, MRI, pyruvate, transplantation

Subject Categories

Translation Studies

HYPERPOLARIZED CARBON-13 MAGNETIC RESONANCE IMAGING AS A TOOL FOR ASSESSING LUNG TRANSPLANTATION OUTCOMES

Sarmad Siddiqui

A DISSERTATION

in

Bioengineering

Presented to the Faculties of the University of Pennsylvania

in

Partial Fulfillment of the Requirements for the

Degree of Doctor of Philosophy

2019

Supervisor of Dissertation

____

Rahim Rizi

Professor of Radiology

Graduate Group Chairperson

____

Ravi Radhakrishnan, Professor of Bioengineering

Dissertation Committee

Mitchell D. Schnall	Chairman, Department of Radiology
Stephen Kadlecek	Research Associate Professor of Radiology
Maurizio Cereda	Associate Professor of Radiology, Associate Professor of Anesthesiology and Critical Care

HYPERPOLARIZED CARBON-13 MAGNETIC RESONANCE IMAGING AS A TOOL FOR ASSESSING LUNG TRANSPLANTATION OUTCOMES

This thesis is dedicated to my family and friends

Thank you for keeping me sane, more or less

Acknowledgements

I would first like to thank my advisor, Rahim Rizi, and the professors in my lab—Stephen Kadlecek, and Maurizio Cereda—who gave me a number of challenging projects to work on, and always had their doors open to provide guidance, support, and mentorship throughout my time here. They gave me enough space to work on problems independently, but were always there to listen to my thoughts, ideas and plans, tolerate the stupider ones, and guide me to find better solutions.

I'd also like to thank my HHMI-Interfaces program's leadership, James Gee, Ann Tiao, Andrew Maidment, and Peter Davies who have designed an excellent, unique program for students like myself whose research interests lie at the intersection of engineering and medicine. They supported me throughout the program, and were always there whenever I had any questions or favors to ask. I'd also like to thank Kathleen Venit in the Department of Bioengineering, who was always on top of things when it came to making sure I wasn't forgetting some important departmental requirement or deadline; her quick replies to my last-minute, ill-timed emails definitely staved off stress-related cardiac diseases until at least after graduate school.

A number of lab members in my group came and went throughout my time here as a graduate student. I appreciate the influence they had in my life, both at work, or outside of work: Harrilla Profka (he knows what he does best), Hoora Shaghaghi (all those perfusion studies), Rajat Ghosh (tennis), Nick Drachman (arguing, the good kind), and everyone else who has played a role one way or another: Justin Clapp, Ian Duncan, Kai Ruppert, Shampa Chatterjee, Andreas Habertheuer, Susan Rostami, Faraz Amzajerdian, Luis

Loza, Tahmina Achekzai, Ryan Baron, Federico Sertic, Caroline Keenan. If I have forgotten anyone, my bad.

A life without my friends would definitely have lead to insanity, and I'm lucky enough to have made several great friends in my time here. Anders, Hooman, Iba, Jason, Jennifer, Laura, Lindsey, Lohith, Mehrdad, Melody, Yi, thanks for being you. Unfortunately, there were quite a few friends who I lost touch with over the years, or perhaps didn't get to know as well as I'd like, but Alex, Aurada, Lisa, Lori, Matt, and Nathalie, you were as great a learning team a pretender could ask for; Matt, Francisco, Ben, we made a great cohort. And my friends back home: Anish, Han, Kabi, Konner, Nick, Rakesh, Raman, Sri, Steph, even though I was quite far away, you reached out and checked-in every few months, and thank you for keeping me in your thoughts.

Lastly, I'd like to thank my family: my father, my mother, Saad, Saami, Sameed, Mehvash, Sarah, Haniya, and Ifrah. I'm pretty sure the last one doesn't quite know that I exist yet, but I appreciate her nonetheless. You guys have always wished and prayed for my best. That's all anyone can ask for. Thank You.

ABSTRACT

HYPERPOLARIZED CARBON-13 MAGNETIC RESONANCE IMAGING AS A TOOL FOR ASSESSING LUNG TRANSPLANTATION OUTCOMES

Sarmad Siddiqui

Rahim Rizi

Lung transplantation is the established treatment for patients with chronic, end-stage lung diseases such as chronic obstructive pulmonary disease (COPD), idiopathic pulmonary fibrosis (IPF) and cystic fibrosis (CF). However, its utility remains limited by the chronic shortage of donor lungs, limited lung preservation strategies and post-transplant complications leading to graft failure. Although efforts have been made to expand the limited pool of viable donor lungs via novel preservation strategies such as *ex vivo* lung perfusion (EVLP), our limited understanding of the mechanism and progression of donor lung injury continues to inhibit our ability to fully exploit these advances to improve lung transplant outcomes. Furthermore, the clinical standard for post-transplant assessment is limited to whole lung measurement such as pulmonary functional tests (PFTs) and structural imaging via radiography or HRCT, both of which lack the necessary sensitivity to detect lung rejection early. Given these limitations of currently available pre- and post-transplant lung assessment tools, a novel metabolic biomarker may provide higher sensitivity for determining the viability of donated lungs, as well as for assessing the onset of rejection before permanent structural changes in the lungs become apparent. We proposed that hyperpolarized (HP) [1-^{13}C]pyruvate magnetic resonance imaging (MRI)—which provides real-time metabolic assessment of tissue based on the conversion of [1-

^{13}C] pyruvate to [1-^{13}C]lactate via glycolysis, or to ^{13}C bicarbonate via oxidative phosphorylation—may be an effective tool for assessing the health of donated lungs and may also serve as an early biomarker for detecting pulmonary graft dysfunction (PGD)-associated inflammation or acute lung rejection. In a rat model, we demonstrated the feasibility of using HP [1-^{13}C]pyruvate nuclear magnetic resonance (NMR) spectroscopy to assess the viability of *ex vivo* perfused lungs. We further showed that our technique can be used to measure the improved viability of those lungs after treatment with ascorbic acid. Finally, translating our previously developed technique to *in vivo* HP [1-^{13}C]pyruvate imaging of an inflamed rat lung, we not only demonstrated its utility for detecting lung transplantation rejection, but found that the HP lactate-to-pyruvate ratio is a better predictor of acute lung rejection in a rat model than computed tomography.

TABLE OF CONTENTS

LIST OF TABLES

LIST OF ILLUSTRATIONS

Chapter 1: The Current State of Lung Transplantation

Since the first successful long-term lung transplantation was carried out in 1983[1], it has become the established treatment for patients with end-stage chronic lung disease. Approximately 85% of worldwide lung transplantations are for performed for patients with end-stage chronic obstructive pulmonary disease (COPD), pulmonary arterial hypertension (PAH), cystic fibrosis (CF) and interstitial lung diseases (ILD). Over the past three decades, numerous improvements in both pre- and post-operative care[2,3] have dramatically increased survival rates across all diagnoses for which transplantation is a viable option, ensuring significantly improved lung function and overall quality of life for the majority of recipients[4]. This improvement is reflected by the increasing number of transplants performed ever year: according to the most recently data published in 2016, there has been a 40% increase in total transplants over the past ten years[5].

Unfortunately, the long-term success rate of lung transplantation remains significantly lower than that of other solid organs. For example, post-transplant survival is 80% at 1 year and 50% at 5.8 years for the lung[5], compared to 97.3% and 90.4% survival rates at 1 year for kidney and liver, the two most commonly transplanted organs—both of which have median survivals of approximately 10 years[6,7].

The comparatively poor success rate of lung transplantation has two main causes. First, the lung faces the highest oxidative stress of any organ due to the fact that it has two separate blood supplies and is directly exposed to air[8]. Secondly, a majority of transplant lungs are sourced after donor brain death (DBD), which is associated with disrupted endocrine function as well as an increased level of pro-inflammatory factors that include cytokines interleukin-8 (IL-8) and interleukin-6 (IL-6) and human leukocyte antigen-DR (HLA-DR), all of which have been shown to be associated with the development of primary graft dysfunction (PGD), the leading source of transplant failure in the first year post-surgery[8,910]. The DBD-associated inflammatory milieu has also been shown to play a role in the development of both acute and chronic rejection[11]. As such, the best way to mitigate these issues is to optimize methods of lung preservation before transplantation, and monitor lungs for early detection of lung failure or rejection post-transplantation.

1.1. Modes of Transplant Failure

1.1.1. Primary Graft Dysfunction (PGD)

Primary graft dysfunction (PGD) is a is a syndrome characterized by hypoxemia and diffuse radiographic opacities without any other differential diagnoses in the first 24 to 72 hours after lung transplantation[9,12]. The syndrome has also been characterized as early graft dysfunction and is most likely due to ischemia-reperfusion injury[8,13]. PGD is diagnosed on a severity grade from 0 to 3, based on the ratio of arterial fraction of oxygen (P_aO_2)/fraction inspired oxygen (FiO_2), as listed in Table 1.1.

Grade	P_aO_2/FiO_2	Radiographic infiltrates consistent with edema
0	> 300	Absent
1	> 300	Present
2	200-300	Present
3	< 200	Present

Table 1.1: Criteria for grading primary graft dysfunction severity.

Up to 30% of transplant recipients are diagnosed with PGD and it is the leading cause of death within the first 30 days after transplantation[9]. The pathophysiology of PGD depends on a number of factors during the retrieval and transplantation process, the most important of which may the conditioning and treatment of lungs acquired after DBD. As such, a number of donor management strategies have been applied to minimize hemodynamic or inflammatory injury to DBD lungs. For example, treatment with the α-adrenergic antagonist phentolamine prevents DBD-induced systemic hypertension, which can cause increased capillary permeability leading to neurogenic pulmonary edema (NPE), thereby improving oxygenation and lowering airway pressure compared to untreated DBD lungs[14]. Treatment with a vasopressor can block injuries to the donor lung resulting from neurogenic hypotension, such as metabolic acidosis[15–17]. Additionally, glucocorticoids can be used to improve oxygenation and ameliorate inflammatory response by preventing the cortisol deficiency which often follows DBD[18–20]. Pre-treatment with antioxidants, such as Vitamin C or ascorbic acid, has been shown to lower expression of pro-inflammatory cytokines and protect against oxidative stress and microvascular dysfunction[21–23]. Less interventional tactics have also proven effective: several studies suggest that delayed organ retrieval partially reverses DBD-induced hemodynamic injury, improving lung transplantation outcomes by allowing for a partial reversal of early hemodynamic injury subsequent to DBD[14,24,25].

Finally, ex-vivo lung perfusion (EVLP) has recently emerged as a valuable tool for both evaluating and reconditioning lungs prior to transplant[26,27]. In addition to enabling the reassessment of lungs initially deemed unsuitable, EVLP has demonstrated the potential to improve graft viability by enabling alveolar recruitment maneuvers, helping to clear bronchial secretions, removing both inflammatory cells and clots in pulmonary circulation, and reducing the microbial load in donor lungs[28,29]. However, because EVLP itself carries a number of risks—including increased vascular stress over time, metabolic alteration of the perfused organ, and inflammatory upregulation—tailoring the combination of perfusion time, perfusate flow, and perfusate formula to the needs of each individual organ is critical to optimizing its successful use[26,30,31]. Unfortunately, non-invasive EVLP evaluation is typically limited to measuring the P_aO_2/FiO_2 to determine the status of the lungs[32,33]. An imaging modality that can provide more direct assessment of the lung's metabolic state and viability would be a boon to improving these successful lung transplant outcomes.

1.1.2. Acute and Chronic Lung Rejection

Graft rejection is mediated by the adaptive immune system. Specifically, the recognition of allogeneic major histocompatibility complex (MHC) by the host T cells activates the adaptive immune system, stimulating cytotoxic T cells (CTL), as well as the humoral (via stimulated B cells) and complement response[34,35]. The mainstay of preventing lung rejection is the use of immunosuppressants that minimize the T-cell response post-transplantation. Immediately after transplantation, potent induction immunosuppressive induction agents, such as basiliximab (IL-2 inhibitor) or alemtuzumab (CD52 antibody), are administrated to deplete or inhibit T-cell activation and proliferation[36–38]. However, as the use of these drugs severely depresses the immune system, their use has to be balanced by the increased risks of infections. As the highest immune reactivity towards the graft is within the first three to six months, after that period the immune suppression is maintained by low doses of drugs with non-overlapping toxicities. Typically, a combination of a glucocorticoid, calcineurin inhibitor, and a nucleotide blocking agent are prescribed based on the recipient's tolerance profile[37,38].

If no acute rejection occurs within the first few days to months, lungs can undergo rejection via chronic lung allograft dysfunction (CLAD). CLAD presents as one of two phenotypes, bronchiolitis obliterans syndrome (BOS) or restrictive allograft syndrome (RAS)[11]. BOS is the predominant presentation for CLAD and manifests as an obstructive lung disease with fibrosis of the small airways. RAS, on the other hand, is characterized by restrictive pulmonary function. Although the etiology of CLAD is not well defined, its risk factors include PGD, acute rejection, infection and gastroesophageal reflux (GER)[39]. Despite the multitude of factors that could lead to CLAD, monitoring is based pulmonary function decline measured via pulmonary function testing (PFT) followed by chest radiography or high resolution computed tomography (HRCT) to confirm any observed decline.

1.2. Limitations of Current Monitoring Techniques

Typically, patients are monitored post-transplantation with routine spirometry and chest radiographs obtained at regular intervals. Postoperative lung function is considered to be stabilized when the variation in the forced expiratory volume in one second (FEV_1) and the forced vital capacity (FVC) has a less than five percent variance between two measurements taken at least one week apart[40]. A decline of greater than 10% in spirometry values within two days can be a sign of either acute lung rejection or infection[40–42] so follow-up for serology testing, transbronchial biopsy or radiography is needed to rule out differential diagnoses[43]. Furthermore, the sensitivity of spirometry is about 60 percent in detecting lung rejection, so stable pulmonary function as measured doesn't necessarily exclude acute lung rejection[44].

The diagnosis of chronic lung rejection is also based on PFT measurements. Early stage BOS is defined as an FEV_1 decline of more than 20% from baseline and/or forced expiratory flow between 25 and 75 percent (FEF_{25-75}) decline of more than 25% from baseline[39] in two consecutive measurements made at least three weeks apart. It is recommended to acquire chest radiographs or high-resolution computed tomography (HRCT) if such a decline is observed. However, chest radiographs have a low sensitivity for detecting early stages of BOS, although hyperinflation and bronchiectasis can be observed in more advanced disease[45,46]. Although there is no consensus definition of RAS, patients with a FEV_1 decline of greater than 20% and a forced vital capacity (FVC) decline of greater than 20% or a total lung capacity (TLC) decline of greater than 10% are given the diagnosis of the restrictive phenotype[11,47,48]. CT findings are recommended to be followed by transbronchial biopsies to confirm a specific diagnosis[49].

Given the limitations of the currently available tools for both pre-transplant and post-transplant lung assessment, perhaps a metabolic biomarker may provide higher sensitivity than conventional tools for determining the viability of donated lungs, as well as assessing the onset of rejection before permanent structural changes in the lungs become apparent.

1.3. References

1. Toronto Lung Transplant Group. Unilateral Lung Transplantation for Pulmonary Fibrosis. *New England Journal of Medicine*. 1986;314(18):1140-1145. doi:10.1056/NEJM198605013141802

2. Trulock EP, Christie JD, Edwards LB, et al. Registry of the International Society for Heart and Lung Transplantation: twenty-fourth official adult lung and heart-lung transplantation report-2007. *J Heart Lung Transplant*. 2007;26(8):782-795. doi:10.1016/j.healun.2007.06.003

3. Meyers BF, Lynch J, Trulock EP, Guthrie TJ, Cooper JD, Patterson GA. Lung transplantation: a decade of experience. *Ann Surg*. 1999;230(3):362-370; discussion 370-371.

4. Limbos MM, Joyce DP, Chan CK, Kesten S. Psychological functioning and quality of life in lung transplant candidates and recipients. *Chest*. 2000;118(2):408-416.

5. Yusen RD, Edwards LB, Dipchand AI, et al. The Registry of the International Society for Heart and Lung Transplantation: Thirty-third Adult Lung and Heart–Lung Transplant Report—2016; Focus Theme: Primary Diagnostic Indications for Transplant. *The Journal of Heart and Lung Transplantation*. 2016;35(10):1170-1184. doi:10.1016/j.healun.2016.09.001

6. Levitsky J, Goldberg D, Smith AR, et al. Acute Rejection Increases Risk of Graft Failure and Death in Recent Liver Transplant Recipients. *Clinical Gastroenterology and Hepatology*. 2017;15(4):584-593.e2. doi:10.1016/j.cgh.2016.07.035

7. Kim WR, Lake JR, Smith JM, et al. OPTN/SRTR 2017 Annual Data Report: Liver. *American Journal of Transplantation*. 2019;19(S2):184-283. doi:10.1111/ajt.15276

8. de Perrot M, Liu M, Waddell TK, Keshavjee S. Ischemia–Reperfusion–induced Lung Injury. *Am J Respir Crit Care Med*. 2003;167(4):490-511. doi:10.1164/rccm.200207-670SO

9. Christie JD, Carby M, Bag R, Corris P, Hertz M, Weill D. Report of the ISHLT Working Group on Primary Lung Graft Dysfunction Part II: Definition. A Consensus Statement of the International Society for Heart and Lung Transplantation. *The Journal of Heart and Lung Transplantation*. 2005;24(10):1454-1459. doi:10.1016/j.healun.2004.11.049

10. Wilhelm MJ, Pratschke J, Beato F, et al. Activation of the heart by donor brain death accelerates acute rejection after transplantation. *Circulation*. 2000;102(19):2426-2433.

11. Verleden SE, Ruttens D, Vandermeulen E, et al. Restrictive chronic lung allograft dysfunction: Where are we now? *The Journal of Heart and Lung Transplantation*. 2015;34(5):625-630. doi:10.1016/j.healun.2014.11.007

12. Perrot M de, Bonser RS, Dark J, et al. Report of the ISHLT Working Group on Primary Lung Graft Dysfunction Part III: Donor-Related Risk Factors and Markers. *The Journal of Heart and Lung Transplantation*. 2005;24(10):1460-1467. doi:10.1016/j.healun.2005.02.017

13. Lee JC, Christie JD. Primary Graft Dysfunction. *Proceedings of the American Thoracic Society*. 2009;6(1):39-46. doi:10.1513/pats.200808-082GO

14. Avlonitis VS, Wigfield CH, Golledge HDR, Kirby JA, Dark JH. Early hemodynamic injury during donor brain death determines the severity of primary graft dysfunction after lung transplantation. *Am J Transplant*. 2007;7(1):83-90. doi:10.1111/j.1600-6143.2006.01593.x

15. McKeown DW, Bonser RS, Kellum JA. Management of the heartbeating brain-dead organ donor. *Br J Anaesth*. 2012;108(suppl 1):i96-i107. doi:10.1093/bja/aer351

16. van der Hoeven JAB, Ter Horst GJ, Molema G, et al. Effects of Brain Death and Hemodynamic Status on Function and Immunologic Activation of the Potential Donor Liver in the Rat. *Ann Surg*. 2000;232(6):804-813.

17. Rostron AJ, Avlonitis VS, Cork DMW, Grenade DS, Kirby JA, Dark JH. Hemodynamic resuscitation with arginine vasopressin reduces lung injury after brain death in the transplant donor. *Transplantation*. 2008;85(4):597-606. doi:10.1097/TP.0b013e31816398dd

18. Dimopoulou I, Tsagarakis S, Anthi A, et al. High prevalence of decreased cortisol reserve in brain-dead potential organ donors. *Crit Care Med*. 2003;31(4):1113-1117. doi:10.1097/01.CCM.0000059644.54819.67

19. Follette DM, Rudich SM, Babcock WD. Improved oxygenation and increased lung donor recovery with high-dose steroid administration after brain death. *J Heart Lung Transplant*. 1998;17(4):423-429.

20. Shemie SD, Ross H, Pagliarello J, et al. Organ donor management in Canada: recommendations of the forum on Medical Management to Optimize Donor Organ Potential. *CMAJ*. 2006;174(6):S13-32. doi:10.1503/cmaj.045131

21. Kazemi M, Tabei SMB, Najafizadeh K, Mehrabi Sisakht J, Milani S, Khosravi MB. Evaluation of the Effect of Ascorbic Acid Administration on Gene Expression Level of IL-6 and TNF-α Cytokines in Deceased Donors. *Iran J Allergy Asthma Immunol*. 2015;14(2):149-157.

22. Oudemans-van Straaten HM, Man AMS, de Waard MC. Vitamin C revisited. *Crit Care*. 2014;18. doi:10.1186/s13054-014-0460-x

23. Tyml K, Li F, Wilson JX. Delayed ascorbate bolus protects against maldistribution of microvascular blood flow in septic rat skeletal muscle. *Crit Care Med*. 2005;33(8):1823-1828.

24. Straznicka M, Follette DM, Eisner MD, Roberts PF, Menza RL, Babcock WD. Aggressive management of lung donors classified as unacceptable: excellent recipient survival one year after transplantation. *J Thorac Cardiovasc Surg*. 2002;124(2):250-258.

25. Christmas AB, Bogart TA, Etson KE, et al. The reward is worth the wait: a prospective analysis of 100 consecutive organ donors. *Am Surg*. 2012;78(3):296-299.

26. Andreasson ASI, Dark JH, Fisher AJ. Ex vivo lung perfusion in clinical lung transplantation—State of the art. *Eur J Cardiothorac Surg*. 2014;46(5):779-788. doi:10.1093/ejcts/ezu228

27. Wierup P, Haraldsson A, Nilsson F, et al. Ex vivo evaluation of nonacceptable donor lungs. *Ann Thorac Surg*. 2006;81(2):460-466. doi:10.1016/j.athoracsur.2005.08.015

28. Cypel M, Yeung JC, Liu M, et al. Normothermic ex vivo lung perfusion in clinical lung transplantation. *N Engl J Med*. 2011;364(15):1431-1440. doi:10.1056/NEJMoa1014597

29. Mariani AW, Pêgo-Fernandes PM, Abdalla LG, Jatene FB. Ex vivo lung reconditioning: a new era for lung transplantation. *Jornal Brasileiro de Pneumologia*. 2012;38(6):776-785. doi:10.1590/S1806-37132012000600015

30. Noda K, Shigemura N, Tanaka Y, et al. Hydrogen preconditioning during ex vivo lung perfusion improves the quality of lung grafts in rats. *Transplantation*. 2014;98(5):499-506. doi:10.1097/TP.0000000000000254

31. Shaghaghi H, Kadlecek S, Siddiqui S, et al. Ascorbic acid prolongs the viability and stability of isolated perfused lungs: A mechanistic study using 31P and hyperpolarized 13C nuclear magnetic resonance. *Free Radic Biol Med*. 2015;89:62-71. doi:10.1016/j.freeradbiomed.2015.06.042

32. Cypel M, Rubacha M, Yeung J, et al. Normothermic Ex Vivo Perfusion Prevents Lung Injury Compared to Extended Cold Preservation for Transplantation. *American Journal of Transplantation*. 2009;9(10):2262-2269. doi:10.1111/j.1600-6143.2009.02775.x

33. Ingemansson R, Eyjolfsson A, Mared L, et al. Clinical Transplantation of Initially Rejected Donor Lungs After Reconditioning Ex Vivo. *The Annals of Thoracic Surgery*. 2009;87(1):255-260. doi:10.1016/j.athoracsur.2008.09.049

34. Lakkis FG, Sayegh MH. Memory T cells: a hurdle to immunologic tolerance. *J Am Soc Nephrol*. 2003;14(9):2402-2410.

35. Pratt JR, Basheer SA, Sacks SH. Local synthesis of complement component C3 regulates acute renal transplant rejection. *Nature Medicine*. 2002;8(6):582-587. doi:10.1038/nm0602-582

36. Bhorade SM, Stern E. Immunosuppression for Lung Transplantation. *Proc Am Thorac Soc*. 2009;6(1):47-53. doi:10.1513/pats.200808-096GO

37. Korom S, Boehler A, Weder W. Immunosuppressive therapy in lung transplantation: state of the art. *Eur J Cardiothorac Surg*. 2009;35(6):1045-1055. doi:10.1016/j.ejcts.2009.02.035

38. Floreth T, Bhorade SM. Current Trends in Immunosuppression for Lung Transplantation. *Semin Respir Crit Care Med*. 2010;31(2):172-178. doi:10.1055/s-0030-1249112

39. Meyer KC, Raghu G, Verleden GM, et al. An international ISHLT/ATS/ERS clinical practice guideline: diagnosis and management of bronchiolitis obliterans syndrome. *European Respiratory Journal*. 2014;44(6):1479-1503. doi:10.1183/09031936.00107514

40. Morlion B, Knoop C, Paiva M, Estenne M. Internet-based home monitoring of pulmonary function after lung transplantation. *Am J Respir Crit Care Med*. 2002;165(5):694-697. doi:10.1164/ajrccm.165.5.2107059

41. Otulana BA, Higenbottam T, Ferrari L, Scott J, Igboaka G, Wallwork J. The use of home spirometry in detecting acute lung rejection and infection following heart-lung transplantation. *Chest*. 1990;97(2):353-357.

42. Bjørtuft O, Johansen B, Boe J, Foerster A, Holter E, Geiran O. Daily home spirometry facilitates early detection of rejection in single lung transplant recipients with emphysema. *Eur Respir J*. 1993;6(5):705-708.

43. Martinu T, Chen D-F, Palmer SM. Acute Rejection and Humoral Sensitization in Lung Transplant Recipients. *Proceedings of the American Thoracic Society*. 2009;6(1):54-65. doi:10.1513/pats.200808-080GO

44. Van Muylem A, Melot C, Antoine M, Knoop C, Estenne M. Role of pulmonary function in the detection of allograft dysfunction after heart-lung transplantation. *Thorax*. 1997;52(7):643-647.

45. Worthy SA, Park CS, Kim JS, Müller NL. Bronchiolitis obliterans after lung transplantation: high-resolution CT findings in 15 patients. *American Journal of Roentgenology*. 1997;169(3):673-677. doi:10.2214/ajr.169.3.9275875

46. Leung AN, Fisher K, Valentine V, et al. Bronchiolitis obliterans after lung transplantation: detection using expiratory HRCT. *Chest*. 1998;113(2):365-370.

47. Verleden GM, Raghu G, Meyer KC, Glanville AR, Corris P. A new classification system for chronic lung allograft dysfunction. *The Journal of Heart and Lung Transplantation*. 2014;33(2):127-133. doi:10.1016/j.healun.2013.10.022

48. Sato M, Waddell TK, Wagnetz U, et al. Restrictive allograft syndrome (RAS): A novel form of chronic lung allograft dysfunction. *The Journal of Heart and Lung Transplantation*. 2011;30(7):735-742. doi:10.1016/j.healun.2011.01.712

49. Stewart S, Fishbein MC, Snell GI, et al. Revision of the 1996 Working Formulation for the Standardization of Nomenclature in the Diagnosis of Lung Rejection. *The Journal of Heart and Lung Transplantation*. 2007;26(12):1229-1242. doi:10.1016/j.healun.2007.10.017

Chapter 2: An Introduction to Hyperpolarized Carbon-13 Magnetic Resonance Imaging

Abstract

Until recently, molecular imaging using magnetic resonance (MR) has been limited by the modality's low sensitivity, especially with non-proton nuclei. The advent of hyperpolarized (HP) MR overcomes this limitation by substantially enhancing the signal of certain biologically important probes through a process known as external nuclear polarization, enabling real-time assessment of tissue function and metabolism. The metabolic information obtained by HP MR imaging holds significant promise in the clinic, where it could play a critical role in disease diagnosis and therapeutic monitoring. This chapter will provide a comprehensive overview of the developments made in the field of hyperpolarized MR, including advancements in polarization techniques and delivery, probe development, pulse sequence optimization, characterization of healthy and diseased tissues, and the steps made towards clinical translation.

This chapter has been adapted from Siddiqui et al., 'The use of hyperpolarized carbon-13 magnetic resonance for molecular imaging' published in Advanced Drug Delivery Reviews, Vol. 113:3-23.

2.1. Introduction

Molecular imaging refers to a gamut of imaging modalities that—as succinctly defined by the Radiological Society of North America (RSNA)—"directly or indirectly monitor or record the spatiotemporal distribution of molecular or cellular processes for biochemical, biologic, diagnostic, or therapeutic applications"[1]. Numerous modalities fit this description, most prominently positron emission tomography (PET) and single photon emission computed tomography (SPECT), both of which are commonly used in the clinic for diagnosing various disorders and monitoring therapeutic response[2]. More recently, fluorescence and bioluminescence optical imaging have allowed high-sensitivity molecular imaging in pre-clinical research, while computed tomography (CT)—traditionally considered a structural imaging tool—is now being used as a molecular imaging modality with the advent of cell- and tissue-specific nanoparticles and as a combined modality with PET or SPECT[3,4].

Clinical use of magnetic resonance imaging (MRI) has largely been limited to structural assessment. However, proton (^{1}H), sodium (^{23}Na), phosphorus (^{31}P), and carbon (^{13}C) MRI/ nuclear magnetic resonance (NMR) are extensively used as molecular imaging tools in pre-clinical studies in animals and cells. In these studies, the modality's foremost limitation—its low sensitivity—can be overcome by the use of longer scan times and signal averaging[5–7]. As such, molecular MRI/NMR using conventional thermally polarized nuclei is limited to probing quasi-steady-state metabolism. The advent of hyperpolarized (HP) MRI/NMR overcomes this limitation by substantially enhancing the signal of certain biologically important probes through a process known as external nuclear polarization, enabling real-time molecular imaging with unprecedented temporal resolution. The information obtained by HP MR has significant promise in the clinic, where imaging-derived metabolomics could play a critical role in disease diagnosis and therapeutic monitoring.

Hyperpolarized MR is a burgeoning field in which investigators continue to make rapid advancements in an array of areas, which include polarization techniques and delivery, probe development, pulse sequence optimization, characterization of healthy and diseased tissues, and clinical translation. In light of the rapidly changing and multifarious nature of this technology, this review aims to provide a comprehensive overview of the current state of molecular imaging using HP MR, the developments that have led to this point, and the central challenges that hyperpolarized technology faces as it moves towards making a clinical impact.

2.1.1. Molecular Imaging using Non-MR Modalities

Several well-established molecular imaging techniques are actively used in basic and clinical research. This section describes applications of each technology, their advantages and limitations, and how they differ from HP MRI/NMR.

2.1.2. PET and SPECT

Positron emission tomography (PET) and single photon emission computed tomography (SPECT) use radioactively labeled metabolic tracers (e.g., 18F-FDG,) to probe the cellular uptake of their analogous biologically relevant molecules (e.g., glucose). Both techniques are widely used in clinical[2,8,9] and pre-clinical[10–13] scenarios for a broad range of applications including, but not limited to, the diagnosis, staging, and monitoring of a variety of cancers[14–18], drug development—e.g., probing the bio-distribution of new pharmaceuticals[19]— and neuroimaging[20].

Although PET and SPECT provide high sensitivity for detection, they suffer from poor spatial resolution[4,21]. As a result CT or MRI are used for accurate reconstruction and anatomical localization of tracers[22]. Another major shortcoming of both modalities is that they are limited to revealing abnormalities in the uptake or retention of the tracers; they are unable to reveal changes in downstream metabolites that may be crucial to the diagnosis and staging of diseases.

On the other hand, hyperpolarized MRI—which probes analogous pathways to PET—highlights alterations in downstream metabolites using their unique ^{13}C NMR resonance frequencies, thus providing non-invasive interrogation of the size of metabolite pools and the flux through their corresponding pathways[23]. However, unlike PET and SPECT, absolute quantification of HP MR substrates can be challenging due to variations in polarization level and the use of super physiological concentrations of administered agents[24]. Furthermore, despite the large signal gains achieved using hyperpolarization, the near-unity photon detection efficiency of radionuclide agents is not achievable. Nevertheless, hyperpolarized probes can provide complementary imaging information that address the same diagnostic imaging goals as PET and SPECT.

2.1.3. Fluorescence and Bioluminescence Tomography

Optical tomography is widely used for the preclinical study of biology and pathology. The major optical techniques, fluorescence and bioluminescence tomography, are based on different underlying mechanisms, but have similar applications and limitations. Fluorescence tomography uses injected or genetically inserted dyes and proteins which fluoresce at different wavelengths than normal tissue to tag specific cells or molecules and track their distribution, while bioluminescence tomography utilizes the intrinsic light emission of select molecules to similar effect[4,25]. In the latter case, light is produced when the light emitting pigment luciferin is catalyzed by the enzyme luciferase, which is produced by genetically modified cells that synthesize the enzyme.

Optical imaging benefits from minimal background tissue radiation and high photon detection efficiency, and therefore generally has an excellent signal-to-noise (SNR). Both modalities offer spatial resolution of approximately 2-3mm. However, the need for genetic modification of the cells to allow targeted molecular imaging limits their use within human patients; this is particularly an issue with bioluminescence imaging. Additionally, optical techniques suffer from low tissue penetrance and the related need for a high concentration of imaging agent to successfully perform studies of deeper tissue. There has recently been an interest in using fluorescent probes in applications that circumvent this limitation, such as for more accurate identification of malignancies during surgical resection[26]. While PET and hyperpolarized MRI interrogate analogous pathways, those targeted by optical imaging are typically very different, and as such the modality can provide distinct and perhaps complementary molecular information to the former two modalities.

2.1.4. Computed Tomography

Computed tomography (CT) has not traditionally been considered as a molecular imaging technique. However, recent developments in nanoparticle-bound contrast agents (CAs) have allowed for selective imaging of specific cell tissues and molecules using CT. Iodinated nanoparticles, for example, can change the biodistribution of the iodine upon injection depending on the characteristics of the nanoparticle. This method has shown promise both in improving upon traditional CAs in blood pool imaging and in specifically labeling certain cell types in various applications including studying angiogenesis in tumor growth and response to therapy[27–31]. Iodinated nanoparticles have also been labeled with antibodies to increase their molecular specificity to probe expression of particular proteins[32]. Gold nanoparticles have also become popular due to their easy synthesis and low toxicity[33]. These particles have also shown promise in vascular imaging, tumor imaging, and bone tissue damage imaging[3,34–37].

Nanoparticle based CAs are an area of interest for industry due to the wide availability of clinical CT machines, and there are currently several clinical trials examining the safety of gold nanoparticle based contrast agents[38]. Although the use of iodine and gold nanoparticles is promising in molecular imaging, their primary role seems to be to provide better structural contrast and anatomic localization by targeting specific proteins or cell markers, as opposed to deriving metabolic or functional information. Furthermore, ionizing radiation remains a fundamental limitation of this technology when used for clinical studies.

2.2. Hyperpolarized MRI

Hyperpolarization refers to a process in which certain nuclei are aligned to a degree many orders of magnitude greater than is normally achievable under *in vivo* conditions. This leads to a magnetic resonance signal that greatly exceeds that which is otherwise available and makes qualitatively different applications possible, including imaging of gases and low-concentration biological molecules. If the non-equilibrium hyperpolarized state is to be useful for medical imaging, the alignment must persist long enough for the substance to be administered, arrive at the target organ or system, and perhaps be taken into cells and/or metabolized. Typically, the persistent state can be achieved only if several conditions are met. First, the nuclei must be what is known as “spin-½”. Spin-½ nuclei have two distinct quantum states of orientation with respect to a magnetic field; all other classes of nuclei either have no magnetic moment (and are therefore invisible in MRI) or are susceptible to rapid reorientation by the large electric field gradients present in molecules and during atomic or molecular collisions. Second, the nuclei must be relatively segregated from all other magnetic moments, including unpaired electrons or magnetic nuclei on the same molecule. Third, any residual magnetic interactions with the nucleus to be hyperpolarized must be limited in duration or frequently randomized in direction, again in order to prevent loss of alignment in an extended nuclear precession around the depolarizing field.

As a practical matter, this limits hyperpolarization with biological applications to a few nuclear species that are found in *in vivo* (^{13}C, ^{15}N, ^{31}P and potentially ^{1}H), those found in some molecules that are not acutely toxic (^{19}F, ^{29}Si) and the two biologically inert gases ^{3}He and ^{129}Xe. Of these, the gases have been used primarily for imaging of lung function, although molecular biosensors and imaging agents based on ^{129}Xe have been proposed. Agents based on the other nuclei (primarily ^{13}C) have been studied more extensively in molecular imaging applications.

Two straightforward methods have been developed for transferring polarization from light to atomic nuclei, and have been used extensively for atomic gases[39,40]. Unfortunately, these techniques are not applicable to molecules[41]. This is primarily because the strong coupling between coherent rotational motion and nuclear spins cases rapid loss of spin alignment, but practical issues of chemical reactivity and short-lived electronic excited states are also difficult to overcome. There are two alternative approaches, however, that can lead to polarization of order unity of selected nuclei in biologically active compounds. These methods are dynamic nuclear polarization (DNP), and parahydrogen-induced polarization (PHIP).

2.2.1. Dynamic Nuclear Polarization (DNP)

DNP refers to a process in which the alignment of an unpaired electron is achieved at thermal equilibrium, and this alignment is transferred to a nearby nucleus via a process analogous to the Overhauser effect[42,43]. In order to prepare a sample suitable for DNP, the molecule of interest is mixed with a small amount (1 part in 100 or less) of stable free radical that supplies the unpaired electron spin. This mixture is then placed in conditions of reduced temperature and elevated magnetic field sufficient to achieve near-complete electron alignment; as a rule of thumb, the magnetic field (in Tesla) divided by the sample temperature (in Kelvin) must be approximately 1 to achieve full alignment. As an intimate mixture of radical and target molecule is necessary for spin order transfer, and favorable DNP conditions generally imply a frozen sample, additional components may be required to assure a homogeneous (glassed) mixture [44].

The transfer of polarization from electron to nucleus is accomplished by means of a microwave driving field tuned near the resonance frequency of the free electron in the chosen magnetic field. The mechanism of polarization transfer is complex and may differ between samples; however, the electron-nuclear interaction is typically described as one of three processes: the solid effect, the cross effect, and thermal mixing. The solid effect refers to a mechanism in which two closely-spaced magnetic dipoles, one electron and one nucleus, simultaneously invert orientations with respect to the field. Because the vast majority of electrons are aligned, this results in the net polarization of the nuclear ensemble. This process is greatly suppressed by the large energy difference between electronic and nuclear Zeeman transitions, and is only relevant because of the very large number of coupled electron and nuclear pairs available in the sample. The cross effect refers to a related process in which one nucleus and two electrons, differing in frequency by approximately the nuclear Zeeman frequency, are excited simultaneously. Because this process is nearly energy-conserving, it is resonant over a duration consistent with typical solid state electron-nuclear couplings and is therefore quite rapid. However, the number of coupled three-spin systems with the appropriate resonance frequencies is relatively small; the relative contribution of solid effect and cross effect polarization is therefore dependent on the details of the sample's frozen state and external conditions such as temperature and magnetic field[45,46].

Under hyperpolarization conditions useful for molecular imaging studies, the distinction between the above two processes (and those involving more electrons) is obscured by the strong couplings between closely-spaced radical molecules. The polarization process is therefore best described by thermodynamic state transitions in the band-like electron system and couplings to the nuclear system. Incorporating aspects of the other two processes, this theory is termed thermal mixing. Although lacking an intuitive, conceptual explanation, the theory is well-established and successful, and is described in detail in the literature[45,47,48].

2.2.2. Practical Aspects of DNP for Biomolecules

In choosing appropriate conditions for efficient DNP, it is important to consider the magnetic properties of the molecule to be polarized. Small biological molecules typically consist of carbon, oxygen and hydrogen, often contain nitrogen, and sometimes contain other elements (e.g., phosphorus or iron). As a general rule, a nucleus that is suitable for hyperpolarization is spin-½ (to eliminate rapid loss of alignment due to electric field gradients)[49] and is distant from other magnetic nuclei. The latter consideration is necessary to avoid loss of alignment due to strong magnetic interactions in solution, and as it is usually impossible to eliminate all intramolecular magnetism, small molecules (in which interactions change direction frequently due to molecular reorientation) are more successful than large ones. Taken together, these characteristics of polarizable nuclei have suggested use of the spin-½ isotope ^{13}C, as it can be incorporated into nearly all biomolecules in the magnetically isolated carbonyl, quaternary and carboxylic acid forms. Small carboxylic acids in particular are near-ubiquitous as TCA cycle intermediates, amino acids and in many other biologically central functions. For this reason, nearly all of the *in vitro* and *in vivo* work described in this review makes use of this class of molecules.

Suitability of a molecule for hyperpolarization by DNP is also determined by the physical properties of the bulk or dissolved compound. Because the process takes place at cryogenic temperatures, all molecules of interest are in the solid phase; however, the intimate radical/biomolecule mixture necessary is best achieved through dissolution in the liquid. Substances that are gases at room temperature must be cooled or pressurized before mixture, and those that are solids must be co-dissolved with the radical in a suitable solvent. Furthermore, the tendency of many solutions to segregate upon freezing must be avoided, typically by transitioning past the freezing temperature very quickly, and in many cases including a ‘glassing agent’ in solutions that would otherwise crystalize.

Many molecules of interest, particularly those with hydrophobic regions, are sufficiently insoluble in water that the sample to be hyperpolarized must also include additional ingredients to facilitate increased concentration. Thus, although some general strategies are useful in classes of similar molecules, each sample preparation is somewhat individual and is optimized experimentally. A detailed discussion of this process is beyond the scope of this article, but it is described in detail in an excellent review [50]. It is worth noting that one compound, pyruvic acid, is highly favorable from all of the above points of view; it is a small (a three-carbon chain, molecular weight 88 Da) carboxylic acid, when ^{13}C-labeled in the 1 position the nucleus is remarkably isolated (the nearest magnetic nucleus is three bonds away) such that relaxation of the hyperpolarized state is slow[51], the neat acid is liquid at room temperature and glasses without additional ingredients when frozen. Furthermore, pyruvate is metabolized rapidly by most cells, and the metabolic fate is indicative of cellular redox state and other biologically important factors. As is apparent in subsequent sections of this article, this fortuitous set of circumstances has led to pyruvate's central role in the development of hyperpolarized agents.

The final aspect of DNP hyperpolarization under the user's control is the choice of radical species. In the development of the technology, several types of radical were explored, with considerable attention paid to nitroxide moieties and those derived from the triphenylmethyl (trityl) radical. In progressing to *in vivo* and human applications, the latter has become very commonly used, because it has the long electron T_1 and narrow linewidth required to facilitate high polarization under the conditions of low temperature and moderate microwave power used in commercial instruments. A hydrophilic derivative, termed 'OX063' is widely used for pyruvate and similarly hydrophilic substrates[52]. A slightly modified version, known as 'AH111501' or simply 'EPA' (for Electron Paramagnetic Agent), is used in human studies due to the ease with which it can be removed at acidic pH by simple filtration[53]. Other substrate species, including those with hydrophobic properties, are best polarized by other trityl derivatives with less polar functional groups, such as the acidified Finland species successfully used for DNP of frozen Xenon[54].

However, a wide variety of other radicals, including those with similar electronic properties, may be suitable as well. Radicals derived from BDPA have been shown to behave similarly to the trityl family[52,55] and may be synthesized in a more straightforward manner[56]. Nitrioxide radicals (eg., TEMPO[52]) are well suited to higher temperature DNP and hyperpolarization of hydrogen, including that of water[57–59]. A variety of biradical species have been explored, with the hope of maximizing the cross effect[60–62] with judicious chemical shift and coupling values. In pyruvate, there has even been exploration of metastable radical species induced in the frozen pyruvate sample itself by ultraviolet light[63]. Although as yet not consistent with the high polarization required for effective *in vivo* use, such a strategy is very appealing as no additional species are required for DNP.

A few other experimental details have been found to affect the signal level or utility of DNP-derived hyperpolarized species; we mention these here and leave the details to the referenced literature. Inclusion of small concentrations of Gd chelates in the sample has been shown in increase polarization substantially, perhaps through its effect on radical electron T_1[64], although the potential for accelerated loss of polarization after dissolution must be considered[65]. The dependence of polarization on magnetic field and temperature have been explored as well, with the finding that lower temperature and higher field, while more technically challenging, yield generally superior results but require longer polarization times (typical small molecules can take anywhere from less than an hour to several hours to achieve maximum polarization at 1.4K and 3.3T)[66,67]. This is not found to be true in all systems, however. Finally, certain hyperpolarized nuclei, especially those neighboring a nitrogen atom, require transport at elevated magnetic field to avoid substantial loss of polarization[68].

2.2.3. Parahydrogen-Induced Polarization (PHIP)

Two alternate method for liquid state sample hyperpolarization exist, termed Chemically Induced Dynamic Nuclear Polarization (CIDNP)[69,70] and Parahydrogen-Induced Polarization (PHIP)[71,72]. The former mechanism is based on a nuclear state dependence of the recombination rates of optically generated radicals; although it remains an active research area 50 years after its discovery, the level of polarization achieved and the diversity of target compounds are not yet such that *in vivo* or clinical molecular imaging applications can be considered. Compounds polarized using parahydrogen, on the other hand, have been used successfully in cell and animal studies[73–75]. Although recent efforts have been made to design an open-source PHIP polarizer[76], in general the adoption of PHIP techniques currently lags behind DNP because of the lack of commercial instruments, difficulties polarizing small metabolic compounds because of the required chemical reaction, and the lack of development in ensuring a pure and safe end-product. Nonetheless, the method has fundamental advantages with respect to production rate and cost that may justify more widespread use in the near future.

Parahydrogen is the nuclear singlet state of hydrogen gas. Although not hyperpolarized, the gas contains a large degree of nuclear spin order and is easily produced at modestly reduced temperature through contact with a microscopically heterogeneous magnetic substance[77,78]. After undergoing a catalyst-mediated, pairwise addition to an unsaturated substrate, this spin order often persists to a large degree. Subsequent application of a specialized NMR pulse sequence, analogous to the commonly-used INEPT polarization transfer technique[79], results in near-unity transfer of spin order to hyperpolarization of a nearby ^{13}C [80–83]. Alternately, in a process called field cycling, the transfer may be effected by reducing the magnetic field such that the chemical shift difference approximates the internuclear scalar couplings[84,85]. In either case, a level of polarization approaching or even exceeding that which is achievable using DNP[86] has led to the most detailed solution state hyperpolarized images produced to date[74,84].

Use in metabolic imaging, however, has been limited by the need for an unsaturated precursor of the agent of interest. In many cases this precursor does not exist or is not stable. Even in cases where a suitable precursor exists (e.g., for pyruvate or acetate), care must be taken to ensure that only the desired hydrogenation end-product is produced[87–89]. Furthermore, the couplings between the nucleus to be hyperpolarized and the para proton pair must differ by an amount that is large compared to other couplings to the target nucleus[90]. These requirements can generally be addressed by careful choice of reaction conditions and catalyst and by replacing nearby hydrogen by deuterium (or as appropriate, ^{14}nitrogen by the less magnetic ^{15}N). Details of the experimental design and catalyst choice can be found in the referenced literature, but we note that most experimenters have made use of a homogeneous Rh-based bis-phosphene catalyst[75,86,87,91], a plunging liquid jet reactor [92] in an ambient parahydrogen atmosphere of several bar, and somewhat elevated temperature (to speed the hydrogenation reaction)[86,93,94]. More recently, PHIP using a heterogeneous phase catalyst—consisting of platinum nanoparticles capped with glutathione ligands—was demonstrated, enabling easier removal of the toxic catalyst, a necessity for clinical imaging[95].

Although not significantly metabolized *in vivo*, the first biomedical application of PHIP agents utilized hydroxyethyl propionate as an angiography or perfusion measurement agent[74,84]. Use in molecular imaging was first demonstrated using succinate or its esters[75,96,97], which are two-step hydrogenation products of acetylene dicarboxylate. Phospholactate has also been efficiently polarized using this method[87], although biological activity has not yet been shown.

Two important modifications to this basic scheme have been introduced recently, and each has the potential to dramatically improve the PHIP process' flexibility and its utility in imaging. Reineiri *et al*. introduced a method to overcome the lack of suitable precursors for pyruvate and acetate[88]. In this scheme, an allyl or vinyl ester of the target molecule is para-hydrogenated, and the polarization transfer sequence operates over the ester bond to hyperpolarize the labeled carboxyl carbon. Finally, the ester is hydrolyzed, yielding a mixture of the hyperpolarized target and ethyl or propyl alcohol. In addition to allowing PHIP of pyruvate, this recipe may be generally applicable to carboxylic acids, greatly increasing the biological uses of PHIP.

Another novel technique was recently introduced by Adams *et al*.[98], in which the spin order of parahydrogen is transferred to a target molecule during the residence time of a short-lived, catalyst-mediated complex. This method, termed 'NMR Signal Amplification by Reversible Exchange', or NMR-SABRE, has two significant advantages over traditional PHIP. First, the need for an unsaturated precursor is relaxed in that no permanent chemical modification of the target molecule occurs. This simplifies synthetic requirements while broadening the set of candidate compounds. Second, the same solution may be repolarized at will, subject only to availability of parahydrogen and catalyst spoiling.

SABRE-polarized compounds have not yet been used *in vivo* for metabolic imaging, and isolation of the target compound remains a technical challenge. Nonetheless, these advantages (in addition to the low cost and ~1s polarization time characteristic of PHIP) suggest a variety of very useful applications in the near future.

2.3. Hyperpolarized MRI Acquisition Techniques

2.3.1. Hardware and Equipment

The most important development in the field of DNP was the development of a fast dissolution method that rapidly melted the frozen polarized sample with minimal loss of polarization into a liquid state that could then be quickly delivered to an animal or specimen in the imaging magnet[99,100]. This is accomplished by flushing the frozen sample with the dissolution solvent at high pressure (~10 bar) and temperature (~ 180 ^{o}C). The most commonly used DNP polarizer that uses this dissolution method is the commercially available Hypersense polarizer (Oxford Instruments, United Kingdom). Generally it can polarize up to ~200 μL of sample, limiting its use to studies in small animals. More recently, a larger commercially-available polarizer—SpinLab (General Electric)—was developed with a much greater throughput (4 simultaneous samples of volume greater than 1mL), enabling HP imaging in large animals and humans[101,102].

The gyromagnetic ratio of ^{13}C (γ_C) is approximately four times smaller than that of the proton. As such, the MR system must be equipped with a broadband RF amplifier to transmit and receive the NMR signal for multinuclear spectroscopy and imaging. This option is available for many clinical and preclinical scanners. Additionally, the MR system needs to be equipped with transmit/receive coils tuned to the proper frequency. For hyperpolarized ^{13}C studies, surface coils[103] have been commonly used for many applications including cardiac[104], brain[105] and subcutaneous tumor[106,107] imaging and spectroscopy. The key advantage of surface coils is their superior sensitivity over a small region-of-interest. However, surface coils suffer from poor B_1 homogeneity and sensitivity profiles. Alternatively, a setup consisting of a volume transmit, surface receive coil can be used for homogenous power transmission[101]. Volume transmit/receive coils offer superior field homogeneity on both transmit/receive ends and, as such, are well suited for imaging the larger regions of interest typically used in abdominal and thoracic applications[108,109]. For small animal and perfused cell applications, cryocoils have shown to improve the SNR, although the degree of improvement is difficult to determine with certainty[109,110]; imaging researchers have reported SNR increases of 4-7 at 9.4T, consistent with theoretical considerations under low-loading conditions[109]. Utility of the cryocoils is limited due to high cost and diminishing gains for larger animals and humans, in which body noise typically dominates.

2.3.2. Pulse Sequence and Imaging Considerations

Although hyperpolarization dramatically increases the initially available signal amplitudes, the MR data acquisition is highly affected by irreversible signal losses caused by T_1 relaxation back to thermal equilibrium and RF pulse excitations. This limits signal availability to only a brief period after introduction of the agent. Thus, the timing of the data acquisition is of key importance in order to obtain metabolite images with maximum signal-to-noise. For many hyperpolarized substrates, a 25-second delay from the start of the injection has been found to be appropriate as it approximately corresponds to the time of peak amplitude for the downstream metabolites (Figure 2.1)[111]. Accounting for signal dynamics is also important because for the image reconstruction it is typically assumed that the longitudinal magnetization is in steady state for each excitation; departure from this condition can introduce image artifacts or blurring. Variable flip-angle strategies have been proposed to ameliorate this problem, in which the flip angle is increased with each excitation to compensate for the reduction in available longitudinal magnetization. The goal of this strategy is to maintain a constant transverse magnetization throughout the image acquisition[111]. This approach requires accurate calibration of the coil's RF power, which is typically done by placing a labeled ^{13}C phantom inside the coil next to the subject prior to administration of the hyperpolarized agent. Ideally, the coil's B_1 map should also be obtained and incorporated into the reconstruction to improve image fidelity[108,112]. This is particularly important when single-channel receive surface coils or multichannel phased-array receive coils are used for parallel imaging. More difficult to deal with is the potential for severe flow artifacts due to the presence of high concentrations of the administered hyperpolarized agent in the blood pool. Recently, a pair of symmetric flow-sensitizing gradients have been added to imaging pulse sequences in applications such as cardiac and abdominal imaging to suppress image artifacts caused by rapidly flowing blood and thereby improve the accuracy of the spatial information[113,114].

In order to address these challenges and limitations, many pulse sequences have been designed and implemented over the past few years that offer significant improvements with respect to standard gradient echo or spin echo schemes. This has been possible by exploiting the long T_2 and T_2^* relaxation times of ^{13}C species in almost all organs[74,115–118] as well as the sparse nature of the NMR spectrum in which chemical shifts of the ^{13}C species of interest span a wide range of the NMR spectrum (~100ppm)[119]. The most desirable imaging pulse sequences achieve superior spatial coverage as well as high temporal resolution while providing three dimensional dynamic spectroscopic data for accurate and meaningful measurement of cellularity and metabolic pathways.

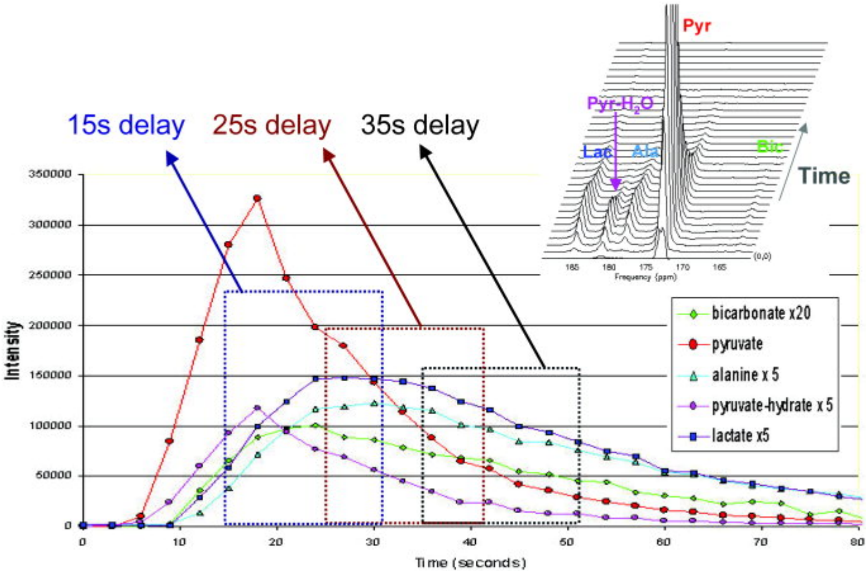

Figure 2.1: Signal-time courses of multiple metabolites derived from dynamic HP [1-^{13}C]pyruvate spectroscopy in a rat. The boxed regions specify the time window for a 17-s CSI acquisition at the following time delays: 15 s, 25 s, and 35 s. The choice of delay determines the best SNR for the metabolites of interest. The insert shows a waterfall plot of the different metabolite peaks: bicarbonate, pyruvate, alanine, pyruvate-hydrate, and lactate (from left to right). Each spectrum was acquired every 3 s. Reproduced from Ref.[111] (License Number #4556230568265).

2.3.3. Global and Local Spectroscopy

The most basic pulse sequence used for hyperpolarized ^{13}C spectroscopy is the nonselective pulse-and-acquire sequence used to assess the time-course of the agent and metabolites within the detection volume of the RF coil[120]. This pulse sequence is ideal for applications such as the study of perfused organs and cells[104,121,122] where changes in flux and pool size of metabolites are being investigated. Spatial selectivity can be incorporated by adding slice selection over a region of interest. This method is useful for organ-specific applications[123,124] as well as tumor xenografts[106,107]. Other methods with 3D localization have been subsequently introduced including a Point RESolved Spectroscopy (PRESS) pulse sequence with a slice-selective 90° RF excitation pulse followed by two refocusing pulse pairs along the other axes[116].

2.3.4. Multi-echo Approaches to Chemical Shift Imaging

Single-point chemical shift imaging (CSI) that uses one RF excitation per sampled FID has been used most frequently for generating maps of individual metabolites[120]. However, it suffers from a long acquisition time (typically on the order of 10-20 s for a single slice with a 16x16 matrix size and 256 RF excitations). In hyperpolarized imaging, this necessitates the use of a low flip-angle which carries a significant signal-to-noise penalty. However, due to its simplicity and availability on most clinical and preclinical MR scanners, single-point CSI sequence is still a popular pulse sequence[102]. Furthermore, its simplicity makes CSI relatively immune to artifacts; thus, even if higher resolutions or faster acquisitions can be achieved using other methods, single-point CSI can yield well-understood reference images for validation.

Alternatively, the long T_2 relaxation time of ^{13}C allows for a long readout duration, during which multiple echoes can be generated and spatially or spectrally encoded to reduce the acquisition time. Echo-planar Spectroscopy Imaging (EPSI) sequences[125] have been extensively used to image hyperpolarized ^{13}C metabolites. In these schemes, each readout is used to spatially encode the data while the accumulated phase between acquisitions associated with the chemical shift, which is not refocused by symmetric gradients, is used to encode the frequency information. Spatial encoding in this manner reduces the number of excitations significantly when compared to the single-point CSI sequence. For instance, a 16x16 single-slice image can be acquired using only 16 RF excitations, drastically reducing the total imaging time and permitting the application of higher flip angles. These improvements have allowed practical use of a 3D implementation of the sequence[126]. Further improvements to spectral information quality were found when using a double spin-echo implementation of EPSI[127]. This modified sequence has been used in many studies, including the first human studies of prostate cancer[101]. Multi-echo spiral readout trajectories with multiple interleaves have also been demonstrated for dynamic two-dimensional[128,129] and volumetric imaging[105]. When compared to the Cartesian echo-planar spectroscopic read-out trajectories, spatial encoding can be performed more efficiently using a spiral readout trajectory. Additionally, spiral trajectories are less sensitive to motion artifacts, making them very robust for cardiac applications. Recently a concentric ring readout trajectory was introduced as another alternative to the echo-planar readout trajectory[130]. This scheme can be easily combined with parallel imaging for further acceleration, while offering improved acquisition speed and robustness to flow artifacts with respect to the echo-planar readout.

Instead of using phase evolution over multiple echoes to encode chemical shift information, it is also possible to use a least-square algorithm to iteratively decompose different chemical shift components of the NMR spectrum. This method, also known as Iterative Decomposition of water and fat with echo Asymmetry and Least square estimation (IDEAL) obtains spectral information by shifting the echo time (TE)[131]. The method is used extensively for selective imaging of water and fat in proton MRI; however it can be extended to a larger number of resonance frequencies if at least as many echoes are acquired as there are spectral peaks[132]. The reconstruction requires fewer echoes than an EPSI sequence but it demands prior knowledge of the location of the peaks in the NMR spectrum and a B_0 map to successfully separate the individual frequency components. The method has been successfully used with Cartesian trajectory gradient echo sequences for two-dimensional[133] and three-dimensional[134] single time-point imaging, spiral[135] and Echo-Planar Imaging (EPI) readout trajectories[136] for 2D dynamic imaging, and as a single-shot spin-echo sequence with multiple Cartesian readouts[120] for high resolution two-dimensional imaging. The latter approach showed an over 30-fold reduction in imaging time compared to a conventional single-point CSI sequence.

2.3.5. Spatial-Spectral Excitation for Chemical Shift Imaging

A completely different approach is to exploit a sufficiently large chemical shift separation between peaks to selectively excite individual metabolites. The advantage of this approach is that it eliminates the need to spectrally encode the NMR signal, thereby reducing the total imaging time and potentially offering higher signal-to-noise[136]. It can also facilitate efficient time-resolved imaging[126] in dynamic applications and in studies requiring triggering such as cardiac imaging[112]. Spatial spectral (SPSP) excitation is achieved by using composite pulses consisting of multiple lobes of short RF excitations accompanied by time-varying gradients (typically an echo planar gradient waveform). Spatial selectivity is determined by the shape of each RF pulse lobe, while spectral selectivity depends on the envelope of all the lobes. With *a priori* knowledge of the underlying spectrum, SPSP RF pulses can be optimized for hyperpolarized ^{13}C MRI to achieve superior spectral selectivity and minimal duration. Multiband RF pulses can also be designed to excite each metabolite with a different flip angle. This technique increases both signal longevity and metabolite SNR[137–140]. SPSP RF pulses can be accompanied by the appropriate EPI readout strategy to support two-dimensional[136,141] and three-dimensional[126,142] time-resolved imaging, or by a spiral readout for multiline cardiac imaging[112], three-dimensional imaging[143] and time-resolved three-dimensional imaging of tumors[144]. The latter sequence generates high-resolution metabolite images with a single SPSP excitation pulse combined with a three-dimensional partial k-space spiral readout over multiple echoes generated via double spin-echoes, yielding a 2-second temporal resolution. The pulse sequence diagram is shown in Figure 2.2. Such RF pulses can be used for outer volume suppression in *in vivo* organ-specific spectroscopy[145] or with multi-echo approaches, such as the EPSI sequence for dynamic imaging[136,137].

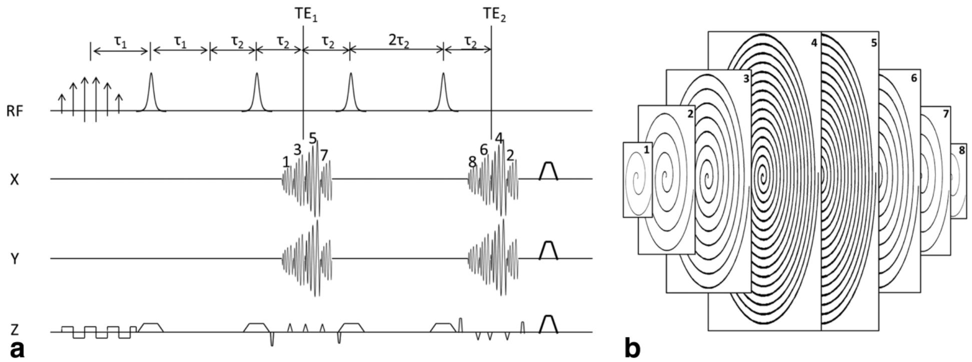

Figure 2.2: A (A) single shot three-dimensional double spin echo pulse sequence and its (B) 3D k-space trajectory. The k-space was acquired as a stack of interleaved spirals. Specific metabolites were excited via a spectral-spatial pulse. Reproduced from Ref.[146] (Re-used under CC-BY-4.0).

2.3.6. Other Approaches to Chemical Shift Imaging

Given the large chemical shift separation between the ^{13}C species, the chemical shift displacement artifact (CSDA) can be exploited to acquire images of the individual metabolites in a single acquisition. Several studies have demonstrated this approach for gradient echo sequences with Cartesian readout trajectories[147,148] in which the chemical shift separation between all peaks relative to the acquisition bandwidth is sufficiently large for complete spatial separation of their corresponding images. Alternatively, the severe smearing artifact of off-resonance peaks when using radial[149] and spiral[150] readout trajectories can be exploited to reconstruct images of a single resonance. While this approach provides images of all metabolites simultaneously, it can suffer from blurring if the T_2^* is shorter than the duration of the readout gradient. Thus, the approach constitutes a tradeoff; progressively lower bandwidth provides superior peak separation, but requires longer gradient durations with the potential for increased blurring.

CSDA can also be used along the slice selection orientation by using a small bandwidth frequency selective RF pulse excitation such that the displaced excitation band of the non-desired metabolites shifts outside of the coil[146]. This approach has advantages over SPSP RF pulses due its simplicity, but provides limited slice selection accuracy and the geometry of the coil and the subject size limits the imaging parameters.

2.3.7. Perfusion Imaging

Imaging of perfusion (non-metabolized) agents is generally much less sophisticated than chemical shift imaging because it does not require spectral encoding. As such, single-shot Fast Spin Echo (FSE)[118] or balanced Stead-State Free Precession (bSSFP) sequences are capable of producing high-resolution multiline or three-dimensional time-resolved images for the quantification of organ perfusion and blood flow[74,115,117,147,151]. Multivalent perfusion imaging[152] or simultaneous perfusion and metabolic imaging[113,153] can be performed as well, as long as some form of spectral encoding is included as discussed above.

2.3.8. Accelerated Imaging

Parallel imaging has been shown to yield significant reductions in acquisition speed and generally does not carry the signal-to-noise penalty that is observed in traditional ^{1}H MRI[130,154,155]. Another approach is to implement compressed sensing into the imaging sequence to exploit the sparsity of the NMR spectrum. Compressed sensing has been combined with single-point CSI[156], three-dimensional EPI with SPSP excitation[157], EPSI and multiband SPSP excitation[158]. Up to a 7-fold reduction in acquisition time has been achieved, allowing efficient time-resolved, three-dimensional imaging.

2.3.9. Quantification Methods

Quantification of HP data is not straightforward because, unlike with other modalities, the signal is not directly proportional to the concentration of the imaging agent or metabolite, and methods for absolute calibration have not been developed. Most studies to date have evaluated the data using one of two divergent methods: through quantification of signal ratios or by deriving fitting parameters from a kinetic model. Relative quantification typically reports the metabolite signal (area under the curve) normalized by either the delivered HP probe's signal, or the total carbon metabolite signal[159–162]. The advantage of this method is that it is trivial to perform, but it limits a direct comparison between studies because the normalization does not explicitly account for the delivered probe concentration, transport mechanics, T_1 or RF-induced relaxation or other sources of signal variation.

The second approach generates kinetic parameters (enzyme kinetic rate constants) by fitting HP data to a set of differential equations that model the HP label exchange between the injected probe and converted metabolites. The most commonly used model is the two-site exchange model[106], although there are a number of other models and analysis techniques that vary in complexity[163–165]. Deriving parameters from a fitted model has the advantage that it reflects a physical value (i.e., the rate constants) that can be compared to other studies. However, the generalizability of the results is limited by the constraints of the chosen model, and thus are in most cases more accurately described as apparent rate constants. Currently, there is no consensus on the ideal model that is applicable to all HP MRI/NMR studies, but development of such a model is necessitated by the current push towards clinical imaging[24].

2.4. Hyperpolarized Probes Used for Metabolic Studies

A number of different probes have been successfully polarized over the years for their use in biological studies. As described in sections 3.2 and 3.3, the ideal probes are small, mobile molecules that have a relatively long T_1 relaxation time. Furthermore, a probe that is used for metabolic or functional imaging must also be metabolically relevant in the organ or tissue of interest. This section highlights the HP ^{13}C probes that have been most actively used in metabolic studies due to their ubiquity in the metabolism of many different tissues, or their specific applicability to assessing the tissue's state.

2.4.1. [1-^{13}C]Pyruvate

As alluded to in the earlier sections, the most widely used hyperpolarized DNP probe is [1-^{13}C]pyruvate. Its physical characteristics make it an ideal probe for DNP. The labeled carbon is a carbonyl that is three bonds away from other magnetic species, minimizing dipolar coupling. As a small molecule, it also has low correlation times (τ_C), resulting in longer T_1 than larger molecules. As a carboxylate, it also has high aqueous solubility. These favorable physical properties enable high polarization (up to 60% polarization reported) and long T_1 of 40-60s[24,166]. Moreover, biologically, pyruvate is an intermediate in several key metabolic pathways. Together, these physical and biological properties make [1-^{13}C]pyruvate perhaps the most attractive HP imaging probe.

Pyruvate is a downstream product of glycolysis, and serves as a key intermediate in several metabolic pathways (Figure 2.3). It rapidly and reversibly catalyzes to lactate via the enzyme lactate dehydrogenase (LDH)[167]. Physiologically, conversion of pyruvate to lactate is determined by LDH activity and the ratio of NADH to NAD$^+$ [168]. However, this does not imply that the HP [1-^{13}C]lactate signal detected after HP [1-^{13}C]pyruvate administration represents net conversion of the substrate. In fact, the observed metabolite signal is largely representative of label exchange between endogenous lactate and injected HP [1-^{13}C]pyruvate[23]. As such, the observed signal reflects the endogenous lactate pool size and the redox state of the system. Many external perturbations or pathologies change the lactate pool, thereby allowing HP pyruvate to be used as a biomarker in many different pathologies, including acute injury, inflammation, or cancer[102,122,169,170].

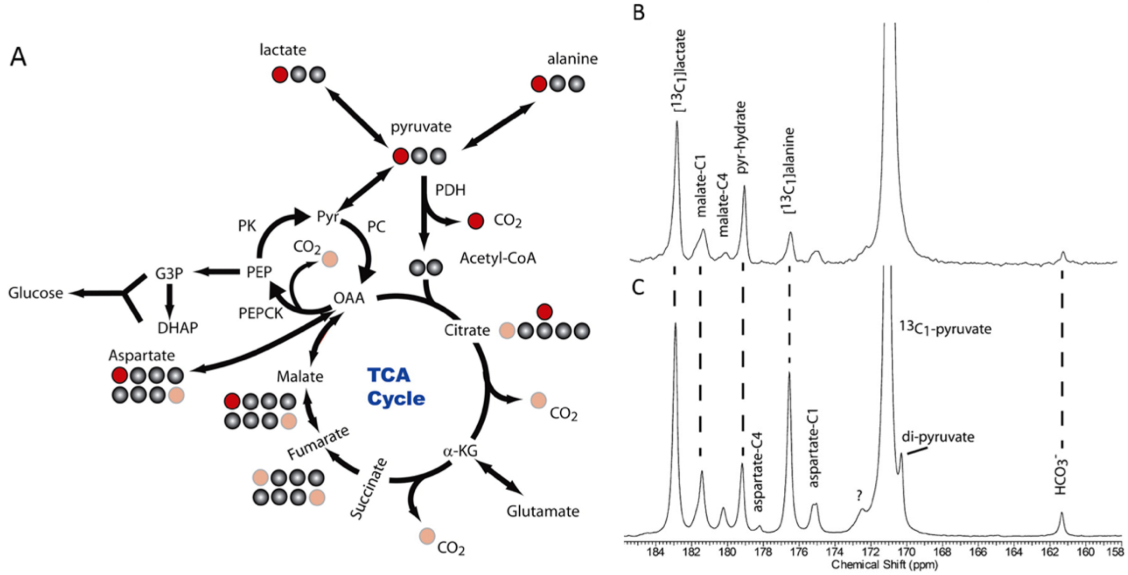

Figure 2.3: (A) The fate of the ^{13}C labeled carbon-1 (red). In most organs, the label will be detected on the lactate, alanine, bicarbonate (via PDH). In the liver, the label can also appear on other TCA cycle intermediates via the enzyme pyruvate carboxylase (PC). Spectra from (B) fasted and (C) fed states of a perfused, isolated rat liver after injection of HP [1-^{13}C]pyruvate. Figures adapted from Ref.[171] under noncommercial and education use.

Pyruvate is also reversibly catalyzed to the amino acid alanine via the enzyme alanine transaminase (ALT). In most tissues, HP [1-^{13}C]alanine signal is substantially less than that of [1-^{13}C]lactate, due to the lower activity of ALT, or the lower alanine pool size, compared to LDH and lactate, respectively[159,172,173]. However, HP[1-^{13}C]pyruvate's conversion to HP [1-^{13}C]alanine is a useful biomarker for tissues that are heavily involved in alanine metabolism, particularly the liver and skeletal muscles[120,174(p13)].

The third most common fate of HP [1-^{13}C]pyruvate is its conversion to acetyl coenzyme A (acetyl-CoA) and $^{13}CO_2$ via pyruvate dehydrogenase (PDH). The $^{13}CO_2$ is then rapidly converted to [^{13}C]bicarbonate via the enzyme carbonic anhydrase (CA)[175]. Although the [^{13}C]bicarbonate SNR is too low to be easily quantifiable in most healthy tissues, it is prominent in the heart, which is much more energetically demanding than most other organs[176]. Because the acetyl-CoA is not labeled, its fate—typically incorporation into the tricarboxylic acid (TCA) cycle via the pyruvate dehydrogenase complex (PDC) or conversion to acetylcarnitine (ALCAR)—cannot be determined. Nonetheless, the use of HP [1-^{13}C]pyruvate to study TCA cycle activity is possible in the liver and other tissues expressing pyruvate carboxylase (PC). This enzyme irreversibly catalyzes pyruvate to oxaloacetate (OAA), which can then be used as a substrate for gluconeogenesis or converted to other TCA cycle intermediates[171].

Due to the versatility of [1-^{13}C]pyruvate, it can be used to study a wide variety of metabolic perturbations in many tissues. The most notable difficulty is that the signal-to-noise is too low to be useful in true tracer applications. Thus, metabolic perturbations by superphysiological agent concentrations (mM and above) must be considered. In some circumstances, this may limit sensitivity to disease and the relevance of quantitative physiological measurements[165,177].

2.4.2. [2-^{13}C]Pyruvate

HP [2-^{13}C]pyruvate is used much less frequently than HP [1-^{13}C]pyruvate. As the 2-carbon is labeled, the closest magnetic interaction is two bonds away. This results in a slightly lower T_1 than that of the 1-carbon[178]. Nonetheless, HP [2-^{13}C]pyruvate imaging is much better suited for studying oxidative phosphorylation. Unlike [1-^{13}C]pyruvate, the HP carbon is found on acetyl-CoA after PDH catalysis, so HP [2-^{13}C]pyruvate can be used to study PDC flux, fatty acid oxidation (acetoacetate, acetylcarnitine), and conversion to TCA cycle intermediates or downstream products (e.g., [1-^{13}C]citrate and [5-^{13}C]glutamate)[179,180]. This is particularly useful for studying cancers that disrupt oxidative phosphorylation. Nevertheless, until recently a limited number of studies have been performed using HP [2-^{13}C]pyruvate because of the relatively low oxidative phosphorylation activity in many tissues.

2.4.3. [1-^{13}C]Acetate

HP [1-^{13}C]acetate is typically used as a probe to study TCA flux and fatty acid oxidation. The enzyme acetyl-CoA synthase (ACS) rapidly converts free acetate into acetyl-CoA. The acetyl-CoA can then either enter the TCA cycle and its conversion to TCA intermediates can be followed, or it can be reversibly converted to acetylcarnitine (ALCAR) via the enzyme carnitine acetyltransferase (CAT), depending on the energy needs of the tissue [181]. As a probe, HP [1-^{13}C]acetate bypasses the PDH complex, so unlike pyruvate, it provides a direct measurement of TCA flux. HP [1-^{13}C]acetate studies are useful in tissues that prioritize fatty-acid metabolism as opposed to glucose metabolism, and consequently most studies have been done in the heart or skeletal muscles[182,183].

2.4.4. [1-^{13}C]Alanine

HP [1-^{13}C]alanine has also been used as an alternate probe for studying pyruvate metabolism. Upon injection, HP [1-^{13}C]alanine is converted to HP [1-^{13}C]pyruvate via ALT, which can then be converted to HP [1-^{13}C]lactate. Using HP [1-^{13}C]alanine is advantageous as it allows relative measurements of endogenous pyruvate and lactate pool size [184] without the analytical difficulties arising from the large extracellular pyruvate signal. Alanine's metabolism varies by organ, but ALT is especially active in the muscle and liver, which play a key role in the Cahill cycle that shuttles alanine and glucose between the two organs[185]. A recent study has also used a modified alanine moiety, HP [1-^{13}C]alanine-NH_2, to specifically target aminopeptidase N, an enzyme that is upregulated in tumor angiogenesis[186].

2.4.5. [^{13}C]Urea

[^{13}C]urea has also been used as a HP probe. Unlike most other probes, urea is metabolically inactive. Instead, it has been used as a contrast agent or a perfusion agent. It is a promising alternative to traditional contrast agents (such as gadolinium) as it offers the unique advantages of high contrast (no background signal), more straightforward quantification, and minimal toxicity[113,117,118].

2.4.6. [1-^{13}C]Dehydroascorbic Acid

Dehydroascorbic acid (DHA) is the oxidized form of ascorbic acid (vitamin C); the relative concentration of the two can provide information on the intracellular redox state[187]. DHA uptake varies wildly by tissue, so it cannot be used as a universal probe[188,189]. Unlike the other smaller metabolites, [1-^{13}C]DHA also has a comparatively short T_1 (~20s) at high fields (9.4-11T), so imaging at those fields requires fast imaging sequences; however, the reported T_1 at clinical MRI fields is much higher (~57s), making studies at the lower field much more feasible[190,191].

2.4.7. [1-^{13}C]Succinate / [1-^{13}C]Diethyl Succinate [1,4-$^{13}C_2$]Diethyl Succinate

Succinate, a TCA cycle intermediate, can be reversibly catalyzed to either succinyl-CoA via the enzyme succinyl-CoA synthetase, or to fumerate via the enzyme succinate dehydrogenase[192,193]. The ability to image the fate of succinate would provide insights into many pathologies that affect oxidative phosphorylation[194,195], especially in tissues where no TCA intermediates are detected with HP [1-^{13}C] or [2-^{13}C]pyruvate. [1-^{13}C] or [1,4-$^{13}C_2$]succinate have not been successfully polarized using DNP. However, [1-^{13}C]succinate has been successfully polarized with PHIP using [1-^{13}C, 2,3-$^{2}H_2$] fumaric acid and [1-^{13}C]acetylenedicarboxylate, with reported T1 values of 27s (at 4.7T) and ~6s (at 1.5T), respectively[96,97,196]. Other attempts to polarize succinate have used ethyl groups to protect the terminal carbonyl groups. The resultant diethyl succinate has been polarized via both PHIP and DNP, with a reported T_1 of ~38s at lower field strengths (3 and 4.7T)[75,197].

2.4.8. Other Hyperpolarized Metabolites

There are other less extensively studied molecules that have also been successfully polarized. One promising probe is [1-^{13}C]bicarbonate, which rapidly converts into HP $^{13}CO_2$ via the enzyme carbonic anhydrase[148,198]. The ratio of bicarbonate-to-carbon dioxide can be used to derive tissue pH, which is a powerful biomarker for both acute and chronic pathologies[199,200]. [U-$^{13}C_6$, U-$^{2}H_7$]glucose, which lies metabolically upstream of pyruvate, has also been successfully polarized, but its *in* vivo use is hindered by its short T_1 (about 10-13s) and complex spectrum[201,202]. For an exhaustive list of the molecules that have been successfully polarized, please refer to the comprehensive review by Keshari and Wilson[119].

2.5. Hyperpolarized Studies by Organ System

A number of excellent reviews on the state of hyperpolarized DNP, each focusing on different aspects of the field, have already been published. Barnes *et al.*[46] focus on the physics of DNP, while Karlsson *et al*.[50], and Keshari and Wilson[119] concentrate on the chemistry of DNP probes. Reviews with a particular biological or pathological focus, e.g., on cancer[203] or neurology[97], also exist. However, none of these reviews has described how HP studies vary according to the different tissue or organ systems they have been used to assess. Accordingly, this section summarizes the major HP studies by organ or tissue in order to characterize their metabolic profile for a given set of HP probes, highlighting the unique challenges that each tissue poses for molecular imaging. For example, probe delivery to the brain is limited by the blood brain-barrier, whereas the lung presents the challenge of the air-tissue interface. *Ex vivo, in vivo*, and *in vitro* studies of the heart, liver, prostate, kidney and lung are described below.

2.51. Heart

Proton MRI is often used for structural cardiac imaging. In addition to its high spatial resolution, MRI's sensitivity to flow and ability to freeze motion during the cardiac cycle make it suitable for answering many clinical important questions. Other nuclei such as ^{31}P have been used to obtain metabolic information about the heart in both healthy and diseased states; however, given their low gyromagnetic ratio and metabolite concentration, *in vivo* application is fairly limited.

Hyperpolarized ^{13}C MRI provides a new opportunity for real-time metabolic imaging of the heart. A number of isolated perfused heart studies, as well as *in vivo* studies in both small and large animals, have been carried out to characterize the metabolic profile of the healthy heart using HP agents. Unlike most other tissues for which HP lactate labeling or HP alanine labeling is primarily observed, significant conversion of HP [1-^{13}C]pyruvate to HP bicarbonate has been detected in the heart[112,159,176,204]. In healthy hearts, the detected HP bicarbonate reflects PDH flux, though not necessarily flux through the TCA cycle[176]. A decrease in HP bicarbonate signal has also been observed in the fasted state, when the heart switches to fatty acid oxidation as its primary energy source[159,177,204]. Adding butyrate or octanoate (even-chained fatty acids) to the perfusate has produced a similar decrease in HP bicarbonate signal while the TCA flux measured via tissue extracts was unchanged, providing direct evidence for decreased PDH flux in the presence of fatty acids[176,205]. Adding dichloroacetate (DCA), a well-known pyruvate dehydrogenase kinase (PDK) inhibitor, promotes PDH flux and yields a stronger HP bicarbonate signal, as expected[181,204,206,207]. Adding dobutamine, a selective β-agonist, increased both PDH and TCA flux, as determined by HP [2-^{13}C]pyruvate MR. As the studies above clearly demonstrate, then, different HP probes can be used to be assess different types of stress on cardiac tissue[181].

Because the heart can derive the acetyl-CoA needed for the TCA cycle from either pyruvate decarboxylation or β-oxidation, a number of studies have focused on using [1-^{13}C]acetate's conversion to downstream TCA intermediates or reversible conversion to acetylcarnitine as another HP biomarker to characterize cardiac metabolism[183,208,209]. These *in vivo* studies in rats and pigs characterized TCA flux using ratiometric modeling of HP acetate, acetylcarnitine, and citrate signals in healthy animals. More recently, HP

[1-^{13}C]butyrate was successfully used to characterize TCA intermediates in fed and fasted isolated perfused rat hearts, confirming previous findings that the presence of fatty acids limits PDH flux without affecting TCA flux[205].

These HP markers have also been used to characterize a number of cardiac pathologies. HP [1-^{13}C]pyruvate studies of ischemia-reperfusion in rats and pigs have shown a decrease in HP bicarbonate signal and an increase in HP lactate signal immediately after ischemia[210–212]. Partial recovery to baseline was observed 15 minutes post-reperfusion[210], suggesting that HP [1-^{13}C]pyruvate could serve as a marker for ischemia-reperfusion injury. The ratio of HP bicarbonate to HP CO_2 was also used to characterize this injury, and it was found that post-ischemia pH was about 7.12, compared to 7.20 in healthy rats[212]. An HP [2-^{13}C]pyruvate MR study yielded complementary findings, showing an increase in HP [2-^{13}C]lactate labeling and a decrease in [1-^{13}C]acetylcarnitine, [1-^{13}C]citrate, and [5-^{13}C]glutamate in isolated perfused ischemic rat hearts[212].

In vivo HP [1-^{13}C]pyruvate NMR also showed a decrease in HP bicarbonate production in a streptozotocin-induced type 1 diabetes model in rats[159], confirming the well-established finding that type 1 diabetes onset decreases glucose oxidation and PDH flux[213].

Although earlier studies were performed in perfused hearts and small animals, the adoption of modern pulse sequences and fast sequences has enabled more *in vivo* studies, as well as studies in larger animals where the signal emanating from the heart chambers and the myocardium can be resolved. In addition to confirming the results from previous studies, these large animal *in vivo* studies have shown the particular region of the myocardium tissue from which the bicarbonate and lactate signals originate[113,142].

2.5.2. Liver

The liver is both the largest gland and the most metabolically active organ in the human body. Unlike most organs, it is heavily involved in whole-body metabolism[214]. Unsurprisingly, a diverse set of metabolic pathways and HP probes has therefore been studied in the liver.

The liver is largely responsible for gluconeogenesis, the process by which glucose is synthesized from lactate and alanine (as part of the Cori and Cahill cycles, respectively) when blood glucose levels are low[185,215]. An HP [1-^{13}C]pyruvate study of the liver in fed (high blood glucose) and fasted (low blood glucose) rats demonstrated this process *in vivo* by detecting the expected decrease in alanine pool size via a decrease in HP alanine labeling in the fasted state[184]. The liver is also one of the few organs that expresses pyruvate carboxylase (PC) and phosphoenolpyruvate carboxykinase (PEPCK), allowing conversion of HP [1-^{13}C]pyruvate to [1-^{13}C]oxaloacetate and additional downstream metabolites ([1-^{13}C]malate, [4-^{13}C]malate and [1-^{13}C]aspartate) (Figure 2.3)[171]. Changes in the PC flux and PEPCK flux after [1-^{13}C]pyruvate injections in a type 2 diabetic mouse model demonstrated that this pathway could be exploited for longitudinal monitoring of diabetes development[216].

Several other studies have focused on tissue non-specific metabolic pathways and how they differ in the liver. Using HP [1-^{13}C]acetate injections, the acetylcarnitine pool size was shown to be lower than that in the heart[217]. HP [1-^{13}C]alanine injections have also been used to estimate the intracellular ratio of the pyruvate and lactate pools[184], a technique that is feasible in the liver due to its relatively high ALT flux compared to other organs.

Ethanol administration resulted in increased lactate production in a rat liver, most likely due to increased NADH availability after ethanol breakdown[124].

A large number of hepatic studies have focused on tumor imaging. Hepatocellular carcinoma (HCC) is an aggressive primary tumor with extremely high morbidity and mortality[218], in which glutamine metabolism plays an important role. The conversion of HP [5-^{13}C]glutamine to HP glutamate has been shown to be a potential biomarker for cell proliferation in human hepatoma (HepG2) cells[219]. Other studies have shown that the conversion rates and T_2 relaxation times of alanine and lactate from HP pyruvate are higher in HCC tumors than in normal liver, suggesting a potential set of biomarkers for tumor characterization[116,220–222]. Another *in vivo* study found that transcatheter arterial embolization (TAE) of HCC in rats lead to the increased conversion of HP [1,4-$^{13}C_2$]fumarate to HP [1,4-$^{13}C_2$]malate after necrosis due to extracellular fumarase, as well as a decrease in HP [^{13}C,$^{15}N_2$]urea and HP [1-^{13}C]pyruvate signal, most likely due to decreased blood perfusion[223]. The conversion of HP [1-^{13}C]α-ketoisocaproate (KIC) to HP leucine was also shown to be associated with branched-chain aminotransferase (BCAT) expression, an enzyme that is more strongly expressed in HCC cells compared to normal liver tissue[221].

2.5.3. Prostate

Hyperpolarized ^{13}C methods have been used extensively to study the prostate, in particular prostate cancer. Conventional clinical methods rely on prostate specific antigen (PSA) for screening and biopsies for diagnosis. In 2011, the United States Preventive Services Task Force (USPTF) recommended against PSA screening, as the risk may outweigh the benefits[224]. Biopsies are often difficult to justify as well, largely due to their invasiveness and the difficulty of accurate sampling in this highly heterogeneous gland. ^{1}H high resolution magic angle spinning (HRMAS) spectroscopy and ^{1}H MRSI studies have shown that changes in choline-containing compounds, polyamines and citrates can be used to improve cancer localization in prostates, but these compounds cannot be easily identified using HP ^{13}C NMR/MRI methods[225]. ^{1}H HRMAS also showed elevated lactate and alanine concentrations in biopsy samples from human prostate cancer patients[226]. *In vivo* imaging of these metabolites using ^{1}H MRSI is challenging, however, as their resonances lie close to the lipid resonances surrounding the prostate tissue. In contrast, HP 1-^{13}C pyruvate imaging is an ideal tool for real-time measurements of lactate and alanine as potential biomarkers for prostate cancer.

A number of HP 1-^{13}C pyruvate studies have been conducted that demonstrate the technique's feasibility for evaluating prostate cancer. The most widely used animal model is the transgenic adenocarcinoma of mouse prostate (TRAMP) model[227], which has shown increased HP lactate labeling in multiple *in vivo* studies[170,172]. The lactate signal (or lactate to pyruvate ratio) was also correlated with increasing tumor grade[228]. It is important to note that, due to the small size and multi-lobar structure of a normal mouse prostate, the tumor lactate measurements in these studies were compared to lactate measurements from either the kidney or liver (unchanged in control and TRAMP cohorts). All of these findings were confirmed using emerging imaging techniques (section 4) which further showed the heterogeneity of the tumor, especially in relationship to disease progression[228,229]. Other TRAMP studies have also demonstrated the use of HP [1-^{13}C]pyruvate spectroscopy to extract kinetic parameters for this disease, but have found the fitted rate constants to be heavily dose-dependent in the simplistic model used[163].

Findings from the *in vivo* TRAMP model have been translated to *ex vivo* and *in vivo* human studies. *Ex vivo* HP [1-^{13}C]pyruvate studies using tissue slice culture (TSC) cells derived from radical prostatectomy specimens showed different metabolic ratios compared to patient biopsies. However, the trend in changes between benign and cancerous tissue were similar in all the studies: i.e., increasing lactate with increasing cancer grade[230]. In 2013, the first in man HP [1-^{13}C]pyruvate study was performed in 31 patients with prostate cancer[101]. As a phase 1 trial, its primary goal was to study the dose dependent effects of delivering HP [1-^{13}C]pyruvate. The study confirmed the safety of the technique at the highest delivered dose of 0.43 mL/kg (of 230 mM agent), paving the way for further human studies by demonstrating increased HP lactate/pyruvate in biopsy-confirmed regions of cancer.

Although most work in the prostate has used HP [1-^{13}C]pyruvate, other HP agents have also been used to study prostate cancer. For example, HP [2-^{13}C]fructose's conversion to fructose-6-phosphate via hexokinase was found to increase in the tumor region[231]; DHA was also used in the TRAMP model, and the ratio of DHA to DHA plus ascorbate was found to increase in the late stage of the disease[187].

2.5.4. Kidney

Over the last decade, hyperpolarized ^{13}C NMR/MRI has been used extensively to study changes in blood flow and metabolism in the kidneys and renal system. The kidneys receive approximately 20% of the cardiac output, making high ^{13}C SNR easily achievable following intravenous administration of a hyperpolarized bolus.

The metabolism of healthy kidneys has been characterized using hyperpolarized [1-^{13}C]pyruvate in a manner similar to other organ systems. An *in vivo* rat study demonstrated significant conversion of HP pyruvate to both HP lactate and HP bicarbonate, while there was minimal conversion to alanine[232]. In another study, when pigs were given an oral sucrose load, it was found that the lactate to pyruvate ratio correlated with the blood glucose level, while all other metabolites of pyruvate remained unchanged[102].

In addition to the metabolically active pyruvate, the metabolically inert [^{13}C]urea has also been used to characterize blood flow and other functional parameters in the kidneys. One *in vivo* rat study using [^{13}C]urea showed a more than three-fold difference in renal blood flow compared to hepatic blood flow[233], while another demonstrated that the T_2 of [^{13}C,^{15}N]urea in kidneys was greater than ten seconds, as opposed to 1.3 seconds in blood, likely due to deoxyhemoglobin-induced paramagnetic relaxation in the latter[117]. Finally, a third *in vivo* rat study demonstrated more rapid medullary [^{13}C]urea enhancement in the antidiuretic state, suggesting that [^{13}C]urea could be used as a marker for urea transporter UT-A1 activity[234].

Hyperpolarized imaging techniques have also been used to characterize disease models in kidneys. For instance, renal cell carcinomas (RCCs) are a broad group of tumors affecting the kidney that have been studied in some detail using hyperpolarized ^{13}C. *In vitro* HP [1-^{13}C]pyruvate studies of two different RCC cell lines (UOK262 and UMRC6) and healthy proximal tubule epithelial (HK-2) cells have shown that the observed pyruvate to lactate ratio and the ratio of HP intracellular lactate to extracellular lactate (efflux ratio) can be used to distinguish the three different cell lines from each other[235,236]. Furthermore, the

HP lactate efflux ratio strongly correlates with MCT4 mRNA expression, suggesting its potential use as a biomarker for differential diagnosis of RCCs.

Acute tubular necrosis (ATN) is the most frequent cause of acute kidney injury, but there is no clinically available noninvasive tool to differentially diagnose ATN from other similar disorders such as glomerulonephritis (GN). An *in vivo* mouse study showed that the conversion of hyperpolarized [1,4-$^{13}C_2$]fumarate to malate was significantly greater in the ATN cohort compared to healthy or GN cohorts[237], indicating that hyperpolarized [1,4-$^{13}C_2$]fumarate could be a useful biomarker by providing differentiable diagnostic information on the causes of acute kidney injury.

Hyperpolarized [1-^{13}C]pyruvate has also been used to study metabolic changes in the renal system following the onset of diabetes. One *in vivo* rat study using a streptozotocin diabetes model showed a 149% increase in the lactate to pyruvate ratio of diabetic rats compared to controls[238]. Another *in vivo* study demonstrated that reduced oxygen availability lead to 23% and 34% increases in lactate and alanine labeling, respectively, in diabetic rats, whereas no such difference was observed in the control cohort.[239].

2.5.5. Lung

Hyperpolarized ^{13}C metabolic imaging of the lungs is quite challenging because of their low tissue density, high susceptibility/B_0 inhomogeneity due to air-tissue interfaces, motion, and low metabolic rate compared to solid organs[240]. At the same time, however, since the lung receives the full blood supply during each circulation and plays a key role in whole body homeostasis, HP carbon MRI can be a valuable tool for evaluating lung metabolism and pathology.

HP ^{13}C MRI was first used in the porcine lung as a contrast agent to demonstrate feasibility as an angiography tool for evaluating pulmonary perfusion and imaging the pulmonary vasculature[74]. When evaluating the suitability of specific hyperpolarized agents in different pulmonary disorders, however, metabolic imaging is most easily performed using *ex vivo* perfused lungs. HP [1-^{13}C]pyruvate spectroscopy of an ischemia-reperfusion model in perfused rat lungs showed a significant increase in HP lactate labeling after ischemia; the lactate labeling was restored to baseline levels approximately 30-40 minutes after reperfusion[173]. As we will see in Chapter 3, HP [1-^{13}C]pyruvate can also been used to investigate the mechanism by which ascorbate prolongs the viability of isolated perfused lungs[162]. We found that ascorbate enhanced viability via interaction with the electron transport chain rather than its more common role as a general antioxidant. HP signal dynamics and the response to perfusate contents in the healthy lung were addressed using a three-compartment model to confirm the experimental finding[241] that HP lactate labeling is primarily determined by the rate at which NAD$^+$ is reduced to NADH, and scales with the intracellular lactate pool size[165]. As discussed in Chapter 4, we also demonstrated a greater than three-fold increase in HP pyruvate-to-lactate ratio during the inflammatory phase of a bleomycin induced lung injury model in perfused rat lungs, which was well correlated with histological neutrophil count[122].

Current research is focused on moving towards *in vivo* HP ^{13}C lung imaging. The first such *in vivo* study in rats demonstrated an increase in HP lactate labeling compared to controls in a radiation-induced lung injury (RILI) model[242]. These results were consistent with lung inflammation as measured from bronchioalveolar lavage. Another pair of studies demonstrated increased HP lactate with inflammation in a two-hit model of acute lung injury, as well as its attenuation with protective ventilation techniques[243,244]. Finally, chapter 5 will focus on studies in which we demonstrated that increased HP lactate can be used as an early biomarker for lung transplant rejection in a rat model.

2.6. Conclusion

Over the past fifteen years, considerable advancements have been made in developing hyperpolarized injectable agents for use in medical imaging, and tangible progress has begun towards the dual goals of developing affordable HP MRI biomedical applications and the robust use of this technology in human studies[245,246].

The technical improvements which HP liquid MR research has achieved over this period are clearly visible in labs around the world. Similar to hyperpolarized gas technology a decade earlier, molecular imaging using DNP-hyperpolarized compounds has progressed from reliance on homemade equipment to the use of commercial devices suitable for *in vitro* and small animal research and, finally, to equipment capable of safely and efficiently producing large samples appropriate for human trials. PHIP has also undergone a technical renaissance sparked by recent demonstrations of spin-order transfer in transient catalytic complexes and chemical modification of the hyperpolarized compound.

Just as importantly, novel imaging methods have proven capable of using the hyperpolarized state more efficiently by improving acquisition speed, metabolite selectivity, spatial and temporal resolution, and immunity to motion artifacts. At the same time, vigorous effort have also been made to extract the quantitative information (e.g., rate uptake and metabolic flux) necessary to attain a fundamental understanding of metabolic signals by combining imaging results with kinetic modeling. Indeed, some of the most promising work highlighted in the organ-specific discussion above relies on these procedural improvements in image acquisition and analysis. For example, the primary focus of most HP MR heart studies has been quantifying PDH flux and its modification with physiological stress or pharmaceutical intervention. Similar efforts have been pursued in isolated, perfused organs, for which the arterial input function is known, as well as in brain and liver, for which it is measured. In addition to detecting low-concentration intermediates, these studies have already yielded unique quantitative metabolic flux and exchange data and can naturally be extended to quantitative assessments of perfusion and/or flux in any organ and in tumors.

The central challenge moving forward will be the clinical translation of sequences and modeling techniques suitable for quantification, with the aim of better understanding the relationship between these new measurements and human disease. Human studies have already begun[101,247–249], and will grow dramatically in the immediate future as the solutions to technical and regulatory challenges are disseminated.

2.7. References

1. Joint SNM/RSNA Molecular Imaging Summit Statement. *J Nucl Med*. 2005;46(9):11N-42N.
2. Hoh CK. Clinical use of FDG PET. *Nucl Med Biol*. 2007;34(7):737-742. doi:10.1016/j.nucmedbio.2007.07.001
3. Popovtzer R, Agrawal A, Kotov NA, et al. Targeted Gold Nanoparticles Enable Molecular CT Imaging of Cancer. *Nano Lett*. 2008;8(12):4593-4596. doi:10.1021/nl8029114
4. James ML, Gambhir SS. A molecular imaging primer: modalities, imaging agents, and applications. *Physiol Rev*. 2012;92(2):897-965. doi:10.1152/physrev.00049.2010
5. Hoult DI, Busby SJ, Gadian DG, Radda GK, Richards RE, Seeley PJ. Observation of tissue metabolites using 31P nuclear magnetic resonance. *Nature*. 1974;252(5481):285-287.
6. Weiss RG, Chacko VP, Gerstenblith G. Fatty acid regulation of glucose metabolism in the intact beating rat heart assessed by carbon-13 NMR spectroscopy: the critical role of pyruvate dehydrogenase. *J Mol Cell Cardiol*. 1989;21(5):469–478.
7. Reddy R, Insko EK, Noyszewski EA, Dandora R, Kneeland JB, Leigh JS. Sodium MRI of human articular cartilage in vivo. *Magn Reson Med*. 1998;39(5):697–701.
8. Rudd JHF, Warburton EA, Fryer TD, et al. Imaging atherosclerotic plaque inflammation with [18F]-fluorodeoxyglucose positron emission tomography. *Circulation*. 2002;105(23):2708-2711.
9. Lucignani G, Paolini G, Landoni C, et al. Presurgical identification of hibernating myocardium by combined use of technetium-99m hexakis 2-methoxyisobutylisonitrile single photon emission tomography and fluorine-18 fluoro-2-deoxy-D-glucose positron emission tomography in patients with coronary artery disease. *Eur J Nucl Med*. 1992;19(10):874-881.
10. Trani D, Yaromina A, Dubois L, et al. Preclinical Assessment of Efficacy of Radiation Dose Painting Based on Intratumoral FDG-PET Uptake. *Clin Cancer Res*. 2015;21(24):5511-5518. doi:10.1158/1078-0432.CCR-15-0290
11. Miyamoto M, Kuroda S, Zhao S, et al. Bone Marrow Stromal Cell Transplantation Enhances Recovery of Local Glucose Metabolism After Cerebral Infarction in Rats: A Serial 18F-FDG PET Study. *J Nucl Med*. 2013;54(1):145-150. doi:10.2967/jnumed.112.109017
12. Khalil MM, Tremoleda JL, Bayomy TB, et al. Molecular SPECT Imaging: An Overview, Molecular SPECT Imaging: An Overview. *Int J Mol Imaging Int J Mol Imaging*. 2011;2011, 2011:e796025. doi:10.1155/2011/796025, 10.1155/2011/796025
13. Franc BL, Acton PD, Mari C, Hasegawa BH. Small-Animal SPECT and SPECT/CT: Important Tools for Preclinical Investigation. *J Nucl Med*. 2008;49(10):1651-1663. doi:10.2967/jnumed.108.055442
14. Gambhir SS. Molecular imaging of cancer with positron emission tomography. *Nat Rev Cancer*. 2002;2(9):683-693. doi:10.1038/nrc882

15. Fletcher JW, Djulbegovic B, Soares HP, et al. Recommendations on the use of 18F-FDG PET in oncology. *J Nucl Med Off Publ Soc Nucl Med*. 2008;49(3):480-508. doi:10.2967/jnumed.107.047787

16. Kubota K. From tumor biology to clinical Pet: a review of positron emission tomography (PET) in oncology. *Ann Nucl Med*. 2001;15(6):471-486.

17. Lopci E, Nanni C, Castellucci P, et al. Imaging with non-FDG PET tracers: outlook for current clinical applications. *Insights Imaging*. 2010;1(5-6):373-385. doi:10.1007/s13244-010-0040-9

18. Belhocine T, Steinmetz N, Hustinx R, et al. Increased uptake of the apoptosis-imaging agent (99m)Tc recombinant human Annexin V in human tumors after one course of chemotherapy as a predictor of tumor response and patient prognosis. *Clin Cancer Res Off J Am Assoc Cancer Res*. 2002;8(9):2766-2774.

19. Matthews PM, Rabiner EA, Passchier J, Gunn RN. Positron emission tomography molecular imaging for drug development. *Br J Clin Pharmacol*. 2012;73(2):175-186. doi:10.1111/j.1365-2125.2011.04085.x

20. Huang WS, Lin SZ, Lin JC, Wey SP, Ting G, Liu RS. Evaluation of early-stage Parkinson’s disease with 99mTc-TRODAT-1 imaging. *J Nucl Med Off Publ Soc Nucl Med*. 2001;42(9):1303-1308.

21. Beyer T, Townsend DW, Brun T, et al. A Combined PET/CT Scanner for Clinical Oncology. *J Nucl Med*. 2000;41:1369–1379.

22. Pichler BJ, Judenhofer MS, Pfannenberg C. Multimodal imaging approaches: PET/CT and PET/MRI. *Handb Exp Pharmacol*. 2008;(185 Pt 1):109-132. doi:10.1007/978-3-540-72718-7_6

23. Tyler DJ, Schroeder MA, Cochlin LE, Clarke K, Radda GK. Application of Hyperpolarized Magnetic Resonance in the Study of Cardiac Metabolism. *Appl Magn Reson*. 2008;34(3-4):523-531. doi:10.1007/s00723-008-0115-7

24. Daniels CJ, McLean MA, Schulte RF, et al. A comparison of quantitative methods for clinical imaging with hyperpolarized 13C-pyruvate. *NMR Biomed*. 2016;29(4):387-399. doi:10.1002/nbm.3468

25. Weissleder R, Ntziachristos V. Shedding light onto live molecular targets. *Nat Med*. 2003;9(1):123-128. doi:10.1038/nm0103-123

26. van Dam GM, Themelis G, Crane LMA, et al. Intraoperative tumor-specific fluorescence imaging in ovarian cancer by folate receptor-α targeting: first in-human results. *Nat Med*. 2011;17(10):1315-1319. doi:10.1038/nm.2472

27. Long-Residence-Time Nano-Scale Liposomal Iohexol for X-ray–Based Blood Pool Imaging - Academic Radiology. http://www.academicradiology.org/article/S1076-6332(03)80055-7/abstract. Accessed May 20, 2016.

28. Schmiedl UP, Krause W, Leike J, Sachse A. CT blood pool enhancement in primates with lopromide-carrying liposomes containing soy phosphatidyl glycerol. *Acad Radiol*. 1999;6(3):164-169. doi:10.1016/S1076-6332(99)80402-4

29. Hyafil F, Cornily J-C, Feig JE, et al. Noninvasive detection of macrophages using a nanoparticulate contrast agent for computed tomography. *Nat Med*. 2007;13(5):636-641. doi:10.1038/nm1571

30. Samei E, Saunders RS, Badea CT, et al. Micro-CT imaging of breast tumors in rodents using a liposomal, nanoparticle contrast agent. *Int J Nanomedicine*. 2009;4:277-282.

31. Karathanasis E, Chan L, Karumbaiah L, et al. Tumor Vascular Permeability to a Nanoprobe Correlates to Tumor-Specific Expression Levels of Angiogenic Markers. *PLOS ONE*. 2009;4(6):e5843. doi:10.1371/journal.pone.0005843

32. Danila D, Partha R, Elrod DB, Lackey M, Casscells SW, Conyers JL. Antibody-labeled liposomes for CT imaging of atherosclerotic plaques: in vitro investigation of an anti-ICAM antibody-labeled liposome containing iohexol for molecular imaging of atherosclerotic plaques via computed tomography. *Tex Heart Inst J Tex Heart Inst St Lukes Episcop Hosp Tex Child Hosp*. 2009;36(5):393-403.

33. Lusic H, Grinstaff MW. X-ray-Computed Tomography Contrast Agents. *Chem Rev*. 2013;113(3):1641-1666. doi:10.1021/cr200358s

34. Cai Q-Y, Kim SH, Choi KS, et al. Colloidal gold nanoparticles as a blood-pool contrast agent for X-ray computed tomography in mice. *Invest Radiol*. 2007;42(12):797-806. doi:10.1097/RLI.0b013e31811ecdcd

35. Wang H, Zheng L, Peng C, et al. Computed tomography imaging of cancer cells using acetylated dendrimer-entrapped gold nanoparticles. *Biomaterials*. 2011;32(11):2979-2988. doi:10.1016/j.biomaterials.2011.01.001

36. Zhang Z, Ross RD, Roeder RK. Preparation of functionalized gold nanoparticles as a targeted X-ray contrast agent for damaged bone tissue. *Nanoscale*. 2010;2(4):582-586. doi:10.1039/B9NR00317G

37. Chanda N, Kattumuri V, Shukla R, et al. Bombesin functionalized gold nanoparticles show in vitro and in vivo cancer receptor specificity. *Proc Natl Acad Sci*. 2010;107(19):8760-8765. doi:10.1073/pnas.1002143107

38. Cormode DP, Naha PC, Fayad ZA. Nanoparticle Contrast Agents for Computed Tomography: A Focus on Micelles. *Contrast Media Mol Imaging*. 2014;9(1):37-52. doi:10.1002/cmmi.1551

39. Happer W. Optical Pumping. *Rev Mod Phys*. 1972;44(2):169-249. doi:10.1103/RevModPhys.44.169

40. Walker TG, Happer W. Spin-exchange optical pumping of noble-gas nuclei. *Rev Mod Phys*. 1997;69(2):629.

41. Schmidt AB, Andrews DL, Rohrbach A, et al. Do twisted laser beams evoke nuclear hyperpolarization? *J Magn Reson San Diego Calif 1997*. 2016;268:58-67. doi:10.1016/j.jmr.2016.04.015

42. Overhauser AW. Polarization of nuclei in metals. *Phys Rev*. 1953;92(2):411.

43. Carver TR, Slichter CP. Polarization of nuclear spins in metals. *Phys Rev*. 1953;92(1):212.

44. Flori A, Liserani M, Bowen S, Ardenkjaer-Larsen JH, Menichetti L. Dissolution Dynamic Nuclear Polarization of Non-Self-Glassing Agents: Spectroscopy and Relaxation of Hyperpolarized [1- ^{13} C]Acetate. *J Phys Chem A*. 2015;119(10):1885-1893. doi:10.1021/jp511972g

45. Abragam A, Goldman M. Principles of dynamic nuclear polarisation. *Rep Prog Phys*. 1978;41(3):395. doi:10.1088/0034-4885/41/3/002

46. Barnes AB, De Paëpe G, van der Wel PCA, et al. High-Field Dynamic Nuclear Polarization for Solid and Solution Biological NMR. *Appl Magn Reson*. 2008;34(3-4):237-263. doi:10.1007/s00723-008-0129-1

47. Hovav Y, Feintuch A, Vega S. Theoretical aspects of dynamic nuclear polarization in the solid state – spin temperature and thermal mixing. *Phys Chem Chem Phys*. 2013;15(1):188-203. doi:10.1039/C2CP42897K

48. Goldman M. Overview of Spin Temperature, Thermal Mixing and Dynamic Nuclear Polarization. *Appl Magn Reson*. 2008;34(3-4):219-226. doi:10.1007/s00723-008-0114-8

49. Osten HJ, Jameson CJ. Quadrupolar spin relaxation due to electric field gradients induced by vibrations and collisions. *Mol Phys*. 1986;57(3):553-571. doi:10.1080/00268978600100411

50. Karlsson M, Jensen PR, Duus JØ, Meier S, Lerche MH. Development of Dissolution DNP-MR Substrates for Metabolic Research. *Appl Magn Reson*. 2012;43(1-2):223-236. doi:10.1007/s00723-012-0336-7

51. Chattergoon N, Martínez-Santiesteban F, Handler WB, Ardenkj\a er-Larsen JH, Scholl TJ. Field dependence of T1 for hyperpolarized [1-13C] pyruvate. *Contrast Media Mol Imaging*. 2013;8(1):57–62.

52. Lumata L, Merritt ME, Kovacs Z. Influence of deuteration in the glassing matrix on 13C dynamic nuclear polarization. *Phys Chem Chem Phys*. 2013;15(19):7032. doi:10.1039/c3cp50750e

53. Cancer Imaging Program. Hyperpolarized Pyruvate (13C) Injection: Investigator’s Brochure. January 2016. http://imaging.cancer.gov/images/documents/c13_pyruvate_IB_PDF.

54. Kuzma NN, Pourfathi M, Kara H, et al. Cluster formation restricts dynamic nuclear polarization of xenon in solid mixtures. *J Chem Phys*. 2012;137(10):104508.

55. Muñoz-Gómez JL, Monteagudo E, Lloveras V, Parella T, Veciana J, Vidal-Gancedo J. A benzyl alcohol derivative of the BDPA radical for fast dissolution dynamic nuclear polarization NMR spectroscopy. *Org Biomol Chem*. 2015;13(9):2689-2693. doi:10.1039/C4OB02356K

56. Haze O, Corzilius B, Smith AA, Griffin RG, Swager TM. Water-Soluble Narrow-Line Radicals for Dynamic Nuclear Polarization. *J Am Chem Soc*. 2012;134(35):14287-14290. doi:10.1021/ja304918g

57. McCarney ER, Armstrong BD, Lingwood MD, Han S. Hyperpolarized water as an authentic magnetic resonance imaging contrast agent. *Proc Natl Acad Sci*. 2007;104(6):1754–1759.

58. Ardenkjaer-Larsen JH, Laustsen C, Pullinger B, Kadlecek S, Emami K, Rizi R. Hyperpolarized Water for Interventional Angiography. In: *Proc. Int. Soc. Mag. Reson. Med*. Vol 19. ; 2011:3534. http://cds.ismrm.org/protected/11MProceedings/files/3534.pdf. Accessed June 9, 2016.

59. Lingwood MD, Siaw TA, Sailasuta N, et al. Hyperpolarized water as an MR imaging contrast agent: feasibility of in vivo imaging in a rat model. *Radiology*. 2012;265(2):418–425.

60. Song C, Hu K-N, Joo C-G, Swager TM, Griffin RG. TOTAPOL: A Biradical Polarizing Agent for Dynamic Nuclear Polarization Experiments in Aqueous Media. *J Am Chem Soc*. 2006;128(35):11385-11390. doi:10.1021/ja061284b

61. Matsuki Y, Maly T, Ouari O, et al. Dynamic Nuclear Polarization with a Rigid Biradical. *Angew Chem Int Ed*. 2009;48(27):4996-5000. doi:10.1002/anie.200805940

62. Hu K-N, Yu H, Swager TM, Griffin RG. Dynamic Nuclear Polarization with Biradicals. *J Am Chem Soc*. 2004;126(35):10844-10845. doi:10.1021/ja039749a

63. Eichhorn TR, Takado Y, Salameh N, et al. Hyperpolarization without persistent radicals for in vivo real-time metabolic imaging. *Proc Natl Acad Sci*. 2013;110(45):18064-18069. doi:10.1073/pnas.1314928110

64. Ardenkjaer-Larsen JH, Macholl S, Jóhannesson H. Dynamic Nuclear Polarization with Trityls at 1.2 K. *Appl Magn Reson*. 2008;34(3-4):509-522. doi:10.1007/s00723-008-0134-4

65. Hurd RE, Yen Y-F, Chen A, Ardenkjaer-Larsen JH. Hyperpolarized ^{13} C metabolic imaging using dissolution dynamic nuclear polarization. *J Magn Reson Imaging*. 2012;36(6):1314-1328. doi:10.1002/jmri.23753

66. Walker SA, Edwards DT, Siaw TA, Armstrong BD, Han S. Temperature dependence of high field 13C dynamic nuclear polarization processes with trityl radicals below 35 Kelvin. *Phys Chem Chem Phys*. 2013;15(36):15106. doi:10.1039/c3cp51628h

67. Jannin S, Comment A, Kurdzesau F, et al. A 140 GHz prepolarizer for dissolution dynamic nuclear polarization. *J Chem Phys*. 2008;128(24):241102. doi:10.1063/1.2951994

68. Shang H, Skloss T, von Morze C, et al. Handheld electromagnet carrier for transfer of hyperpolarized carbon-13 samples. *Magn Reson Med*. March 2015:n/a-n/a. doi:10.1002/mrm.25657

69. Bargon J, Fischer H, Johnsen U. Nuclear magnetic resonance emission lines during fast radical reactions. I. Recording methods and examples. *Z Naturforsch A*. 1967;22:1551–1555.

70. Ward HR, Lawler RG. Nuclear magnetic resonance emission and enhanced absorption in rapid organometallic reactions. *J Am Chem Soc*. 1967;89(21):5518–5519.

71. Bowers CR, Weitekamp DP. Transformation of symmetrization order to nuclear-spin magnetization by chemical reaction and nuclear magnetic resonance. *Phys Rev Lett*. 1986;57(21):2645.

72. Natterer J, Bargon J. Parahydrogen induced polarization. *Prog Nucl Magn Reson Spectrosc*. 1997;31(4):293-315. doi:10.1016/S0079-6565(97)00007-1

73. Bhattacharya P, Chekmenev EY, Reynolds WF, et al. Parahydrogen-induced polarization (PHIP) hyperpolarized MR receptor imaging in vivo: a pilot study of 13C imaging of atheroma in mice: Towards Imaging Plaque In Vivo using 13C Hyperpolarization. *NMR Biomed*. 2011;24(8):1023-1028. doi:10.1002/nbm.1717

74. Ishii M, Emami K, Kadlecek S, et al. Hyperpolarized13C MRI of the pulmonary vasculature and parenchyma. *Magn Reson Med*. 2007;57(3):459-463. doi:10.1002/mrm.21168

75. Zacharias NM, Chan HR, Sailasuta N, Ross BD, Bhattacharya P. Real-Time Molecular Imaging of Tricarboxylic Acid Cycle Metabolism in Vivo by Hyperpolarized 1- ^{13} C Diethyl Succinate. *J Am Chem Soc*. 2012;134(2):934-943. doi:10.1021/ja2040865

76. Coffey AM, Shchepin RV, Truong ML, Wilkens K, Pham W, Chekmenev EY. Open-Source Automated Parahydrogen Hyperpolarizer for Molecular Imaging Using (13)C Metabolic Contrast Agents. *Anal Chem*. 2016;88(16):8279-8288. doi:10.1021/acs.analchem.6b02130

77. Juarez AM, Cubric D, King GC. A compact catalytic converter for the production of para-hydrogen. *Meas Sci Technol*. 2002;13(5):N52.

78. Weitzel D, Loebenstein W, Draper J, Park O. Ortho-Para Catalysis in Liquid-Hydrogen Production. *J Res Natl Bur Stand*. 1958;60(3):221.

79. Morris GA, Freeman R. Enhancement of nuclear magnetic resonance signals by polarization transfer. *J Am Chem Soc*. 1979;101(3):760–762.

80. Kadlecek S, Emami K, Ishii M, Rizi R. Optimal transfer of spin-order between a singlet nuclear pair and a heteronucleus. *J Magn Reson*. 2010;205(1):9-13. doi:10.1016/j.jmr.2010.03.004

81. Barkemeyer J, Bargon J, Sengstschmid H, Freeman R. Heteronuclear Polarization Transfer Using Selective Pulses during Hydrogenation with Parahydrogen. *J Magn Reson*. 1996;120:129-132. doi:10.1006/jmra.1996.0109

82. Haake M, Natterer J, Bargon J. Efficient NMR Pulse Sequences to Transfer the Parahydrogen-Induced Polarization to Hetero Nuclei. *J Am Chem Soc*. 1996;118(36):8688-8691. doi:10.1021/ja960067f

83. Goldman M, Jóhannesson H. Conversion of a proton pair para order into 13C polarization by rf irradiation, for use in MRI. *Comptes Rendus Phys*. 2005;6(4-5):575-581. doi:10.1016/j.crhy.2005.03.002

84. Golman K, Axelsson O, Jóhannesson H, M\a ansson S, Olofsson C, Petersson JS. Parahydrogen-induced polarization in imaging: Subsecond 13C angiography. *Magn Reson Med*. 2001;46(1):1–5.

85. Jóhannesson H, Axelsson O, Karlsson M. Transfer of para-hydrogen spin order into polarization by diabatic field cycling. *Comptes Rendus Phys*. 2004;5(3):315-324. doi:10.1016/j.crhy.2004.02.001

86. Kadlecek S, Vahdat V, Nakayama T, Ng D, Emami K, Rizi R. A simple and low-cost device for generating hyperpolarized contrast agents using parahydrogen: LOW-COST IMPLEMENTATION OF PARAHYDROGEN-INDUCED POLARIZATION. *NMR Biomed*. 2011;24(8):933-942. doi:10.1002/nbm.1757

87. Shchepin RV, Coffey AM, Waddell KW, Chekmenev EY. Parahydrogen Induced Polarization of 1- ^{13} C-Phospholactate- *d* $_2$ for Biomedical Imaging with >30,000,000-fold NMR Signal Enhancement in Water. *Anal Chem*. 2014;86(12):5601-5605. doi:10.1021/ac500952z

88. Reineri F, Boi T, Aime S. ParaHydrogen Induced Polarization of 13C carboxylate resonance in acetate and pyruvate. *Nat Commun*. 2015;6:5858. doi:10.1038/ncomms6858

89. Shchepin RV, Barskiy DA, Coffey AM, Manzanera Esteve IV, Chekmenev EY. Efficient Synthesis of Molecular Precursors for Para-Hydrogen-Induced Polarization of Ethyl Acetate-1-13C and Beyond. *Angew Chem Int Ed*. 2016;55(20):6071-6074. doi:10.1002/anie.201600521

90. Cavallari E, Carrera C, Boi T, Aime S, Reineri F. Effects of Magnetic Field Cycle on the Polarization Transfer from Parahydrogen to Heteronuclei through Long-Range J-Couplings. *J Phys Chem B*. 2015;119(31):10035-10041. doi:10.1021/acs.jpcb.5b06222

91. Gridnev ID, Higashi N, Asakura K, Imamoto T. Mechanism of Asymmetric Hydrogenation Catalyzed by a Rhodium Complex of (*S,S*)-1,2-Bis(*tert* -butylmethylphosphino)ethane. Dihydride Mechanism of Asymmetric Hydrogenation. *J Am Chem Soc*. 2000;122(30):7183-7194. doi:10.1021/ja000813n

92. Burgess JM, Molloy NA. Gas absorption in the plunging liquid jet reactor. *Chem Eng Sci*. 1973;28(1):183–190.

93. Hövener J-B, Chekmenev EY, Harris KC, et al. PASADENA hyperpolarization of 13C biomolecules: equipment design and installation. *Magn Reson Mater Phys Biol Med*. 2009;22(2):111-121. doi:10.1007/s10334-008-0155-x

94. Goldman M, Jóhannesson H, Axelsson O, Karlsson M. Design and implementation of 13C hyper polarization from para-hydrogen, for new MRI contrast agents. *Comptes Rendus Chim*. 2006;9(3-4):357-363. doi:10.1016/j.crci.2005.05.010

95. Glöggler S, Grunfeld AM, Ertas YN, et al. A Nanoparticle Catalyst for Heterogeneous Phase Para-Hydrogen-Induced Polarization in Water. *Angew Chem Int Ed*. 2015;54(8):2452-2456. doi:10.1002/anie.201409027

96. Bhattacharya P, Chekmenev EY, Perman WH, et al. Towards hyperpolarized 13C-succinate imaging of brain cancer. *J Magn Reson*. 2007;186(1):150-155. doi:10.1016/j.jmr.2007.01.017

97. Ross BD, Bhattacharya P, Wagner S, Tran T, Sailasuta N. Hyperpolarized MR Imaging: Neurologic Applications of Hyperpolarized Metabolism. *Am J Neuroradiol*. 2010;31(1):24-33. doi:10.3174/ajnr.A1790

98. Adams RW, Aguilar JA, Atkinson KD, et al. Reversible Interactions with para-Hydrogen Enhance NMR Sensitivity by Polarization Transfer. *Science*. 2009;323(5922):1708-1711. doi:10.1126/science.1168877

99. Ardenkjær-Larsen JH, Fridlund B, Gram A, et al. Increase in signal-to-noise ratio of > 10,000 times in liquid-state NMR. *Proc Natl Acad Sci*. 2003;100(18):10158-10163. doi:10.1073/pnas.1733835100

100. Comment A. Dissolution DNP for in vivo preclinical studies. *J Magn Reson*. 2016;264:39-48. doi:10.1016/j.jmr.2015.12.027

101. Nelson SJ, Kurhanewicz J, Vigneron DB, et al. Metabolic Imaging of Patients with Prostate Cancer Using Hyperpolarized [1-13C]Pyruvate. *Sci Transl Med*. 2013;5(198):198ra108-198ra108. doi:10.1126/scitranslmed.3006070

102. Laustsen C, Hansen ESS, Kjaergaard U, Bertelsen LB, Ringgaard S, Stødkilde-Jørgensen H. Acute porcine renal metabolic effect of endogastric soft drink administration assessed with hyperpolarized [1-13c]pyruvate: Oral Sucrose Load Assessed with MRS in Porcine Kidney. *Magn Reson Med*. 2015;74(2):558-563. doi:10.1002/mrm.25692

103. Giovannetti G, Frijia F, Menichetti L, et al. Hyperpolarized [sup 13]C MRS surface coil: Design and signal-to-noise ratio estimation. *Med Phys*. 2010;37(10):5361. doi:10.1118/1.3491437

104. Chen AP, Hurd RE, Schroeder MA, et al. Simultaneous investigation of cardiac pyruvate dehydrogenase flux, Krebs cycle metabolism and pH, using hyperpolarized [1,2-13C2]pyruvate in vivo: HYPERPOLARIZED [1,2-13C2]PYRUVATE IN HEART. *NMR Biomed*. 2012;25(2):305-311. doi:10.1002/nbm.1749

105. Park JM, Josan S, Jang T, et al. Volumetric spiral chemical shift imaging of hyperpolarized [2-13c]pyruvate in a rat c6 glioma model. *Magn Reson Med*. May 2015:n/a-n/a. doi:10.1002/mrm.25766

106. Day SE, Kettunen MI, Gallagher FA, et al. Detecting tumor response to treatment using hyperpolarized 13C magnetic resonance imaging and spectroscopy. *Nat Med*. 2007;13(11):1382-1387. doi:10.1038/nm1650

107. Asghar Butt S, Søgaard LV, Ardenkjaer-Larsen JH, et al. Monitoring mammary tumor progression and effect of tamoxifen treatment in MMTV-PymT using MRI and magnetic resonance spectroscopy with hyperpolarized [1-13C]pyruvate. *Magn Reson Med*. 2015;73(1):51-58. doi:10.1002/mrm.25095

108. Dominguez-Viqueira W, Geraghty BJ, Lau JYC, Robb FJ, Chen AP, Cunningham CH. Intensity correction for multichannel hyperpolarized ^{13} C imaging of the heart: Intensity Correction for Multichannel ^{13} C. *Magn Reson Med*. 2016;75(2):859-865. doi:10.1002/mrm.26042

109. Sack M, Wetterling F, Sartorius A, Ende G, Weber-Fahr W. Signal-to-noise ratio of a mouse brain ^{13} C CryoProbe^{TM} system in comparison with room temperature coils: spectroscopic phantom and *in vivo* results: SNR OF A ^{13} C CRYOPROBE^{TM} IN COMPARISON WITH ROOM TEMPERATURE COILS. *NMR Biomed*. 2014;27(6):709-715. doi:10.1002/nbm.3110

110. Kovacs H, Moskau D, Spraul M. Cryogenically cooled probes—a leap in NMR technology. *Prog Nucl Magn Reson Spectrosc*. 2005;46(2-3):131-155. doi:10.1016/j.pnmrs.2005.03.001

111. Yen Y-F, Kohler SJ, Chen AP, et al. Imaging considerations for in vivo ^{13} C metabolic mapping using hyperpolarized ^{13} C-pyruvate. *Magn Reson Med*. 2009;62(1):1-10. doi:10.1002/mrm.21987

112. Lau AZ, Chen AP, Ghugre NR, et al. Rapid multislice imaging of hyperpolarized 13C pyruvate and bicarbonate in the heart. *Magn Reson Med*. 2010;64(5):1323-1331. doi:10.1002/mrm.22525

113. Lau AZ, Miller JJ, Robson MD, Tyler DJ. Simultaneous assessment of cardiac metabolism and perfusion using copolarized [1- ^{13} C]pyruvate and ^{13} C-urea: Simultaneous Hyperpolarized Cardiac Perfusion and Metabolic Imaging. *Magn Reson Med*. January 2016:n/a-n/a. doi:10.1002/mrm.26106

114. Gordon JW, Niles DJ, Adamson EB, Johnson KM, Fain SB. Application of flow sensitive gradients for improved measures of metabolism using hyperpolarized 13c MRI. *Magn Reson Med*. May 2015:n/a-n/a. doi:10.1002/mrm.25584

115. Svensson J, Månsson S, Johansson E, Petersson JS, Olsson LE. Hyperpolarized ^{13} C MR angiography using trueFISP: Hyperpolarized ^{13} C MRA Using TrueFISP. *Magn Reson Med*. 2003;50(2):256-262. doi:10.1002/mrm.10530

116. Yen Y-F, Le Roux P, Mayer D, et al. T $_{2}$ relaxation times of ^{13} C metabolites in a rat hepatocellular carcinoma model measured *in vivo* using ^{13} C-MRS of hyperpolarized [1- ^{13} C]pyruvate. *NMR Biomed*. 2010:n/a-n/a. doi:10.1002/nbm.1481

117. Reed GD, von Morze C, Bok R, et al. High Resolution 13C MRI With Hyperpolarized Urea: In Vivo Mapping and 15N Labeling Effects. *IEEE Trans Med Imaging*. 2014;33(2):362-371. doi:10.1109/TMI.2013.2285120

118. Laustsen C, Stokholm Nørlinger T, Christoffer Hansen D, et al. Hyperpolarized ^{13} C urea relaxation mechanism reveals renal changes in diabetic nephropathy: [^{13} C]Urea Apparent Relaxation Contrast Reveals Diabetic Nephropathy. *Magn Reson Med*. 2016;75(2):515-518. doi:10.1002/mrm.26036

119. Keshari KR, Wilson DM. Chemistry and biochemistry of 13C hyperpolarized magnetic resonance using dynamic nuclear polarization. *Chem Soc Rev*. 2014;43(5):1627. doi:10.1039/c3cs60124b

120. Golman K, Zandt R in 't, Thaning M. Real-time metabolic imaging. *Proc Natl Acad Sci*. 2006;103(30):11270-11275. doi:10.1073/pnas.0601319103

121. Harris T, Eliyahu G, Frydman L, Degani H. Kinetics of hyperpolarized 13C1-pyruvate transport and metabolism in living human breast cancer cells. *Proc Natl Acad Sci*. 2009;106(43):18131–18136.

122. Shaghaghi H, Kadlecek S, Deshpande C, et al. Metabolic spectroscopy of inflammation in a bleomycin-induced lung injury model using hyperpolarized 1-13C pyruvate. *NMR Biomed*. 2014;27(8):939-947. doi:10.1002/nbm.3139

123. Park I, Larson PEZ, Tropp JL, et al. Dynamic hyperpolarized carbon-13 MR metabolic imaging of nonhuman primate brain. *Magn Reson Med*. 2014;71(1):19-25. doi:10.1002/mrm.25003

124. Spielman DM, Mayer D, Yen Y-F, Tropp J, Hurd RE, Pfefferbaum A. In vivo measurement of ethanol metabolism in the rat liver using magnetic resonance spectroscopy of hyperpolarized [1- ^{13} C]pyruvate. *Magn Reson Med*. 2009;62(2):307-313. doi:10.1002/mrm.21998

125. Mulkern RV, Panych LP. Echo planar spectroscopic imaging. *Concepts Magn Reson*. 2001;13(4):213-237. doi:10.1002/cmr.1011

126. Cunningham CH, Chen AP, Lustig M, et al. Pulse sequence for dynamic volumetric imaging of hyperpolarized metabolic products. *J Magn Reson*. 2008;193(1):139-146. doi:10.1016/j.jmr.2008.03.012

127. Cunningham CH, Chen AP, Albers MJ, et al. Double spin-echo sequence for rapid spectroscopic imaging of hyperpolarized 13C. *J Magn Reson*. 2007;187(2):357-362. doi:10.1016/j.jmr.2007.05.014

128. Mayer D, Yen Y-F, Tropp J, Pfefferbaum A, Hurd RE, Spielman DM. Application of subsecond spiral chemical shift imaging to real-time multislice metabolic imaging of the rat in vivo after injection of hyperpolarized ^{13} C $_1$ -pyruvate. *Magn Reson Med*. 2009;62(3):557-564. doi:10.1002/mrm.22041

129. Mayer D, Yen Y-F, Levin YS, et al. In vivo application of sub-second spiral chemical shift imaging (CSI) to hyperpolarized 13C metabolic imaging: Comparison with phase-encoded CSI. *J Magn Reson*. 2010;204(2):340-345. doi:10.1016/j.jmr.2010.03.005

130. Jiang W, Lustig M, Larson PEZ. Concentric rings K-space trajectory for hyperpolarized 13C MR spectroscopic imaging. *Magn Reson Med*. December 2014:n/a-n/a. doi:10.1002/mrm.25577

131. Dixon WT. Simple proton spectroscopic imaging. *Radiology*. 1984;153(1):189–194.

132. Reeder SB, Wen Z, Yu H, et al. Multicoil Dixon chemical species separation with an iterative least-squares estimation method. *Magn Reson Med*. 2004;51(1):35-45. doi:10.1002/mrm.10675

133. Reeder SB, Brittain JH, Grist TM, Yen Y-F. Least-squares chemical shift separation for13C metabolic imaging. *J Magn Reson Imaging*. 2007;26(4):1145-1152. doi:10.1002/jmri.21089

134. Wiens CN, Friesen-Waldner LJ, Wade TP, Sinclair KJ, McKenzie CA. Chemical shift encoded imaging of hyperpolarized ^{13} C pyruvate: Chemical Shift Encoded Imaging of ^{13} C Pyruvate. *Magn Reson Med*. 2015;74(6):1682-1689. doi:10.1002/mrm.25532

135. Wiesinger F, Weidl E, Menzel MI, et al. IDEAL spiral CSI for dynamic metabolic MR imaging of hyperpolarized [1-13C]pyruvate. *Magn Reson Med*. 2012;68(1):8-16. doi:10.1002/mrm.23212

136. Sigfridsson A, Weiss K, Wissmann L, et al. Hybrid multiband excitation multiecho acquisition for hyperpolarized ^{13} C spectroscopic imaging: Hybrid Multiband Excitation Multiecho Acquisition Metabolic Imaging. *Magn Reson Med*. May 2014:n/a-n/a. doi:10.1002/mrm.25294

137. Larson PEZ, Kerr AB, Chen AP, et al. Multiband excitation pulses for hyperpolarized 13C dynamic chemical-shift imaging. *J Magn Reson*. 2008;194(1):121-127. doi:10.1016/j.jmr.2008.06.010

138. Lau AZ. Frequency-selective methods for hyperpolarized 13 C cardiac magnetic resonance imaging. 2012. https://tspace.library.utoronto.ca/handle/1807/34779. Accessed July 7, 2016.

139. Xing Y, Reed GD, Pauly JM, Kerr AB, Larson PEZ. Optimal variable flip angle schemes for dynamic acquisition of exchanging hyperpolarized substrates. *J Magn Reson*. 2013;234:75-81. doi:10.1016/j.jmr.2013.06.003

140. Marco-Rius I, Cao P, von Morze C, et al. Multiband spectral-spatial RF excitation for hyperpolarized [2- ^{13} C]dihydroxyacetone ^{13} C-MR metabolism studies: Spectral-Spatial Excitation of HP ^{13} C-Dihydroxyacetone. *Magn Reson Med*. March 2016:n/a-n/a. doi:10.1002/mrm.26226

141. Gordon JW, Vigneron DB, Larson PEZ. Development of a symmetric echo planar imaging framework for clinical translation of rapid dynamic hyperpolarized ^{13} C imaging: Rapid Imaging of Hyperpolarized ^{13} C with Symmetric EPI. *Magn Reson Med*. February 2016:n/a-n/a. doi:10.1002/mrm.26123

142. Miller JJ, Lau AZ, Teh I, et al. Robust and high resolution hyperpolarized metabolic imaging of the rat heart at 7 t with 3d spectral-spatial EPI: Hyperpolarized Cardiac Imaging with 3D Spectral-Spatial EPI. *Magn Reson Med*. 2016;75(4):1515-1524. doi:10.1002/mrm.25730

143. Lau AZ, Miller JJ, Tyler DJ. Mapping of intracellular pH in the in vivo rodent heart using hyperpolarized [1-13C]pyruvate: Cardiac Intracellular pH Mapping. *Magn Reson Med*. April 2016. doi:10.1002/mrm.26260

144. Wang J, Wright AJ, Hu D, Hesketh R, Brindle KM. Single shot three-dimensional pulse sequence for hyperpolarized ^{13} C MRI: Fast 3D Hyperpolarized ^{13} C Imaging. *Magn Reson Med*. February 2016:n/a-n/a. doi:10.1002/mrm.26168

145. Chen AP, Leung K, Lam W, Hurd RE, Vigneron DB, Cunningham CH. Design of spectral-spatial outer volume suppression RF pulses for tissue specific metabolic characterization with hyperpolarized 13C pyruvate. *J Magn Reson*. 2009;200(2):344-348. doi:10.1016/j.jmr.2009.06.021

146. Yang S, Lee J, Joe E, et al. Metabolite-selective hyperpolarized 13C imaging using extended chemical shift displacement at 9.4T. *Magn Reson Imaging*. 2016;34(4):535-540. doi:10.1016/j.mri.2015.12.023

147. von Morze C, Reed G, Shin P, et al. Multi-band frequency encoding method for metabolic imaging with hyperpolarized [1-13C]pyruvate. *J Magn Reson*. 2011;211(2):109-113. doi:10.1016/j.jmr.2011.04.007

148. Ghosh RK, Kadlecek SJ, Pourfathi M, Rizi RR. Efficient production of hyperpolarized bicarbonate by chemical reaction on a DNP precursor to measure pH. *Magn Reson Med*. November 2014:n/a-n/a. doi:10.1002/mrm.25530

149. Ramirez MS, Lee J, Walker CM, et al. Radial spectroscopic MRI of hyperpolarized [1- ^{13} C] pyruvate at 7 tesla: Radial MRI of Hyperpolarized Pyruvate at 7T. *Magn Reson Med*. 2014;72(4):986-995. doi:10.1002/mrm.25004

150. Mayer D, Levin YS, Hurd RE, Glover GH, Spielman DM. Fast metabolic imaging of systems with sparse spectra: Application for hyperpolarized13C imaging. *Magn Reson Med*. 2006;56(4):932-937. doi:10.1002/mrm.21025

151. Golman K, Olsson LE, Axelsson O, Månsson S, Karlsson M, Petersson JS. Molecular imaging using hyperpolarized ^{13} C. *Br J Radiol*. 2003;76(suppl_2):S118-S127. doi:10.1259/bjr/26631666

152. von Morze C, Bok RA, Reed GD, Ardenkjaer-Larsen JH, Kurhanewicz J, Vigneron DB. Simultaneous multiagent hyperpolarized ^{13} C perfusion imaging: Multiagent HP ^{13} C Perfusion MRI. *Magn Reson Med*. 2014;72(6):1599-1609. doi:10.1002/mrm.25071

153. von Morze C, Sukumar S, Reed GD, et al. Frequency-specific SSFP for hyperpolarized 13C metabolic imaging at 14.1 T. *Magn Reson Imaging*. 2013;31(2):163-170. doi:10.1016/j.mri.2012.06.037

154. Arunachalam A, Whitt D, Fish K, et al. Accelerated spectroscopic imaging of hyperpolarized C-13 pyruvate using SENSE parallel imaging. *NMR Biomed*. 2009;22(8):867-873. doi:10.1002/nbm.1401

155. Shin PJ, Larson PEZ, Uecker M, et al. Chemical shift separation with controlled aliasing for hyperpolarized ^{13} C metabolic imaging: Accelerated Metabolite Imaging in Hyperpolarized ^{13} C MR. *Magn Reson Med*. 2015;74(4):978-989. doi:10.1002/mrm.25473

156. Cao P, Shin PJ, Park I, et al. Accelerated high-bandwidth MR spectroscopic imaging using compressed sensing: Random Walk MRSI. *Magn Reson Med*. May 2016. doi:10.1002/mrm.26272

157. Geraghty BJ, Lau JYC, Chen AP, Cunningham CH. Accelerated 3D echo-planar imaging with compressed sensing for time-resolved hyperpolarized ^{13} C studies: Compressed Sensing ^{13} C 3D EPI. *Magn Reson Med*. January 2016:n/a-n/a. doi:10.1002/mrm.26125

158. Hu S, Lustig M, Balakrishnan A, et al. 3D compressed sensing for highly accelerated hyperpolarized ^{13} C MRSI with in vivo applications to transgenic mouse models of cancer. *Magn Reson Med*. 2010;63(2):312-321. doi:10.1002/mrm.22233

159. Schroeder MA, Cochlin LE, Heather LC, Clarke K, Radda GK, Tyler DJ. In vivo assessment of pyruvate dehydrogenase flux in the heart using hyperpolarized carbon-13 magnetic resonance. *Proc Natl Acad Sci*. 2008;105(33):12051-12056. doi:10.1073/pnas.0805953105

160. Seth P, Grant A, Tang J, et al. On-target Inhibition of Tumor Fermentative Glycolysis as Visualized by Hyperpolarized Pyruvate. *Neoplasia*. 2011;13(1):60-71. doi:10.1593/neo.101020

161. Hill DK, Orton MR, Mariotti E, et al. Model Free Approach to Kinetic Analysis of Real-Time Hyperpolarized 13 C Magnetic Resonance Spectroscopy Data. *PLOS ONE*. 2013;8(9):e71996. doi:10.1371/journal.pone.0071996

162. Shaghaghi H, Kadlecek S, Siddiqui S, et al. Ascorbic acid prolongs the viability and stability of isolated perfused lungs: A mechanistic study using 31P and hyperpolarized 13C nuclear magnetic resonance. *Free Radic Biol Med*. 2015;89:62-71. doi:10.1016/j.freeradbiomed.2015.06.042

163. Zierhut ML, Yen Y-F, Chen AP, et al. Kinetic modeling of hyperpolarized 13C1-pyruvate metabolism in normal rats and TRAMP mice. *J Magn Reson*. 2010;202(1):85-92. doi:10.1016/j.jmr.2009.10.003

164. Li LZ, Kadlececk S, Xu HN, et al. Ratiometric analysis in hyperpolarized NMR (I): test of the two-site exchange model and the quantification of reaction rate constants: RATIOMETRIC DATA ANALYSIS FOR HYPERPOLARIZED NMR. *NMR Biomed*. 2013;26(10):1308-1320. doi:10.1002/nbm.2953

165. Kadlecek S, Shaghaghi H, Siddiqui S, Profka H, Pourfathi M, Rizi R. The effect of exogenous substrate concentrations on true and apparent metabolism of hyperpolarized pyruvate in the isolated perfused lung. *NMR Biomed*. 2014;27(12):1557-1570. doi:10.1002/nbm.3219

166. Yoshihara HAI, Bastiaansen JAM, Berthonneche C, Comment A, Schwitter J. An Intact Small Animal Model of Myocardial Ischemia-Reperfusion: Characterization of Metabolic Changes by Hyperpolarized 13C MR Spectroscopy. *Am J Physiol - Heart Circ Physiol*. October 2015:ajpheart.00376.2015. doi:10.1152/ajpheart.00376.2015

167. Zewe V, Fromm HJ. Kinetic studies of rabbit muscle lactate dehydrogenase. *J Biol Chem*. 1962;237(5):1668–1675.

168. Borgmann U, Laidler KJ, Moon TW. Kinetics and thermodynamics of lactate dehydrogenases from beef heart, beef muscle, and flounder muscle. *Can J Biochem*. 1975;53(11):1196–1206.

169. Golman K, Zandt R i., Lerche M, Pehrson R, Ardenkjaer-Larsen JH. Metabolic Imaging by Hyperpolarized 13C Magnetic Resonance Imaging for In vivo Tumor Diagnosis. *Cancer Res*. 2006;66(22):10855-10860. doi:10.1158/0008-5472.CAN-06-2564

170. Chen AP, Albers MJ, Cunningham CH, et al. Hyperpolarized C-13 spectroscopic imaging of the TRAMP mouse at 3T—Initial experience. *Magn Reson Med*. 2007;58(6):1099-1106. doi:10.1002/mrm.21256

171. Merritt ME, Harrison C, Sherry AD, Malloy CR, Burgess SC. Flux through hepatic pyruvate carboxylase and phosphoenolpyruvate carboxykinase detected by hyperpolarized 13C magnetic resonance. *Proc Natl Acad Sci*. 2011;108(47):19084-19089. doi:10.1073/pnas.1111247108

172. Albers MJ, Bok R, Chen AP, et al. Hyperpolarized 13C Lactate, Pyruvate, and Alanine: Noninvasive Biomarkers for Prostate Cancer Detection and Grading. *Cancer Res*. 2008;68(20):8607-8615. doi:10.1158/0008-5472.CAN-08-0749

173. Pullinger B, Profka H, Ardenkjaer-Larsen JH, Kuzma NN, Kadlecek S, Rizi RR. Metabolism of hyperpolarized [1-13C]pyruvate in the isolated perfused rat lung - an ischemia study:

MEASUREMENTS OF LUNG METABOLISM USING HYPERPOLARIZED 1-13C PYRUVATE. *NMR Biomed*. 2012;25(10):1113-1118. doi:10.1002/nbm.2777

174. Hu S, Chen AP, Zierhut ML, et al. In Vivo Carbon-13 Dynamic MRS and MRSI of Normal and Fasted Rat Liver with Hyperpolarized 13C-Pyruvate. *Mol Imaging Biol*. 2009;11(6):399-407. doi:10.1007/s11307-009-0218-z

175. Maren TH. Carbonic anhydrase: chemistry, physiology, and inhibition. *Physiol Rev*. 1967;47(4):595–781.

176. Merritt ME, Harrison C, Storey C, Jeffrey FM, Sherry AD, Malloy CR. Hyperpolarized 13C allows a direct measure of flux through a single enzyme-catalyzed step by NMR. *Proc Natl Acad Sci*. 2007;104(50):19773-19777. doi:10.1073/pnas.0706235104

177. Moreno KX, Sabelhaus SM, Merritt ME, Sherry AD, Malloy CR. Competition of pyruvate with physiological substrates for oxidation by the heart: implications for studies with hyperpolarized [1-13C]pyruvate. *Am J Physiol - Heart Circ Physiol*. 2010;298(5):H1556-H1564. doi:10.1152/ajpheart.00656.2009

178. Marjańska M, Iltis I, Shestov AA, et al. In vivo 13C spectroscopy in the rat brain using hyperpolarized [1-13C]pyruvate and [2-13C]pyruvate. *J Magn Reson*. 2010;206(2):210-218. doi:10.1016/j.jmr.2010.07.006

179. Schroeder MA, Atherton HJ, Ball DR, et al. Real-time assessment of Krebs cycle metabolism using hyperpolarized 13C magnetic resonance spectroscopy. *FASEB J*. 2009;23(8):2529-2538. doi:10.1096/fj.09-129171

180. Hu S, Yoshihara HAI, Bok R, et al. Use of hyperpolarized [1-13C]pyruvate and [2-13C]pyruvate to probe the effects of the anticancer agent dichloroacetate on mitochondrial metabolism in vivo in the normal rat. *Magn Reson Imaging*. 2012;30(10):1367-1372. doi:10.1016/j.mri.2012.05.012

181. Schroeder MA, Atherton HJ, Dodd MS, et al. The Cycling of Acetyl-Coenzyme A Through Acetylcarnitine Buffers Cardiac Substrate Supply A Hyperpolarized 13C Magnetic Resonance Study. *Circ Cardiovasc Imaging*. 2012;5(2):201-209. doi:10.1161/CIRCIMAGING.111.969451

182. Bastiaansen JAM, Cheng T, Mishkovsky M, Duarte JMN, Comment A, Gruetter R. In vivo enzymatic activity of acetylCoA synthetase in skeletal muscle revealed by 13C turnover from hyperpolarized [1-13C]acetate to [1-13C]acetylcarnitine. *Biochim Biophys Acta BBA - Gen Subj*. 2013;1830(8):4171-4178. doi:10.1016/j.bbagen.2013.03.023

183. Flori A, Liserani M, Frijia F, et al. Real-time cardiac metabolism assessed with hyperpolarized [1- ^{13} C]acetate in a large-animal model: [^{13} C]ACETATE FOR REAL-TIME CARDIAC METABOLISM. *Contrast Media Mol Imaging*. 2015;10(3):194-202. doi:10.1002/cmmi.1618

184. Hu S, Zhu M, Yoshihara HAI, et al. In vivo measurement of normal rat intracellular pyruvate and lactate levels after injection of hyperpolarized [1-13C]alanine. *Magn Reson Imaging*. 2011;29(8):1035-1040. doi:10.1016/j.mri.2011.07.001

185. Felig P. The glucose-alanine cycle. *Metabolism*. 1973;22(2):179-207. doi:10.1016/0026-0495(73)90269-2

186. Hata R, Nonaka H, Takakusagi Y, Ichikawa K, Sando S. Design of a Hyperpolarized Molecular Probe for Detection of Aminopeptidase N Activity. *Angew Chem*. 2016;128(5):1797-1800. doi:10.1002/ange.201509457

187. Keshari KR, Sai V, Wang ZJ, VanBrocklin HF, Kurhanewicz J, Wilson DM. Hyperpolarized [1-13C]Dehydroascorbate MR Spectroscopy in a Murine Model of Prostate Cancer: Comparison with 18F-FDG PET. *J Nucl Med*. June 2013:jnumed.112.115402. doi:10.2967/jnumed.112.115402

188. Willis RJ, Kratzing CC. Transport of ascorbic acid in perfused rat lung. *Pflüg Arch*. 1975;356(1):93–98.

189. Du J, Cullen JJ, Buettner GR. Ascorbic acid: Chemistry, biology and the treatment of cancer. *Biochim Biophys Acta BBA - Rev Cancer*. 2012;1826(2):443-457. doi:10.1016/j.bbcan.2012.06.003

190. Bohndiek SE, Kettunen MI, Hu D, et al. Hyperpolarized [1- ^{13} C]-Ascorbic and Dehydroascorbic Acid: Vitamin C as a Probe for Imaging Redox Status in Vivo. *J Am Chem Soc*. 2011;133(30):11795-11801. doi:10.1021/ja2045925

191. Keshari KR, Kurhanewicz J, Bok R, Larson PEZ, Vigneron DB, Wilson DM. Hyperpolarized 13C dehydroascorbate as an endogenous redox sensor for in vivo metabolic imaging. *Proc Natl Acad Sci*. 2011;108(46):18606-18611. doi:10.1073/pnas.1106920108

192. Fraser ME, James MN, Bridger WA, Wolodko WT. A detailed structural description of Escherichia coli succinyl-CoA synthetase. *J Mol Biol*. 1999;285(4):1633–1653.

193. Oyedotun KS, Lemire BD. The Quaternary Structure of the Saccharomyces cerevisiae Succinate Dehydrogenase: HOMOLOGY MODELING, COFACTOR DOCKING, AND MOLECULAR DYNAMICS SIMULATION STUDIES. *J Biol Chem*. 2004;279(10):9424-9431. doi:10.1074/jbc.M311876200

194. Ishii N, Fujii M, Hartman PS, et al. A mutation in succinate dehydrogenase cytochrome b causes oxidative stress and ageing in nematodes. *Nature*. 1998;394(6694):694–697.

195. Selak MA, Armour SM, MacKenzie ED, et al. Succinate links TCA cycle dysfunction to oncogenesis by inhibiting HIF-α prolyl hydroxylase. *Cancer Cell*. 2005;7(1):77-85. doi:10.1016/j.ccr.2004.11.022

196. Hövener J-B, Chekmenev EY, Harris KC, et al. Quality assurance of PASADENA hyperpolarization for 13C biomolecules. *Magn Reson Mater Phys Biol Med*. 2008;22(2):123-134. doi:10.1007/s10334-008-0154-y

197. Billingsley KL, Josan S, Park JM, et al. Hyperpolarized [1,4- ^{13} C]-diethylsuccinate: a potential DNP substrate for *in vivo* metabolic imaging: HYPERPOLARIZED DIETHYLSUCCINATE: A DNP SUBSTRATE FOR IN VIVO IMAGING. *NMR Biomed*. 2014;27(3):356-362. doi:10.1002/nbm.3071

198. Gallagher FA, Kettunen MI, Day SE, et al. Magnetic resonance imaging of pH in vivo using hyperpolarized 13C-labelled bicarbonate. *Nature*. 2008;453(7197):940-943. doi:10.1038/nature07017

199. Kottmann RM, Kulkarni AA, Smolnycki KA, et al. Lactic Acid Is Elevated in Idiopathic Pulmonary Fibrosis and Induces Myofibroblast Differentiation via pH-Dependent Activation of Transforming Growth Factor-β. *Am J Respir Crit Care Med*. 2012;186(8):740-751. doi:10.1164/rccm.201201-0084OC

200. Hanahan D, Weinberg RA. Hallmarks of Cancer: The Next Generation. *Cell*. 2011;144(5):646-674. doi:10.1016/j.cell.2011.02.013

201. Harris T, Degani H, Frydman L. Hyperpolarized ^{13}C NMR studies of glucose metabolism in living breast cancer cell cultures: HYPERPOLARIZED ^{13}C GLUCOSE NMR OF LIVING BREAST CANCER CELL METABOLISM. *NMR Biomed*. 2013;26(12):1831-1843. doi:10.1002/nbm.3024

202. Timm KN, Hartl J, Keller MA, et al. Hyperpolarized [U-2H, U-13C]Glucose reports on glycolytic and pentose phosphate pathway activity in EL4 tumors and glycolytic activity in yeast cells. *Magn Reson Med*. December 2014:n/a-n/a. doi:10.1002/mrm.25561

203. Kurhanewicz J, Vigneron DB, Brindle K, et al. Analysis of Cancer Metabolism by Imaging Hyperpolarized Nuclei: Prospects for Translation to Clinical Research. *Neoplasia*. 2011;13(2):81-97. doi:10.1593/neo.101102

204. Dodd MS, Ball V, Bray R, et al. In vivo mouse cardiac hyperpolarized magnetic resonance spectroscopy. *J Cardiovasc Magn Reson*. 2013;15(1):19.

205. Ball DR, Rowlands B, Dodd MS, et al. Hyperpolarized butyrate: A metabolic probe of short chain fatty acid metabolism in the heart. *Magn Reson Med*. 2014;71(5):1663-1669. doi:10.1002/mrm.24849

206. Mayer D, Yen Y-F, Josan S, et al. Application of hyperpolarized [1-13C]lactate for the in vivo investigation of cardiac metabolism: INVESTIGATION OF CARDIAC METABOLISM WITH HYPERPOLARIZED [1-13C]LACTATE. *NMR Biomed*. 2012;25(10):1119-1124. doi:10.1002/nbm.2778

207. Atherton HJ, Dodd MS, Heather LC, et al. Role of Pyruvate Dehydrogenase Inhibition in the Development of Hypertrophy in the Hyperthyroid Rat Heart A Combined Magnetic Resonance Imaging and Hyperpolarized Magnetic Resonance Spectroscopy Study. *Circulation*. 2011;123(22):2552-2561. doi:10.1161/CIRCULATIONAHA.110.011387

208. Bastiaansen JAM, Cheng T, Lei H, Gruetter R, Comment A. Direct noninvasive estimation of myocardial tricarboxylic acid cycle flux in vivo using hyperpolarized 13C magnetic resonance. *J Mol Cell Cardiol*. 2015;87:129-137. doi:10.1016/j.yjmcc.2015.08.012

209. Koellisch U, Gringeri CV, Rancan G, et al. Metabolic imaging of hyperpolarized [1-^{13}C]acetate and [1-^{13}C]acetylcarnitine - investigation of the influence of dobutamine induced stress: Metabolic Imaging of Acetate and Acetylcarnitine. *Magn Reson Med*. 2015;74(4):1011-1018. doi:10.1002/mrm.25485

210. Merritt ME, Harrison C, Storey C, Sherry AD, Malloy CR. Inhibition of carbohydrate oxidation during the first minute of reperfusion after brief ischemia: NMR detection of hyperpolarized ^{13}CO$_2$ and H^{13}CO3−. *Magn Reson Med*. 2008;60(5):1029-1036. doi:10.1002/mrm.21760

211. Golman K, Petersson JS, Magnusson P, et al. Cardiac metabolism measured noninvasively by hyperpolarized 13C MRI. *Magn Reson Med*. 2008;59(5):1005-1013. doi:10.1002/mrm.21460

212. Schroeder MA, Swietach P, Atherton HJ, et al. Measuring intracellular pH in the heart using hyperpolarized carbon dioxide and bicarbonate: a 13C and 31P magnetic resonance spectroscopy study. *Cardiovasc Res*. 2010;86(1):82-91. doi:10.1093/cvr/cvp396

213. Kerbey AL, Randle PJ, Cooper RH, Whitehouse S, Pask HT, Denton RM. Regulation of pyruvate dehydrogenase in rat heart. Mechanism of regulation of proportions of dephosphorylated and

phosphorylated enzyme by oxidation of fatty acids and ketone bodies and of effects of diabetes: role of coenzyme A, acetyl-coenzyme A and reduced and oxidized nicotinamide-adenine dinucleotide. *Biochem J*. 1976;154(2):327-348. doi:10.1042/bj1540327

214. Rui L. Energy Metabolism in the Liver. In: Terjung R, ed. *Comprehensive Physiology*. Hoboken, NJ, USA: John Wiley & Sons, Inc.; 2014:177-197. http://doi.wiley.com/10.1002/cphy.c130024. Accessed June 10, 2016.

215. Reichard GA, Moury NF, Hochella NJ, Patterson AL, Weinhouse S. Quantitative Estimation of the Cori Cycle in the Human. *J Biol Chem*. 1963;238(2):495-501.

216. Lee P, Leong W, Tan T, Lim M, Han W, Radda GK. In Vivo hyperpolarized carbon-13 magnetic resonance spectroscopy reveals increased pyruvate carboxylase flux in an insulin-resistant mouse model. *Hepatology*. 2013;57(2):515-524. doi:10.1002/hep.26028

217. Jensen PR, Peitersen T, Karlsson M, et al. Tissue-specific Short Chain Fatty Acid Metabolism and Slow Metabolic Recovery after Ischemia from Hyperpolarized NMR in Vivo. *J Biol Chem*. 2009;284(52):36077-36082. doi:10.1074/jbc.M109.066407

218. CLIP. A new prognostic system for hepatocellular carcinoma: A retrospective study of 435 patients. *Hepatology*. 1998;28(3):751-755. doi:10.1002/hep.510280322

219. Gallagher FA, Kettunen MI, Day SE, Lerche M, Brindle KM. ^{13} C MR spectroscopy measurements of glutaminase activity in human hepatocellular carcinoma cells using hyperpolarized ^{13} C-labeled glutamine. *Magn Reson Med*. 2008;60(2):253-257. doi:10.1002/mrm.21650

220. Darpolor MM, Yen Y-F, Chua M-S, et al. In vivo MRSI of hyperpolarized [1-13C]pyruvate metabolism in rat hepatocellular carcinoma. *NMR Biomed*. 2011;24(5):506-513. doi:10.1002/nbm.1616

221. Darpolor MM. Human Hepatocellular Carcinoma Metabolism: Imaging by Hyperpolarized 13C Magnetic Resonance Spectroscopy. *J Liver Dis Transplant*. 2012;01(01). doi:10.4172/2325-9612.1000101

222. Bard-Chapeau EA, Nguyen A-T, Rust AG, et al. Transposon mutagenesis identifies genes driving hepatocellular carcinoma in a chronic hepatitis B mouse model. *Nat Genet*. 2013;46(1):24-32. doi:10.1038/ng.2847

223. Düwel S, Durst M, Gringeri CV, et al. Multiparametric human hepatocellular carcinoma characterization and therapy response evaluation by hyperpolarized ^{13} C MRSI: HCC Therapy Response Evaluation By Hyperpolarized ^{13} C MRSI. *NMR Biomed*. 2016. doi:10.1002/nbm.3561

224. Moyer VA. Screening for Prostate Cancer: U.S. Preventive Services Task Force Recommendation Statement. *Ann Intern Med*. 2012;157(2):120-134. doi:10.7326/0003-4819-157-2-201207170-00459

225. Kurhanewicz J, Vigneron DB. Advances in MR Spectroscopy of the Prostate. *Magn Reson Imaging Clin N Am*. 2008;16(4):697-710. doi:10.1016/j.mric.2008.07.005

226. Tessem M-B, Swanson MG, Keshari KR, et al. Evaluation of lactate and alanine as metabolic biomarkers of prostate cancer using 1H HR-MAS spectroscopy of biopsy tissues. *Magn Reson Med*. 2008;60(3):510-516. doi:10.1002/mrm.21694

227. Hurwitz AA, Foster BA, Allison JP, Greenberg NM, Kwon ED. The TRAMP mouse as a model for prostate cancer. *Curr Protoc Immunol Ed John E Coligan Al*. 2001;Chapter 20:Unit 20.5. doi:10.1002/0471142735.im2005s45

228. Lupo JM, Chen AP, Zierhut ML, et al. Analysis of hyperpolarized dynamic 13C lactate imaging in a transgenic mouse model of prostate cancer. *Magn Reson Imaging*. 2010;28(2):153-162. doi:10.1016/j.mri.2009.07.007

229. Larson PEZ, Bok R, Kerr AB, et al. Investigation of tumor hyperpolarized [1- **13** C]-pyruvate dynamics using time-resolved multiband RF excitation echo-planar MRSI. *Magn Reson Med*. 2010;63(3):582-591. doi:10.1002/mrm.22264

230. Keshari KR, Sriram R, Van Criekinge M, et al. Metabolic Reprogramming and Validation of Hyperpolarized 13C Lactate as a Prostate Cancer Biomarker Using a Human Prostate Tissue Slice Culture Bioreactor. *The Prostate*. 2013;73(11):1171-1181. doi:10.1002/pros.22665

231. Keshari KR, Wilson DM, Chen AP, et al. Hyperpolarized [2-13C]-Fructose: A Hemiketal DNP Substrate for In Vivo Metabolic Imaging. *J Am Chem Soc*. 2009;131(48):17591-17596. doi:10.1021/ja9049355

232. Kohler S j., Yen Y, Wolber J, et al. In vivo 13carbon metabolic imaging at 3T with hyperpolarized 13C-1-pyruvate. *Magn Reson Med*. 2007;58(1):65-69. doi:10.1002/mrm.21253

233. von Morze C, Larson PEZ, Hu S, et al. Imaging of blood flow using hyperpolarized [13C]Urea in preclinical cancer models. *J Magn Reson Imaging*. 2011;33(3):692-697. doi:10.1002/jmri.22484

234. von Morze C, Bok RA, Sands JM, Kurhanewicz J, Vigneron DB. Monitoring urea transport in rat kidney in vivo using hyperpolarized 13C magnetic resonance imaging. *AJP Ren Physiol*. 2012;302(12):F1658-F1662. doi:10.1152/ajprenal.00640.2011

235. Keshari KR, Sriram R, Koelsch BL, et al. Hyperpolarized 13C-Pyruvate Magnetic Resonance Reveals Rapid Lactate Export in Metastatic Renal Cell Carcinomas. *Cancer Res*. 2013;73(2):529-538. doi:10.1158/0008-5472.CAN-12-3461

236. Sriram R, Van Criekinge M, Hansen A, et al. Real-time measurement of hyperpolarized lactate production and efflux as a biomarker of tumor aggressiveness in an MR compatible 3D cell culture bioreactor. *NMR Biomed*. 2015;28(9):1141-1149. doi:10.1002/nbm.3354

237. Clatworthy MR, Kettunen MI, Hu D-E, et al. Magnetic resonance imaging with hyperpolarized [1,4-13C2]fumarate allows detection of early renal acute tubular necrosis. *Proc Natl Acad Sci*. 2012;109(33):13374-13379. doi:10.1073/pnas.1205539109

238. Laustsen C, Østergaard JA, Lauritzen MH, et al. Assessment of early diabetic renal changes with hyperpolarized [1- ^{13} C]pyruvate: Renal Hyperpolarized ^{13} C-MRI in Diabetes. *Diabetes Metab Res Rev*. 2013;29(2):125-129. doi:10.1002/dmrr.2370

239. Laustsen C, Lycke S, Palm F, et al. High altitude may alter oxygen availability and renal metabolism in diabetics as measured by hyperpolarized [1-13C] pyruvate magnetic resonance imaging. *Kidney Int*. 2014;86(1):67–74.

240. Lutterbey G, Gieseke J, Falkenhausen M von, Morakkabati N, Schild H. Lung MRI at 3.0 T: a comparison of helical CT and high-field MRI in the detection of diffuse lung disease. *Eur Radiol*. 2004;15(2):324-328. doi:10.1007/s00330-004-2548-1

241. Brindle KM, Bohndiek SE, Gallagher FA, Kettunen MI. Tumor imaging using hyperpolarized 13C magnetic resonance spectroscopy. *Magn Reson Med*. 2011;66(2):505-519. doi:10.1002/mrm.22999

242. Thind K, Chen A, Friesen-Waldner L, et al. Detection of radiation-induced lung injury using hyperpolarized ^{13} C magnetic resonance spectroscopy and imaging: Detection of RILI. *Magn Reson Med*. 2013;70(3):601-609. doi:10.1002/mrm.24525

243. Pourfathi M, Xin Y, Kadlecek SJ, et al. In vivo imaging of the progression of acute lung injury using hyperpolarized [1-13C] pyruvate. *Magn Reson Med*. January 2017. doi:10.1002/mrm.26604

244. Pourfathi M, Cereda M, Chatterjee S, et al. Lung Metabolism and Inflammation during Mechanical Ventilation; An Imaging Approach. *Sci Rep*. 2018;8(1):3525. doi:10.1038/s41598-018-21901-0

245. Brindle KM. Imaging Metabolism with Hyperpolarized ^{13} C-Labeled Cell Substrates. *J Am Chem Soc*. 2015;137(20):6418-6427. doi:10.1021/jacs.5b03300

246. Ardenkjaer-Larsen JH. On the present and future of dissolution-DNP. *J Magn Reson*. 2016;264:3-12. doi:10.1016/j.jmr.2016.01.015

247. Cunningham Charles H., Lau Justin Y.C., Chen Albert P., et al. Hyperpolarized 13C Metabolic MRI of the Human Heart. *Circ Res*. 2016;119(11):1177-1182. doi:10.1161/CIRCRESAHA.116.309769

248. Miloushev VZ, Granlund KL, Boltyanskiy R, et al. Metabolic Imaging of the Human Brain with Hyperpolarized 13C Pyruvate Demonstrates 13C Lactate Production in Brain Tumor Patients. *Cancer Res*. 2018;78(14):3755-3760. doi:10.1158/0008-5472.CAN-18-0221

249. Aggarwal R, Vigneron DB, Kurhanewicz J. Hyperpolarized 1-[13C]-Pyruvate Magnetic Resonance Imaging Detects an Early Metabolic Response to Androgen Ablation Therapy in Prostate Cancer. *Eur Urol*. 2017;72(6):1028-1029. doi:10.1016/j.eururo.2017.07.022

Chapter 3: A Mechanistic Study of Lung Viability during *Ex Vivo* Lung Perfusion (EVLP) Using ^{31}P and Hyperpolarized (HP) [1-^{13}C] Pyruvate Nuclear Magnetic Resonance

Abstract

Ex vivo lung perfusion (EVLP) has recently shown promise as a means of assessing and revitalizing the health of lung grafts and improving post-transplant graft performance. However, perfusion of ischemic lung promotes energy depletion and leads to a progressive loss of normal mitochondrial function; it remains unclear to what extent EVLP itself contributes to this metabolic decline. The anti-oxidant ascorbate has been shown to mitigate the effects of ischemia–reperfusion injury, but the nature of its effects during EVLP are also not clear. In this study we used hyperpolarized (HP) [1-^{13}C] pyruvate NMR in conjunction with the more established ^{31}P NMR to answer a series of complementary questions on lung metabolism during EVLP and its response to the administration of ascorbate. Our experiments demonstrated that the oxidative phosphorylation capacity and pyruvate dehydrogenase flux of lungs decline during *ex vivo* perfusion. The addition of ascorbate to the perfusate increased the hyperpolarized ^{13}C bicarbonate signal by a factor of 2.7 and prolonged lung viability by 80%. Furthermore, we used HP [1-^{13}C] pyruvate spectroscopy to show that the ascorbate effect is not due to its antioxidant properties, but rather due to its ability to energize pulmonary mitochondrial activity through an independent interaction with ETC complexes. This study established that HP [1-^{13}C] pyruvate MRS can be used to assess the response to treatment during EVLP for improving procurement and preservation of lungs for transplantation.

This chapter has been adapted from the published article, ‘Ascorbic acid prolongs the viability and stability of isolated perfused lungs: A mechanistic study using ^{31}P and hyperpolarized ^{13}C nuclear magnetic resonance’ in *Free Radical Biology and Medicine*, 89:62-71(2015)

3.1. Introduction

Lung transplantation is the established treatment for patients with chronic, end-stage lung disease[1]. However, its utility is limited both by the chronic shortage of donor lungs as well as post-transplant complications[2]. Although efforts have been made to expand the pool of available organs via aggressive donor management and novel lung preservation strategies, our incomplete understanding of the mechanism and progression of donor lung injury continues to limit our ability to fully exploit these advances to improve lung transplant outcomes. In recent years, *ex vivo* lung perfusion (EVLP) shown promise as a valuable technique for reassessing the health of grafts initially classified as high risk[3], thereby allowing a greater percentage of lungs to be transplanted. Moreover, as compared with cold preservation alone, the application of EVLP before transplant results in significantly higher post-transplant oxygenation and slower edema formation[4].

Despite these highly promising developments, uncertainty about the role of *ex vivo* perfusion in lung graft health remains. The most common mechanism of early mortality subsequent to lung transplantation is ischemia–reperfusion injury (IRI)[5,6], which can cause acute graft dysfunction. When hypoxic cells are reperfused with oxygenated perfusate (or blood), reactive oxygen species (ROS) form which are generally accepted as the major source of the cellular damage and pulmonary edema characteristic of IRI[7–10]. Reperfusion of ischemic lung leads to fundamental metabolic alterations, including a decline in oxidative phosphorylation capacity and reduced activity of the electron transport chain (ETC) complexes[11–14]; in cardiac tissue, ischemia–reperfusion has also been shown to decrease activity of the pyruvate dehydrogenase complex (PDHc)[15]. It is not known, however, whether this energy decline is due solely to the reaction of ischemic lung to reperfusion, or whether EVLP itself contributes to these changes.

In tandem with investigating lung health during reperfusion, recent research has focused on identifying methods that can improve graft viability. For example, antioxidant therapy and/or preconditioning[12,14,16–19] have been shown to limit the extent of IRI, an effect conventionally attributed to antioxidants' mitigation of ROS-induced damage[20–24]. Among all antioxidants, ascorbate appears to be the most attractive option for treating and preventing IRI in the lung and other organs[25–30]. Ascorbate administration has been shown to reduce oxidative damage in endothelial cells, improve tissue perfusion, inhibit tumor necrosis factor α (TNF α), reduce mitochondrial swelling and damage, preserve mitochondrial respiration, reduce edema , reduce proinflammatory chemokine expression and reduce oxidative damage[31–37].

The goal of this study was to determine whether hyperpolarized (HP) [1-^{13}C] pyruvate NMR can be used in conjunction with the more established ^{31}P NMR to answer a series of complementary questions on lung metabolism during EVLP and its response to ascorbate. First, is the energy decline previously observed during reperfusion completely due to reperfusion of ischemic lungs, or does EVLP itself affect the energy status of the lungs? Second, how does the administration of ascorbate affect lung energy status during EVLP? Third, is the effect of ascorbate on *ex vivo* perfused lung metabolism a result of its antioxidant property, or is it related to other mechanisms (e.g., its ability to energize the respiratory chain)?

To assess these questions, we used ^{31}P NMR (nuclear magnetic resonance) to continuously monitor adenine nucleotides and energy status during perfusion. We also used HP^{13}C NMR to noninvasively and simultaneously measure the conversion of [1-

^{13}C]pyruvate into [1-^{13}C]lactate and [^{13}C]bicarbonate, which serve as indicators of glycolytic and oxidative metabolism, respectively. Persistent lactate release during reperfusion as a result of glycolytic upregulation has previously been observed and correlated with lung graft quality[11,12]. In addition, we previously demonstrated a significant increase in hyperpolarized [1-^{13}C]lactate signal as a result of anaerobic metabolism of [1-^{13}C]pyruvate in ischemic isolated perfused lungs[38]; however, this affect has yet to be observed during EVLP itself under normoxic conditions.

3.2. Materials and Methods

3.2.1. Animals

All animal experiments were conducted in accordance with protocols approved by the institutional animal care and use committee of the University of Pennsylvania. Male Sprague–Dawley rats weighing 320±70 g were used for all experiments. All rats were housed under similar environments and dietary conditions.

3.2.2. Isolated Perfused Lungs

All imaging studies were performed in *ex vivo*, isolated, perfused lungs. Prior to excision of the lungs, rats were anesthetized with intraperitoneal (IP) pentobarbital, tracheostomy was performed, and 200 U of heparin was administered via tail vein. The lungs were prepared for NMR study according to the previously reported method of degassing[39,40]. In short, the animals were ventilated with pure O_2 (50 breaths/min, 11–14 cmH_2O peak inspiration pressure) for 10 min to remove all N_2 from the airways. Immediately after ventilation, the trachea was sealed (end exhalation) with a suture, allowing residual O_2 to be absorbed by the circulating blood and perfusate. Thoracotomy was immediately started, the heart was cut transversely, and the pulmonary artery was cannulated via the right ventricle. After perfusion was started, the lungs were rapidly excised and placed in a 20 mm NMR tube. Lungs were perfused at 10 ml/min with 500 ml of modified Krebs–Henseleit buffer that contained 119 mM NaCl, 25 mM $NaHCO_3$, 1.3 mM $CaCl_2$, 1.2 mM $MgSO_4$, 4.7 mM KCl, 10 mM glucose, 2 mM lactate, 0.2 mM pyruvate, and 3% (w/v) fatty-acid-free bovine serum albumin (BSA, Fisher Bioreagents). The perfusate was passed through an oxygenating column under a constant flow of 1 atm 95:5 O_2 /CO_2 and warmed via passage through water-jacketed tubing. The CO_2 concentration in the oxygenating column was chosen to maintain constant perfusate pH during oxygenation, although periodic adjustment with 1 N HCl or NaOH was needed to maintain a physiological value of 7.4 ± 0.05. The lung was perfused at constant flow throughout the experiment. The temperature of the perfusate in the NMR tube was continuously monitored and maintained at 36.5 ± 1 °C.

3.2.3. Preparation and Administration of Hyperpolarized [1-^{13}C]pyruvate

Some of the studies were conducted using hyperpolarized [1-^{13}C]pyruvate. Here, 28.7 mg [1-^{13}C]pyruvic acid (Cambridge Isotope Laboratories) was mixed with 15 mM OX063 trityl radical (Oxford Instruments) and 1.5 mM Dotarem Gd chelate (Guerbet). This mixture was polarized to approximately 20% at 1.42 K and 94.062 GHz with a HyperSense DNP system (Oxford Instruments). Then, 4 ml of Tris-buffered saline with 100 mg/L ethylenediaminetetraacetic acid (EDTA) was heated to 190 °C at 10 bar and was used to rapidly dissolve the frozen sample. Next, 1 ml of this sample was further diluted in 19 ml of oxygenated Krebs–Henseleit buffer (without BSA, which was found to cause unacceptable signal loss during sample transport) to yield a neutral isotonic solution of 4 mM [1-^{13}C]pyruvate. This solution was injected into the perfusate line at 10 ml/min in lieu of the steady-state perfusion buffer. After the 120 s required to inject the hyperpolarized solution, normal lung perfusion was restarted.

3.2.4. Magnetic Resonance Spectroscopy

All magnetic resonance spectra and images were obtained using a 9.4-T vertical bore magnet (Varian, Palo Alto, CA, USA) equipped with a gradient insert (Resonance Research, Billerica, MA, USA) and a 20 mm 1 H/broadband probe (Doty Scientific, Columbia, SC, USA). After inserting the probe, the sample was tuned and matched. A ^{1}H gradient echo image (1 slice in each axis, field of view = 30x30 mm) was acquired to confirm the position and integrity of the organ (lack of edema). The sample was then shimmed on proton to a linewidth of approximately 35 Hz. The above-mentioned steps required approximately 10 to 20 min.

In each lung studied, a series of ^{31}P spectra was acquired to assess high-energy phosphate status during the entire perfusion period. In some cases, one or two sets of HP [1-^{13}C]pyruvate spectra were also acquired, bracketed by ^{31}P spectra to evaluate the stability of the lung condition and its metabolic activity as well as the reproducibility of the measurement. HP ^{13}C spectrum series were separated by the 1 hour required to hyperpolarize another pyruvate sample. The ^{31}P spectrum was acquired with the following parameters: repetition time (TR) = 1 s, nominal flip angle (α) = 60 °, acquisition time (AT) = 200 ms, spectral width (SW) = 100 kHz, and averages (NT) = 512, with a total scan time of 8:32 min. If the ^{31}P spectroscopy was followed by HP ^{13}C spectroscopy, the probe was then tuned to ^{13}C. During ^{13}C acquisition, the perfusate pump was turned off as the hyperpolarized solution was injected via a secondary line. Low flip-angle spectra were acquired for the several-minute duration of the hyperpolarized signal (TR = 1 s, nominal α = 10°, AT = 800 ms, SW = 50 kHz, 300 individual spectra acquired), after which the steady-state perfusion was restored.

3.2.5. Study Protocols

The study was divided into four sections.

3.2.5.A. Study I: Control and Ascorbate Studies

In this study, the longevity of the perfused lungs was measured in the absence (control) and presence of 2 mM ascorbate (henceforth referred to as the "ascorbate cohort") dissolved in the perfusate. The perfusate was otherwise the same for the two cohorts and was as described above. The perfused rat lungs were observed longitudinally by ^{31}P NMR in the two cohorts: control (n = 5) and ascorbate (n = 5). Ascorbate (Sigma–Aldrich, St. Louis, MO, USA) was dissolved into the perfusate 10 min before the lungs were perfused. The perfusate and the particle filter were replaced by fresh oxygenated perfusate after 3 h of perfusion to replenish depleted nutrients. A phosphorus spectrum was acquired every 40 min until the endpoint of the study was reached. The study ended when the nucleoside signal was undetectable by ^{31}P NMR or when perfusion stopped due to lung edema. Edema was detected by a gradient echo image that showed a distended lung as well as the abrupt increase in backpressure in the perfusion apparatus.

3.2.5.B. Study II: Hyperpolarized [1-^{13}C]pyruvate Studies of Control and Ascorbate Cohorts

In this study, the metabolic activity of the lungs in the absence (control, n = 11) and presence of 2 mM ascorbate (ascorbate, n = 12) in the perfusate was evaluated. An HP ^{13}C spectrum series, bracketed by a pre- and post- ^{31}P spectrum, was acquired 40 min after lung perfusion was started. In 6 of the controls, the entire series (^{31}P spectrum, HP spectrum series, ^{31}P spectrum) was repeated after a 1 h delay to determine the metabolic stability of the perfused lung. In 3 of these repeated controls perfusion was continued with the control perfusate, but in the other 3 repeats 2 mM ascorbate was dissolved in the perfusate after the first set of spectra was acquired.

3.2.5.C. Study III: Antioxidant Studies

The goal of this study was to determine whether the primary mechanism of ascorbate's effect on lung stability and metabolism was due to its antioxidant effect. As such, the perfused lungs were evaluated in the presence of the following compounds: dehydroascorbate (DHA, n = 3), glutathione (GSH, n = 3), and α -lipoic acid (ALA, n = 3). Here, 2 mM of each compound was added to the perfusate approximately 10 min before starting perfusion. The effect of ascorbate's concentration on the perfused lung was also evaluated by dissolving 0, 0.5, 1, 2, 4, 8, and 16 mM ascorbate in the perfusate (n = 3 each except for the larger 0- and 2 mM cohorts described above). Similar to study II, the lungs were perfused and monitored by a series of NMR acquisitions (^{31}P spectrum, HP spectrum series, ^{31}P spectrum).

3.2.5.D. Study IV: Electron Transport Chain Studies

The goal of this study was to determine the effect of activating complex IV with a cytochrome c reducing agent and/or inhibiting complex I (via rotenone) on pyruvate metabolism. Similar to studies I to III, the lungs (n = 13) were perfused with control perfusate and an initial ^{31}P spectrum was acquired. After this acquisition, the perfusion parameters were modified as follows. The flow rate of the perfusate was decreased to 9 ml/min, and a second infusion at a flow rate of 1 ml/min was started. The two lines were merged so that the final flow rate was still 10 ml/min. The second reservoir contained identical perfusate except for the addition of either rotenone or TMPD (N,N,N',N'-tetramethyl-p-phenylenediamine) + ascorbate, such that the combined infusion contained 20 mM rotenone or 25 mM TMPD + 250 mM ascorbate. After perfusing the lung with either rotenone for 10 min or TMPD + ascorbate for 40 min, the second pump was stopped and the main line's flow rate was returned to 10 ml/min. An HP ^{13}C spectrum series was then acquired, followed by post-injection ^{31}P spectra to assess the lung's metabolic and energetic state after the HP [1-^{13}C]pyruvate study. Rotenone-perfused lungs (n = 8) were subjected to a second HP pyruvate administration. The second HP pyruvate injection was administered after either 40 min of treatment with 25 mM TMPD + 250 mM ASA (ascorbic acid) (n = 5) or 40 min of additional perfusion by normal perfusate (n = 3). The concentration of rotenone was selected based on a previously reported study that demonstrated complete blockade of complex I and depression of whole-lung oxygen consumption with no detectable impact on complexes III and IV [41]. To determine the effective concentration of TMPD/ASA, the effect of different concentrations of TMPD/ASA (12.5–100 μ M TMPD/10 # ASA, n = 3) was studied on HP pyruvate metabolism.

3.2.6. Post-processing of Spectra

Spectra (carbon and phosphorus) were downloaded for offline processing using custom MATLAB (MathWorks, Natick, MA, USA) routines. In general, the spectra were automatically Fourier-transformed, line-broadened, baseline-corrected, phase-corrected, and then peak-fitted for data evaluation.

31P spectra were least-squares fit to 13 Lorentzian peaks, allowing the individual peak heights and common peak width to vary freely. The peak frequencies were kept fixed; peak identities (ppm chemical shifts relative to phosphocreatine [PCr]) were PME (phosphomonoester, 6.70), Pi (inorganic phosphate, 5.08, 4.32), GPC (glycerol 3-phosphorylcholine, 3.03), GPE (glycerol 3-phosphorylethanolamine, 2.24), PG (phosphoglycans, 1.80), PCr (0.00), γ-ATP + β-ADP (–2.36), α-ATP + ADP + AMP (–7.52), diphosphodiester/NAD(H) (–8.18, –9.68, –11.49, –13.30), and β-ATP (–16.13). The quality of the fit was found to improve substantially by including three additional peaks of fixed position (3.5, –4, and –10 ppm) and width (3, 8, and 4 ppm, respectively) to account for contributions from unresolved ^{31}P species. Although consistent with previous measurements [42,43], the number and identity of resonances are uncertain. The β-ATP peak was the best resolved peak with a good fit quality. Because ATP content is accepted as a valid viability marker of cells, the β-ATP peak intensity normalized by total ^{31}P signal (summation of all ^{31}P peak intensities) was used to evaluate lung viability [44–46]. The duration of viability and rate of β -ATP reduction for each lung were calculated by considering time points for which the β -ATP/total ^{31}P ratio exceeded 50% of the initial ratio and total ^{31}P signals exceeded 90% of the initial value (indicating no or minimal edema). The greater than 50% β -ATP/total ^{31}P index was chosen as a measure of viability because we observed an abrupt energy status deterioration and the onset of edema once that threshold was crossed. The lung's energy status was evaluated by the adenylate energy charge (EC) which is calculated from the peak intensities [47,48] as

$$EC = \frac{ATP + \frac{1}{2}ADP}{AMP + ADP + ATP}$$

^{13}C spectra were least-squares fit to five Lorentzian peaks, allowing the individual peak heights to vary. The peak positions and widths were set using an initial free fit (amplitude, width, and position) to the average of all spectra with a signal-to-noise ratio greater than 30. The peaks were identified as pyruvate, alanine, pyruvate hydrate, lactate, and bicarbonate with ppm chemical shifts relative to pyruvate of 0.00, 5.68, 8.42, 12.26, and –9.98, respectively. Additional peaks representing natural abundance nuclei or impurities were not included in the fit. All metabolite signals were normalized by the integrated pyruvate signal and the lung's weight as calculated from the body mass[49]. Metabolite ratios were calculated by dividing the individual metabolite signals by the total HP ^{13}C metabolite signal (lactate + alanine + bicarbonate).

3.2.7. Statistical Methods

All data in the text, figures, and tables are presented as means + standard errors (SE). Separate two-tailed Student's t-tests with Bonferroni correction were used to evaluate significance and calculate P-values of the control and ascorbate cohorts in studies I and II. In studies III and IV, to determine whether the model groups were characterized by different means when measured using ^{13}C or ^{31}P spectroscopy, analysis of variance (ANOVA) followed by Tukey's HSD (honestly significant difference) post hoc test was performed. To determine the extent of a direct relationship between the viability markers as measured using ^{13}C and ^{31}P spectroscopy, simple correlations were calculated across all measurements in which both metrics were available. All statistical analyses were performed using the open source R statistical package (http://www.r-project.org).

3.3. Results

Figure 3.1 shows representative time series of ^{31}P spectra acquired during perfusion of the isolated lungs with (panel A) and without (panel B) 2 mM ascorbate. In all lungs, intensities of the PCr and ATP peaks decreased with time, whereas intensity of Pi increased. Perfused lungs in the ascorbate cohort remained viable, defined as greater than 50% of the initial β-ATP/total ^{31}P ratio, for a longer duration (6.1±0.3 h) than the control lungs (3.4±0.5 h). Figure 3.1C depicts the average β-ATP peak area as a function of perfusion time for each cohort. As seen in the figure, the rate of β-ATP decrease was reduced approximately 2-fold in lungs treated with ascorbate. In both cohorts, the β-ATP decrease accelerated abruptly when the ATP/total ^{31}P ratio was less than 50% of the initial ratio.

Figure 3.2A displays a representative series of hyperpolarized ^{13}C spectra from rat lungs of the 2 mM ascorbate cohort. The observed linewidths were typically approximately 10 Hz. Peaks corresponding to [1-^{13}C]pyruvate and [1-^{13}C]pyruvate hydrate appear first, followed within a few seconds by [1-^{13}C]lactate, [1-^{13}C]alanine, and [^{13}-C]bicarbonate. In control lungs, the [^{13}C]bicarbonate peak is typically small or undetectable in a single ^{13}C spectrum, perhaps due to a combination of the lung's low tissue density and low oxidative metabolism. However, all of the ascorbate cohort lungs exhibited both a larger and more rapidly appearing bicarbonate signal. The Figure 3.2A inset compares representative averaged ^{13}C spectra of control and ascorbate lungs, exemplifying this several-fold ^{13}C bicarbonate signal increase.

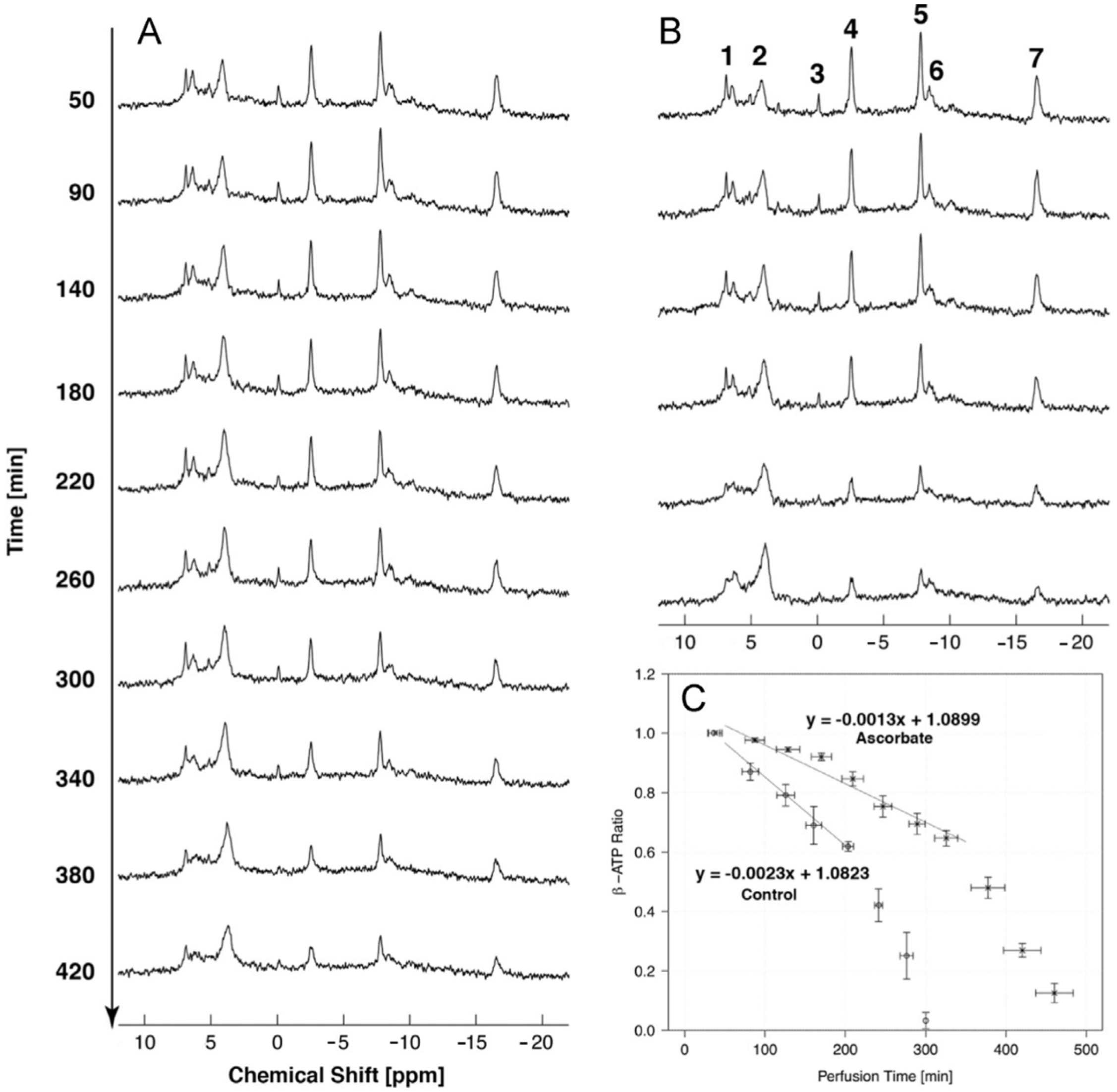

Figure 3.1: Representative series of ^{31}P spectra during perfusion in the presence (A) and absence (B) of 2 mM ascorbate. ^{31}P NMR spectra assignment: 1, PMEs; 2, Pi; 3, PCr; 4, γ- ATP and β-ADP; 5, α-ATP, α-ADP, and AMP; 6, NADs (nicotinamide adenine dinucleotides); 7, β-ATP. (C) Comparison of ^{31}P β-ATP peak intensity during perfusion in the absence (open circles, control) and presence (stars, ascorbate) of 2 mM ascorbate. Data are expressed as percentage changes from baseline. Only the points greater than 50% were used to fit the trend linear lines.

Figure 3.2.B summarizes the differences in averaged lactate, alanine, and bicarbonate signals between the control (n = 11), and ascorbate (n = 12) lungs. On average, the

bicarbonate signal is 2.7 times larger ($P < 0.005$) in the ascorbate cohort. Average lactate and alanine intensities were also larger in the lungs perfused with ascorbate, but these increases did not individually reach the level of significance (lactate and alanine, $P = 0.70$). These ascorbate-dependent metabolic changes are summarized in Table 1.

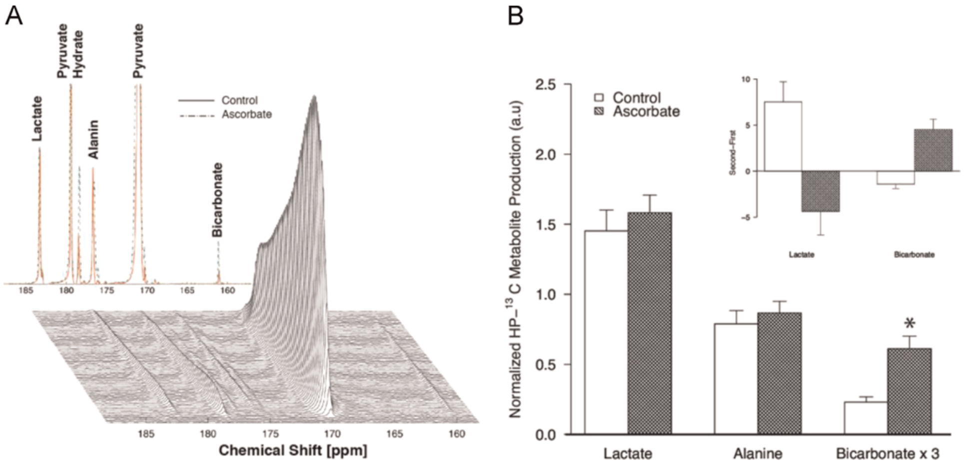

Figure 3.2: (A) Representative time series of stacked ^{13}C spectra (bottom) and comparison of two averaged ^{13}C spectra (top) for lungs in the absence and presence of 2 mM ascorbate. The stacked series was acquired in an ascorbate lung; bicarbonate signal is typically difficult to observe in control lungs. Undefined peaks are due to agent impurities. (B) Comparison of averaged HP ^{13}C metabolite production in rat lungs perfused without (control, n = 11) and with (ascorbate, n = 12) 2 mM ascorbate dissolved in the perfusate. Bicarbonate production in the ascorbate cohort is significantly higher than in the control cohort (2.7-fold, $P < 0.005$). The inset shows the change between two hyperpolarized pyruvate administrations (n = 6) with and without 2 mM ascorbate dissolved in the perfusate after the first series of HP spectra were acquired. In all cases, the addition of ascorbate resulted in a partial reversal of the decline in bicarbonate and the increase in lactate signals.

On average, the total metabolite signal (lactate + alanine + bicarbonate) was 24% larger in the ascorbate cohort. To distinguish the observed bicarbonate signal increase from overall changes in metabolism or transport, Table 3.1 also summarizes the fraction of apparent metabolic activity accounted for by each observed process. The bicarbonate ratio (i.e., bicarbonate / [lactate + alanine + bicarbonate]) was still 2.3 times higher ($P < 0.05$) in the ascorbate group than in the control group. The inset of Figure 3.2B shows the progression of metabolite ratios between the first and second administrations of HP pyruvate in both cohorts. The bicarbonate ratio decreased in all three control lungs for which two HP administrations were performed and increased in all three lungs treated with ascorbate. The lactate ratio increased in all control lungs and decreased in all lungs treated with ascorbate. Differences between the cohorts are significant for both lactate and bicarbonate ratios ($P < 0.05$).

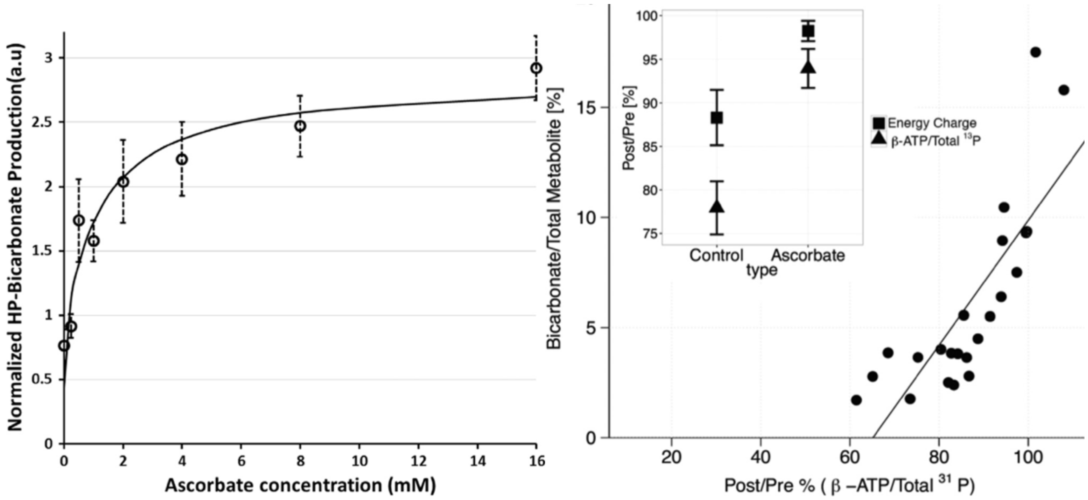

Figure 3.3: (A) All averaged ($n = 3$ except for control, $n = 11$) and 2 mM control ($n = 12$) hyperpolarized ^{13}C bicarbonate signals as a function of perfusate ascorbate concentration. The data were fitted to $B = B_0 + B_{sat} [ASA] / (K + [ASA])$, where B_{sat} is the maximum effect achieved by the system at maximum (saturating) substrate concentrations and K is the substrate concentration at which the effect is half of B_{sat}. (B) Correlation of ^{13}C bicarbonate ratio with the ratio of post-injection to pre- injection β-ATP/total ^{31}P ($r = 0.84$, $P < 0.0001$). The post/pre ratio of β-ATP/total ^{31}P for controls is significantly lower than for the ascorbate cohort (20%, $P < 0.0005$). The pre/post ratio of energy charge for controls also is significantly lower than for the ascorbate cohort (11%, figure inset, $P < 0.01$).

The effective concentration of ascorbate was evaluated by observing hyperpolarized [1-^{13}C]pyruvate metabolism with varying amounts (0–16 mM) ascorbic acid added to the perfusate. The bicarbonate signal increased in a concentration-dependent manner and showed saturation behavior. Figure 3.3A displays the averaged [^{13}C]bicarbonate signal B as a function of ascorbate concentration [ASA] and the curve fit to the general form of:

$$B = B_0 + \frac{B_{sat}[ASA]}{K + [ASA]}$$

as suggested by Kepner, et al[50]. In this expression, B_{sat} is the maximum effect achieved by the system at maximum (saturating) substrate concentrations, and K is the substrate concentration at which the effect is half of B_{sat}. Best fit parameters were $B_{sat}/B_0 = 4.9$ and $K = 1.21$ mM. The observed HP pyruvate metabolite signals and ratios for each ascorbate concentration studied are summarized in Table 3.1.

Cohort	*n*	Conc [mM]	Lactate	%	Alanine	%	Bicarbonate	%
Control	11	-	1.45±0.15	62.7±1.6	0.79±0.10	33.7±1.7	0.08±0.01	3.6±0.5
Ascorbate	12	2	1.58±0.13	59.9±6.0	0.87±0.08	32.0±4.7	0.20±0.03	8.1±4.7
Ascorbate	3	0.25	1.59±0.11	61.7±0.7	0.84±0.04	34.0±0.5	0.09±0.01	4.2±0.3
Ascorbate	3	0.5	1.33±0.16	59.7±2.0	0.80±0.12	35.4±1.3	0.11±0.03	4.9±1.2
Ascorbate	3	1	1.37±0.23	61.9±1.5	0.71±0.11	32.0±1.2	0.15±0.01	6.7±0.7
Ascorbate	3	4	1.66±0.04	54.6±1.6	1.16±0.12	38.1±2.3	0.22±0.03	7.4±1.3
Ascorbate	3	8	1.57±0.17	57.9±3.7	0.91±0.09	34.0±8.1	0.22±0.01	8.1±0.6
Ascorbate	3	16	1.91±0.12	62.5±2.8	0.93±0.09	30.6±3.0	0.21±0.03	6.9±0.6
DHA	3	2	1.45±0.25	61.9±1.6	0.84±0.12	35.7±1.8	0.05±0.04	2.2±0.2
DHA + ASA	3	1	1.46±0.08	57.3±0.7	0.94±0.08	36.9±1.3	0.18±0.01	6.9±0.7
ALA	3	2	1.88±0.51	65.7±5.9	0.84±0.10	32.5±5.0	0.04±0.01	1.82±0.9
GSH	3	2	1.47±0.16	59.4±0.5	0.92±0.11	37.0±0.5	0.09±0.01	3.7±0.1
TMPD/ASA	5	0.025/0.25	1.61±0.06	58.9±1.9	0.93±0.00	33.5±1.9	0.21±0.01	7.5±2.8
Rotenone(F)	8	0.02	2.23±0.17	81.7±3.6	0.51±0.15	17.3±4.6	0.03±0.00	1.1±0.1
TMPD/Roten.(S)*	5	-	1.53±0.21	64.0±3.1	0.80±0.11	32.5±3.0	0.06±0.00	2.5±0.3
Rotenone(S)	3	-	1.98±0.04	82.3±3.1	0.45±0.18	16.8±4.0	0.002±0.00	0.4±0.3

Table 3.1: HP ^{13}C metabolite signals as a fraction of [1-^{13}C]pyruvate signal in each of the study cohorts. The ratios are reported as % and represent the sum of all signals acquired during a series of spectra. The ratios reported in parenthesis are the fraction of total metabolites signals accounted for by each metabolite. Data are reported as mean ± SE. The (F) and (S) indicate first and second HP pyruvate injections, respectively. *Perfusate contained 25 mM TMPD + 250 μM ascorbate for 40 min after 20 μM rotenone administration for 10 min.

The energy charge of the perfused lungs increased from 0.82 ± 0.05 in controls to 0.88 ± 0.03 ($P < 0.05$) in the ascorbate-treated lungs (pre-injection ^{31}P NMR, after 40 min perfusion). Analysis of the post-injection ^{31}P NMR spectra showed a significant decrease in the lung energy charge of the control cohort compared with the pre-injection energy charge (11%, $P < 0.05$) and no significant change in the energy charge of the ascorbate cohort. The β-ATP/total ^{31}P ratio was also significantly decreased after hyperpolarized agent injection in the control cohort (22%, $P < 0.001$) but was unchanged in the ascorbate cohort.

Across all cohorts, the bicarbonate ratio was significantly correlated to the post/pre ratio of β-ATP/total ^{31}P ($r = 0.80$, $P < 0.0001$) as well as to the energy charge ($r = 0.47$, $P < 0.05$) (Figure 3.3B). The inset of Figure 3.3B compares the post/pre ratio of EC and β-ATP/total ^{31}P in the control and ascorbate cohorts. Both the post/pre ratios of EC and β-ATP/total ^{31}P for the controls are significantly lower than corresponding ratios of the ascorbate cohort ($P < 0.01$).

Metabolic changes resulting from the addition of antioxidants and the oxidized form of ascorbate (DHA) were also examined to elucidate ascorbic acid's mechanism of action in the isolated lung. The effect of 2 mM GSH and 2 mM ALP, two water-soluble anti-oxidants, on HP [^{13}C]bicarbonate ratio can be seen in Figure 3.4A. Measurements of bicarbonate production in the presence of GSH were indistinguishable from the control cohort. On the other hand, GSH significantly increased the alanine ratio (48%) and decreased the lactate ratio by 26% ($P < 0.01$; data not shown). ALP (insignificantly) decreased the bicarbonate ratio and significantly elevated the lactate ratio by 20% ($P < 0.05$; data not shown). No significant effect was observed in the post/pre ratio of EC and β-ATP/total ^{31}P for either GSH or ALP cohorts. Because ascorbate is oxidized to DHA in solution during the perfusion, the effect of 2 mM DHA and 1 mM DHA + 1 mM ASA on lung pyruvate metabolism (Figure 3.4B) were also studied. No significant effect was observed on the bicarbonate in the presence of DHA alone. However, 1 mM DHA + 1 mM ASA increased the bicarbonate ratio by 94%, which is comparable to the effect of 1 mM ASA alone. The lactate and alanine ratios did not change in the presence of either DHA or 1 mM DHA + 1 mM ASA.

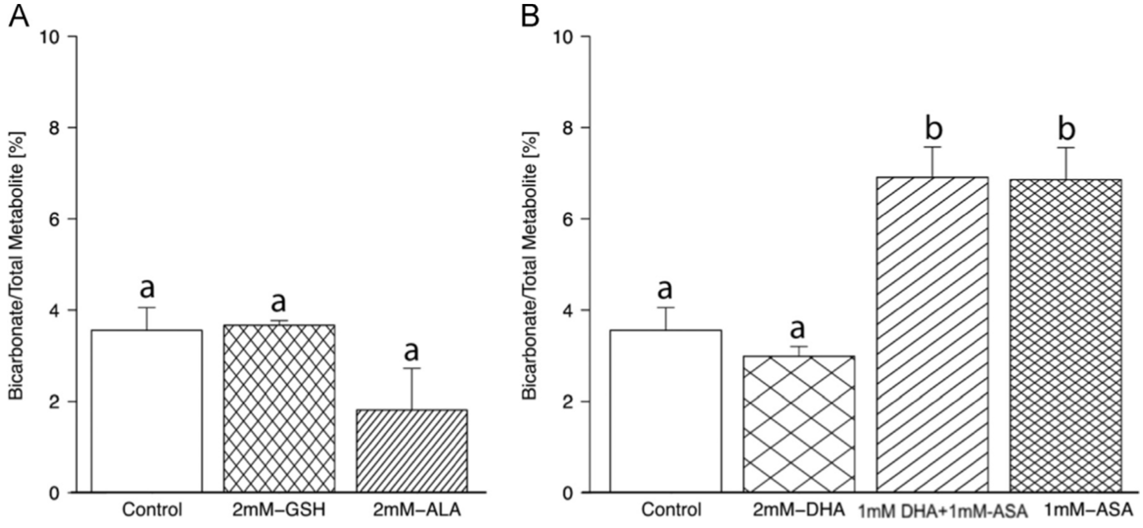

Figure 3.4: Comparison of ^{13}C bicarbonate ratio in perfused control lungs (n = 11) and lungs treated with 2 mM GSH (n = 3) or 2 mM ALA (n = 3) (A) and lungs treated with 2 mM DHA (n = 3), 1 mM DHA þ 2 mM ASA (n = 3), or 1 mM ASA (B). Means with different letter designations are significantly different from one another ($P < 0.05$), and means with similar letter designations do not differ significantly (P 4 0.05).

The metabolism of [1-^{13}C]pyruvate in perfused lungs was also studied in the presence of rotenone and TMPD, two compounds commonly used in mitochondrial respiration and electron transport chain activity studies, to evaluate whether the observed increase in bicarbonate production may be related to increased ETC activity arising from ascorbate's reduction of cytochrome c. Figs. 5A and 5B (top) compare the lactate and bicarbonate ratios in three cohorts of isolated perfused lungs: control (n = 11), 10 min perfusion with 20 mM rotenone (n = 8), and 40 min perfusion with 25 mM TMPD + 250 mM ASA (n = 5). As seen in the figure, rotenone depressed the bicarbonate production ratio by approximately 68% ($P < 0.005$), whereas TMPD elevated the bicarbonate ratio by approximately 120% ($P < 0.001$), with respect to control lungs. Rotenone increased the lactate signal by 32% ($P < 0.005$), whereas TMPD did not cause any significant change in the lactate ratio compared with the control. Neither rotenone nor TMPD significantly altered alanine production (data not shown). Subsequent treatment of rotenone-perfused lungs with 25 mM TMPD + 250 mM ASA restored the bicarbonate ratio and depressed the lactate ratio, such that both metabolites became statistically indistinguishable from those of the control cohort.

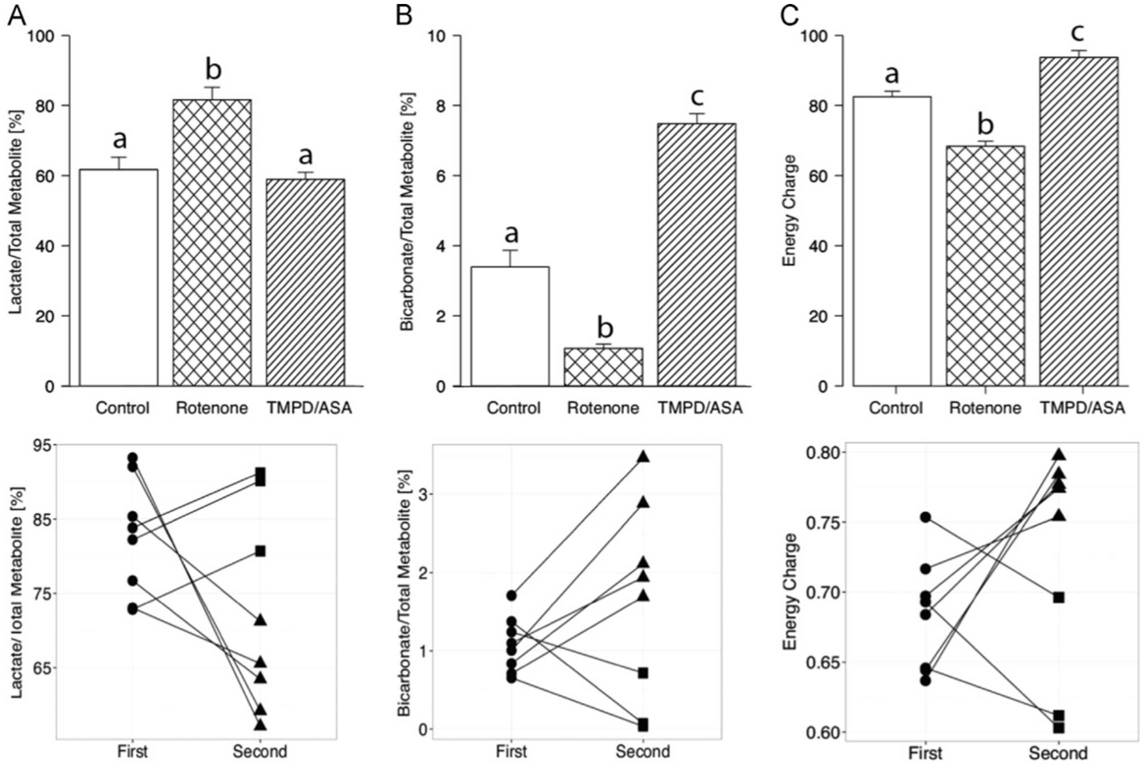

Figure 3.5: (A,B) Hyperpolarized ^{13}C lactate/total metabolite ratio (A, top) and ^{13}C bicarbonate/total metabolite ratio (B, top). (C) Top: Effect on energy charge of treatment with 20 mM rotenone for 10 min and with 25 mM TMPD þ 0.25 mM ASA for 40 min. The bottom panels show comparison of the lactate ratio (A), the bicarbonate ratio (B), and the energy charge (C) for two hyperpolarized pyruvate administrations in individual lungs. “First” and “Second” indicate first and second injections, respectively, and are linked by lines. First injections were performed after 10 min of rotenone perfusion (filled circles). Second injections representing perfusion with 25 mM TMPD þ 0.25 mM ascorbate for 40 min after rotenone administration are shown as filled triangles. Those representing perfusion with normal perfusate after rotenone administration are shown as filled squares. Means with different letter designations are significantly different from one another ($P < 0.01$), and means with similar letter designations do not differ significantly ($P > 0.01$).

This increase in bicarbonate ratio and decrease in lactate ratio was seen in all lungs where rotenone treatment was followed by TMPD + ASA, whereas those not exposed to TMPD

+ ASA continued to decline (Figs. 5A and 5B, bottom). Rotenone treatment also depressed the ^{31}P-derived energy charge by 18%, and TMPD enhanced it by 14% ($P < 0.001$). These results appear in Figure 3.5C. Subsequent treatment of the rotenone-perfused lung with 25 mM TMPD + 250 mM ASA also significantly improved the lung's energy charge. The increase in energy charge was seen in all lungs where rotenone treatment was followed by TMPD + ASA, whereas those not exposed to TMPD + ASA continued to decline (Figure 3.5C, bottom). The calculated energy charges were significantly correlated with lactate ratios ($r = -0.71$, $P < 0.0001$) and bicarbonate ratios ($r = 0.80$, $P < 0.0001$). These correlations are shown in Figure 3.6.

3.4. Discussion

The studies described above yielded three principal observations which are then further explained by additional experimental work. First, the phosphorylation capacity of control lungs, as determined by the β -ATP peak in the ^{31}P spectrum, decreased to 50% of its initial value after perfusion for 204 ± 30 min. Second, the addition of ascorbate to the perfusate improved both the lung's viability and metabolic stability, as evidenced by the fact that the oxidative phosphorylation capacity dropped to 50% of its initial value only after a significantly longer perfusion period of 366 ± 18 min. Third, the addition of ascorbate also shifted hyperpolarized [1-^{13}C]pyruvate metabolism toward the oxidative phosphorylation pathway, as inferred from the increased bicarbonate ratio (from 3.6% in the control cohort to 8.1% in the ascorbate cohort).

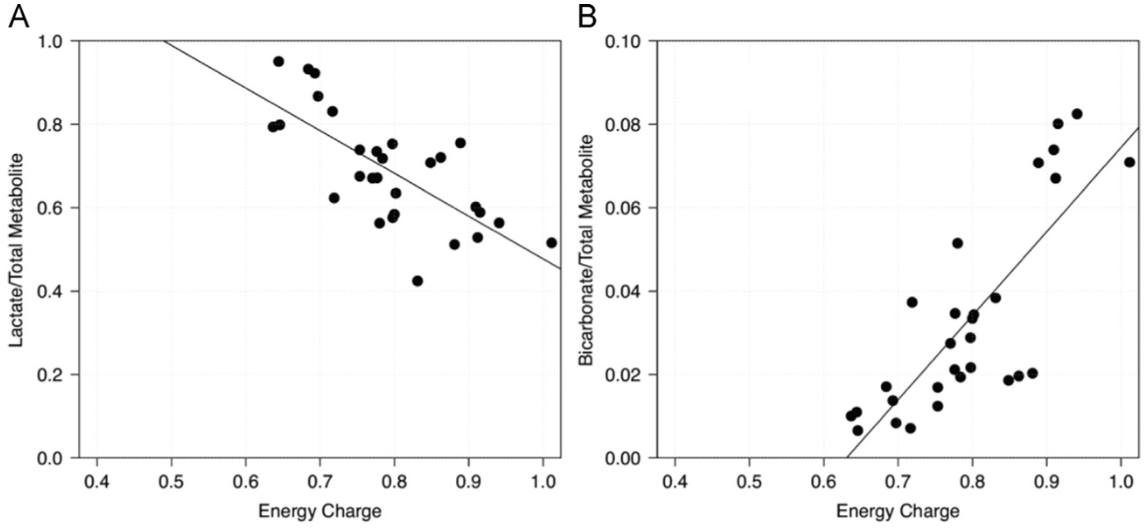

Figure 3.6: Correlation of calculated energy charge with (A) HP lactate ratio (r = –0.71, P < 0.001) and (B) HP bicarbonate ratio (r = 0.80, P < 0.001).

Further complementary studies quantified the effect of varying ascorbate concentrations and elucidated some of the mechanisms by which ascorbate increases PDHc activity. Ultimately, we concluded that ascorbate influences pyruvate metabolism primarily by stimulating the electron transport chain. This in turn influences mitochondrial Ca 2^+ concentration, which is known to regulate PDH activity in vertebrates[51,52]. The following discussion covers two main topics: (i) the possible pathways for increasing both the HP bicarbonate signal and the β-ATP peak intensity in the presence of ascorbate, and (ii) the possible mechanism through which ascorbate affects pulmonary oxidative phosphorylation.

3.5.1. Origin of Increased HP Bicarbonate Signal

The HP ^{13}C NMR and ^{31}P NMR experiments of study II suggest that ascorbate improves lung viability by increasing oxidative phosphorylation. The HP pyruvate 1-^{13}C NMR studies showed that bicarbonate production (Figure 3.2) increased 2.7-fold in ascorbate-perfused lungs compared with controls. Furthermore, ascorbate slowed both the decline in apparent PDHc activity and the increase in lactate production that was seen in repeated HP ^{13}C NMR measurements of control lungs (Figure 3.2, insets), suggesting an improvement in mitochondrial metabolism[12,41,53].

Although the observed increase in labeled bicarbonate signal in the ascorbate cohort could be due to several different pathways, we believe that the increase of HP bicarbonate production is a result of HP [1-^{13}C]pyruvate's conversion to $^{13}CO_2$ and acetyl-CoA (coenzyme A) through the pyruvate dehydrogenase complex at an increased rate. One potential alternate explanation is the direct decarboxylation of pyruvate by intracellular reactive oxygen species. We recently measured this process in reaction with hydrogen peroxide[54] and found that an intracellular ROS concentration approximately 10^5 times higher than the steady-state physiological concentration would be needed for these results[55,56]. Furthermore, the ROS concentration would need to decrease during both extended perfusion and induced mitochondrial dysfunction (study III), and would have to show either no response or a counterintuitive response to reduction by ascorbate or steady-state perfusion with pyruvate[57]. We therefore find it highly unlikely that ROS-induced decarboxylation is a significant contributor to the observed bicarbonate signal.

While intracellular HP CO_2/HCO_3^- could also potentially be produced by the conversion of pyruvate to phosphoenolpyruvate during gluconeogenesis, the lung is not actively involved in gluconeogenesis and displays low phosphoenolpyruvate carboxykinase activity[58]. Furthermore, we have been unable to detect ^{13}C aspartate or ^{13}C malate peaks in the hyperpolarized ^{13}C NMR spectra, which would have been present if ^{13}C oxaloacetate had been generated from the hyperpolarized pyruvate (these peaks are observed during gluconeogenesis in the gluconeogenically active liver[59]). Scholz and Evans previously reported that the majority of $^{14}CO_2$ production from [1-^{14}C]pyruvate in the lung resulted from PDHc activity[60], and we expect the same to be true in the studies reported here: namely, that PDHc-derived $^{13}CO_2$ is quickly brought into equilibrium with $H^{13}CO_3^-$ by carbonic anhydrase and leads to the observed HP $H^{13}CO_3^-$ signal. Moreover, ascorbate has been shown to increase pyruvate oxidation in different cells by minimizing oxidative stress and serving as a reducing agent in the electron transport chain. [2-^{14}C]-pyruvate studies indicated that the increase in released $^{14}CO_2$ originates from decarboxylase activity in the Krebs cycle [61–63].

3.5.2. Concentration-dependent Effect of Ascorbate

Ascorbate increased the HP bicarbonate signal in a concentration-dependent manner, with saturation occurring at higher concentrations (Figure 3.3A). Although this saturation could in principle arise from limited uptake or intracellular concentration as the ascorbate concentration is increased, a variety of previously published results suggest that this is not the case. Among all cell types of the noninflammatory lung, energy metabolism and pyruvate uptake occur primarily in type II pneumocytes and pulmonary alveolar macrophages (PAMs) of the normal lung[64,65]. According to previous studies, transport of ascorbate into type II pneumocytes and PAMs is characterized by saturation kinetics with K_M values of 2 and 5 mM, respectively[66]—significantly higher than the observed saturation kinetics in these studies. However, more detailed measurements highlight the contribution of passive diffusion to ascorbate transport in the lung[67], particularly at superphysiological concentrations. Wright and coworkers[68] presented results that are consistent with uni-directional saturable transport with K_M = 0.16 mM, accompanied by diffusion such that the two processes' contribution to ascorbate influx is equal at an extracellular concentration of approximately 3 mM. This allows a quantitative estimation of steady-state intracellular ascorbate concentrations under the conditions relevant to our work:

$$[ASA]_{in} = [ASA]_{ex} + \frac{3.3mM}{[ASA]_{ex} + K_M}$$

where $[ASA]_{in}$ and $[ASA]_{ex}$ refer to intracellular and extracellular ascorbate concentrations, respectively. This expression is consistent with previous measurements showing intracellular accumulation such that the intracellular ascorbate level of rat lungs is 16 to 22 times higher than that in plasma at typical physiological concentrations (0.1 mM)[68]. Notably, although the preceding discussion refers to cytosolic ascorbate, previous measurements have shown the activity of sodium-dependent vitamin C transporters (SVCTs) in transporting reduced ascorbate across the mitochondrial membrane and have demonstrated a linear relationship between the mitochondrial and cytosolic ascorbate isolated mitochondria[69,70].

In interpreting the concentration-dependent effect of ascorbate on apparent PDHc activity, it is important to also consider the rate at which equilibrium intracellular concentrations are reached. In a previous measurement, perfusion of rat lungs without ascorbate caused a 17% loss of ascorbate content after 50 min[67], indicating a rate constant of approximately 4.5 h to reach equilibrium under conditions where passive diffusion dominates ascorbate transport. The results of Ref.[68] also support the slow approach to equilibrium under these conditions. It is therefore reasonable to suppose that at the high extracellular ascorbate concentrations of Figure 3.3A (e.g., 8 and 16 mM) there was insufficient time for diffusion to the intracellular concentration to reach its equilibrium value during the perfused lung experiment. The observed concentration dependence may thus represent saturation of the fundamental ascorbate-dependent process (e.g., reduction of cytochrome c), the transition to diffusion-dominated ascorbate transport, or a combination of the two. Unfortunately, the data of Figure 3.3A are not sufficient to distinguish between these possibilities.

3.5.3. Changes in Apparent PDHc Activity

The increased bicarbonate signal could potentially be caused by a change in the uptake of pyruvate by the lung tissue. Although not significantly, the lactate and alanine signals were also increased in the presence of ascorbate (Figure 3.2B and Table 3.1), possibly indicating a small effect of ascorbate on monocarboxylate transporter activity[71]. To eliminate the HP pyruvate uptake effect, the bicarbonate signals were normalized by the sum of all ^{13}C metabolite signals, which is likely to more accurately reflect pyruvate uptake. Unlike with other metabolites, the bicarbonate ratio of the ascorbate (2 mM)-treated lungs is significantly higher than that of controls (by a factor of 2.3; Table 3.1), suggesting that ascorbate's effect on apparent PDHc activity is qualitatively different from the other metabolic processes observed and that transport alone is not responsible for this effect. In an attempt to remove altered transporter activity from the analysis, and in light of uncertainty regarding the contribution of extracellular pyruvate to the observed signal, metabolite fractions (rather than metabolite / pyruvate ratios) are employed in the following discussion.

3.5.4. Mitochondrial Function in the Lungs

Because approximately 85% of the total lung ATP is derived from mitochondrial respiration, and because mitochondrial aerobic metabolism is required to maintain the lung's normal energy status, the observed decline in ATP production over time is most likely due to declining mitochondrial function during perfusion[72]. Our HP pyruvate metabolic studies also point to this mechanism, as the bicarbonate ratio continues to decrease while the lactate ratio increases with perfusion time (Figure 3.2B, inset) due to a relative increase in glycolytic metabolism[73–75]. Recent studies with isolated perfused heart and *ex vivo* perfused lung graft models have also demonstrated increasingly deficient mitochondrial oxidative phosphorylation and significant decline in electron transport chain enzyme activities with increasing perfusion time[12,76].

The calculated energy charge (after 40 min of perfusion) showed an 8% increase in the ascorbate cohort compared with controls. Furthermore, the post/pre ratio (Figure 3.3B, inset) of the control lungs' EC (0.88) is much lower than that of the ascorbate-perfused lungs (0.99), suggesting that the oxidative phosphorylation pathway is not only more active in the ascorbate-perfused lungs, but also remains stable at those levels for a longer duration. This finding is consistent with previous studies[77].

3.5.5. Role of Ascorbate in Maintaining Mitochondrial Function

Ascorbate plays multiple roles in cellular regulation, the most well-understood of which is as an antioxidant and ROS scavenger. However, based on previously reported experiments as well as studies III and IV as interpreted below, we believe that the observed changes to lung viability and metabolism are primarily the result of ascorbate's effect on the ETC rather than its role as an antioxidant.

Ascorbate is known to prevent ROS-induced damage in ischemia–reperfusion injury, aging and as a result of drug side effects[6,22,78,79]. It has also been shown that PDHc activity decreases in the presence of ROS in a concentration- and time-dependent manner [80]. To evaluate whether the observed ascorbate effect is related to altered ROS concentration in the lung, the effects of two physiological water-soluble antioxidants, glutathione and α-lipoic acid, were studied on lung's HP [1-^{13}C]pyruvate metabolism. Both of these antioxidants have been reported to have a significant effect on ischemia–reperfusion injury [14,81].

GSH is one of the most important hydrophilic antioxidants in the lungs, protecting cells against both exogenous and endogenous toxins, including ROS [82]. What is more, given that the deficiency of one anti-oxidant leads to a decrease of the other, the antioxidant effect of GSH is directly correlated with ascorbate[83,84]. The hyperpolarized bicarbonate signal in the presence of 2 mM GSH in the perfusate did not change significantly relative to controls (Figure 3.4A). Although glutathione uptake by the lung remains incompletely understood, the significant increase in alanine ratio and decrease in lactate ratio are consistent with previous studies and suggest that GSH was taken up by the lung cells that are actively metabolizing pyruvate [85–87]. ALA is a coenzyme of the PDHc and an effective antioxidant against ROS and associated mitochondrial dysfunction[81,88]. Although the decrease in the bicarbonate ratio in the presence of 2 mM ALA was not significant (Figure 3.4A), the increase in lactate ratio in ALA-perfused lungs shows that sufficient ALA was taken up to influence metabolism as well[89]. These studies suggest that the primary means by which ascorbic acid increases PDHc activity is not related to a general ROS-scavenging or antioxidant effect.

Another related mechanism by which circulating ascorbate could affect PDHc activity is through a reaction with its oxidized form, dehydroascorbate: dihydrolipoic acid + DHA → ascorbate + ALA. This reaction could serve to regenerate intramitochondrial ALA, which serves as a cofactor in PDHc activity[90]. Furthermore, it is worth noting that, during the experiments described here, ascorbic acid is slowly converted to DHA by reaction with dissolved O_2[91]. Although this oxidation reaction occurs over a relatively long time scale of approximately 1 h[91], DHA is nonetheless always present in the studies. To assess the effect of DHA, we performed perfusion experiments in which 2 mM DHA was added to the perfusate as well as others in which 1 mM DHA + 1 mM ASA were used. In the former, the hyperpolarized [^{13}C]bicarbonate signal was indistinguishable from that of the control cohort; in the latter, this signal was indistinguishable from that of 1 mM ASA alone (Figure 3.4B). These results suggest that oxidation of dihydrolipoic acid is not the dominant mechanism by which ascorbate affects PDHc activity. We note, however, that although glucose transporter 1 transports DHA [97], previous studies have suggested that DHA is not taken up efficiently by perfused lung and lung cells[91]; it is therefore impossible to entirely rule out a mechanism in which ascorbate is taken up, oxidized to DHA, and subsequently regenerates ALA by the oxidation of dihydrolipoic acid based on the studies described here.

Nonetheless, the most likely route by which ascorbate influences lung metabolism is through its role as a reducing agent in the electron transport chain. Previous studies of ascorbate’s protective effects in cardiac arrest and electrical shock, ischemia–reperfusion injury, drug side effects and aging have shown that ascorbate plays a role as an activator of the ETC complexes[6,35,62,78,92]. This study and other previous works have shown a reduction in EC and ATP production during extended perfusion, indicating a gradual decrease in mitochondrial function and oxidative phosphorylation[12,76]. Accordingly, we hypothesized that the direct reduction of cytochrome c by ascorbate is a possible mechanism by which PDHc flux (as observed in HP bi-carbonate signal) and mitochondrial function (as observed in energy charge) might be simultaneously protected or activated[93,94]. Study IV was designed to evaluate this hypothesis: lungs were first perfused with TMPD + ascorbate, a combination that reduces cytochrome c at a rate 30-fold faster than ascorbate alone [100]. Note that adding a small amount of ascorbate is necessary to ensure that TMPD remains in the reduced form, but that, as seen in Figure 3.3A, this amount is too small to account for the observed effects. Additional studies were performed in which the ascorbate concentration was increased to 500 mM (data not shown).

This change did not alter either the bicarbonate ratio or EC, confirming that ascorbate is not the primary agent reducing cytochrome c in the presence of TMPD[94]. In the lung perfused with 25 mM TMPD + 250 mM ascorbate, the bicarbonate ratio increased by a factor of 2.2—comparable to with the addition of 2 mM ascorbate. The energy charge of the TMPD-perfused lung also increased significantly (by 13%) compared with controls (Figure 3.5). As shown in study II, ascorbate alone also significantly increased the lung's energy charge (8%), confirming previously reported data in ascorbate-treated cartilage cells[77]. We may therefore conclude that the reduction of cytochrome c and concomitant activation of ETC complex IV increases apparent PDHc flux.

In a subset of study IV, lungs perfused with 20 mM rotenone showed a significant decrease in both the bicarbonate ratio (68%) and EC (18%). Rotenone-perfused lungs that were then perfused with TMPD + ascorbate returned to a state indistinguishable from controls in terms of PDHc activity and energy charge, whereas those perfused without TMPD + ascorbate continued to decline. Moreover, in agreement with a previous study[41], increased HP lactate ratio and decreased EC were observed in the rotenone-perfused lungs due to the inhibition of mitochondrial electron transport. Both measurements returned to baseline after perfusion with TMPD + ascorbate as a result of ETC activation. Further evidence of the link between the electron transport chain and PDHc activity can be seen in the strong positive correlation between EC and HP bicarbonate ratio across all cohorts (Figure 3.6). A complementary effect is also observed in the strong negative correlation between EC and HP lactate ratio across all cohorts: low ETC activity leads to overreliance on glycolytic ATP generation and an increase in cytosolic lactate [57].

We note that both correlations are observed independent of the manner in which ETC activity is influenced, a fact which appears somewhat counterintuitive at first. Because TMPD is known to directly reduce cytochrome c, thereby providing a source of electrons for respiratory activity that does not require PDHc-derived NADH, it would be reasonable to assume that PDHc activity would be suppressed. However, it is also true that an active electron transport chain results in an increased proton concentration gradient across the mitochondrial membrane. To maintain charge balance, this gradient is mirrored by a Ca^{2+} gradient; the active mitochondrion is thus characterized by an increased intramitochondrial Ca^{2+} concentration, a condition which is well understood to cause PDHc activity by activating pyruvate dehydrogenase phosphatase[51,52]. We therefore hypothesize that ascorbate maintains mitochondrial function during perfusion by activating the electron transport chain and that the intramitochondrial Ca^{2+} concentration of the active ETC, rather than a direct interaction between ascorbate and PDHc or its cofactors, is responsible for maintaining and stimulating PDHc activity. The exact mechanism by which ascorbate activates the ETC is unknown, although many previous studies have highlighted important interactions with complex I and complex IV—maintaining their activity after cardiac arrest, as well as in aging fibroblasts—which in turn prevents the loss of cytochrome c and maintains the mitochondrial membrane polarization[6,35,92,95,96]. Any of these effects, either singly or in combination, may be responsible for increased viability and the observed stimulation of the PDHc in ascorbate-perfused lungs.

3.6. Conclusions

In this study, we demonstrated that the energy status and PDHc activity of perfused lungs declines during EVLP, and concluded that a part of the energy depletion and loss of viability observed in reperfused ischemic lungs[12] is due to perfusion alone. We also provided evidence that ascorbate regulates the *ex vivo* perfused lung's metabolism toward oxidative phosphorylation. Although ascorbate's role in lessening ischemia-reperfusion injury via its ROS scavenging function has been discussed previously[21,22], our studies suggest that ascorbate can also slow the decline in pulmonary mitochondrial activity through an independent interaction with ETC complexes. Based on the observation that lungs experiencing significant decline in energy status are highly prone to edema, it seems clear that maintaining mitochondrial function during EVLP is critical to maintaining organ viability. Finally, we also demonstrated hyperpolarized [1-^{13}C]pyruvate's suitability as a tool for evaluating the lung's mitochondrial status in *ex vivo* lung perfusion models due to its ability to simultaneously probe both glycolytic and oxidative phosphorylation pathways. The study also demonstrates that the addition of ascorbate to the perfusate during EVLP may be beneficial in prolonging the viability of the lungs being excised, transported and reperfused before transplant. Further studies are warranted to assess the relevance of these findings to human lung transplant maintenance and evaluation procedures.

3.7. References

1. Avlonitis VS, Fisher AJ, Kirby JA, Dark JH. Pulmonary Transplantation: the role of brain death in donor lung injury. *Transplantation*. 2003;75(12):1928. doi:10.1097/01.TP.0000066351.87480.9E

2. Punch JD, Hayes DH, LaPorte FB, McBride V, Seely MS. Organ Donation and Utilization in the United States, 1996–2005. *American Journal of Transplantation*. 2007;7(s1):1327-1338. doi:10.1111/j.1600-6143.2007.01779.x

3. Cypel M, Yeung JC, Liu M, et al. Normothermic Ex Vivo Lung Perfusion in Clinical Lung Transplantation. *New England Journal of Medicine*. 2011;364(15):1431-1440. doi:10.1056/NEJMoa1014597

4. Cypel M, Rubacha M, Yeung J, et al. Normothermic Ex Vivo Perfusion Prevents Lung Injury Compared to Extended Cold Preservation for Transplantation. *American Journal of Transplantation*. 2009;9(10):2262-2269. doi:10.1111/j.1600-6143.2009.02775.x

5. den Hengst WA, Gielis JF, Lin JY, Van Schil PE, De Windt LJ, Moens AL. Lung ischemia-reperfusion injury: a molecular and clinical view on a complex pathophysiological process. *American Journal of Physiology-Heart and Circulatory Physiology*. 2010;299(5):H1283-H1299. doi:10.1152/ajpheart.00251.2010

6. Sharma P, Rupar CA, Rip JW. Consequences of Aging on Mitochondrial Respiratory Chain Enzymes in Cultured Human Fibroblasts Treated with Ascorbate. *GER*. 1998;44(2):78-84. doi:10.1159/000021988

7. Weyker PD, Webb CAJ, Kiamanesh D, Flynn BC. Lung Ischemia Reperfusion Injury: A Bench-to-Bedside Review. *Semin Cardiothorac Vasc Anesth*. 2013;17(1):28-43. doi:10.1177/1089253212458329

8. Ovechkin AV, Lominadze D, Sedoris KC, Robinson TW, Tyagi SC, Roberts AM. Lung ischemia–reperfusion injury: implications of oxidative stress and platelet–arteriolar wall interactions. *Archives of Physiology and Biochemistry*. 2007;113(1):1-12. doi:10.1080/13813450601118976

9. de Perrot M, Liu M, Waddell TK, Keshavjee S. Ischemia–Reperfusion–induced Lung Injury. *Am J Respir Crit Care Med*. 2003;167(4):490-511. doi:10.1164/rccm.200207-670SO

10. Kalogeris T, Bao Y, Korthuis RJ. Mitochondrial reactive oxygen species: A double edged sword in ischemia/reperfusion vs preconditioning. *Redox Biology*. 2014;2:702-714. doi:10.1016/j.redox.2014.05.006

11. Koike T, Yeung JC, Cypel M, et al. Kinetics of lactate metabolism during acellular normothermic ex vivo lung perfusion. *The Journal of Heart and Lung Transplantation*. 2011;30(12):1312-1319. doi:10.1016/j.healun.2011.07.014

12. Noda K, Shigemura N, Tanaka Y, et al. Hydrogen Preconditioning During Ex Vivo Lung Perfusion Improves the Quality of Lung Grafts in Rats. *Transplantation*. 2014;98(5):499. doi:10.1097/TP.0000000000000254

13. Sommer S-P, Sommer S, Sinha B, et al. Ischemia-reperfusion injury–induced pulmonary mitochondrial damage. *The Journal of Heart and Lung Transplantation*. 2011;30(7):811-818. doi:10.1016/j.healun.2011.02.001

14. Sommer A, Wieser R. Die beschränkte Körperschaftsteuerbefreiung gemeinnütziger Bauvereinigungen als im europarechtlichen Sinn staatliche Beihilfe? *wobl*. 2012;25(4):140-144. doi:10.1007/s00719-012-0049-y

15. Schöder H, Knight RJ, Kofoed KF, Schelbert HR, Buxton DB. Regulation of pyruvate dehydrogenase activity and glucose metabolism in post-ischaemic myocardium. *Biochimica et Biophysica Acta (BBA) - Molecular Basis of Disease*. 1998;1406(1):62-72. doi:10.1016/S0925-4439(97)00088-4

16. Ferrari RS, Andrade CF. Oxidative Stress and Lung Ischemia-Reperfusion Injury. Oxidative Medicine and Cellular Longevity. doi:10.1155/2015/590987

17. Nagel E, Meyer A zu V, Bartels M, Pichlmayr R. Antioxidative vitamins in prevention of ischemia/reperfusion injury. *Int J Vitam Nutr Res*. 1997;67(5):298-306.

18. Okutan H, Savas C, Delibas N. The antioxidant effect of melatonin in lung injury after aortic occlusion–reperfusion. *Interact CardioVasc Thorac Surg*. 2004;3(3):519-522. doi:10.1016/j.icvts.2004.05.005

19. Fu Z, Liu X, Geng B, Fang L, Tang C. Hydrogen sulfide protects rat lung from ischemia–reperfusion injury. *Life Sciences*. 2008;82(23-24):1196-1202. doi:10.1016/j.lfs.2008.04.005

20. Inci I, Zhai W, Arni S, Hillinger S, Vogt P, Weder W. N-Acetylcysteine Attenuates Lung Ischemia–Reperfusion Injury After Lung Transplantation. *The Annals of Thoracic Surgery*. 2007;84(1):240-246. doi:10.1016/j.athoracsur.2007.03.082

21. Demertzis S, Scherer M, Langer F, Dwenger A, Hausen B, Schäfers H-J. Ascorbic acid for amelioration of reperfusion injury in a lung autotransplantation model in sheep. *The Annals of Thoracic Surgery*. 2000;70(5):1684-1689. doi:10.1016/S0003-4975(00)01846-4

22. Baltalarli A, Ozcan V, Ferda B, et al. Ascorbic Acid (Vitamin C) and Iloprost Attenuate the Lung Injury Caused by Ischemia/Reperfusion of the Lower Extremities of Rats. *Annals of Vascular Surgery*. 2006;20(1):49-55. doi:10.1007/s10016-005-9284-0

23. Adluri RS, Thirunavukkarasu M, Zhan L, et al. Cardioprotective Efficacy of a Novel Antioxidant Mix VitaePro Against Ex Vivo Myocardial Ischemia–Reperfusion Injury. *Cell Biochem Biophys*. 2013;67(2):281-286. doi:10.1007/s12013-011-9300-7

24. Guler L, Tavlasoglu M, Yucel O, et al. Taurine attenuates lung ischemia–reperfusion injury after lung transplantation in rats. *J Anesth*. 2014;28(3):347-353. doi:10.1007/s00540-013-1741-2

25. Lehr Hans-Anton, Frei Balz, Olofsson A. Maria, Carew Thomas E., Arfors Karl-E. Protection From Oxidized LDL–Induced Leukocyte Adhesion to Microvascular and Macrovascular Endothelium In Vivo by Vitamin C but Not by Vitamin E. *Circulation*. 1995;91(5):1525-1532. doi:10.1161/01.CIR.91.5.1525

26. Korkmaz A, Kolankaya D. The Protective Effects of Ascorbic Acid against Renal Ischemia-Reperfusion Injury in Male Rats. *Renal Failure*. 2009;31(1):36-43. doi:10.1080/08860220802546271

27. Lee J, Son H-Y, Kim M. Attenuation of ischemia-reperfusion injury by ascorbic acid in the canine renal transplantation. *Journal of Veterinary Science*. 2006;7(4):375-379. doi:10.4142/jvs.2006.7.4.375

28. Lee W-Y, Lee J-S, Lee S-M. Protective Effects of Combined Ischemic Preconditioning and Ascorbic Acid on Mitochondrial Injury in Hepatic Ischemia/Reperfusion. *Journal of Surgical Research*. 2007;142(1):45-52. doi:10.1016/j.jss.2006.08.043

29. Hsu C-C, Wang J-J. L-Ascorbic Acid and Alpha-tocopherol Attenuates Liver Ischemia-Reperfusion Induced of Cardiac Function Impairment. *Transplantation Proceedings*. 2012;44(4):933-936. doi:10.1016/j.transproceed.2012.01.098

30. Sağsöz N, Kisa Ü, Apan A. Ischaemia–reperfusion injury of rat ovary and the effects of vitamin C, mannitol and verapamil. *Hum Reprod*. 2002;17(11):2972-2976. doi:10.1093/humrep/17.11.2972

31. May JM. HOW DOES ASCORBIC ACID PREVENT ENDOTHELIAL DYSFUNCTION? *Free Radical Biology and Medicine*. 2000;28(9):1421-1429.

32. Biesalski H, McGregor G. Antioxidant therapy in critical care—Is the microcirculation the primary target? *Critical Care Medicine*. 2007;35(9). doi:10.1097/01.CCM.0000278598.95294.C5

33. Basili S, Tanzilli G, Mangieri E, et al. Intravenous Ascorbic Acid Infusion Improves Myocardial Perfusion Grade During Elective Percutaneous Coronary Intervention. *JACC: Cardiovascular Interventions*. 2010;3(2):221-229. doi:10.1016/j.jcin.2009.10.025

34. Mo S-J, Son E-W, Rhee D-K, Pyo S. Modulation of tnf-α-induced icam-1 expression, no and h202 production by alginate, allicin and ascorbic acid in human endothelial cells. *Arch Pharm Res*. 2003;26(3):244. doi:10.1007/BF02976837

35. Tsai M-S, Huang C-H, Tsai C-Y, et al. Ascorbic acid mitigates the myocardial injury after cardiac arrest and electrical shock. *Intensive Care Med*. 2011;37(12):2033-2040. doi:10.1007/s00134-011-2362-6

36. Fisher BJ, Seropian IM, Kraskauskas D, et al. Ascorbic acid attenuates lipopolysaccharide-induced acute lung injury*. *Critical Care Medicine*. 2011;39(6):1454-1460. doi:10.1097/CCM.0b013e3182120cb8

37. Iwata N, Okazaki M, Xuan M, Kamiuchi S, Matsuzaki H, Hibino Y. Orally Administrated Ascorbic Acid Suppresses Neuronal Damage and Modifies Expression of SVCT2 and GLUT1 in the Brain of Diabetic Rats with Cerebral Ischemia-Reperfusion. *Nutrients*. 2014;6(4):1554-1577. doi:10.3390/nu6041554

38. Pullinger B, Profka H, Ardenkjaer-Larsen JH, Kuzma NN, Kadlecek S, Rizi RR. Metabolism of hyperpolarized [1-13C]pyruvate in the isolated perfused rat lung - an ischemia study: MEASUREMENTS OF LUNG METABOLISM USING HYPERPOLARIZED 1-13C PYRUVATE. *NMR in Biomedicine*. 2012;25(10):1113-1118. doi:10.1002/nbm.2777

39. Hayashi Y, Inubushi T, Nioka S, Forster RE. ^ 3^ 1P-NMR spectroscopy of isolated perfused rat lung. *Journal of Applied Physiology*. 1993;74:1549–1549.

40. Pillai RP, Buescher PC, Pearse DB, Sylvester JT, Eichhorn GL. 31P NMR spectroscopy of isolated perfused lungs. *Magn Reson Med*. 1986;3(3):467-472.

41. Bongard RD, Yan K, Hoffmann RG, et al. Depleted energy charge and increased pulmonary endothelial permeability induced by mitochondrial complex I inhibition are mitigated by coenzyme Q1 in the isolated perfused rat lung. *Free Radical Biology and Medicine*. 2013;65:1455-1463. doi:10.1016/j.freeradbiomed.2013.07.040

42. Kasimos JN, Merchant TE, Gierke LW, Glonek T. 31P Magnetic Resonance Spectroscopy of Human Colon Cancer. :7.

43. Pettegrew JW, Keshavan MS, Minshew NJ. 31P Nuclear Magnetic Resonance Spectroscopy: Neurodevelopment and Schizophrenia. *Schizophr Bull*. 1993;19(1):35-53. doi:10.1093/schbul/19.1.35

44. Riss TL, Moravec RA, Niles AL, et al. *Cell Viability Assays*. Eli Lilly & Company and the National Center for Advancing Translational Sciences; 2016. https://www.ncbi.nlm.nih.gov/books/NBK144065/. Accessed March 24, 2019.

45. Nishiwaki M, Fujise Y, Yoshida TO, Matsuzawa E, Nishiwaki Y. Evaluation of the effects of photodynamic therapy with phosphorus 31 magnetic resonance spectroscopy. *British Journal of Cancer*. 1999;80(1-2):133-141. doi:10.1038/sj.bjc.6690332

46. Schunk K, Pitton M, Düber C, Kersjes W, Schadmand-Fischer S, Thelen M. Dynamic Phosphorus-31 Magnetic Resonance Spectroscopy of the Quadriceps Muscle. *Investigative Radiology*. 1999;34(2):116-125.

47. Atkinson DE. Energy charge of the adenylate pool as a regulatory parameter. Interaction with feedback modifiers. *Biochemistry*. 1968;7(11):4030-4034. doi:10.1021/bi00851a033

48. Ballard FJ. Adenine nucleotides and the adenylate kinase equilibrium in livers of foetal and newborn rats. *Biochemical Journal*. 1970;117(2):231-235. doi:10.1042/bj1170231

49. Tillery SI, Lehnert BE. Age-bodyweight relationships to lung growth in the F344 rat as indexed by lung weight measurements. *Laboratory Animals*. 1986;20(3):189-194. doi:10.1258/002367786780865610

50. Kepner GR. Saturation Behavior: a general relationship described by a simple second-order differential equation. *Theoretical Biology and Medical Modelling*. 2010;7(1):11. doi:10.1186/1742-4682-7-11

51. Denton RM, Randle PJ, Martin BR. Stimulation by calcium ions of pyruvate dehydrogenase phosphate phosphatase. *Biochemical Journal*. 1972;128(1):161-163. doi:10.1042/bj1280161

52. Denton RM. Regulation of mitochondrial dehydrogenases by calcium ions. *Biochimica et Biophysica Acta (BBA) - Bioenergetics*. 2009;1787(11):1309-1316. doi:10.1016/j.bbabio.2009.01.005

53. Sasaki M, Fujimoto S, Sato Y, et al. Reduction of Reactive Oxygen Species Ameliorates Metabolism-Secretion Coupling in Islets of Diabetic GK Rats by Suppressing Lactate Overproduction. *Diabetes*. 2013;62(6):1996-2003. doi:10.2337/db12-0903

54. Ghosh RK, Kadlecek SJ, Pourfathi M, Rizi RR. Efficient production of hyperpolarized bicarbonate by chemical reaction on a DNP precursor to measure pH. *Magn Reson Med*. November 2014:n/a-n/a. doi:10.1002/mrm.25530

55. Chance B, Sies H, Boveris A. Hydroperoxide metabolism in mammalian organs. *Physiological Reviews*. 1979;59(3):527-605. doi:10.1152/physrev.1979.59.3.527

56. Cadenas E, Davies KJA. MITOCHONDRIAL FREE RADICAL GENERATION, OXIDATIVE STRESS, AND AGING. *oxidative stress.*:9.

57. Kadlecek S, Shaghaghi H, Siddiqui S, Profka H, Pourfathi M, Rizi R. The effect of exogenous substrate concentrations on true and apparent metabolism of hyperpolarized pyruvate in the isolated perfused lung. *NMR Biomed*. 2014;27(12):1557-1570. doi:10.1002/nbm.3219

58. Scholz RW. Lipid metabolism by rat lung in vitro. Utilization of citrate by normal and starved rats. *Biochemical Journal*. 1972;126(5):1219-1224. doi:10.1042/bj1261219

59. Merritt ME, Harrison C, Sherry AD, Malloy CR, Burgess SC. Flux through hepatic pyruvate carboxylase and phosphoenolpyruvate carboxykinase detected by hyperpolarized 13C magnetic resonance. *Proceedings of the National Academy of Sciences*. 2011;108(47):19084-19089. doi:10.1073/pnas.1111247108

60. Scholz RW, Evans RM. Pyruvate metabolism by rat lung in vitro. *Lipids*. 1973;8(6):360–365.

61. Piontek GE, Milner JA, Cain CA. Effects of Hyperthermia and L-Ascorbic Acid on Glucose, Pyruvate, and Lactate Metabolism in Ehrlich Ascites Carcinoma Cells. *Experimental Biology and Medicine*. 1979;161(4):597-599. doi:10.3181/00379727-161-40604

62. Werner P, Mytilineou C, Cohen G, Yahr MD. Impaired oxidation of pyruvate in human embryonic fibroblasts after exposure to L-dopa. *European journal of pharmacology*. 1994;263(1):157–162.

63. Lane M, Maybach JM, Gardner DK. Addition of ascorbate during cryopreservation stimulates subsequent embryo development. *Hum Reprod*. 2002;17(10):2686-2693. doi:10.1093/humrep/17.10.2686

64. Simon LM, Robin ED, Raffin T, Theodore J, Douglas WHJ. Bioenergetic pattern of isolated type II pneumocytes in air and during hypoxia. *Journal of Clinical Investigation*. 1978;61(5):1232.

65. Massaro GD, Gail DB, Massaro D. Lung oxygen consumption and mitochondria of alveolar epithelial and endothelial cells. *Journal of applied physiology*. 1975;38(4):588–592.

66. Castranova V, Wright JR, Colby HD, Miles PR. Ascorbate uptake by isolated rat alveolar macrophages and type II cells. *Journal of Applied Physiology*. 1983;54(1):208–214.

67. Arad ID, Forman HJ, Fisher AB. Ascorbate efflux from guinea pig and rat lungs: Effect of starvation and O2 exposure. *The Journal of Laboratory and Clinical Medicine*. 1980;96(4):673-681. doi:10.5555/uri:pii:0022214380900712

68. Wright JR, Castranova V, Colby HD, Miles PR. Ascorbate uptake by isolated rat lung cells. *J Appl Physiol*. 1981;51:1477–1483.

69. May JM. The SLC23 family of ascorbate transporters: ensuring that you get and keep your daily dose of vitamin C. *British Journal of Pharmacology*. 2011;164(7):1793-1801. doi:10.1111/j.1476-5381.2011.01350.x

70. Azzolini C, Fiorani M, Cerioni L, Guidarelli A, Cantoni O. Sodium-dependent transport of ascorbic acid in U937 cell mitochondria. *IUBMB Life*. 2013;65(2):149-153. doi:10.1002/iub.1124

71. Castro MA, Angulo C, Brauchi S, Nualart F, Concha II. Ascorbic acid participates in a general mechanism for concerted glucose transport inhibition and lactate transport stimulation. *Pflügers Archiv - European Journal of Physiology*. 2008;457(2):519-528. doi:10.1007/s00424-008-0526-1

72. Fisher A B. Intermediary metabolism of the lung. *Environmental Health Perspectives*. 1984;55:149-158. doi:10.1289/ehp.8455149

73. Fisher AB, Dodia C. Lactate and regulation of lung glycolytic rate. *American Journal of Physiology-Endocrinology and Metabolism*. 1984;246(5):E426-E429. doi:10.1152/ajpendo.1984.246.5.E426

74. Brooks GA. Lactate. *Sports Med*. 2007;37(4):341-343. doi:10.2165/00007256-200737040-00017

75. Bassett DJ, Bowen-Kelly E. Pyruvate metabolism of perfused rat lungs after exposure to 100% oxygen. *J Appl Physiol*. 1986;60:1605–1609.

76. Kurian GA. ROLE OF NORMAL PERFUSION TIME ON FUNCTIONAL ENZYME ACTIVITIES AND PHYSIOLOGY OF INTERFIBRILLAR AND SUB-SARCOLEMMAL MITOCHONDRIA FROM ISOLATED RAT HEART. 6(11):8.

77. Shapiro IM, Leboy PS, Tokuoka T, et al. Ascorbic acid regulates multiple metabolic activities of cartilage cells. *Am J Clin Nutr*. 1991;54(6):1209S-1213S. doi:10.1093/ajcn/54.6.1209s

78. Nishinaka Y, Sugiyama S, Yokota M, Saito H, Ozawa T. The effects of a high dose of ascorbate on ischemia-reperfusion-induced mitochondrial dysfunction in canine hearts. *Heart Vessels*. 1992;7(1):18-23. doi:10.1007/BF01745863

79. Kaufmann P, Török M, Hänni A, Roberts P, Gasser R, Krähenbühl S. Mechanisms of benzarone and benzbromarone-induced hepatic toxicity. *Hepatology*. 2005;41(4):925-935. doi:10.1002/hep.20634

80. Tabatabaie T, Potts JD, Floyd RA. Reactive oxygen species-mediated inactivation of pyruvate dehydrogenase. *Archives of biochemistry and biophysics*. 1996;336(2):290–296.

81. He L, Liu B, Dai Z, et al. Alpha lipoic acid protects heart against myocardial ischemia–reperfusion injury through a mechanism involving aldehyde dehydrogenase 2 activation. *European Journal of Pharmacology*. 2012;678(1-3):32-38. doi:10.1016/j.ejphar.2011.12.042

82. Aquilano K, Baldelli S, Ciriolo MR. Glutathione: new roles in redox signaling for an old antioxidant. *Front Pharmacol*. 2014;5. doi:10.3389/fphar.2014.00196

83. Meister A. On the antioxidant effects of ascorbic acid and glutathione. *Biochemical Pharmacology*. 1992;44(10):1905-1915. doi:10.1016/0006-2952(92)90091-V

84. Jain A, Mårtensson J, Mehta T, Krauss AN, Auld PA, Meister A. Ascorbic acid prevents oxidative stress in glutathione-deficient mice: effects on lung type 2 cell lamellar bodies, lung surfactant, and skeletal muscle. *PNAS*. 1992;89(11):5093-5097. doi:10.1073/pnas.89.11.5093

85. M\a artensson J, Jain A, Frayer W, Meister A. Glutathione metabolism in the lung: inhibition of its synthesis leads to lamellar body and mitochondrial defects. *Proceedings of the National Academy of Sciences*. 1989;86(14):5296–5300.

86. Wimberger P, Ebner S, Marin-Grez M. Reduced glutathione inhibits rabbit and rat skeletal muscle lactate dehydrogenase and prevents dinitrophenol induced extracellular acidification by an epithelial cell line. *Life Sciences*. 1997;61(4):403-409. doi:10.1016/S0024-3205(97)00397-4

87. Bai C, Brown LAS, Jones DP. Glutathione transport by type II cells in perfused rat lung. *American Journal of Physiology-Lung Cellular and Molecular Physiology*. 1994;11(4):L447.

88. Hagen TM, Ingersoll RT, Lykkesfeldt J, et al. (R)-α-Lipoic acid-supplemented old rats have improved mitochondrial function, decreased oxidative damage, and increased metabolic rate. *The FASEB Journal*. 1999;13(2):411-418. doi:10.1096/fasebj.13.2.411

89. Vigil M, Berkson BM, Garcia AP. Adverse Effects of High doses of Intravenous Alpha Lipoic Acid on Liver Mitochondria. *Global Advances in Health and Medicine*. 2014;3(1):25-27. doi:10.7453/gahmj.2013.011

90. Xu DP, Wells WW. α-Lipoic acid dependent regeneration of ascorbic acid from dehydroascorbic acid in rat liver mitochondria. *J Bioenerg Biomembr*. 1996;28(1):77-85. doi:10.1007/BF02150681

91. Willis RJ, Kratzing CC. Transport of ascorbic acid in perfused rat lung. *Pflügers Archiv*. 1975;356(1):93–98.

92. Ghneim HK, Al-Sheikh YA. The effect of aging and increasing ascorbate concentrations on respiratory chain activity in cultured human fibroblasts. *Cell Biochemistry and Function*. 2010;28(4):283-292. doi:10.1002/cbf.1653

93. Slater EC. The measurement of the cytochrome oxidase activity of enzyme preparations. *Biochemical Journal*. 1949;44(3):305-318. doi:10.1042/bj0440305

94. Kimelberg H, Nicholls P. Kinetic studies on the interaction of TMPD with cytochrome c and cytochrome c oxidase. *Archives of Biochemistry and Biophysics*. 1969;133(2):327-335. doi:10.1016/0003-9861(69)90461-5

95. Gruss-Fischer T, Fabian I. Protection by ascorbic acid from denaturation and release of cytochrome c, alteration of mitochondrial membrane potential and activation of multiple caspases induced by H2O2, in human leukemia cells. *Biochemical Pharmacology*. 2002;63(7):1325-1335. doi:10.1016/S0006-2952(02)00863-8

96. Hattori T, Watanabe K, Uechi Y, Yoshioka H, Ohta Y. Repetitive Transient Depolarizations of the Inner Mitochondrial Membrane Induced by Proton Pumping. *Biophysical Journal*. 2005;88(3):2340-2349. doi:10.1529/biophysj.104.041483

Chapter 4: Translating from *Ex Vivo* Metabolic Spectroscopy to *In Vivo* Metabolic Imaging of HP [1-^{13}C] Pyruvate Using an Acute Inflammation Model

Abstract

In this study, we investigated the feasibility of hyperpolarized [1-^{13}C]pyruvate as a potential marker for inflammation in lung tissue. In the first part of the study, we report *ex vivo* metabolic measurements in the isolated, perfused rat lung of healthy controls and in lungs undergoing acute inflammation using hyperpolarized [1-^{13}]C-labeled pyruvate. The overall apparent lactate labelling was shown to increase significantly (on average by a factor of 3.3) at the 7-day acute stage and then revert substantially to baseline at 21 days, while other markers indicating monocarboxylate uptake and transamination rate were unchanged. In the second part of the study, we successfully translated our hyperpolarized imaging technique for *in vivo* imaging. The overall lactate-to-pyruvate ratio showed a similar trend as the *ex vivo* study; it was found to be significantly increased on day 7 (by a factor of 1.6) and then reverted to baseline by day 21. Elevated lung lactate signal levels correlated well with phosphodiester levels as determined with ^{31}P spectroscopy and to the presence of neutrophils as determined by histology, consistent with a relationship between intracellular lactate pool labeling and the density and type of inflammatory cells present.

This *ex* vivo spectroscopy findings from this chapter have been published as ‘Metabolic spectroscopy of inflammation in a bleomycin-induced lung injury model using hyperpolarized 1-13C pyruvate’ by Shaghaghi et al, in NMR in Biomedicine, 27(8):939-947 (2014). Some of the *in vivo* findings have been presented at the International Society for Magnetic Resonance in Imaging (ISMRM) Conference in Paris, France as, ‘A Multimodal Imaging Approach to Characterize the Onset of Pulmonary Fibrosis’ by Siddiqui et al. (2018).

4.1. Introduction

The adaptive immune system's response is essential to the process of lung rejection: the mismatch between host and donor MHC molecules stimulates cytotoxic T cells (CTLs), which then target the graft tissue for rejection. Directly visualizing the progression of lung inflammation would therefore be very useful for detecting lung rejection earlier. Unfortunately, conventional techniques for measuring inflammatory cell activity—biopsies and lavage—are not very effective in sampling regional differences, while radiological methods' dependence on edema, fibrosis, emphysema, and other alterations to tissue density than on the weak direct x-ray absorption of the inflammatory cells make them unsuitable as well. However, it has been amply demonstrated that the metabolic state of inflammatory cells, and particularly their glycolytic activity, is much greater than that of normal lung tissue[1]. In this study, we therefore investigated the uptake of hyperpolarized [1-^{13}C]pyruvate as a potential marker for inflammation in lung tissue.

As described in Chapter 2, although HP MRI uses external nuclear polarization to overcome its low sensitivity, several challenges not present in other organs have thus far limited HP studies in lungs. These include low tissue density, high susceptibility/B_0 inhomogeneity caused by air- tissue interfaces, cardiac and respiratory motion, and the low metabolic rate of the lungs compared to solid organs. In order to minimize many of the difficulties mentioned above, we first demonstrated that HP ^{13}C MR spectroscopy can be used to differentiate inflamed tissue from healthy tissue in *ex vivo* isolated, perfused lungs before translating this technique to *in vivo* HP ^{13}C MR imaging.

Although our ultimate goal is to develop a translatable method for imaging lung rejection, we used a bleomycin-induced lung injury (BILI) model of inflammation for this study. The etiology of the BILI model is substantially different from that of lung rejection—most significantly in that, unlike tissue rejection, it is an innate immune response primarily driven by the infiltration of neutrophils into the tissue. Like T cells, however, neutrophils depend on glycolysis for their energy[1–3], so the successful development of HP [1-^{13}C] pyruvate imaging is nevertheless applicable to imaging post-transplantation outcomes. There are, moreover, a number of advantages to using a BILI rather than a transplant model for developing this technique. For example, the BILI model is a well-developed animal model with a large number of studies[4] characterizing its inflammatory and eventual fibrotic response after bleomycin induction. The model induction itself is rapid, and inflammation can be observed within three to seven days. Finally, the imaging technique can be developed using half the number of animals that would be needed with a lung transplantation model, which requires donor animals as well.

4.2. Materials and Methods

All animal experiments were conducted in accordance with protocols approved by the Institutional Animal Care and Use Committee of the University of Pennsylvania. Eight-week-old male Sprague Dawley rats weighing 320 ± 20 g were used for all experiments. All rats were carefully age matched and maintained under very similar environments and dietary conditions. The cohort sizes for both *ex* and *in vivo* studies are listed in Table 4.1

	***Ex Vivo* Isolated Perfused Lung Spectroscopy**	***In Vivo* Lung Imaging**
Control	7	3
Day 7	10	3
Day 14	-	3
Day 21	3	2

Table 4.1: Cohort sizes for the ex vivo and in vivo studies.

4.2.1 Bleomycin Model Induction

Bleomycin rats were anesthetized using inhaled 2.5% isoflurane, placed supine, and intubated with a 2-inch long, 14-gauge angiocatheter. A 2.5 U/kg concentration of bleomycin (Bedford Laboratories, Bedford, OH) was then instilled through the catheter, followed by a 3 mL injection of air to clear the catheter. Animals were then rocked from side to side to distribute the bleomycin throughout the lungs as evenly as possible. The animals were subsequently recovered from anesthesia and briefly ventilated with a rodent ventilator (CWE, Ardmore, PA); supplemental oxygen was given if they failed to recover from anesthesia in a timely manner.

4.2.2. Preparation of Hyperpolarized [1-^{13}C]Pyruvate

The solid-state pyruvic acid mixture was prepared similarly to the method described in the previous chapter; however, the liquid-state concentrations and duration of the HP injections were different for these studies. 28.5 mg [1-^{13}C]pyruvic acid (Cambridge Isotope Laboratories, Andover, MA, USA) mixed with 15 mM OX063 trityl radical (Oxford Instruments, Tubney Woods, Abingdon, Oxfordshire, OX13 5QX, UK) and 1.5 mM Dotarem Gd chelate (Guerbet, Roissy, France) was polarized to ~30% at 1.42 K and 94 GHz with a HyperSense dynamic nuclear polarization system (Oxford Instruments). 4 mL of buffer, containing 50 mM Tris, 80 mM NaOH, and 100 mg/L EDTA, was heated to 190 °C at 10 bar and used to rapidly dissolve the frozen sample.

4.2.3 *Ex Vivo* Isolated Perfused Lung Studies

4.2.3.A. Isolating Perfused Lungs

The procedure for excising and perfusing the lungs is similar to that described in the previous chapter. In brief, animals were anesthetized with intraperitoneal (IP) pentobarbital, tracheostomy was performed, and 200 U heparin was administered via the tail vein. The lungs were degassed[5,6] by ventilating with pure O_2 for 10 minutes to remove any residual N_2. The trachea was then sealed, and a thoracotomy was performed to access the heart. The pulmonary artery was cannulated via the right ventricle for perfusion. Once sealed, the lungs were rapidly excised and placed in a 20 mm NMR tube. Lungs were then perfused at 10 mL/min with a modified Krebs–Henseleit buffer: 119 mM NaCl, 25 mM $NaHCO_3$, 1.3 mM $CaCl_2$, 1.2 mM $MgSO_4$, 4.7 mM KCl, 10 mM glucose, 2 mM lactate, 0.2 mM pyruvate, and 3% (w/v) fatty-acid-free bovine serum albumin (BSA, Fisher Bioreagents). The perfusate was passed through an oxygenating column under a constant flow of 1 atm 95:5 O_2 /CO_2 and warmed via passage through water-jacketed tubing. The CO_2 concentration in the oxygenating column was chosen to maintain constant perfusate pH during oxygenation, although periodic adjustment with 1 N HCl or NaOH was needed to maintain a physiological value of 7.4±0.05. The lung was perfused at constant flow throughout the experiment. The temperature of the perfusate in the NMR tube was continuously monitored and maintained at 36.5±1 °C.

4.2.3.B. Administration of HP [1-^{13}C]Pyruvate for *Ex* Vivo Spectroscopy

This 4.0mL sample from the polarizer was further diluted in 6.0 mL oxygenated Krebs–Henseleit buffer (without BSA) to yield a neutral, isotonic solution of 32 mM [1-^{13}C] pyruvate (in the studies described in the previous chapter, a much lower final concentration of [1-^{13}C] pyruvate was used). This solution was injected into the perfusate line at 10 mL/min in lieu of the steady-state perfusion buffer. After the 60 s required to inject the HP solution, lung perfusion was restored.

4.2.3.C. *Ex Vivo* NMR Spectroscopy for Isolated Perfused Lungs

All MR spectra and images were obtained using a 9.4 T vertical bore magnet (Varian, Palo Alto, CA) equipped with a gradient insert (Resonance Research, Billerica, MA) and a 20 mm 1 H/broadband probe (Doty Scientific, Columbia, SC). After insertion into the bore of the magnet, the sample was tuned, matched and shimmed to a linewidth of about 40 Hz. This process required approximately 20 min. Immediately following, the lung was ^{1}H imaged (10 axial 2 mm slices, field of view = 30 × 30 mm) for positioning and to ensure the integrity of the organ and the absence of edema. Next, a whole-lung, averaged ^{31}P spectrum was acquired to assess energy status (repetition time T R = 1 s, nominal flip-angle $\alpha = 60°$, acquisition time AT = 200 ms, spectral width SW = 100 kHz, 512 averages). The probe was then tuned to ^{13}C and the perfusate was temporarily replaced by the HP solution. Low flip-angle spectra were acquired for the several-minute duration of the HP signal (T R = 1 s, nominal $\alpha = 10°$, AT = 800 ms, SW = 20 kHz, 300 individual spectra acquired). Following the ^{13}C spectroscopy, another averaged ^{31}P spectrum was acquired in order to evaluate changes in ATP status due to the HP compound injection. In six instances, the entire series was then repeated (^{31}P spectrum, HP spectrum series, ^{31}P spectrum) after a 1 h delay required to hyperpolarize another pyruvate sample. This repetition was performed to evaluate the stability and reproducibility of the lung and its metabolic activity.

4.2.3.D. Quantification of NMR Spectra from *Ex Vivo* Perfused Lung Studies

^{31}P spectra were least-squares fit to 13 Lorentzian peaks, allowing the individual peak heights and common peak width to vary freely. The peak frequencies were kept fixed; peak identities (ppm chemical shifts relative to PCr; see figure 4.4 caption for acronyms) were PME (6.70), P_i (5.08, 4.32), GPC (3.03), GPE (2.24), PG (1.80), PCr (0.00), γ-NTP (2.36), α-NTP (7.52), diphosphodiester/NAD(H) (8.18, 9.68, 11.49, 13.30), and β-NTP (16.13). Fit quality was found to improve substantially when including three additional peaks of fixed position (3.5, 4, and 10 ppm) and width (3, 8, and 4 ppm, respectively) to account for contributions from unresolved ^{31}P species. We note that the region containing GPC, GPE, and PG is poorly resolved and likely contains other phosphodiesters as well. Although consistent with previous measurements[7,8] the number and identity of resonances is uncertain.

^{13}C spectra were least-squares fit to five Lorentzian peaks, allowing the individual peak heights to vary. The peak positions and widths were set using an initial free fit (amplitude, width, and position) to the average of all spectra with signal-to-noise ratio > 30. The peaks were identified as pyruvate, alanine, pyruvate hydrate, lactate and bicarbonate, with ppm chemical shifts relative to pyruvate of 0.00, 5.68, 8.42, 12.26 and 9.98, respectively. Additional peaks representing natural abundance nuclei or impurities were not included in the fit. All peak fitting was done using custom software written in MATLAB (Natick, MA).

4.2.3.E. Histological Evaluation (*Ex Vivo* Study)

Immediately after the final MRS acquisition, nine of the lungs (three each of control, day 7, and day 21 inflammation) were prepared for histological evaluation. The steady-state perfusion buffer was replaced by a 10% formalin solution and perfusion was continued for

1 min, after which the lungs were submerged in 10% formalin for 5–7 days and subsequently embedded in paraffin. Due to the uncertainty of their response to re-inflation, the lungs were not inflated prior to fixation. Although inflating the lungs would have made the gross structure easier to visualize, we do not expect that it would have affected our ability to count the cells of interest. 25 transverse 5 μm sections were cut from each lung (five groups of five contiguous sections spaced by 2 mm). Previous studies have indicated that neutrophils and macrophages represent the bulk of the inflammatory response to bleomycin-induced injury in rats (18,19). Sections from each group were therefore stained with hematoxylin and eosin (H&E), and with anti-neutrophil elastase antibody (ab21595, abcam, Cambridge, MA) or CD68 antibody (SPM130, Santa Cruz Biotechnology, Dallas, TX), which have previously shown reactivity to rat neutrophils and macrophages, respectively. Because of significant non-specific binding, only the H&E sections were used to evaluate the extent of neutrophil and macrophage infiltration.

An experienced lung pathologist blindly examined the five whole lung sections from each sample and assigned a grade from 0 to 4 with respect to neutrophils, macrophages, lymphocytes and organizing pneumonia (OP) foci, based on the number of cells or sites present. No distinction was made among lymphocyte types. For each cell type, lungs with minimal cell density were assigned a grade of 0, whereas lungs with severe and widely distributed inflammatory cells were assigned a grade of 4. The grading scale was relative for each type of cell. For example, a section that scored a grade of 4 for both neutrophils and macrophages had a much greater number of neutrophils than macrophages. Each lung was then assigned a score for each cell type equal to the average rating among the sections.

4.2.4 *In Vivo* MR Imaging Studies

4.2.4.A. Administration of HP [1-^{13}C]Pyruvate for *In Vivo* Imaging

4 mL/kg (~1.3mL) of the HP solution was then transferred into a syringe and injected into the animal via a tail vein catheter within 10 s of dissolution. The injection lasted 6 s and was followed by a 250μL saline flush. The scan started 18 s after beginning injection.

4.2.4.B. *In Vivo* Magnetic Resonance Imaging

Animals were anesthetized with isoflurane (2%) on 100% O_2 (1.5mL/min) and a tail vein catheter was placed before starting the imaging session. MRI imaging was performed on a 4.7T horizontal bore magnet (Inova 200, Varian Inc, Palo Alto, CA) using a 72mm dual tuned ^{1}H/^{13}C quadrature transmit/receive birdcage coil (Polarean Imaging Plc., Cleveland, OH). A T_1-weighted coronal 1H GRE of the lungs was acquired for positioning the slice-selective CSI with HP [1-^{13}C] pyruvate. The acquisition parameters were: TR/TE = 80/1.55 ms, FOV = 60x60x2 mm^3, matrix = 128x128, slices = 16, averages = 16, flip-angle = 20^o, scan time = 2:03 min. The lungs were manually shimmed using the proton channel to a proton linewidth of about 130Hz using a 15mm slice-selective pulse acquire sequence. HP [1-^{13}C] pyruvate chemical shift imaging (CSI) was performed immediately after shimming.

HP ^{13}C CSI was performed using a spiral 2D slice-selective phase-encoded free-induction decay chemical shift imaging (FID-CSI) sequence (Figure 4.1A). The k-space center ($k_{x,y} = 0$) was re-acquired at every 11th acquisition to de-blur the point spread function (PSF) of the spectra (Figure 4.1B). The 15mm slice was positioned on the lungs superior to the dome of the diaphragm. The scan was started 16 s after the start of the HP injection (see above). The acquisition parameters were: TR/TE =35/0.5 ms, FOV = 45x45x15 mm^3, matrix size = 16x16, spectral width = 4 kHz, spectral points = 128, flip-angle = 9°, scan time = 9s. The matrix size and flip angle were optimized based on the available hyperpolarization, such that enough residual signal was left after each excitation (256 for our selected parameters).

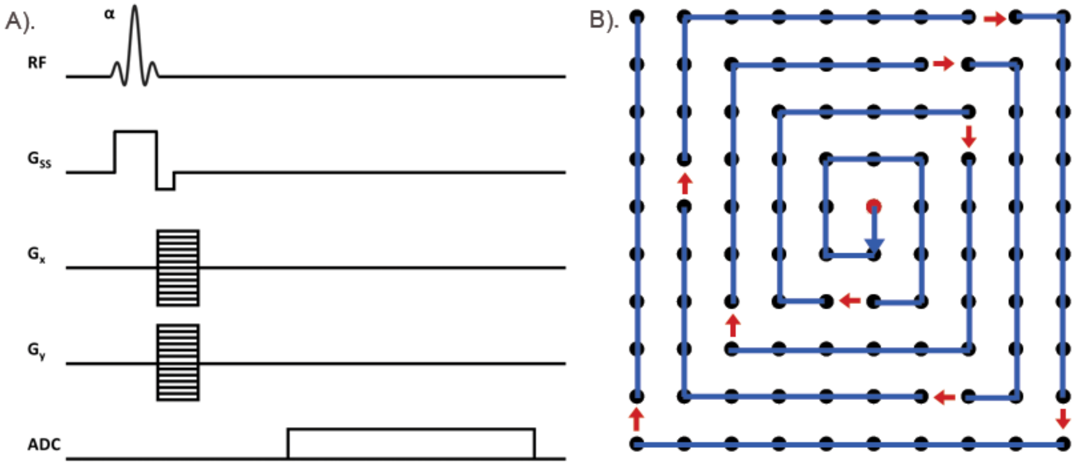

Figure 4.1: (A) Pulse sequence diagram for the FID-CSI sequence for in vivo rat imaging. The k-space was traversed using a spiral trajectory, so Gx and Gy are not the traditional frequency and phase encoding directions. **(B)** The k-space was traversed from the lower k-space to the higher k-space ('spiral out'). Unlike a conventional trajectory, the kx,y=0 was re-acquired every 11th acquisition and then the outward trajectory continued (shown as breaks with red arrows). The repeated kx,y=0 acquisitions were used to deblur the reconstructed image.

4.2.4.C. MRSI Data Processing

All data were processed offline using custom routines in MATLAB 2017b (MathWorks, Natick, MA, USA). The free-induction decays (FID) were line-broadened by 30 Hz and then Fourier transformed to obtain the spatially resolved spectra. The periodic acquisition of the k-space center ($k_{x,y} = 0$) was used to de-blur the spectra via amplitude normalization, thereby providing improved localization. The resultant spectra were then baseline-corrected (fourth-order polynomial), local zero-order and global first-order phase-corrected; the lactate and pyruvate peaks were then fit to Lorentzian functions. The processed carbon-13 spectra were overlaid on the corresponding proton images of the thorax and voxels were manually selected from the native lung, transplanted lung and heart for regional quantification. Voxels overlying large vessels in the lung parenchyma were excluded from selection. As the number of selected voxels from each region varied, the average pyruvate, lactate and lactate-to-pyruvate was calculated by summing the respective spectra and dividing by the number of voxels. The fitted pyruvate and lactate spectra were also used to generate corresponding metabolic maps, which were linearly interpolated to match the voxel size of the underlying proton images for clearer visualization.

4.2.5. Statistical Methods

Statistical significance was tested using analysis-of-variance (ANOVA), followed by Tukey's HSD post-hoc test across the different cohorts. In order to determine whether there was any evidence that the two measurements made in the same lung were systematically different, repeated measures ANOVA was performed in the subset of six lungs for which ^{13}C spectroscopy was repeated as well as the 18 lungs in which repeated ^{31}P spectroscopy was performed. In order to determine the extent of direct relationships between inflammation as measured using ^{13}C and ^{31}P spectroscopy, as well as between ^{13}C spectroscopy and inflammatory cell counts, simple correlations were calculated across all measurements in which both metrics were available. All statistical analyses were performed using the R software. R is an open-source project that is distributed under the GNU General Public License (copyright 2007 Free Software Foundation)

4.3. RESULTS

4.3.1. *Ex Vivo* ^{13}C Spectroscopy

Figure 4.2 displays a representative series of individual spectra from an inflamed lung.

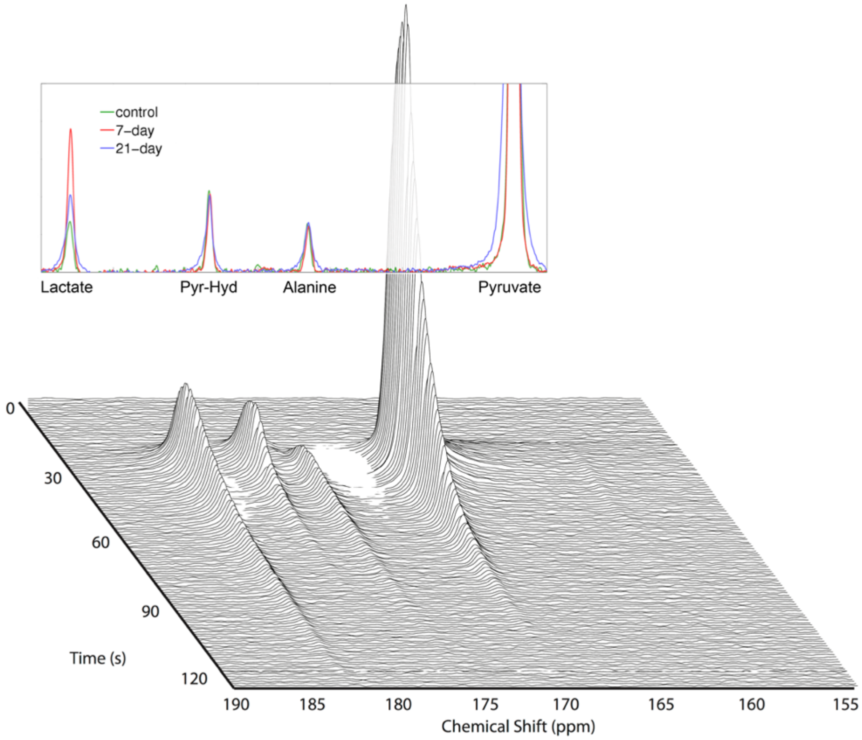

Figure 4.2: A time-series of stacked C spectra (bottom) shows the appearance of pyruvate and pyruvate hydrate signals, followed by lactate and alanine. The unidentified peaks are impurities from the HP pyruvate sample and not indicative of biological activity. Signal level evolution over time is very similar between control and inflammatory groups, with the exception of the lactate signal, which is significantly increased in the diseased cohort. This can be seen in the three overlaid spectra, which are averages of the ten spectra between 20 and 30 s after the end of the HP injection (top). The day 7 inflammatory model spectrum (red) is visually indistinguishable from the day 21 (blue) and control (green) spectra, except at the position of the lactate peak.

As with all such series, peaks corresponding to [1-^{13}C]pyruvate and [1-^{13}C]pyruvate hydrate appeared first, followed within a few seconds by [1-^{13}C]lactate and [1-^{13}C]alanine peaks. All peaks were clearly distinguishable and quantifiable for a period of approximately 2 min after the first appearance of HP signal. Additional peaks corresponding to natural abundance ^{13}C, impurities and ^{13}C-bicarbonate, though smaller, were also reliably quantifiable. In the Figure 4.2 inset, we overlaid spectra acquired 20–30 s after the end of the HP injection in control, day 7 and day 21 inflammatory model animals. As expected, pyruvate, pyruvate hydrate and alanine signal levels were very similar, but the integrated lactate signal of the inflammatory model exceeded that of the control animal by a factor of approximately three.

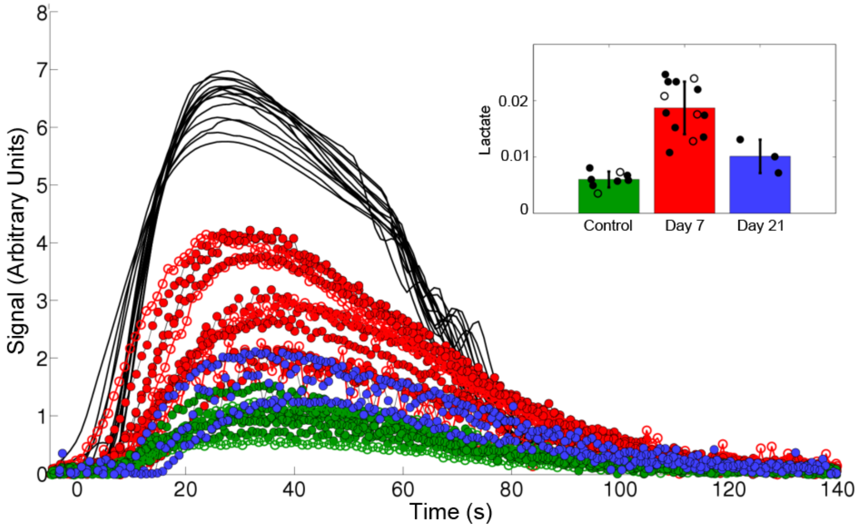

Figure 4.3: The full time-series of fit peak areas, in which the day 7 inflammatory group lactate peaks exceed those of the control group at all times and by an average factor of 3.3. Note that the signal amplitudes are scaled such that the sum of pyruvate areas Σp(t) = 1, and times are shifted such that each injection is centered around t = 50. The inset bar graph shows the mean and average integrated lactate signal in the control (green), day 7 (red), and day 21 (blue) groups. In both plots, solid circles represent data acquired on the first HP ^{13}C injection and open circles represent data acquired on the second HP ^{13}C injection. When only first injections are considered, the day 7 group is statistically distinguishable from the other two groups ($p = 0.0003$). Although only six studies were repeated, no systematic change is evident (visually or by repeated measures ANOVA) between the groups due to the time delay between the two HP agent injections.

Figure 4.3 displays the result of fits to each spectrum of the timeseries in each subject. Although the observed lactate signal is more variable among the inflammatory model cohort, each of the day 7 inflammatory model lungs exhibited a greater observed lactate signal at all times than any of the control lungs; integrated lactate signals in the day 7 inflammatory group exceeded those of the control group by a factor of 3.1 on average (if repeated measurements in the same lung are excluded from the analysis, the day 7 group’s signals are higher by an average factor of 3.3). Lactate signal levels in the day 21 cohort were midway between the control and day 7 groups, exceeding the control group by a factor of 1.8 on average. Means and standard deviations of all three groups are summarized in the Figure 4.3 inset.

4.3.2. Ex Vivo ^{31}P Spectroscopy

Figure 4.4 shows two averaged ^{31}P spectra representing normal (green) and day 7 inflammatory (red) lung cohorts. Eight distinct ^{31}P-containing species can be discerned[7–10], of which only phosphoglycans and phosphodiesters (primarily GPC and GPE) differ significantly between the normal and inflamed lung; on average, these are elevated by a factor of 2.5 in inflammation. Some inconsistency in the fit values arises from limited signal-to-noise ratio in the ^{31}P spectra. Some inconsistency in the position and width of the P_i peak is seen as well, which may indicate variability in tissue pH despite the narrow range of perfusate pH.

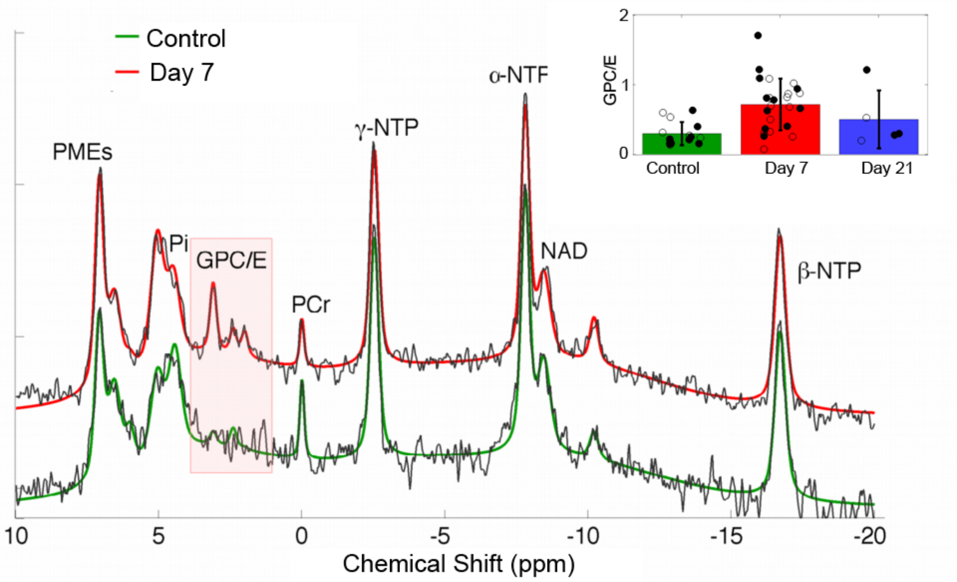

Figure 4.4. Sample P spectra from control (black with green fit) and day 7 (black with red fit) inflammatory model lungs show very similar patterns of high energy phosphates (NTP), inorganic

phosphate (Pi), phosphomonoesters (PME) and phosphocreatine (PCr), but differ in a set of three peaks consistent with the known chemical shifts of the phosphodiesters glycerophosphocholine and glycerophosphoethanolamine (GPC/E) and, slightly upfield, phosphoglycans (PG). The figure inset shows a comparison of the three cohorts' summed GPC/E + GP fit peak areas. Cohort means and standard deviations are summarized by the corresponding black bars, and individual GPC/E + GP peak areas appear as filled/open black circles for first/second injections. Note that the individual peak areas are offset randomly in the horizontal direction for better visibility. Only the GPC/E/PG peaks differ between the groups; this difference is highly significant when comparing control and day 7 bleomycin groups ($p < 0.01$ whether all points or only first injections are compared). The day 21 group was not significantly different from either of the other groups. All amplitudes are scaled to the corresponding Pi peak area.

4.3.3. Histology

Representative H&E sections from the control, day 7 and day 21 inflammatory cohorts appear in Figure 4.5. These sections were chosen to highlight the visually apparent trend of dramatically elevated neutrophils at day 7, which were partially resolved by day 21, and of progressively increasing macrophage count from day 7 to day 21. This trend can be seen more clearly in the inflammatory cell scores from each lung (Table 4.2).

	Control	Day 7	Day 21
Neutrophil	0.6	2.7	1.0
	0.4	2.8	0.8
	0.8	1.4	2.8
Macrophage	0.4	1.4	3.2
	0.4	1.8	2.8
	0.6	2.2	3.2
Lymphocyte	0.4	0.6	1.2
	0.0	0.6	0.4
	0.0	1.0	0.4

Table 4.2: Average neutrophil, macrophage and lymphocyte score for each of the nine animals examined histologically.

On average, the neutrophil scores at 7 and 21 days exceeded the control scores by factors of 3.8 and 2.6, respectively; the inflammatory macrophage scores exceeded the control scores by respective factors of 3.9 and 6.6. There are some transient OP foci present in day 7 sections, but most of these foci are resolved by day 21. The day 21 sections have minimal OP foci but are characterized by protein deposits (Figure 4.5) that can signify fibrotic remodeling, and which were only minimally apparent at day 7.

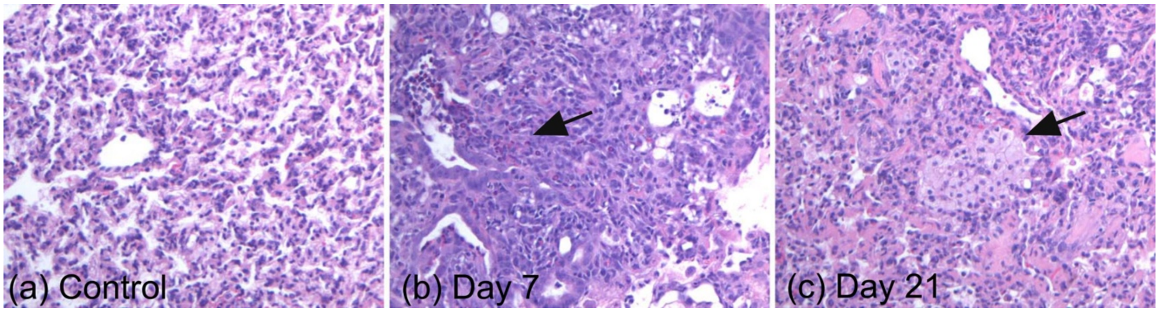

Figure 4.5: Representative histological sections from control lung (a), day 7 post-bleomycin lung (b) and day 21 post-bleomycin lung (c). The sections were chosen to highlight the common characteristics of each group – in particular, the elevated neutrophils at 7 days and elevated macrophages at 21 days. A more objective evaluation of inflammatory cell density can be seen in Table 1. Note that the alveolar structure is somewhat distorted in all of the sections because the lungs were collapsed during the NMR studies and were not reinflated for histology.

Notably, the day 21 cohort contained one subject that was visually similar to the day 7 cohort with respect to both active neutrophilic inflammation and relative lack of fibrosis. This subject also exhibited ^{13}C and ^{31}P spectroscopy results that were elevated with respect to both control and the other day 21 lungs, but that were consistent with the day 7 cohort (Figures 4.2 and 4.3).

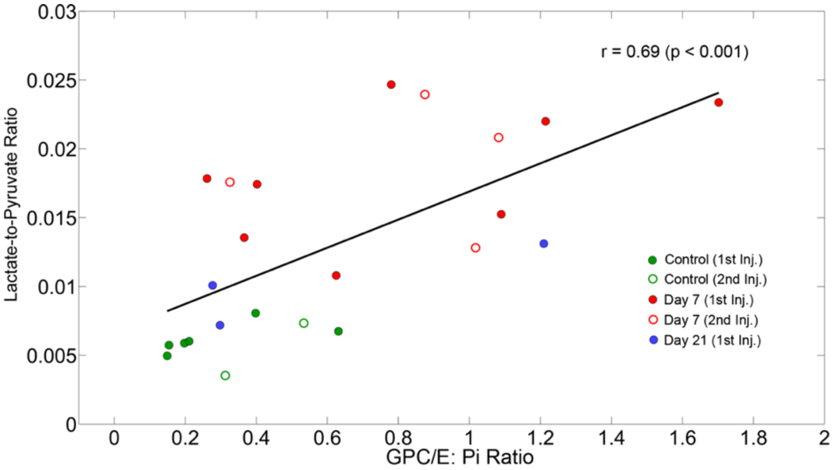

Figure 4.6: Among all lungs, the increase in lactate produced by inflamed lungs is significant (approximately a factor of 3.3 at day 7 and a factor of 1.8 at day 21) and correlates moderately well to the GPC/E peak increase observed using time-averaged 31P spectroscopy. In the figure, the

cohorts are distinguished as control (green), day 7 (red) and day 21 (blue). First and second injections in the same lung are distinguished as closed and open circles, respectively.

Applying ANOVA to the 16 first ^{13}C measurements revealed that the three experimental groups are characterized by significantly different means (F(2,13) = 15.9, p = 0.0004). Further analysis using the Tukey HSD test was performed to determine whether significance exists between the cohorts. The mean lactate labeling was significantly higher for the day 7 bleomycin group than for both control ($p < 0.001$) and day 21 ($p = 0.03$) groups; on the other hand, we could not show a significant difference between the day 21 bleomycin and the control group ($p = 0.33$). Although with less significance, the ^{31}P spectroscopy data yielded identical results in post-hoc analysis. Applying repeated measures ANOVA to the six repeated ^{13}C spectroscopy measurements in the two groups (two controls, four day 7 bleomycin) showed that there was a significant difference between the means of the two groups (F(1,4) = 193.4, p = 0.0002), and the hypothesis that the repeated ^{13}C measurements are characterized by the same mean within experimental repeats was not rejected ($p = 0.88$). Similarly, applying repeated measures ANOVA among the 18 repeated ^{31}P spectroscopy tests in three groups (six control, ten bleomycin day 7, two bleomycin day 21) shows that there is a significant difference among the means of the three groups (F(1,4) = 4.27, p = 0.036). Similar to the ^{13}C data, there was no difference in the repeated experimental measurements within groups ($p = 0.26$). There is no statistical evidence for any interaction between the experimental group and measurement number (p = 0.84 and 0.16 for ^{13}C and ^{31}P spectra, respectively). Figure 4.6 summarizes the relationship between elevated GPC/E levels and elevated lactate production within and between study groups.

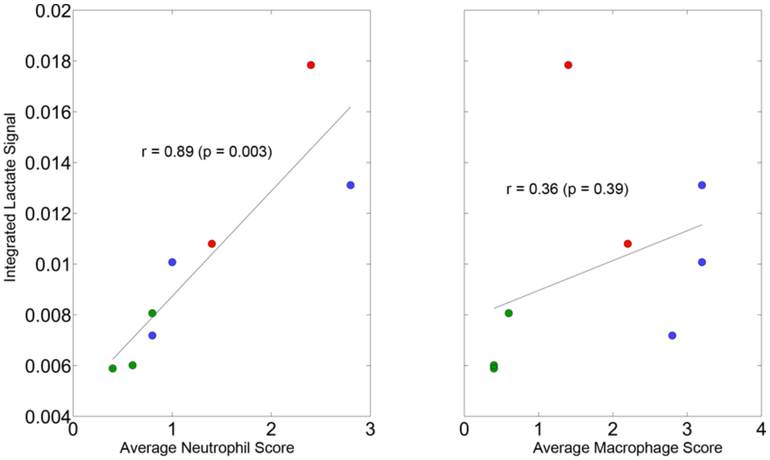

Figure 4.7: Among all lungs for which histology was performed, the integrated lactate signal (normalized to integrated pyruvate signal) correlates well with the average neutrophil score as graded by a pulmonary pathologist. The correlation to the average macrophage score was not statistically significant. Scores were assigned from 0 (normal cell count) to 4 (severe and widely distributed inflammatory cells) based on a blinded, qualitative assessment of five H&E sections distributed throughout the lung.

Across all study animals, a significant correlation was found ($r = 0.69/0.74$ if all/first injections are analyzed; $p < 0.001$ in both cases). Figure 4.7 shows the correlation between the measured lactate signal and the histologically determined neutrophil and macrophage scores for the eight subjects for which both measures were available. The correlation coefficient is statistically significant ($r = 0.89$, $p < 0.005$) when lactate signal and neutrophil score are compared, but is not significant ($r = 0.36$, $p = 0.39$) when lactate signal and macrophage score are compared.

4.3.4. Reconstructing CSI Images from *In Vivo* Studies

Having demonstrated the feasibility of HP [1-^{13}C]pyruvate imaging for *ex vivo* studies in the bleomycin-induced inflammation model, a set of *in vivo* studies using the spiral FID-CSI were subsequently carried out to determine the translatability of our technique.

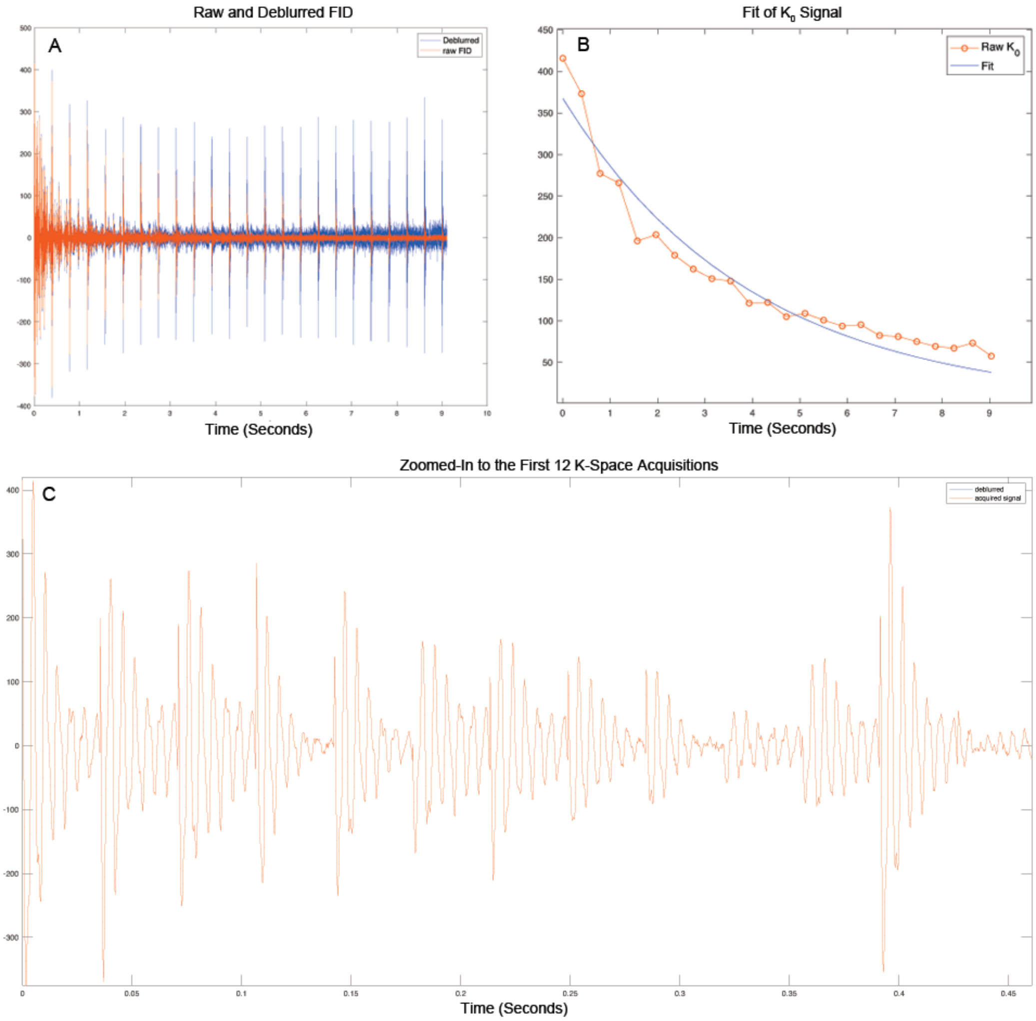

Figure 4.8: (A). The raw (orange) and de-blurred (blue) FID of the spiral CSI sequence. The correction was based on the exponential fit at k_0 as seen in (B). (C) The first 11 k-space acquisitions as well as the repeat acquisition of k_0 can been seen in this zoomed in sub-region of the FID.

Figure 4.8A shows a representative raw FID (orange) alongside the de-blurred FID (blue) based on the exponential fitting of the repeated $k_{x,y=0}$ acquisitions, as seen in Figure 4.8B. Figure 4.8C is zoomed-in to the first 12 acquisitions of the acquired FID. The signal at $k_{x,y=0}$ has the largest SNR contribution to the final Fourier transformed image.

The FID was processed as described in Methods section 3.2.4.C to generate a 16x16 spectroscopic image of the lungs (Figure 4.9A). The highest signal is observed in the heart, followed by the lungs, with some signal apparent in the peripheral muscles as well.

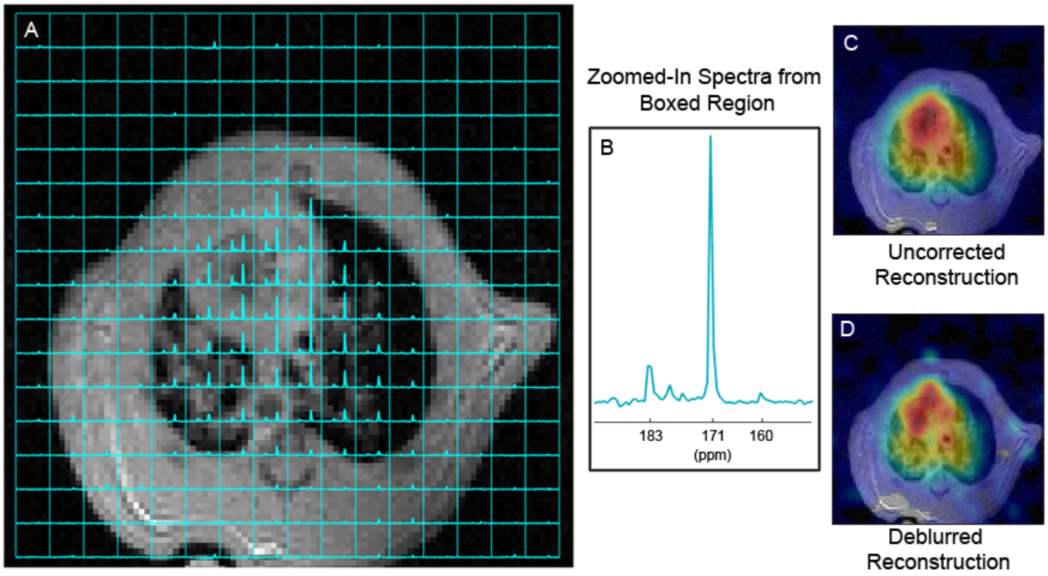

Figure 4.9: (A): A representative carbon-13 MRSI overlaid on a proton image from a day 7 inflamed animal. The inset (B) shows the signal from one manually selected voxel in the heart. The three peaks that can be quantified are lactate (183 ppm), pyruvate (171 ppm) and bicarbonate (160 ppm). The uncorrected (C) and de-blurred (D) reconstructed images can be seen, with the improved resolution of the latter easily observable in the heart.

Figure 4.9B shows the spectrum from a single voxel in the heart. The pyruvate is centered at 171ppm and the lactate peak can be observed at 183 ppm; a small bicarbonate peak at 160ppm can also be observed. The latter peak is not typically found in the lungs, most likely due to both a lower pyruvate signal and the lower metabolic activity of healthy lungs. Figures 4.9C and 4.9D demonstrate the difference between an uncorrected and de-blurred reconstruction. We can qualitatively observe the higher resolution of the de-blurred image: the uncorrected reconstruction shows a blurry pyruvate distribution over the entire heart, while the pyruvate distribution is resolved into two regions in the corrected version, each of which is centered over a separate heart chamber.

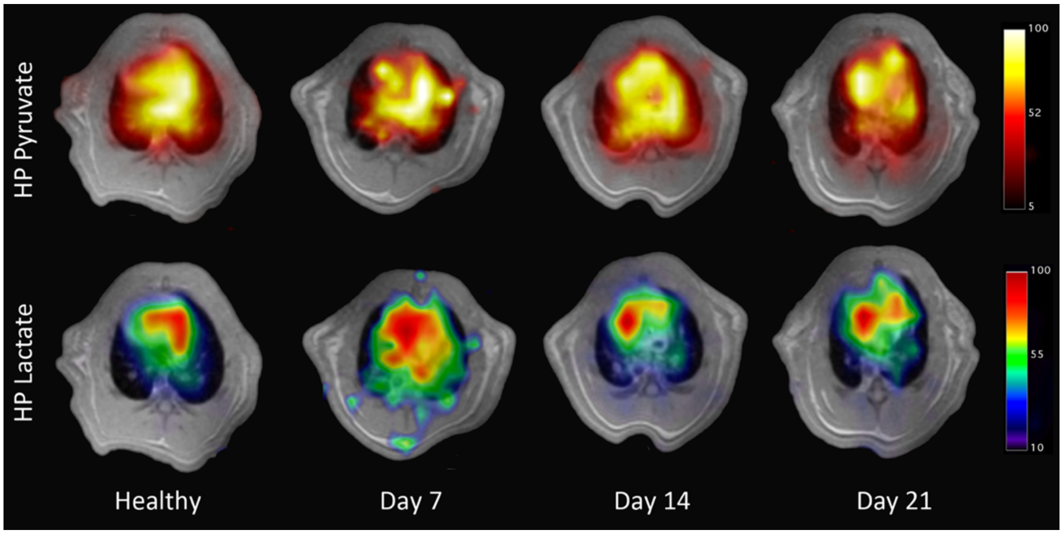

Figure 4.10: Representative HP pyruvate (top) and HP lactate (bottom) maps for the healthy, day 7, 14 and 21 cohorts. The pyruvate distribution is similar across all four cohorts; however, an increased lactate distribution can be observed on day 7. The quantified lactate-to-pyruvate values can be observed in Figure 11.

As described in Methods 3.2.4.C, the fitted pyruvate and lactate spectra were used to generate their respective metabolic maps (Figure 4.10). The lactate-to-pyruvate ratio of the heathy, day 7, day 14 and day 21 cohorts were 0.15±0.08, 0.25±0.8, 0.16±0.6 and 0.11±0.06, respectively. The day 7 cohort was significantly different than all three other cohorts ($p < 0.001$ in all cases). The day 21 cohort was significantly different than the control ($p = 0.03$) and day 14 ($p = 0.003$) cohorts. The control and day 14 cohorts were not significantly different ($p = 0.71$). (Figure 4.11).

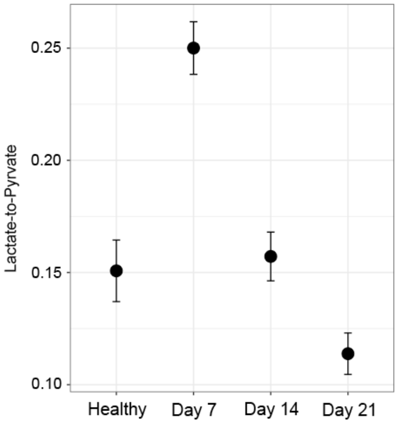

Figure 4.11: Mean lactate-to-pyruvate ratios for all four cohorts from the *in vivo* MRI study.

4.4. Discussion

The main finding of this work is that a common experimental model of lung inflammation affects the metabolic activity of the lung such that the overall apparent lactate labeling is increased substantially 7 days post-induction. Activity largely returns to baseline 21 days post-induction, although the smaller sample size at the latter timepoint means that there is a possibility that activity remains somewhat elevated. Although the magnitude of change was different between the *ex vivo* and *in* vivo models, both models showed this trend. We believe that the observed increase at 7 days is indicative of direct uptake and metabolism of pyruvate by inflammatory cells—primarily neutrophils—which have infiltrated the lung in response to the bleomycin insult.

Several other explanations are possible, however, all of which we will discuss individually. First, it is known that other conditions may affect apparent LDH activity. In a previous study[11], for instance, we showed that temporary hypoxia can increase lactate labeling in the perfused lung by a factor similar to that observed here, most likely due to the increased intracellular lactate pool size and consequent increase in oxidized nicotinamide adenine dinucleotide (NAD^+) reduction rate. While it is possible that damage to the lung (e.g. fibrosis or emphysema-like tissue degradation) may adversely affect gas transport and tissue oxygenation, the primary means of oxygenation in this study is via the oxygenated perfusate. Any tissue damage that prevents adequate contact with the perfusate would also hinder access to the HP agent delivered through the same flow path, making HP lactate signals unobtainable in these regions. Furthermore, the hypoxic lung exhibited a distinctively low PCr and NTP signal in ^{31}P spectroscopy when studied previously[11]—distinctive changes that were not observed in this study.

Another possible cause of increased lactate signal is a change in the uptake of pyruvate by the lung tissue. Although transporter activity may be affected by energy status, pH and other factors of the extra- and intracellular environment, no alteration in transport was detected in the inflammatory model lungs[12]. We note that HP alanine signal is not significantly increased in the inflammatory model animals; if pyruvate uptake by pneumocytes were increased sufficiently to explain the increased lactate signal, we would expect a measurably increased rate of transamination in these cells as well. It is possible that pyruvate uptake and transamination were both significantly and inversely altered such that label transfer to the alanine pool remained unchanged. However, we would consider this an unlikely coincidence.

Third, it is possible that the increased apparent LDH activity observed arises in part from extracellular LDH. Although intracellular in healthy tissue, LDH is known to be present in substantial concentration in the extracellular space in regions experiencing cell death; tests of bronchoalveolar lavage fluid LDH activity are a common non-specific indicator of tissue damage[13,14]. In this case, however, the persistence of the lactate signal (along with pyruvate and alanine, but in contrast to pyruvate hydrate) is a clear indication of its intracellular origin; extracellular signal would be washed out rapidly once ordinary perfusion was restored, as is the case for the extracellular pyruvate hydrate and other impurities (Figure 4.2). The continued linear increase of the lactate/pyruvate ratio during this washout period most likely indicates the intracellular rate constant for forward LDH activity, although it may also reflect the efflux of pyruvate from the lung epithelium—a process which has been shown to be rapid and dynamic[15].

A final possible cause of increased lactate signal in the inflammatory model lungs is the change in redox status of the lung tissue due to reactive oxygen species originating from the respiratory burst phase of neutrophil activity. These compounds may interact directly with the NADH/NAD + redox couple, indirectly through modulation of glutathione-mediated inhibition of LDH, or through a variety of other inflammatory signaling pathways[16,17]. Although this possibility cannot be ruled out based on the studies described here, it seems more likely that the increased lactate production arises from the rapid glycolysis of inflammatory cells. With respect to the similarly increased ^{18}FDG-PET signal in inflammation, autoradiographic studies[18–20] have confirmed that the source of the increase is primarily neutrophilic uptake rather than an inflammatory-mediated change in lung tissue activity, and that the significantly greater glycolytic rate of neutrophils (11) is sufficient to overwhelm signal originating in the lung epithelium[1]. Given that the neutrophil glycolytic rate is not limited by LDH activity[21], we expect that similar dynamics are responsible for the substantial increase in lactate signal observed here.

It is possible that increased macrophage density is responsible for some of the lactate signal as well. However, the results shown in Figure 4.6 provide evidence that the increased lactate labeling is primarily neutrophilic in origin. As seen in Table 1 (and described previously[22]), neutrophil count in the bleomycin rat model peaks after approximately 7 days before re-approaching baseline 21 days after insult. In contrast, macrophage count continues to rise, peaking between 14 and 21 days. The neutrophil count time course is in qualitative agreement with the observed lactate signal time course (which is significantly higher at 7 days than at 21 days), and this agreement is reflected in the significance of the corresponding correlation plot in Figure 4.6.

The degree of lactate increase is also fairly consistent with estimates of cell populations and metabolic characteristics available from previous *ex vivo* or *in vitro* studies. Pyruvate uptake and transformation to lactate in the normal lung is likely dominated by type II pneumocytes due to both their rapid and highly glycolytic metabolism and large population (~5.5×10^7 cells per lung, double that of type I pneumocytes and about six times that of alveolar macrophages), as well as conclusions based on cell morphology and oxygen uptake experiments[23–25]. Assuming, as demonstrated previously[26], that the lavage cell counts are representative of inflammatory cell sub-populations, bleomycin model lavage results suggest that the total inflammatory cell population increases from baseline by a factor of approximately six at 7 days and a factor of three at 21 days (Fig. 6 of Ref[22]), and that this increase consists almost exclusively of neutrophilic and macrophagic components[27,28]. Previous studies have also shown that the type II pneumocyte population is slightly but not substantially diminished in this model[29–31]. Although the degree and type of inflammatory cell activation is not known, we may approximate the expected relative contribution to HP lactate signal by measured lactate production rates in cell culture; published results show that per cell lactate production of isolated alveolar macrophages (61 nmol/h/10^6) and neutrophils (53 nmol/h/10^6) are approximately equal, and exceed that of type II pneumocytes by approximately a factor of three (17 nmol/h/10^6 cells[23,32,33]). These general considerations suggest that we should expect HP lactate produced in the day 7 and day 21 bleomycin lungs to exceed that of the control lungs by factors of approximately 2.7 and 1.7, respectively. These values are comparable to the observed factors of 3.1 and 1.8, demonstrating that our explanation is at least plausible given what is known about cell populations and metabolic activity.

The correlation between GPC/E levels as derived from ^{31}P NMR and lactate signal is another indication that HP lactate imaging provides information about the extent and location of lung inflammation. It has been previously demonstrated that granulocytes contain very high levels of the phosphodiesters GPC and GPE, PG and related (and spectroscopically indistinguishable) compounds[34,35]. We therefore believe that the GPC/E levels of Figure 4.4 are indicative of elevated inflammatory cell count characteristic of inflammation, and that the strong correlation with lactate signal seen in Figure 4.5 provides evidence that both spectroscopic measures are further elevated in more severe inflammation.

However, PET studies have also revealed the need to interpret the signal increase carefully by showing that the period of most rapid neutrophil energy metabolism does not correspond to the respiratory burst phase, but rather to cell migration and polarization[36]. Because the former phase of neutrophil activity and the associated release of reactive oxygen species is likely responsible for the lung tissue damage associated with inflammatory exacerbations[37,38], it is possible that the period of maximum deleterious effect on the lung is not as conspicuous as the initial phase of neutrophil invasion when using either HP [1-^{13}C]pyruvate MRI or ^{18}FDG-PET.

A secondary finding of this study is that no systematic difference was observed between repeated measurements of inflammation in the same model lung using either ^{13}C or ^{31}P spectroscopy. Although the number of repeated ^{13}C spectroscopy measurements was limited, it is clear that the effect of repeated or delayed measurement on the lung is much smaller than the between-group differences. This serves as an indicator of model stability during perfusion and suggests that small variations in timing do not affect the results of the experiment.

As the *ex vivo* study was limited to two time-points (7 and 21 days), further investigation and comparison to histological markers will be required to relate its findings to more established measures of lung inflammation. In particular, we emphasize the highly dynamic nature[39] of cell counts and metabolic rates during acute inflammation. Alveolar macrophages and neutrophils are known to take on a greatly increased glycolytic rate during phagocytosis or when exposed to even the lowered O_2 tension of the healthy lung[40]. Thus, the quantitative estimate of expected metabolic activity in inflammation is intended only as a plausibility argument based on cell populations, not as direct evidence for the source of the observed signal.

Furthermore, although the perfused lung model chosen has been shown to recapitulate many metabolic features of the *ex vivo* lung, the utility of this technique for localizing and grading lung inflammation relies in part on a low baseline activity of the healthy tissue. The lung has previously been demonstrated to play a substantial role in maintaining glycolytic intermediate balance in the blood, which suggests that pyruvate and lactate transport and interconversion in the healthy organ may depend on whole-body metabolic activity, dynamical perfusion effects, feeding and exercise status.

This can be seen by the difference in magnitude in lactate labeling between the *ex vivo* and *in vivo* studies. In the *ex vivo* study, lactate labeling was increased by a factor of 3.1 and 1.8 on days 7 and 21, respectively, compared to the baseline. In comparison, the lactate labeling was increased by a factor of 1.7 on day 7 but decreased by 0.7-fold on day 21 compared to baseline in the *in vivo* study. As the same induction model was used, this change may be due to a number of factors. Firstly, the concentration of HP [1-^{13}C] pyruvate in the *ex vivo* study was much higher than that used in the *in vivo* study. A final concentration of 32 mM was used in the former studies, whereas in the latter studies the effective bolus concentration was about 1.1mL of 80mM pyruvate diluted by the blood volume. Based on estimated blood volumes[41], this would be an approximate concentration of 4-5 mM HP [1-^{13}C] pyruvate. Although both concentrations are superphysiological[42], the lower dosage was used to minimize injected blood volume, acidosis, and signal saturation given the SNR difference between the *in vivo* pyruvate and lactate signals. Lastly, the observed difference in magnitudes between the two studies may also be a function of acquisition timing. In the *ex vivo* study, the fresh HP pyruvate signal is replenished continuously over a period of one minute. Any lactate that is converted from the still-magnetized pyruvate signal would still be detected during acquisition. On the hand, the HP pyruvate bolus is injected within 6s and imaging is acquired after 18s for a total of 9s. The pyruvate has to traverse the vena cava and the heart before any pyruvate is delivered to the lungs. Some blood cells that uptake pyruvate may already have converted HP pyruvate to HP lactate before acquisition has even started. Furthermore, during the imaging acquisition period, no new HP pyruvate is delivered, and any pyruvate within the

RF coil will suffer RF-induced depolarization. Although pyruvate may be converted to lactate, the SNR may be too low to quantify it. All these factors may have contributed to the lower observed difference between the three relevant cohorts.

Lung regions may also express high apparent LDH activity during several other pathologies, including cancer, environmental exposure to agents causing oxidative stress, or interstitial inflammation[43,44]. It is important to note that, while the metabolic process examined here is related to the uptake and sequestration of ^{18}FDG in that increased glycolytic activity can be expected to yield a larger signal, the two measurements are not equivalent. In particular, the imaging agents are transported into the cell via different mechanisms (glucose transporter 1 versus, primarily, monocarboxylate transporter 2[45]). The two enzymatic conversion processes are also regulated through different means: e.g., hexokinase is inhibited by the FDG product FDG-6-phosphate and is the rate-limiting enzyme in neutrophilic glycolysis[21], while LDH depends directly on cytosolic redox state and is regulated through a variety of other mechanisms including the inhibitory effect of the redox-coupled reduced glutathione concentration[16]. Accurately assessing the relative merits of each agent therefore requires further study in a model system.

4.5. Conclusions

We have demonstrated the use of non-ionizing, HP ^{13}C spectroscopy to detect pulmonary inflammation and have provided evidence that infiltrating neutrophils provide the primary source of the observed signal. Although HP ^{13}C spectroscopy is dependent on enzymatic and transport processes different from those involved in ^{18}FDG imaging, many features of the techniques appear to be similar, including the several-fold increase of signal in inflammation and the apparent sensitivity to direct metabolism of the neutrophilic inflammatory component. Because the baseline metabolic activity of the lung epithelium is relatively low, neutrophilic activity is apparent in high contrast. The overall signal levels are raised such that imaging applications become feasible, although the consistency of this low baseline and potential sensitivity to other conditions must be further investigated in both the isolated and *in vivo* lung[46,47].

4.6. References

1. Borregaard N, Herlin T. Energy Metabolism of Human Neutrophils during Phagocytosis. *J Clin Invest*. 1982;70(3):550-557. doi:10.1172/JCI110647

2. McCall CE, Bass DA, Cousart S, DeChatelet LR. Enhancement of hexose uptake in human polymorphonuclear leukocytes by activated complement component C5a. *PNAS*. 1979;76(11):5896-5900. doi:10.1073/pnas.76.11.5896

3. Jain V, Hasselquist S, Delaney MD. PET scanning in sarcoidosis. *Annals of the New York Academy of Sciences*. 2011;1228(1):46-58. doi:10.1111/j.1749-6632.2011.06075.x

4. Moeller A, Ask K, Warburton D, Gauldie J, Kolb M. The bleomycin animal model: A useful tool to investigate treatment options for idiopathic pulmonary fibrosis? *The International Journal of Biochemistry & Cell Biology*. 2008;40(3):362-382. doi:10.1016/j.biocel.2007.08.011

5. Hayashi Y, Inubushi T, Nioka S, Forster RE. 31P-NMR spectroscopy of isolated perfused rat lung. *Journal of Applied Physiology*. 1993;74(4):1549-1554. doi:10.1152/jappl.1993.74.4.1549

6. Pillai RP, Buescher PC, Pearse DB, Sylvester JT, Eichhorn GL. 31P NMR spectroscopy of isolated perfused lungs. *Magn Reson Med*. 1986;3(3):467-472.

7. Kasimos JN, Merchant TE, Gierke LW, Glonek T. 31P Magnetic Resonance Spectroscopy of Human Colon Cancer. *Cancer Res*. 1990;50(3):527-532.

8. Pettegrew JW, Keshavan MS, Minshew NJ. 31P Nuclear Magnetic Resonance Spectroscopy: Neurodevelopment and Schizophrenia. *Schizophr Bull*. 1993;19(1):35-53. doi:10.1093/schbul/19.1.35

9. Anthony ML, Williams SNO, Brindle KM. Nuclear Magnetic Resonance Methods of Monitoring Cell Metabolism. *Animal Cell Biotechnology*. 1999:165-175. doi:10.1385/0-89603-547-6:165

10. Park JM, Park JH. Human in-vivo 31P MR Spectroscopy of Benign and Malignant Breast Tumors. *Korean Journal of Radiology*. 2001;2(2):80-86. doi:10.3348/kjr.2001.2.2.80

11. Pullinger B, Profka H, Ardenkjaer-Larsen JH, Kuzma NN, Kadlecek S, Rizi RR. Metabolism of hyperpolarized [1-13C]pyruvate in the isolated perfused rat lung - an ischemia study: MEASUREMENTS OF LUNG METABOLISM USING HYPERPOLARIZED 1-13C PYRUVATE. *NMR in Biomedicine*. 2012;25(10):1113-1118. doi:10.1002/nbm.2777

12. Klier M, Schüler C, Halestrap AP, Sly WS, Deitmer JW, Becker HM. Transport Activity of the High-affinity Monocarboxylate Transporter MCT2 Is Enhanced by Extracellular Carbonic Anhydrase IV but Not by Intracellular Carbonic Anhydrase II. *J Biol Chem*. 2011;286(31):27781-27791. doi:10.1074/jbc.M111.255331

13. Cobben NA m., Jacobs J a., Van Dieijen-Visser M p., Mulder PG., Wouters EF m., Drent M. Diagnostic value of BAL fluid cellular profile and enzymes in infectious pulmonary disorders. *European Respiratory Journal*. 1999;14(3):496-502. doi:10.1034/j.1399-3003.1999.14c04.x

14. Drent M, Cobben NA, Henderson RF, Wouters EF, Dieijen-Visser M van. Usefulness of lactate dehydrogenase and its isoenzymes as indicators of lung damage or inflammation. *European Respiratory Journal*. 1996;9(8):1736-1742.

15. Johnson ML, Hussien R, Horning MA, Brooks GA. Transpulmonary pyruvate kinetics. *AJP: Regulatory, Integrative and Comparative Physiology*. 2011;301(3):R769-R774. doi:10.1152/ajpregu.00206.2011

16. Wimberger P, Ebner S, Marin-Grez M. Reduced glutathione inhibits rabbit and rat skeletal muscle lactate dehydrogenase and prevents dinitrophenol induced extracellular acidification by an epithelial cell line. *Life Sciences*. 1997;61(4):403-409. doi:10.1016/S0024-3205(97)00397-4

17. Rahman I, Li XY, Donaldson K, Harrison DJ, MacNee W. Glutathione homeostasis in alveolar epithelial cells in vitro and lung in vivo under oxidative stress. *Am J Physiol*. 1995;269(3 Pt 1):L285-292.

18. Chen DL, Rosenbluth DB, Mintun MA, Schuster DP. FDG-PET imaging of pulmonary inflammation in healthy volunteers after airway instillation of endotoxin. *Journal of Applied Physiology*. 2006;100(5):1602-1609. doi:10.1152/japplphysiol.01429.2005

19. Jones HA, Clark RJ, Rhodes CG, Schofield JB, Krausz T, Haslett C. In vivo measurement of neutrophil activity in experimental lung inflammation. *Am J Respir Crit Care Med*. 1994;149(6):1635-1639. doi:10.1164/ajrccm.149.6.7516252

20. Jones HA, Schofield JB, Krausz T, Boobis AR, Haslett C. Pulmonary Fibrosis Correlates with Duration of Tissue Neutrophil Activation. *Am J Respir Crit Care Med*. 1998;158(2):620-628. doi:10.1164/ajrccm.158.2.9711075

21. Beck WS. A kinetic analysis of the glycolytic rate and certain glycolytic enzymes in normal and leucemic leucocytes. *Journal of Biological Chemistry*. 1955;216(1):333–350.

22. Otsuka M, Takahashi H, Shiratori M, Chiba H, Abe S. Reduction of bleomycin induced lung fibrosis by candesartan cilexetil, an angiotensin II type 1 receptor antagonist. *Thorax*. 2004;59(1):31-38. doi:10.1136/thx.2003.000893

23. Simon LM, Robin ED, Raffin T, Theodore J, Douglas WHJ. Bioenergetic pattern of isolated type II pneumocytes in air and during hypoxia. *Journal of Clinical Investigation*. 1978;61(5):1232.

24. Rehn B, Bruch J, Zou T, Hobusch G. Recovery of rat alveolar macrophages by bronchoalveolar lavage under normal and activated conditions. *Environmental Health Perspectives*. 1992;97:11-16. doi:10.1289/ehp.929711

25. Massaro GD, Gail DB, Massaro D. Lung oxygen consumption and mitochondria of alveolar epithelial and endothelial cells. *Journal of applied physiology*. 1975;38(4):588–592.

26. Yoshii C, Nagata N, Tao Y, Suematsu R, Nikaido Y, Kido M. Relationship between Inflammatory Cells in Bronchoalveolar Lavage Fluid and Pathologic Changes in the Lung Interstitium. *RES*. 1998;65(5):386-392. doi:10.1159/000029300

27. Dik WA, McAnulty RJ, Versnel MA, et al. Short course dexamethasone treatment following injury inhibits bleomycin induced fibrosis in rats. *Thorax*. 2003;58(9):765-771. doi:10.1136/thorax.58.9.765

28. Aytemur ZA, Hacievliyagil SS, Iraz M, et al. Effects of iloprost on bleomycin-induced pulmonary fibrosis in rats compared with methyl-prednisolone. *Revista Portuguesa de Pneumologia*. 2012;18(6):272-277. doi:10.1016/j.rppneu.2012.04.010

29. Yi ES, Salgado M, Williams S, et al. Keratinocyte Growth Factor Decreases Pulmonary Edema, Transforming Growth Factor-Beta and Platelet-Derived Growth Factor-BB Expression, and Alveolar Type II Cell Loss in Bleomycin-Induced Lung Injury. *Inflammation*. 1998;22(3):315-325. doi:10.1023/A:1022304317111

30. Li X, Zhang H, Soledad-Conrad V, Zhuang J, Uhal BD. Bleomycin-induced apoptosis of alveolar epithelial cells requires angiotensin synthesis de novo. *American Journal of Physiology-Lung Cellular and Molecular Physiology*. 2003;284(3):L501-L507. doi:10.1152/ajplung.00273.2002

31. Christensen PJ, Bailie MB, Goodman RE, O'Brien AD, Toews GB, Paine R. Role of diminished epithelial GM-CSF in the pathogenesis of bleomycin-induced pulmonary fibrosis. *American Journal of Physiology-Lung Cellular and Molecular Physiology*. 2000;279(3):L487-L495. doi:10.1152/ajplung.2000.279.3.L487

32. Drath DB, Harper A, Gharibian J, Karnovsky ML, Huber GL. The effect of tobacco smoke on the metabolism and function of rat alveolar macrophages. *Journal of Cellular Physiology*. 1978;95(1):105-113. doi:10.1002/jcp.1040950113

33. Fisher AB, Furia L. Isolation and metabolism of granular pneumocytes from rat lungs. *Lung*. 1976;154(1):155-165. doi:10.1007/BF02713531

34. Ojima-Uchiyama A, Masuzawa Y, Sugiura T, et al. Phospholipid analysis of human eosinophils: High levels of alkylacylglycerophosphocholine (PAF precursor). *Lipids*. 1988;23(8):815-817. doi:10.1007/BF02536227

35. Dube DH, Bertozzi CR. Glycans in cancer and inflammation — potential for therapeutics and diagnostics. *Nature Reviews Drug Discovery*. 2005;4(6):477-488. doi:10.1038/nrd1751

36. Jones HA, Cadwallader KA, White JF, Uddin M, Peters AM, Chilvers ER. Dissociation Between Respiratory Burst Activity and Deoxyglucose Uptake in Human Neutrophil Granulocytes: Implications for Interpretation of 18F-FDG PET Images. *J Nucl Med*. 2002;43(5):652-657.

37. Sapey E, Stockley RA. COPD exacerbations · 2: Aetiology. *Thorax*. 2006;61(3):250-258. doi:10.1136/thx.2005.041822

38. Tanabe N, Muro S, Hirai T, et al. Impact of Exacerbations on Emphysema Progression in Chronic Obstructive Pulmonary Disease. *Am J Respir Crit Care Med*. 2011;183(12):1653-1659. doi:10.1164/rccm.201009-1535OC

39. Bakowska J, Adamson IYR. Collagenase and gelatinase activities in bronchoalveolar lavage fluids during bleomycin-induced lung injury. *The Journal of Pathology*. 1998;185(3):319-323. doi:10.1002/(SICI)1096-9896(199807)185:3<319::AID-PATH114>3.0.CO;2-L

40. Crystal RG. *The Alveolar Macrophage*.; 2013. https://proxy.library.upenn.edu:5502/t/2307/the-alveolar-macrophage/. Accessed March 26, 2019.

41. Lee HB, Blaufox MD. Blood Volume in the Rat. *J Nucl Med*. 1985;26(1):72-76.

42. Landon J, Fawcett JK, Wynn V. Blood pyruvate concentration measured by a specific method in control subjects. *J Clin Pathol*. 1962;15(6):579-584.

43. Golman K, Zandt R i., Lerche M, Pehrson R, Ardenkjaer-Larsen JH. Metabolic Imaging by Hyperpolarized 13C Magnetic Resonance Imaging for In vivo Tumor Diagnosis. *Cancer Research*. 2006;66(22):10855-10860. doi:10.1158/0008-5472.CAN-06-2564

44. Devlin RB, McDonnell WF, Mann R, et al. Exposure of Humans to Ambient Levels of Ozone for 6.6 Hours Causes Cellular and Biochemical Changes in the Lung. *Am J Respir Cell Mol Biol*. 1991;4(1):72-81. doi:10.1165/ajrcmb/4.1.72

45. Merezhinskaya N, Ogunwuyi SA, Mullick FG, Fishbein WN. Presence and Localization of Three Lactic Acid Transporters (MCT1, −2, and −4) in Separated Human Granulocytes, Lymphocytes, and Monocytes. *Journal of Histochemistry & Cytochemistry*. 2004;52(11):1483-1493. doi:10.1369/jhc.4A6306.2004

46. Thind K, Chen A, Friesen-Waldner L, et al. Detection of radiation-induced lung injury using hyperpolarized ^{13} C magnetic resonance spectroscopy and imaging: Detection of RILI. *Magnetic Resonance in Medicine*. 2013;70(3):601-609. doi:10.1002/mrm.24525

47. MacKenzie JD, Yen Y-F, Mayer D, Tropp JS, Hurd RE, Spielman DM. Detection of Inflammatory Arthritis by Using Hyperpolarized 13C-Pyruvate with MR Imaging and Spectroscopy. *Radiology*. 2011;259(2):414-420. doi:10.1148/radiol.10101921

Chapter 5: Detection of lung transplant rejection in a rat model using hyperpolarized [1-^{13}C] pyruvate-based metabolic imaging

Abstract:

The current standard for non-invasive imaging of acute lung rejection consists of X-ray/CT, which derive their contrast from changes in ventilation, the presence of inflammation and edema, and structural remodeling during rejection. We propose the use of hyperpolarized [1-^{13}C] pyruvate MRI—which provides real-time metabolic assessment of tissue—as an early biomarker for tissue rejection. In this study, we used µCT-derived parameters and HP ^{13}C MR-derived biomarkers to predict rejection in an orthotopic left lung transplant model in both allogeneic and syngeneic rats. On day 3, the normalized lung density—a parameter that accounts for both lung volume (mL) and density (HU)—was -0.335 (CI:-0.598,-0.073) and -0.473 (CI:-0.726,-0.220) for the allograft and isograft, respectively, showing no significant difference (p=0.40) between the two cohorts. On the other hand, the respective HP ^{13}C MRI-derived lactate-to-pyruvate ratios of 0.200 (CI:0.161,0.240) and 0.114 (CI:0.074,0.153) for the allograft and isograft were significantly different (p=0.020) on day 3. Both techniques show tissue rejection on day 7. A separate sub-study revealed CD8+ cells as the primary source of lactate-to-pyruvate signal. Our study suggests that hyperpolarized (HP) [1-^{13}C] pyruvate MRI is a promising early biomarker that may be able to predict tissue rejection earlier than X-ray/CT by providing a real-time assessment of changes in pulmonary cellularity as well as metabolic alterations in lung tissue and infiltrating inflammatory cells.

This chapter has been adapted from Siddiqui et al., 'Detection of lung transplant rejection in a rat model using hyperpolarized [1-^{13}C] pyruvate based metabolic imaging' accepted for publication in NMR in Biomedicine, 2019.

5.1. Introduction

Over the last five decades, lung transplantation has evolved from a purely experimental technique to an established treatment for end-stage pulmonary disease[1]. Advances in pre- and post-transplantation management have led to a continuous increase in the number of lung transplants, with a reported 3973 performed worldwide in 2014[2]. Yet immunological rejection continues to contribute significantly to post-transplant morbidity and mortality[3,4], which remains far higher than that of any other solid organ transplant. Acute lung rejection is currently monitored using radiographs or CT, followed by surveillance biopsies. An improved biomarker would be able to detect lung rejection earlier and, ideally, non-invasively.

Several biomarkers have been proposed to improve the detection of lung transplant rejection—including ^{1}H magnetic resonance imaging (MRI) with ultra-small superparamagnetic iron oxide (USPIO) particles, very short echo time (TE) ^{1}H MRI, technetium-99m based single photon emission computed tomography (SPECT), as well as blood-based biomarkers like transplant tissue-specific exosomal microRNA and proteomic profiles[5–8]. None of these techniques are routinely used to detect lung rejection in the clinic, however, where radiography remains the predominant screening method[9–11].

After transplantation, the contrast observed in X-ray/CT images results from inflammation and edema combined with changes in ventilation, as well as permanent structural alterations due to remodeling during rejection. An imaging technique that derives its contrast from the changes in the cellularity and metabolism of lung tissue and the infiltrating inflammatory cells that precipitate lung tissue rejection might therefore be able to predict tissue rejection earlier than X-ray/CT. Hyperpolarized (HP) [1-^{13}C] pyruvate MRI is a novel imaging technique that provides such a real-time metabolic assessment of tissue. The signal of an injected carbon-13 enriched molecular probe can be enhanced more than 10,000-fold compared to thermal polarization via dynamic nuclear polarization (DNP), allowing molecular pathways to be imaged within minutes[12], and the lactate-to-pyruvate (LtP) ratio derived from this technique has been used in rat models of lung injury as a biomarker for ischemia-reperfusion, acute injury and inflammation[13–16]. Given the central role that these mechanisms play in lung tissue rejection, HP [1-^{13}C] pyruvate MRI appears to hold significant promise as a biomarker for its early detection.

In this study, we used an orthotopic left lung transplant model in both allogeneic and syngeneic rats to investigate HP [1-^{13}C] pyruvate MRI's ability to generate metabolic biomarkers for the non-invasive metabolic assessment of lungs post-transplantation. The measured HP lactate-to-pyruvate ratio was compared to micro-CT imaging in predicting lung rejection, and a histological sub-study was conducted to elucidate the source of the observed signal.

5.2. Methods

5.2.1. Animals

20 pairs of rats (40 total) were used for this study. Syngeneic lung transplantation was performed in 8 male Wistar-Furth to Wistar-Furth (295±35g) rat pairs, while allogeneic transplantation was performed in 12 male Wistar to Lewis (305±27 g) rat pairs. n=5 recipients from each cohort were used for longitudinal imaging studies on days 3, 7 and 14, as described in Methods 5.2.3; the remaining recipients were used for the histological studies described in Methods 5.2.4. All animal procedures and studies were approved by the Institutional Animal Care and Use Committee of the University of Pennsylvania

(Philadelphia, PA) and were performed in accordance with the relevant guidelines and regulations.

5.2.2. Transplant Procedure

Detailed methods of the left orthotopic lung transplantation technique were published previously[12]. Transplants was performed under clean, non-sterile conditions, and the animals were heated continuously via an infra-red heating bulb. Anesthesia was induced in both donor and recipient rats with 100 mg/kg ketamine and 4 mg/kg xylazine, and maintained with 1.5% isoflurane/100% oxygen for the duration of the transplantation. Rats were intubated with a 14-gauge catheter (BD, Franklin Lakes, NJ, USA) and mechanically ventilated using pressure control (VentElite small animal ventilator, Harvard Apparatus, Holliston, MA, USA) with the following settings: 16-18 cmH_2O peak inspiratory pressure (PIP), 2-4 cmH_2O positive end-expiratory pressure (PEEP), 1:3 inspiration:expiration ratio at a ventilation rate of 52 bpm. All transplantations were performed using a binocular surgical microscope (Leica M651, Leica Microsystems, Buffalo Grove, IL, USA).

5.2.2.A. Donor Procedure

Donor rats were placed in supine position during lung harvest. A median incision from the jugular notch to the pubic symphysis was used to access both thoracic and abdominal cavities. First, donor animals were systemically heparinized (5000 IU) via the inferior vena cava. The diaphragm was then incised, and a median sternotomy was performed to access the thoracic cavity via the abdominal route. The thymus was removed, the left atrial appendage was then cut, the pulmonary trunk was cannulated and the lungs were perfused with 10 mL of cold (4°C) dextran-based preservation solution (Perfadex, XVIVO Perfusion AB, Goteborg, Sweden). The thoracic cavity was filled with ice to induce cardiac arrest. The trachea was ligated at end inspiration, and the heart and lungs were removed *en bloc*. On the back table, the left pulmonary vein and pulmonary artery were dissected, cut to an appropriate length for secure anastomosis, and flushed with heparin (500 IU). Lastly, the left main bronchus was dissected and the distal trachea and proximal right main bronchus were ligated and cut to keep the lung inflated during cold ischemic storage. Ischemia time was standardized to 2 hours. Subcutaneous buprenorphine (0.1 mg/kg) was delivered every 8 hours for the first 24 hours, and subcutaneous meloxicam (2 mg/kg) was delivered every 12 hours on days 2-4 for post-operational pain relief.

5.2.2.B. Recipient Procedure

Recipient rats were placed in a right lateral position for full access to the left hemithorax. A transverse incision was made about 1 cm below the inferior margin of the scapula to expose the chest wall. Access to the thoracic cavity was gained via the fourth intercostal space. The ribs were retracted, after which the left lung was mobilized outside of the thoracic cavity. When necessary, bipolar cautery (Erbe GmbH, Germany) was used throughout the procedure. The pulmonary artery was clamped prior to the pulmonary vein to minimize blood pooling in the lung. The distal pulmonary artery and the inferior segmental vein were ligated (7-0 silk suture, Catgut, Markneukirchin, Germany) and cut distally. The left main bronchus was clamped (Aesculap FE720 aneurysm clip, Center Valley, PA, USA) and the native left lung was excised. A third-hand device was used to stabilize the vascular clips for the anastomosis procedure.

The donor lung was placed into the recipient thoracic cavity and covered with ice-cooled wet gauze to keep it cool during the implantation procedure. The donor left main bronchus was shortened as needed before being anastomosed end-to-end with 10 interrupted sutures (BV130-5, 8-0 Prolene sutures, Ethicon, Somverville, NJ). Anastomosis was checked for patency by re-inflating the lung, and for air leakage by filling the left thoracic cavity with warm normal saline. Vascular anastomoses (end-to-end pulmonary artery to pulmonary artery and end-to-end pulmonary vein to pulmonary vein) were completed using the cuff technique described previously[12]. In brief, recipient vessels were passed through a 1mm cylinder cuff cut from a polyethylene catheter (18-gauge for the artery, 16-gauge for the vein), everted over the cuff and secured with a 7-0 silk ligature. The donor vessels were then pulled over the cuff and secured with a 7-0 silk ligature and the clips were then removed for reperfusion and ventilation.

The thoracic cavity was drained with a 20-gauge catheter and the ribs were closed with 4-0 Prolene sutures. Muscular layers, subcutaneous layers and skin layers were re-approximated in multiple layers with running 4-0 vicryl sutures. Animals were weaned from mechanical ventilation, extubated and monitored until fully awake.

5.2.3. Imaging Timeline

Micro-CT images were acquired on the following days: 0 (60-120 minutes post-surgery), 1, 2, 3, 7, 14. Proton MRI and hyperpolarized [1-^{13}C] pyruvate MRS were acquired on days 3, 7 and 14.

5.2.3.A. CT Imaging

High resolution CT scans were acquired using a microCT scanner (eXplore CT120, Gamma Medica, Inc., Northbridge, CA). Animals were anesthetized with isoflurane (2%) on 100% O_2 (1.5mL/min) during the scan. Because the animals' breathing was unstable under anesthesia on days 0, 1 and 2, non-gated scans were performed at those time points in order to keep the time under anesthesia under 10 minutes. End-expiratory gating was used during imaging on days 3, 7 and 14, which extended the total time under anesthesia to about 30 minutes. CT scans had the following parameters: voltage: 32.0 mA, current: 80 kV (70 kV for the non-gated sequence), exposure time: 16 ms, angle of rotation: 0.877^{O}, views: 220 (half-scan), reconstructed resolution = 200 μm (isotropic). Total scan time for the non-gated scans was 30 s, whereas gated scans ranged between 6-9 minutes based on the respiration rate (typically 50-70 bpm).

5.2.3.B. Hyperpolarized Pyruvate Preparation

The HP [1-^{13}C] pyruvate probe was prepared by adding 15mM OX063 radical (GE Healthcare, Little Chalfont, UK) and 1.5mM gadoterate meglumine (Dotarem, Guerbet LLC, Bloomington, IN, USA) to neat [1-^{13}C] pyruvate (Cambridge Isotope Laboratories, Tewksbury, MA, USA). 28.3mg of this mixture was polarized to a solid state polarization of 19.8±1.3% using a commercial DNP polarizer (Hypersense, Oxford Instruments, Abingdon, United Kingdom) in approximately 50 minutes. The polarized samples were melted with a 4 mL neutral buffered solution (40mM TRIS base, 80 mM NaOH, 50 mM NaCl, and 0.1 mg/L EDTA) at 10 bar and 180 ˚C to yield a 80 mM HP [1-^{13}C] pyruvate solution at 37 ˚C. 1.1±0.2 mL (4 mL/kg) of the HP solution was then transferred and injected into the animal via a tail vein catheter within 10 s of dissolution. Injection lasted 6 s and was followed by a 200μL saline flush. The scan started 16 s after beginning injection.

5.2.3.C. MRI Imaging

MRI imaging was performed on a 4.7T horizontal bore magnet (Inova 200, Varian Inc, Palo Alto, CA) using a 72mm dual tuned ^{1}H/^{13}C quadrature transmit/receive birdcage coil (Polarean Imaging Plc., Cleveland, OH). A T_1-weighted coronal 1H GRE of the lungs was acquired for positioning the slice-selective CSI with HP [1-^{13}C] pyruvate. The acquisition parameters were: TR/TE = 80/1.55 ms, FOV = 60x60x2 mm^3, matrix = 128x128, slices = 16, averages = 16, flip-angle = 20^o, scan time = 2:03 min. The lungs were manually shimmed using the proton channel to a proton linewidth of about 100Hz using a 15mm slice-selective pulse acquire sequence. HP [1-^{13}C] pyruvate chemical shift imaging (CSI) was performed immediately after shimming.

HP 13C CSI was performed using a 2D slice-selective phase-encoded free-induction decay chemical shift imaging (FID-CSI) sequence. The 15mm slice was positioned on the lungs superior to the dome of the diaphragm. The scan was started 16 s after the start of the HP injection (see above). The acquisition parameters were: TR/TE =35/0.5 ms, FOV = 45x45x15 mm^3, matrix size = 16x16, spectral width = 4 kHz, spectral points = 128, flip-angle = 9^o, scan time = 9s. The MRI imaging session typically lasted 60-90 minutes.

5.2.3.D. CT Data Processing

The CT images were imported into ITK-SNAP for segmentation and quantification, and the lungs were semi-automatically quantified via a two-step process. First, the lungs were automatically segmented using active-contour technique with an upper threshold of -250 HU. Once segmentation was complete, the trachea was manually removed and the lung masks were separated into native and transplanted. The segmented lungs were then used to obtain the average lung density (HU)—a marker for ventilation— and volume (mL) for each lung. Both the aforementioned parameters were also used to calculate normalized lung density (L*HU), which accounts for the skewed lung density due to the upper bound of -250 HU when segmenting the lungs.

5.2.3.E. MRSI Data Processing

All data were processed offline using custom routines in MATLAB 2017b (MathWorks, Natick, MA, USA). The free-induction decays (FID) were line-broadened by 30 Hz and then Fourier transformed to obtain the spatially resolved spectra. The periodic acquisition of the k-space center ($k_{x,y} = 0$) was used to de-blur the spectra via amplitude normalization, providing improved localization. The resultant spectra were then baseline-corrected (fourth-order polynomial), local zero-order and global first-order phase-corrected; the lactate and pyruvate peaks were then fit to Lorentzian functions. The processed carbon-13 spectra were overlaid on the corresponding proton images of the thorax, and voxels were manually selected from the native lung, transplanted lung and heart for regional quantification. Voxels overlying large vessels in the lung parenchyma were excluded from selection. As the number of selected voxels from each region varied, the average pyruvate, lactate and lactate-to-pyruvate was calculated by summing the respective spectra and dividing by the number of voxels. The fitted pyruvate and lactate spectra were also used to generate corresponding metabolic maps, which were linearly interpolated to match the voxel size of the underlying proton images for clearer visualization.

5.2.4. Histology and Immunostaining of Lungs

Because the imaging study was longitudinal, a parallel assessment of both lung tissue ultrastructure and distribution of cellular infiltrates post-transplantation on days 3 (n=3 rejected cohort) and 7 (n=4 rejected cohort, n=3 non-rejected cohort) was also performed. After euthanasia, lungs were excised and filled with 10% formalin at a tidal volume of 10mL/kg to keep the alveoli open. After fixation, lungs were sectioned and sliced axially.

The slides were stained with either hematoxylin and eosin (H&E) or Masson Trichrome to assess tissue morphology or fibrotic changes, respectively. For H&E staining, each slide was divided into 10 sections that were then visually scored at 20x magnification for semi-quantitative grading. Injury was assessed in the H&E stains by a combination of infiltration (scale of 0-2), alveolar structure disruption (scale of 0-3), remodeling (scale of 0-5) and edema (scale of 0-3) (Table 5.1). Fibrosis was assessed using the Ashcroft Score of the Trichrome stained sections, ranging from 0 (normal lung) to 8 (total fibrous obliteration of the field) (Table 5.2)[13,14]. The final score was expressed as a mean of individual scores observed on all microscopic fields across three axial slides from the superior, medial and inferior regions of the lungs.

Feature	Score	Findings
Infiltration	0	No infiltrate
	1	Infiltrate in the perivascular compartment
	2	Infiltrate in alveolar compartment
Alveolar Structure Disruption	0	Regular
	1	Distorted
	2	Collapsed with torn capillary-alveolar membrane
	3	Collapsed with opacity
Remodeling	0	None
	1	Detected in 1 or 2 areas
	2	Detected in 3 or 4 areas
	3	Detected in 5 or 7 areas
	4	Detected in 7 or 8 areas
	5	Detected in 9 or 10 areas
Edema	0	Regular alveolus
	1	Slight thickening
	2-3	Dilated vessels in alveolar walls and proteinaceous material in alveolus

Table 5.1: Grading H&E sections for lung injury based on four sub-categories

Additional slices were used to assess polymorphonuclear leukocytes (PMN) by monitoring myeloperoxidase expression as well as CD4+ and CD8+ T lymphocytes in grafts post-transplant. Briefly, the paraffinized sections were deparaffinized in xylene and, after sequential ethanol and PBS washes, were immunostained with both anti-MPO and rat-CD4+/CD8+ primary antibodies. The secondary antibodies used were goat-anti-rat Alexa 488 (green). Fluorescence imaging was done using a Nikon fluorescence microscope (Nikon Diaphot TMD, Melville, NY). Images were acquired at an excitation wavelength of 488 nm (for MPO, CD4+ and CD8+). All images were acquired at 100 ms exposure time using a preset scale of 0-4095. The PMN, CD4+ and CD8+ were assessed by quantifying fluorescence intensity over 5 fields using Metamorph Software (Molecular Devices, Downington PA).

Grade	Histological Features
0	Normal lung
1	Minimal fibrous thickening of alveolar or bronchiolar walls
2-3	Moderate thickening of walls without obvious damage to lung architecture
4-5	Increased fibrosis with definite damage to lung structure and formation of fibrous bands or small fibrous masses
6-7	Severe distortion of structure and large fibrous areas (“Honeycombing”)
8	Total fibrous obliteration of the field

Table 5.2: Criteria for grading lung fibrosis to derive the Ashcroft Score

5.2.5. Statistical Analysis

Statistical significance between the transplanted and non-transplanted lungs was tested using two-way analysis-of-variance (ANOVA). Post-hoc analysis was performed using Tukey’s honest significance test. If no significance was observed using ANOVA, a

Student's t-test with the Bonferroni correction was used for post-hoc analysis. α=0.05 was considered statistically significant. All data were expressed as mean±SD.

5.3. Results

5.3.1. HP [1-^{13}C] Pyruvate Imaging

Figure 5.1 shows representative ^{13}C spectroscopic images overlaid on the corresponding proton images (Figure 5.1A,B) for syngeneic and allogeneic rats on day 7.

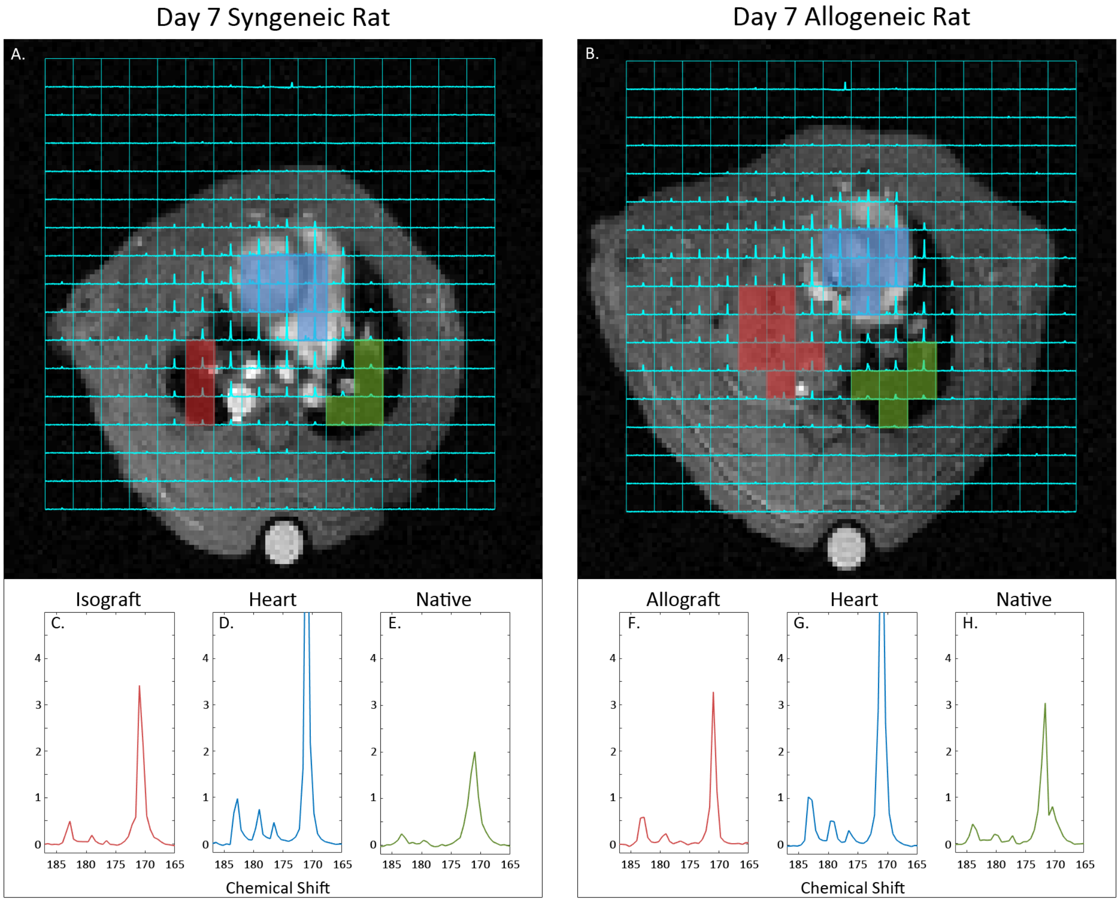

Figure 5.1: Representative carbon-13 MRSI overlaid on proton images in day 7 syngeneic (A) and allogeneic (B) rats. Voxels in the graft (red), native lung (green) and heart (blue) were manually selected for regional quantification (insets C-I) of HP pyruvate and HP lactate. The signal in the heart is generally much higher than in either lung. Linewidths are broadest in the native lungs and narrowest in the heart (Table 5.3).

The insets for figures 5.1A-D show a zoomed-in view of the average spectra in the selected voxels for the native lung, transplant lung and heart, respectively. As can be seen from these spectra, the linewidths of the voxels depend on the region and state of the organ. The quantified linewidths of each tissue are summarized in Table 5.3.

	Day 3		**Day 7**		**Day 14**	
	Syngeneic	**Allogeneic**	**Syngeneic**	**Allogeneic**	**Syngeneic**	**Allogeneic**
Heart	10.2 ± 1.8	11.5 ± 4.4	12.6 ± 0.8	10.9 ± 3.7	12.0 ± 2.6	8.2 ± 6.6
Native	28.4 ± 6.0	34.2 ± 3.6	32.6 ± 3.3	32.7 ± 11.2	30.1 ± 8.3	34.8 ± 0.5
Graft	20.3 ± 9.2	12.7 ± 4.8	22.7 ± 6.6	10.6 ± 2.2	25.6 ± 8.1	10.7 ± 2.9

Table 5.3: Pyruvate linewidth (Hz) quantification in the heart, native lung and grafted lung in syngeneic and allogeneic cohorts on days 3, 7 and 14 (n=5 for both cohorts on all three timepoints). The average linewidth was 11.0±3.2 Hz and 31.8±6.0 Hz in the heart and native lung, respectively, across both cohorts and all three timepoints. In contrast, the average linewidth across all three timepoints in the isograft was 22.7±7.7 Hz (compared to 11.0±3.2 Hz in the allograft).

As described in the Methods section, the fitted pyruvate and lactate spectra were used to generate their respective metabolic maps (Figure 5.2). While the metabolites cannot be absolutely quantified, their respective mean intensities from each lung were normalized to those from the heart for comparison (Table 5.4). On day 3, the normalized pyruvate intensities in the native and transplanted (isograft) lungs of the syngeneic cohort are 0.44±0.11 and 0.55±0.11, respectively (Figure 5.3A). On day 7, these intensities decrease to 0.42±0.10 and 0.45±0.09, respectively, and further decrease to 0.37±0.12 and 0.42±0.19 on day 14 (not significant, minimum p >0.69).

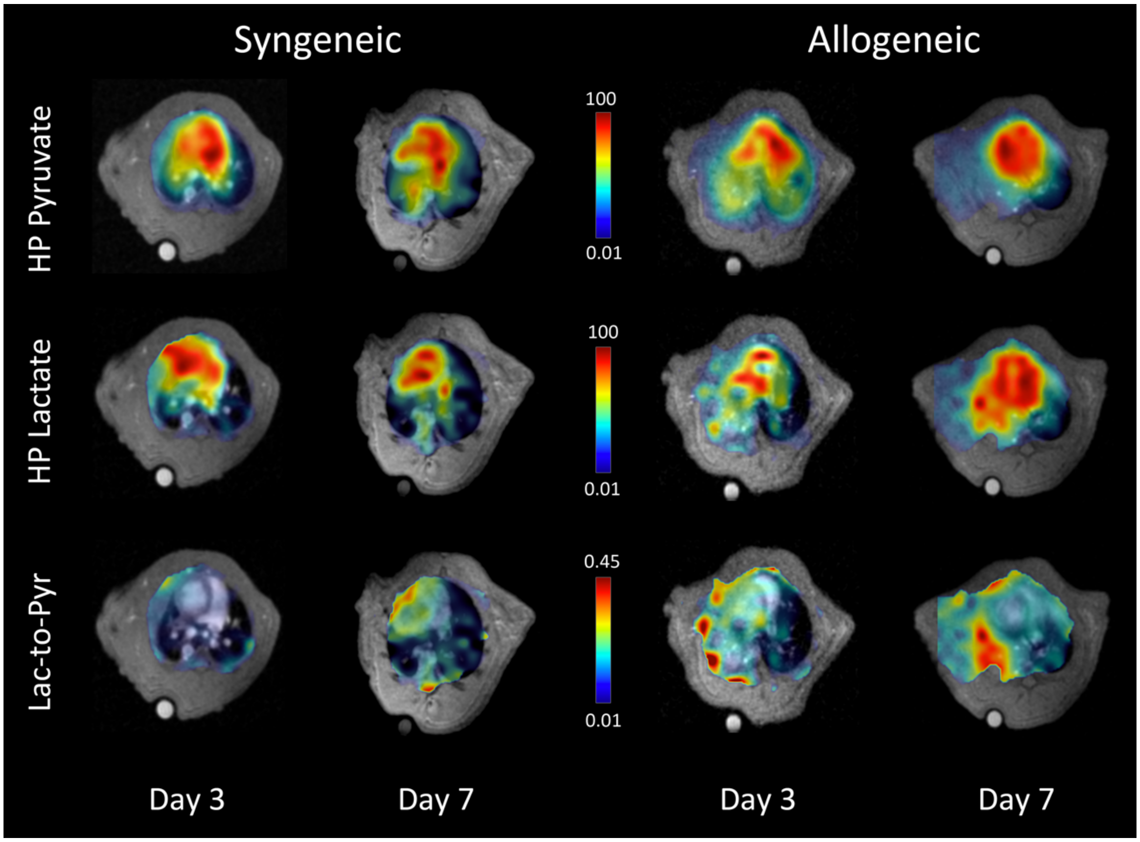

Figure 5.2: HP pyruvate (top), HP lactate (middle), and lactate-to-pyruvate (bottom) maps for syngeneic (left) and allogeneic (right) cohorts on days 3 and 7. In each map, the transplanted lung is displayed on the left and the native lung is on the right. The scale is normalized to the maximum metabolite signal in each map. In the syngeneic (non-rejected) cohort, pyruvate hyperperfusion can be observed, most likely due to IR injury; this dissipates by day 7, as the tissue returns to baseline. The lactate signal is increased over the lungs (compared to the heart) on day 3 but decreases by day 7. Though we see similar hyperperfusion in the allogeneic (rejected) cohort, some of the pyruvate is shunted towards the native lung. The allograft has minimal perfusion by day 7 (see Figure 5.3), yet a large lactate distribution is observed in that lung. The lactate-to-pyruvate ratio is low in both lungs on days 3 and 7 the syngeneic cohorts. On the other hand, the lactate-to-pyruvate ratios of the allograft and native lung in the allogeneic cohort are measurably different on day 3; this difference is enhanced further by day 7, when the transplanted lung is fully rejected.

In contrast, the pyruvate distribution in the allogeneic cohort has a greater difference between the native and transplanted (allograft) lungs. On day 3, the former's intensity is 0.75±0.37, whereas the latter's is 0.48±0.25 (p=0.22). Pyruvate intensity in the native lung drops to 0.47±0.10 by day 7, and to 0.45±0.05 by day 14, which is within the range of both lungs from the syngeneic cohort and suggests a return to baseline perfusion. In contrast, pyruvate intensity in the transplanted lung was less than the native lungs on days 7 (0.24±0.12, p=0.004) and 14 (0.29±0.09, p=0.075) post-transplant.

Metabolite	Cohort	Lung	Day 3		Day 7		Day 14	
			Mean	**SD**	**Mean**	**SD**	**Mean**	**SD**
Normalized Pyruvate (to Heart)	Allogeneic	Native	0.75	0.37	0.47	0.10	0.45	0.05
		Allograft	0.48	0.25	0.24	0.12	0.29	0.09
	Syngeneic	Native	0.44	0.11	0.42	0.10	0.37	0.12
		Isograft	0.55	0.11	0.45	0.09	0.42	0.19
Normalized Lactate (to Heart)	Allogeneic	Native	0.50	0.17	0.36	0.08	0.28	0.11
		Allograft	0.45	0.27	0.56	0.16	0.38	0.19
	Syngeneic	Native	0.36	0.13	0.29	0.09	0.27	0.04
		Isograft	0.64	0.19	0.43	0.11	0.39	0.11
Lactate-to-Pyruvate Ratio	Allogeneic	Native	0.160	0.083	0.123	0.029	0.131	0.065
		Allograft	0.200	0.05	0.413	0.146	0.257	0.097
	Syngeneic	Native	0.078	0.028	0.113	0.037	0.079	0.027
		Isograft	0.114	0.045	0.153	0.027	0.100	0.032

Table 5.4: Quantitative analysis summary for pyruvate, lactate and lactate-to-pyruvate ratio in the native and transplanted (graft) lungs in both syngeneic and allogenic cohorts. The isograft and allograft are the transplanted lungs in the syngeneic and allogeneic cohorts, respectively. The pyruvate and lactate signals are normalized to that of the heart. The sample size for both cohorts was n=5 at all three timepoints (day 3, 7, 14).

In the syngeneic cohort, the HP lactate intensity is higher in the grafts than in the native lungs at all three timepoints (significant, maximum p<0.007) (Figure 5.3B). Lactate intensity for the isografts is 0.64±0.19, 0.43±0.11, and 0.39±0.11 on days 3, 7 and 14, respectively. In comparison, the normalized intensity for the native lung is 0.36±0.13, 0.29±0.09, and 0.27±0.04 at the same timepoints. Although lactate intensity decreases by 32.8% in the isografts between days 3 and 14, it is still 44.4% higher than in the native lungs on day 14, suggesting incomplete recovery from the transplant procedure.

The native and transplanted lungs in the allogeneic cohort show no significant difference in lactate intensity on day 3 (0.50±0.17 and 0.45±0.27, respectively). However, lactate intensity in the allografts increases to 0.56±0.16 and 0.38±0.19 on days 7 and 14, respectively, whereas it decreases to 0.36±0.08 and 0.28±0.11 on days 7 and 14 in the native lungs.

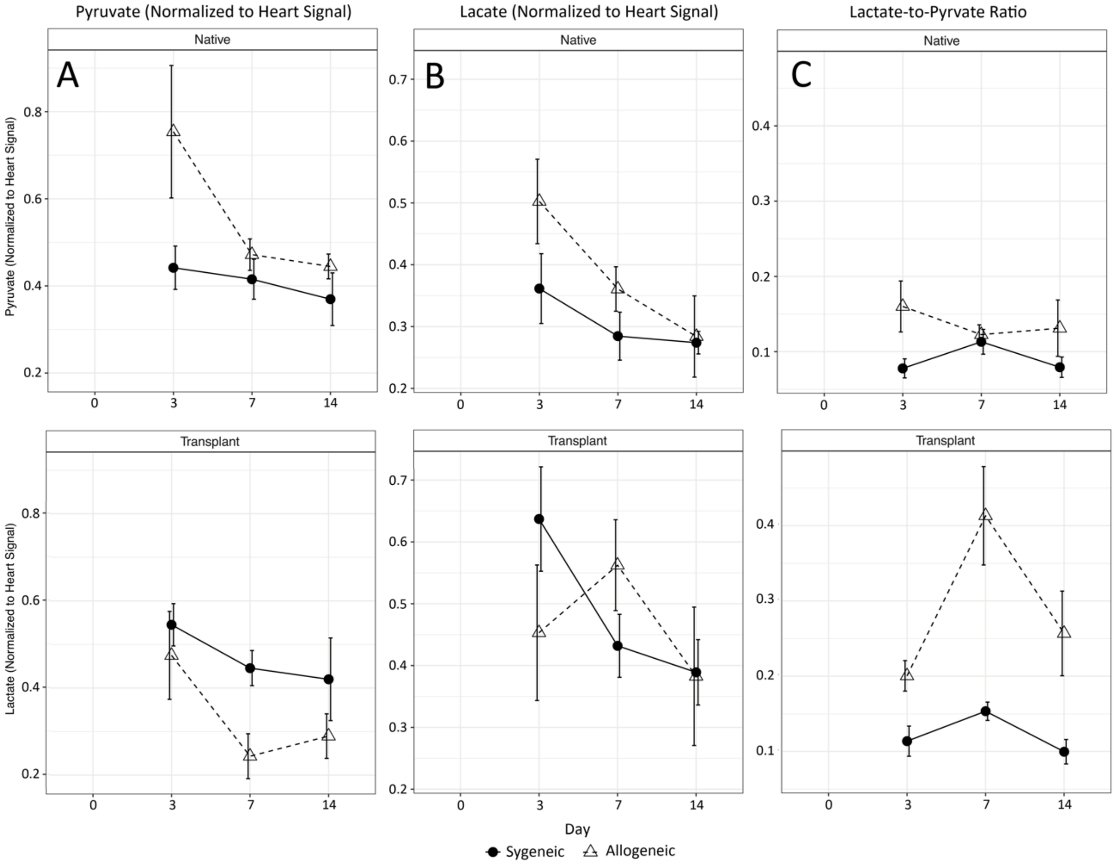

Figure 5.3: Biomarkers derived from quantified HP [1-13C] pyruvate MRI. A) The average pyruvate signal in each lung, normalized by the average signal in the heart. The sample size for both cohorts was n=5 at all three timepoints (day 3, 7, 14). On day 3, a much larger pyruvate signal is observed in the native lung of the allogeneic cohort compared to the other three lungs; by day 14, this signal is within the range of both syngeneic lungs, while the signal from the allograft remains comparatively low, most likely because perfusion is hampered due to rejection. B) The average lactate signal in each lung, normalized by the average lactate signal in the heart. Both syngeneic lungs and the native lung from the allogeneic cohort show a decreasing lactate signal with time, most likely due to recovery from post-transplant ischemia-perfusion injury. In the allograft, on the other hand, lactate signal does not show a monotone decrease, and is similar to that in the isograft lungs despite lower perfusion. C) The average HP lactate-to-pyruvate (LtP) ratio in each lung. On day 3, The LtP of the allograft is significantly greater than that of the isograft, and continues to

increase on day 7, when the lung is fully rejected. The other three lungs show a similar LtP on day 14, while that of the allograft remains high.

5.3.2. HP Lactate-to-Pyruvate (LtP) Ratio

Although the pulmonary lactate and pyruvate intensities reported above are normalized against the heart, the LtP provides the metabolic state of each lung independent of any other organ's metabolic status. On day 3, the native lungs in the syngeneic and allogeneic cohorts have a LtP of 0.078±0.028 and 0.160±0.083 (p=0.090), respectively, whereas the grafts show respective ratios of 0.114±0.045 and 0.200±0.05 (p=0.020) (Figure 5.3C). There is no significant difference between the native lungs and grafts within the same cohort (minimum p > 0.18); however, there is a significant difference between the same types of lung in different cohorts. Furthermore, the LtP of the transplanted lung in the allogeneic (rejected) cohort is 75.4% greater than in the syngeneic (non-rejected) cohort, making it a viable predictor for lung rejection.

On day 7, the LtP in the native lungs is 0.113±0.037 and 0.123±0.029 in syngeneic and allogeneic cohorts, respectively. The LtP of the isografts is 0.153±0.027, whereas it has increased to 0.413±0.146 in allografts (p=0.0015). This increased LtP coincides with full lung rejection, as observed in CT images of the non-aerated allografts. On day 14, the LtP of the native lungs in the syngeneic and allogeneic cohorts is 0.079±0.027 and 0.131±0.065 (p=0.29), respectively; the transplanted lungs have respective LtPs of 0.100±0.032 and 0.257±0.097 (p=0.097). Although less than on day 7, this is still a 2.57-fold inter-cohort difference between transplanted lungs.

5.3.3. Qualitative Assessment of CT Imaging

CT images for both cohorts show large aeration variances on day 0 (Figure 5.4A,E): typically, the native lungs are partially to fully aerated, while the grafts are non- or slightly aerated. By day 3, the native lungs in both cohorts appear almost fully aerated (Figure 5.4B,F); however, the allogeneic cohort tends to display a higher variance than the syngeneic cohort. Meanwhile, the transplanted lungs remain either poorly or partially aerated on day 3, with minimal discernible difference between the two cohorts. It is therefore difficult to predict the fate of the transplanted lungs based on the day 3 CT images. On days 7 and 14, the allografts are completely non-aerated (Figure 5.4G,H), whereas both lungs appear fully aerated in the syngeneic cohort (Figure 5.4C,D).

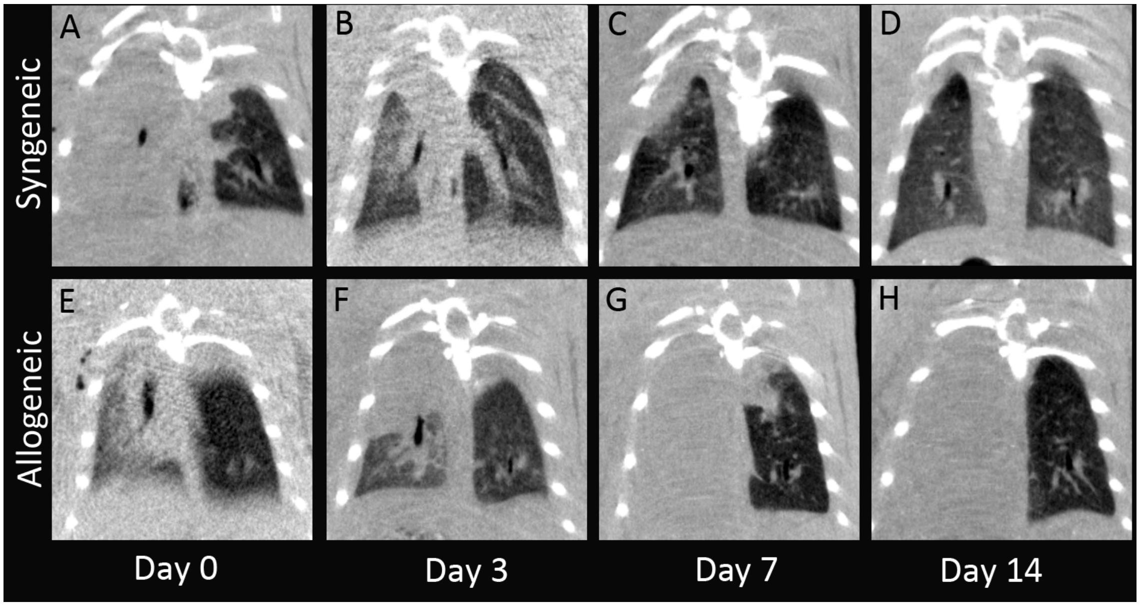

Figure 5.4: Representative coronal CT slices for syngeneic (top) and allogeneic (bottom) transplanted lungs. The slices displayed here best represent the median lung density of their respective cohorts. In general, there was a much larger variation in both lungs on days 0 and 3 compared to days 7 and 14, as seen in Figure 5.5.

5.3.4. Quantitative Assessment of CT Imaging

The quantitative parameters—ventilated lung volume (mL), lung density (HU), and normalized lung density (L*HU)—confirm the qualitative assessment of the CT images.

On day 3, the volume of the native lungs in the syngeneic and allogeneic cohorts is 3.63±0.51mL and 3.91±0.1.67mL (p=0.71), respectively; the respective volumes of the grafts are 1.1±0.63mL and 0.53±0.71mL (Figure 5.5A). Although the mean volume of the isografts is more than double that of the allografts, this difference is insignificant (p=0.40) due to their large overlapping ranges. On day 7, the volume of the native lungs in the syngeneic and allogeneic cohorts is 3.88±0.27mL and 4.17±1.025mL (p=0.62), respectively, while the respective volumes of the grafts are 1.27±0.17mL and 0.01±0.01mL (p<0.00001), suggesting that the allografts have been completely rejected by day 7. The isograft volume increases by 21% to 1.54±0.15mL on day 14, whereas the allograft volume remains unchanged. The native lung volume increased by 5.3% to 4.09±0.65mL and by 21.3% to 5.063±.91mL in the syngeneic and allogeneic cohorts, respectively.

Similarly, the difference in lung density between the two cohorts on day 3 is insignificant. The native lungs of the syngeneic and allogeneic cohorts have a density of -512±24 HU and -486±66 HU (p=0.60), respectively, compared to respective densities of -438±29 HU and -425±39 HU (p=0.40) in the grafts on day 3 (Figure 5.5B). The density of the native lungs in both cohorts decreases slightly on days 7 and 14 as the lungs recover ventilation. The isografts have a density of -517±52 HU and -498±59 HU on days 7 and 14, respectively, also suggesting recovering ventilation. The nominal density in the allograft on day 7 is meaningless given the almost zero volume of the lung at that time point (indicating complete consolidation).

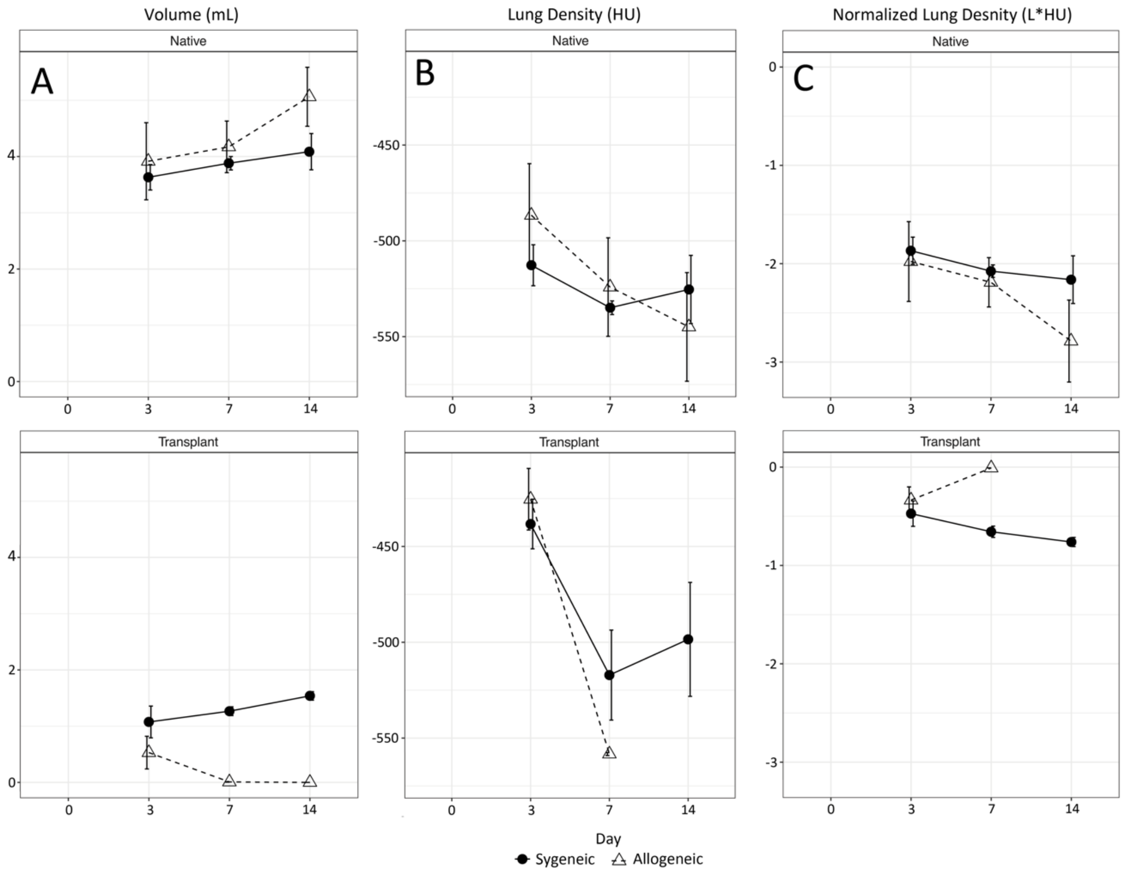

Figure 5.5: The aerated lung volume (A), lung density (B) and normalized lung density (C) in native (left) and transplanted (right) lungs in both cohorts, based on segmentation of gated CT images. CT images could not be accurately segmented before day 3 due to heavy motion artifacts in the non-gated CT images. (A) The volume of the native lungs was larger than that of the transplanted lungs, as donor rats were typically about 50g smaller than recipient rats. The volume of the native lung increases to compensate for the failing transplanted lung on days 7 and 14 in the allogeneic cohort. (B) Because values are based on an upper threshold of -250 HU, these lung densities are biased towards aerated regions of the lung and, as a result, cannot distinguish between a lung with very low overall aeration (high density) versus a lung with high aeration in some regions (low density); they are therefore of minimal use as diagnostic markers. (C) The normalized lung density (L*Hu) is the product of lung volume and density, and serves as a quantitative surrogate for the visual inspection of a radiograph or CT image by a radiologist. The results show a similar trend to the previous two CT-derived parameters: the native lungs in both cohorts share a similar longitudinal trajectory, whereas the transplanted lungs show similar normalized densities on day 3 before lung failure in the allogeneic cohort starting on day 7. Note that there are no lung density and normalized lung density values on day 14 for the allograft in the allogeneic cohort because the segmented lung volume of 0mL. The sample size for both cohorts was n=5 at all three timepoints (day 3, 7, 14).

The normalized lung density –which attempts to succinctly quantify the qualitative reading of a radiograph—similarly reflects CT imaging’s lack of predictive power. On day 3, the native lungs in the syngeneic and allogeneic cohorts have a normalized density of -1.87±0.31 L*HU and -1.98±0.99 L*HU (p=0.80), respectively, whereas the transplanted lungs show respective normalized densities of -0.47±0.29 L*HU and -0.34±0.13 L*HU (p=0.53) (Figure 5.5C). The normalized density of the native lungs in both cohorts and the isografts continues to decrease on days 7 and 14, reflecting the increased lung volume and improved ventilation seen above. In contrast, given the complete consolidation of the allografts, the normalized density is zero L*HU on day 7.

5.3.5. H&E and Trichrome Staining

On day 7, isografts presented with minor infiltration in the peribronchiolar regions, but no edema. The native lung showed very little particulate infiltration. Overall, the isograft showed no signs of rejection. Isografts and native lungs scored 4.0 and 3.1, respectively (Figure 5.6A,C).

In contrast, allografts showed extensive infiltration as well as complete remodeling of the graft, with granulated tissue filling the lumen of the airway. There was alveolar collapse and tissue consolidation in most of the graft tissue, marked proliferation of the intima along the vessels, and the lumen of most of the vessel had disappeared. Extensive fibrotic lesions were observed throughout the graft. Thus, all the classic features of rejection were noted. Infiltrates and edema were also observed in the native lungs of the allogeneic (rejected) cohort. On our semi-quantitative scale, allografts and native lungs scored 13 and 5.8, respectively (Figure 5.6E,G).

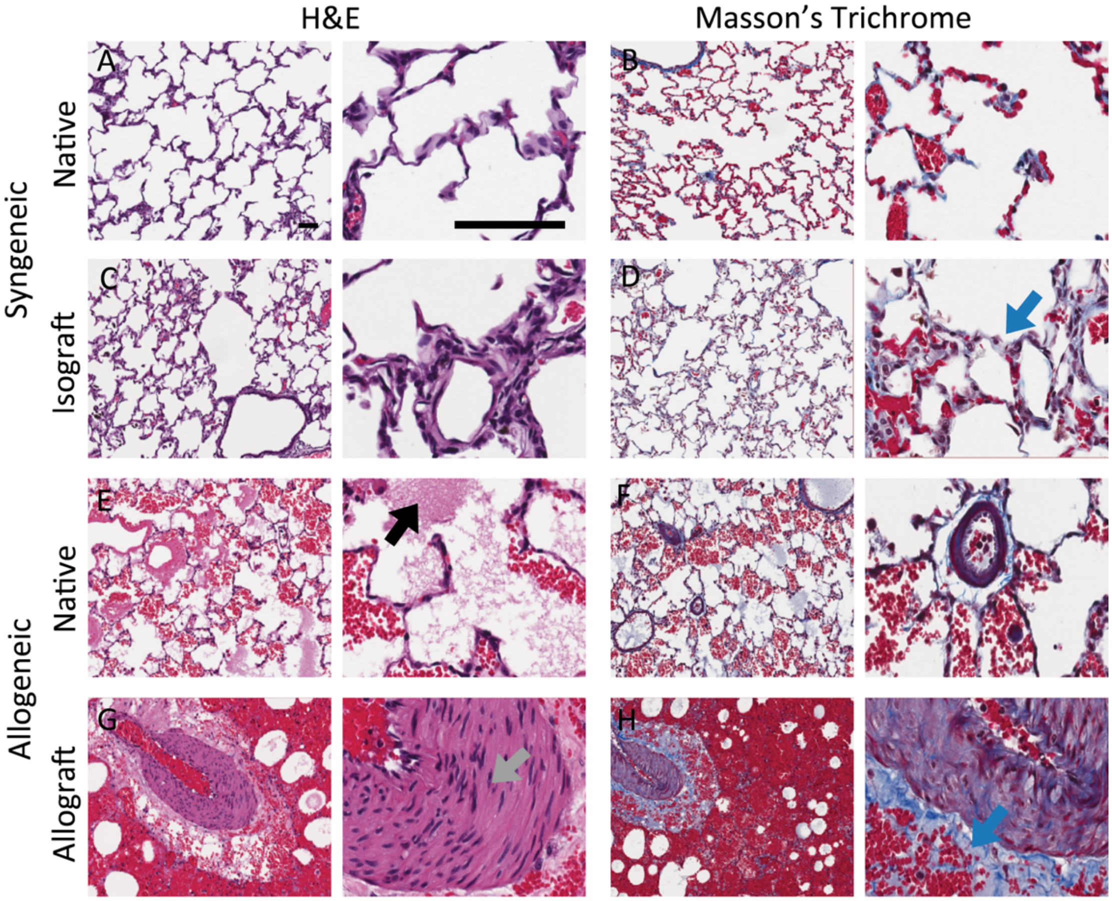

Figure 5.6: H&E staining (left panel) and Masson's Trichrome (right panel) of both non-rejected (A-D) and rejected (E-H) cohorts on day 7 post-transplant. A sub-field is magnified in the adjacent panels. The blue arrows show collagen deposition in the isograft (D) and allograft (H). The alveolar structure and lung architecture appear normal in the non-rejected cohort, with some minor remodeling seen in the isograft. In the rejected cohort, the black arrow (E) is proteinaceous edema in the alveolus, while the grey arrow (G) shows thickening (smooth muscle proliferation) of an airway. Airways are obliterated and the lung architecture is completely destroyed in the allograft. Collagen deposition (blue) indicates extensive remodeling of lung tissue. Scale bar is 100 microns.

The average Ashcroft score for both lungs in the syngeneic cohort was 1.0 (Figure 5.6B,D). Isografts showed the presence of infiltrates and thickening of the alveolar septa in some areas. In contrast, allografts showed extensive fibrosis, massive infiltrate accumulation and tissue consolidation, and total obliteration of alveoli and extensive collagen deposition throughout the graft (Figure 5.6F,H). The allograft's Ashcroft score was 7-8, whereas the native lung's was 2.5.

5.3.6. Immunostaining for Myeloperoxidase (MPO)

Fluorescence microscopy of immunostained lungs showed high MPO expression in the allografts on days 3 and 7 compared to the native lungs (not shown) and the isograft (Figure 5.7). In the allograft, MPO expression was marginally higher on day 7 compared to day 3, but that difference was not significant (Table 5.5). MPO was predominantly expressed along the vessel wall, with some PMN accumulation in the alveolar space.

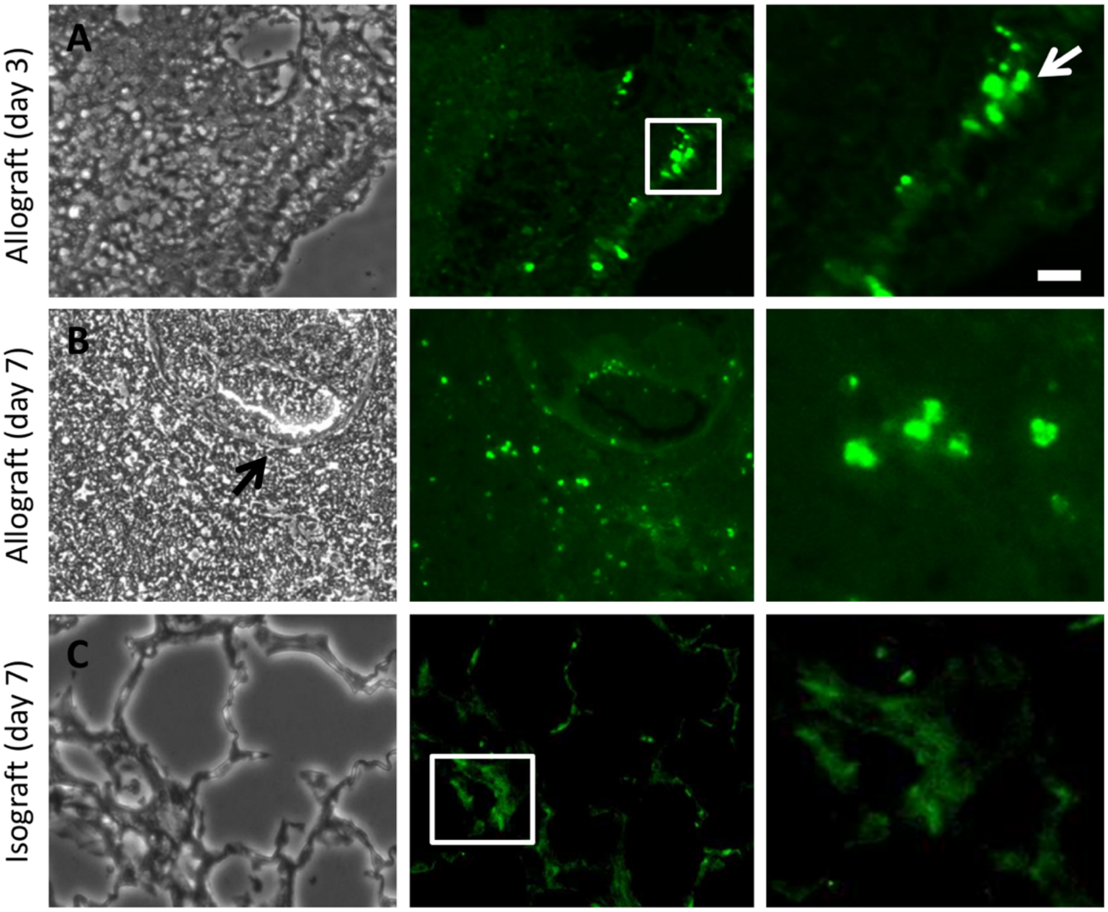

Figure 5.7: MPO Staining – Immunostaining for immune cells (neutrophils and macrophages) in post-transplant grafts from both allogeneic and syngeneic transplants. Lung sections were stained for myeloperoxidase (MPO) using rabbit polyclonal anti-MPO. Goat anti-rabbit-Alexa 488 was used as a secondary antibody. The boxed inset is expanded to show the presence of MPO positive (i.e. azurophilic granulocytes) neutrophils, which are seen as clusters within the allogeneic lung graft tissue and were not limited to the lumen. No such cell clusters were observed in syngeneic grafts. The black arrow shows an obliterated lumen. Quantifying fluorescence signal (Table 5.5) suggested

a high expression of MPO in the transplanted grafts compared to the isograft; in allografts, MPO was slightly higher on day 7 than on day 3. Scale bar is 10 microns.

5.3.7. Immunostaining for CD4+ and CD8+ Cells

The syngeneic cohort showed minimal staining for both CD4+ (Figure 5.8E) and CD8+ (Figure 5.9E) in both lungs. Fluorescence imaging showed high CD4+ expression in allografts on days 3 and 7 (Figure 5.8A,C, Table 5.5). There was no appreciable expression of CD4+ in the native lungs (Figure 5.8B,D). In contrast, CD8+ expression was low in day 3 allografts (Figure 5.9A), but increased several-fold at day 7 (Figure 5.9C). Both CD4+ and CD8+ expressing T cells accumulated predominantly along the obliterated lumen, with little to no accumulation in either the alveolar region or other areas of the lung tissue; some T cells were also found along the endothelial layer of the original vessel.

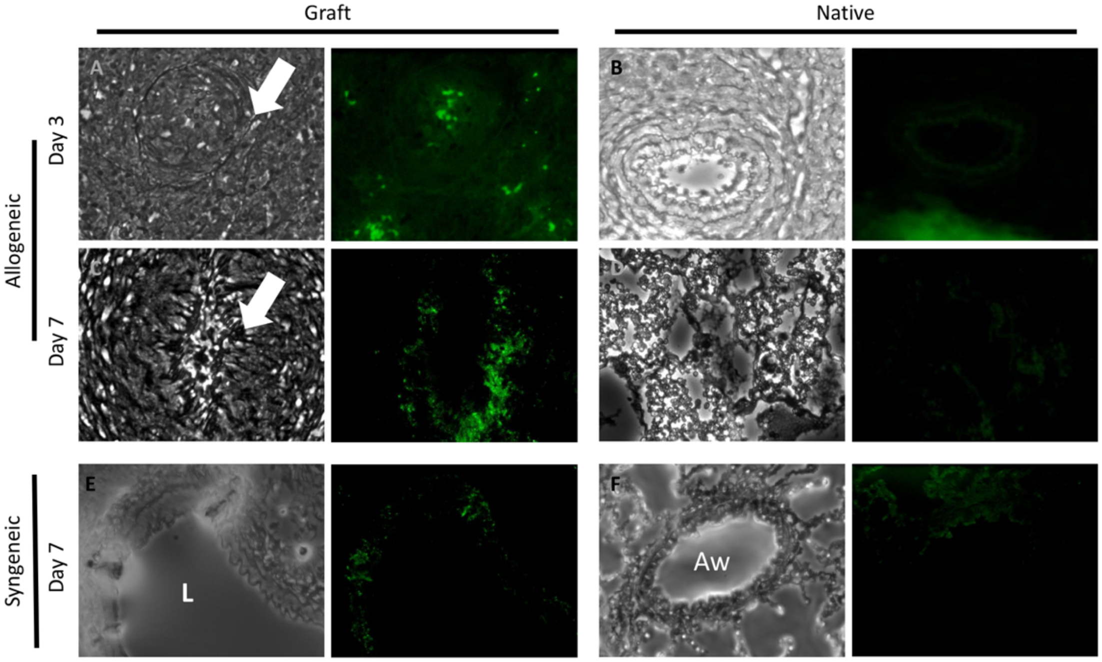

Figure 5.8: Sections depicting airways and lumen are shown (Aw=airway; L=lumen). The presence of T-lymphocytes using anti-CD4+ antibodies is indicated by green fluorescent signal in the allogeneic cohort on days 3 (A, B) and 7 (C, D), as well as in the syngeneic cohort on day 7 (E, F). The syngeneic cohort showed minimal staining for CD4+. The lung allografts showed appreciable signal on both day 3 and day 7 (A, C), while the native lungs in this cohort showed minimal signal (B,D)—see Table 5.5 for quantification.

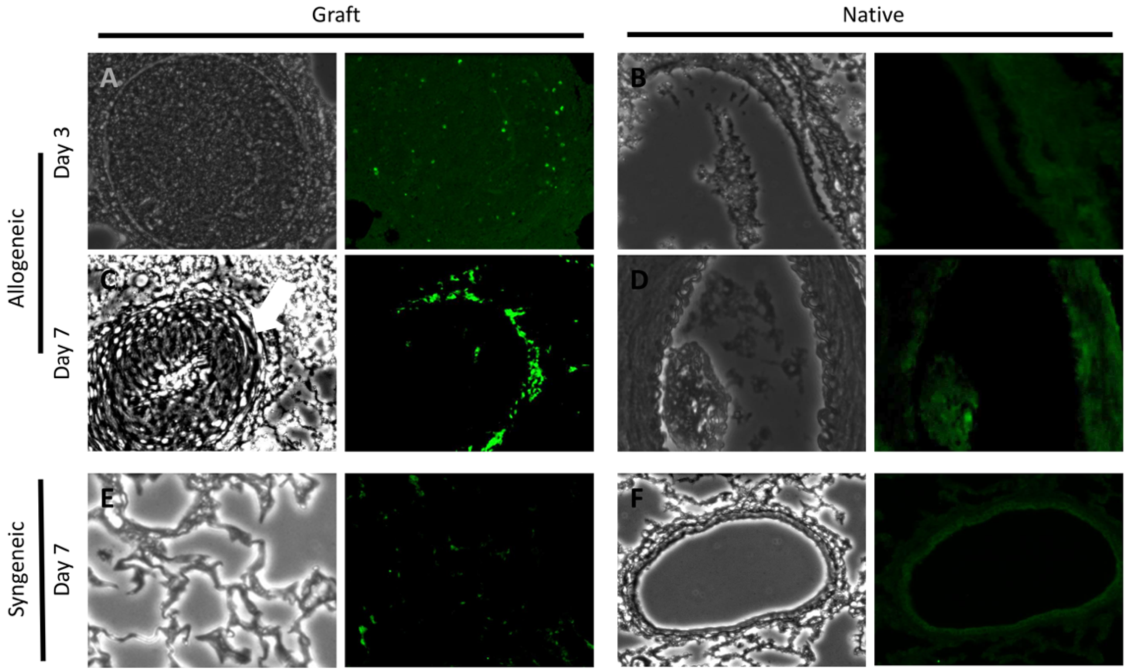

Figure 5.9: Sections depicting airways and lumen are shown (Aw=airway; L=lumen). Green fluorescent signal indicates the presence of T-lymphocytes using anti-CD8+ antibodies in the allogeneic cohort on days 3 (A, B) and 7 (C, D), as well as in the syngeneic cohort on day 7 (E, F). Most of the CD8+ T lymphocytes were expressed along the lumen. Minimal CD8+ expression is apparent in the native lungs in all three cohorts as well as the isograft on day 7. The allograft shows elevated fluorescence on day 3, which more than doubles by day 7 (see Table 5.5 for quantification).

5.4. Discussion

In this animal study, we assessed HP [1-^{13}C] pyruvate MRI's potential as a predictor for lung rejection compared to micro-CT, an appropriate analog to clinical radiography. We found that the lactate-to-pyruvate (LtP) ratio derived via our technique was able to discriminate allografts and isografts better than micro-CT-derived parameters on day 3. While the transplanted allografts were completely rejected by day 7 in our model, the normalized lung density derived via micro-CT showed no significant difference between allografts- and isografts on day 3, whereas the LtP showed a significant difference between the two cohorts at this timepoint.

Images derived using both these modalities reflect the underlying mechanism of graft rejection, which is primarily driven by the adaptive immune system. The recognition of the donor MHC complexes by CD4+ and CD8+ T-cell lymphocytes stimulates the development of cytotoxic CD8+ T-lymphocytes (CTL) which lyse the cells and tissue, leading to organ destruction[20,21]. While the relative contributions of CD4+ and CD8+ T cell subsets to rejection are unclear, the CD4+ alloimmune response is typically short-lived due to the destruction of donor antigen-presenting cells (APCs) post-transplantation[22–24]. The principal alloimmune response therefore appears to be largely mediated by CD8+ CTLs, although this response may vary according to the transplant model and species[25–27]. In our study, both CD4+ and CD8+ seemingly play a role in the rejection process on day 3; the CD4+ signal declines on day 7, however, while the CD8+ signal doubles, suggesting that the CD8+ T-cell response is the principal mediator of rejection (Figure 5.8,9).

Although the adaptive immune response is the major driver for tissue rejection, other immune responses driven by neutrophils also occur during the rejection process. Ischemia-reperfusion (IR) injury due to the transplant procedure results in infiltrating leukocytes[28] and vascular permeability[29,30], and the cascade of events up-regulates fibroblast activity in the allograft, eventually resulting fibrosis[31,32]. Indeed, a major hallmark of graft rejection is the complete solidification of the graft tissue, as observed in Figure 5.6.

Because of its sensitivity to most of the physiological changes described above, CT imaging is useful for monitoring post-transplant tissue rejection. The lack of aeration immediately after transplantation, along with any edema or inflammation due to IR injury, increases the lung density. Effects of IR injury have been demonstrated in the contralateral lungs[33–35], suggesting that the observed decrease in CT lung density from day 3 to 14 in the native lungs of both cohorts is most likely due to recovery from such IR injury. Transplanted lungs from both cohorts are non-aerated immediately post-transplant (Figure 5.4AE), but are partially aerated by day 3. The isograft recovers from the IR injury between days 3 and 7, as confirmed by H&E histology. In contrast, the lung density of the allografts increases and the lung aeration decreases as the CTL lyse donor lung cells, typically those in the endothelium of the vessels and airway epithelium, as seen in Figure 5.6[36]. Despite its utility as a monitoring tool for lung rejection, however, CT is only capable of detecting this rejection after native immune cells have induced these structural changes[37]. This deficiency is most apparent in our model on day 3, when both the allografts and isografts show overlapping CT volumes and densities despite only the allograft staining positive for CD4+ and CD8+ cells.

As seen in our Results, there is a significant difference in LtP between the allograft and isograft on day 3, suggesting that this technique can be used as an earlier predictor of lung rejection than CT, which does not differentiate between the two grafts at this timepoint. The HP lactate signal measured by HP [1-^{13}C] pyruvate MRI is generally based on the metabolism and cellularity of the imaged tissue[15]. The lung has both low cellularity and a low glycolytic rate, whereas immune cells have high aerobic glycolysis [38,39]. Importantly, both activated CD8+ cells and neutrophils have high aerobic glycolysis, so an increased lactate and LtP could be attributed to either source[40–42]; a combination of both mechanisms likely produces the contrast observed in our imaging technique.

The observed LtP in the syngeneic cohort is likely primarily due to post-transplant IR injury. Although no immunohistochemistry was done on day 3 for this cohort, day 7 results show minimal fluorescence for CD4+/CD8+, but ~40% signal for MPO compared to the allografts (Table 5.5). Furthermore, the HP [1-^{13}C] pyruvate signal, which has been previously used as a perfusion marker[43–45], shows that both the isograft and native lung have a high pyruvate signal (normalized to the heart) on day 3 that continues to decrease until day 14, most likely as inflammation subsides. In contrast, the LtP in the allogeneic cohort is most likely a function of both IR injury and T-cell response. Both MPO and CD4+ fluorescence of the allografts on day 3 and 7 increase about 2.3-fold and 15-fold, respectively, compared to the day 7 isograft—suggesting an origin of the increased LtP. Additionally, CD8+ fluorescence of the allografts increases from 7.5-fold to 18.9-fold of the day 7 isografts between days 3 and 7, suggesting that the observed 2-fold increase in LtP between days 3 and 7 results from the increased CD8+ cells in the allografts.

IHC	**Cohort**	**Lung**	**Day 3**		**Day 7**	
			Mean	**SD**	**Mean**	**SD**
MPO	Allogeneic	Allograft	1159.1	49.6	1226.6	195.2
	Syngeneic	Isograft	-	-	512.6	49.7
CD4+	Allogeneic	Native	65.6	10.5	91.5	21.6
		Allograft	848.7	58.7	921.6	282.6
	Syngeneic	Native	-	-	118.3	70.4
		Isograft	-	-	76.2	40.1
CD8+	Allogeneic	Native	74.9	14.8	135.5	32.4
		Allograft	858.8	115.5	2169.1	243.7
	Syngeneic	Native	-	-	114.7	48.9
		Isograft	-	-	71.9	35.5

Table 5.5: Fluorescence quantification of MPO, CD4+ and CD8+ immunohistochemical stains on days 3 (n=3 allogeneic cohort) and 7 (n=4 allogeneic cohort, n=3 syngeneic cohort). MPO expression is used as a marker for neutrophil activity, whereas CD4+ and CD8+ T-cells play a role

in the immune rejection of allogeneic tissue. The images were acquired at an excitation wavelength of 488 nm. All images were acquired at 100 ms exposure time using a preset scale of 0-4095. The PMN, CD4+ and CD8+ were assessed by quantifying fluorescence intensity over 5 fields, and the averages are presented here. The data suggests that the majority of the observed lactate-to-pyruvate signal likely originates from increasing CD8+ cell presence in the allografts.

Based on our day 14 imaging data, both the CT-derived volume and normalized density, as well as the perfusion and LtP based on HP [1-^{13}C] pyruvate MRI, suggest recovery to baseline in the native lungs and isografts. The CT images clearly show the rejected allograft on day 14. The corresponding LtP is 2.6-fold greater than that of the day 14 isograft, likely due to a decrease in lymphocyte activity since day 7, after the onset of lung fibrosis.

Although this study employed HP [1-^{13}C] pyruvate MRI in contrast to CT, other MR or imaging-based techniques have been used previously to study graft rejection. Conventional T_1-weighted gradient echo images and T_2-weighted spin echo images result in poor SNR of the lung parenchyma due to their long echo times and the lung's short T_2^*; however, ultra-short echo (UTE) imaging has been shown to differentiate between allografts and isografts as early as day 3 based on their relaxation characteristics in a murine model[37]. UTE also has a number of advantages compared to our HP ^{13}C CSI sequence; for example, UTE has a much higher spatial resolution than HP ^{13}C CSI and, compared to carbon-13 imaging, would require little or no new hardware (broadband amplifier, coils, polarizer, etc.) for translation to modern clinical MRI scanners. It should be noted, however, that the implementation of ^{13}C HASTE imaging would provide enhanced in-plane spatial resolution comparable to that of UTE[46,47]. In a different murine study, FDG-PET differentiated between allografts and isografts, showing a significant difference in %injected dose per cc of lung (%ID/cc) by day 7; this study further showed that the largest glucose utilization was by CD8+ T cells in particular[48], a finding echoed in our study.

This work demonstrates the sensitivity of HP [1-^{13}C] pyruvate MRI for the early detection of lung rejection. However, both our own and other future small animal studies[37,48] of novel imaging methods must address a number of shortcomings if this technique is to be extended to a clinical setting. Comparison with human pathophysiology is limited, as the time course of rejection in rat lungs is quite distinct from that in humans; in rats, the onset of rejection occurs within days, whereas acute and chronic rejection in humans are distinct in both time and presentation[49,50]. Furthermore, the use of immunosuppressive drugs in transplant patients means that the effects of ischemia-reperfusion—which are seen within the first few days post-transplantation—can be separated from those of rejection, which typically occurs weeks or months later. In this study, the use of syngeneic animals as a sham cohort was intended to minimize the complications arising from the use of immunosuppressive drugs and account for ischemia-reperfusion injury while investigating the feasibility of our imaging technique; further studies should develop a chronic rejection model by using immunosuppressive drugs in allografts to better represent the clinical presentation.

Although this study proposes that the lactate signal may be attributed to the activity and cellularity of both leukocytes and lymphocytes, other possible sources of this increased lactate signal are extracellular LDH activity due to cell death during rejection[51], or even increased B-cell activity and humoral response. However, these avenues were not further investigated, as previous findings have shown that in most cases the dominant response is T-cell mediated rejection[52–54]. Another limitation of investigating this technique in an animal model is that it lacks specificity with other differential diagnoses, e.g. aspiration-induced injury or infections[4,55]. This is also a limitation of FDG-PET imaging, which relies on glucose uptake to drive cellular contrast[48]. However, given the broad range of available HP probes, HP [1-^{13}C] pyruvate could potentially be combined with more specific probes to address that shortcoming[12,56,57]. Overall, this technique has the potential to be a promising new tool for post-transplantation monitoring of lung rejection.

5.5. References

1. Hardy JD, Webb WR, Dalton ML, Walker GR. Lung Homotransplantation in Man: Report of the Initial Case. *JAMA*. 1963;186(12):1065-1074. doi:10.1001/jama.1963.63710120001010

2. Yusen RD, Edwards LB, Dipchand AI, et al. The Registry of the International Society for Heart and Lung Transplantation: Thirty-third Adult Lung and Heart–Lung Transplant Report—2016; Focus Theme: Primary Diagnostic Indications for Transplant. *J Heart Lung Transplant*. 2016;35(10):1170-1184. doi:10.1016/j.healun.2016.09.001

3. Goldfarb SB, Benden C, Edwards LB, et al. The Registry of the International Society for Heart and Lung Transplantation: Eighteenth Official Pediatric Lung and Heart-Lung Transplantation Report—2015; Focus Theme: Early Graft Failure. *J Heart Lung Transplant*. 2015;34(10):1255-1263. doi:10.1016/j.healun.2015.08.005

4. Yusen RD, Edwards LB, Kucheryavaya AY, et al. The Registry of the International Society for Heart and Lung Transplantation: Thirty-second Official Adult Lung and Heart-Lung Transplantation Report—2015; Focus Theme: Early Graft Failure. *J Heart Lung Transplant*. 2015;34(10):1264-1277. doi:10.1016/j.healun.2015.08.014

5. Kanno S, Lee PC, Dodd SJ, Williams M, Griffith BP, Ho C. A novel approach with magnetic resonance imaging used for the detection of lung allograft rejection. *J Thorac Cardiovasc Surg*. 2000;120(5):923-934. doi:10.1067/mtc.2000.110184

6. Jungraithmayr W, Chuck N, Frauenfelder T, Weder W, Boss A. MR imaging by using very short echo–time sequences after syngeneic lung transplantation in mice. *Radiology*. 2012;265(3):753–761.

7. Sharif-Paghaleh E, Yap ML, Meader LL, et al. Noninvasive Imaging of Activated Complement in Ischemia-Reperfusion Injury Post-Cardiac Transplant: Imaging of Complement Post-Cardiac Transplant. *Am J Transplant*. 2015;15(9):2483-2490. doi:10.1111/ajt.13299

8. Vallabhajosyula P, Korutla L, Habertheuer A, et al. Tissue-specific exosome biomarkers for noninvasively monitoring immunologic rejection of transplanted tissue. *J Clin Invest*. 2017;127(4):1375-1391. doi:10.1172/JCI87993

9. Li Ng Y, Paul N, Patsios D, et al. Imaging of Lung Transplantation: *Review*. *Am J Roentgenol*. 2009;192(3_supplement):S1-S13. doi:10.2214/AJR.07.7061

10. Krishnam MS, Suh RD, Tomasian A, et al. Postoperative Complications of Lung Transplantation: Radiologic Findings along a Time Continuum. *RadioGraphics*. 2007;27(4):957-974. doi:10.1148/rg.274065141

11. Gotway MB, Dawn SK, Sellami D, et al. Acute Rejection Following Lung Transplantation: Limitations in Accuracy of Thin-Section CT for Diagnosis. *Radiology*. 2001;221(1):207-212. doi:10.1148/radiol.2211010380

12. Siddiqui S, Xin Y, Emami K, et al. Hyperpolarized< sup> 3</sup> He diffusion MRI and histology of secreted frizzled related protein-1 (SFRP1) deficient lungs in a Murine model. *Magn Reson Imaging*. 2014;32(5):535–540.

13. Pullinger B, Profka H, Ardenkjaer-Larsen JH, Kuzma NN, Kadlecek S, Rizi RR. Metabolism of hyperpolarized [1-13C]pyruvate in the isolated perfused rat lung - an ischemia study: MEASUREMENTS OF LUNG METABOLISM USING HYPERPOLARIZED 1-13C PYRUVATE. *NMR Biomed*. 2012;25(10):1113-1118. doi:10.1002/nbm.2777

14. Pourfathi M, Xin Y, Kadlecek SJ, et al. In vivo imaging of the progression of acute lung injury using hyperpolarized [1-13C] pyruvate. *Magn Reson Med*. January 2017. doi:10.1002/mrm.26604

15. Shaghaghi H, Kadlecek S, Deshpande C, et al. Metabolic spectroscopy of inflammation in a bleomycin-induced lung injury model using hyperpolarized 1-13C pyruvate. *NMR Biomed*. 2014;27(8):939-947. doi:10.1002/nbm.3139

16. Pourfathi M, Cereda M, Chatterjee S, et al. Lung Metabolism and Inflammation during Mechanical Ventilation; An Imaging Approach. *Sci Rep*. 2018;8(1):3525. doi:10.1038/s41598-018-21901-0

17. Habertheuer A, Kocher A, Laufer G, et al. Innovative, simplified orthotopic lung transplantation in rats. *J Surg Res*. 2013;185(1):419-425. doi:10.1016/j.jss.2013.05.006

18. Ashcroft T, Simpson JM, Timbrell V. Simple method of estimating severity of pulmonary fibrosis on a numerical scale. *J Clin Pathol*. 1988;41(4):467-470. doi:10.1136/jcp.41.4.467

19. Hübner R-H, Gitter W, Eddine El Mokhtari N, et al. Standardized quantification of pulmonary fibrosis in histological samples. *BioTechniques*. 2008;44(4):507-517. doi:10.2144/000112729

20. Higuchi T, Kaleem Z, Patterson GA, Mohanakumar T. Different kinetics of obliterative airway disease development in heterotopic murine tracheal allografts induced by CD4+ and CD8+ T cells1. *Transplantation*. 2002;74(5):646–651.

21. Higuchi T, Maruyama T, Jaramillo A, Mohanakumar T. Induction of Obliterative Airway Disease in Murine Tracheal Allografts by CD8+ CTLs Recognizing a Single Minor Histocompatibility Antigen. *J Immunol*. 2005;174(4):1871-1878. doi:10.4049/jimmunol.174.4.1871

22. Krieger NR, Yin DP, Fathman CG. CD4+ but not CD8+ cells are essential for allorejection. *J Exp Med*. 1996;184(5):2013-2018. doi:10.1084/jem.184.5.2013

23. Csencsits K, Wood SC, Lu G, et al. Graft rejection mediated by CD4+ T cells via indirect recognition of alloantigen is associated with a dominant Th2 response. *Eur J Immunol*. 2005;35(3):843-851. doi:10.1002/eji.200425685

24. Hall BM. Cells mediating allograft rejection. *Transplantation*. 1991;51(6):1141-1151.

25. Shrikant P, Khoruts A, Mescher MF. CTLA-4 blockade reverses CD8+ T cell tolerance to tumor by a CD4+ T cell- and IL-2-dependent mechanism. *Immunity*. 1999;11(4):483-493.

26. Yamada Y, Windirsch K, Dubs L, et al. Chronic Airway Fibrosis in Orthotopic Mouse Lung Transplantation Models – An Experimental Reappraisal: *Transplantation*. August 2017:1. doi:10.1097/TP.0000000000001917

27. Gelman AE, Okazaki M, Lai J, et al. CD4+ T Lymphocytes Are Not Necessary for the Acute Rejection of Vascularized Mouse Lung Transplants. *J Immunol*. 2008;180(7):4754-4762. doi:10.4049/jimmunol.180.7.4754

28. Belperio JA, Keane MP, Burdick MD, et al. CXCR2/CXCR2 Ligand Biology during Lung Transplant Ischemia-Reperfusion Injury. *J Immunol*. 2005;175(10):6931-6939. doi:10.4049/jimmunol.175.10.6931

29. Eppinger MJ, Jones ML, Deeb GM, Bolling SF, Ward PA. Pattern of Injury and the Role of Neutrophils in Reperfusion Injury of Rat Lung. *J Surg Res*. 1995;58(6):713-718. doi:10.1006/jsre.1995.1112

30. de Perrot M, Liu M, Waddell TK, Keshavjee S. Ischemia–Reperfusion–induced Lung Injury. *Am J Respir Crit Care Med*. 2003;167(4):490-511. doi:10.1164/rccm.200207-670SO

31. Ofek E, Sato M, Saito T, et al. Restrictive allograft syndrome post lung transplantation is characterized by pleuroparenchymal fibroelastosis. *Mod Pathol*. 2013;26(3):350. doi:10.1038/modpathol.2012.171

32. Royer P-J, Olivera-Botello G, Koutsokera A, et al. Chronic Lung Allograft Dysfunction: A Systematic Review of Mechanisms. *Transplantation*. 2016;100(9):1803-1814. doi:10.1097/TP.0000000000001215

33. Wickersham NE, Johnson JJ, Meyrick BO, Gilroy RJ, Loyd JE. Lung ischemia-reperfusion injury in awake sheep: protection with verapamil. *J Appl Physiol*. 1991;71(4):1554-1562. doi:10.1152/jappl.1991.71.4.1554

34. Watanabe A, Kawaharada N, Kusajima K, Komatsu S, Takahashi H. Contralateral lung injury associated with single-lung ischemia-reperfusion injury. *Ann Thorac Surg*. 1996;62(6):1644–1649.

35. Ng CSH, Wan S, Arifi AA, Yim APC. Inflammatory Response to Pulmonary Ischemia–Reperfusion Injury. *Surg Today*. 2006;36(3):205-214. doi:10.1007/s00595-005-3124-2

36. Grau V, Fuchs-Moll G, Wilker S, Weimer R, Padberg W. Proliferation of CD8-Positive T Cells in Blood Vessels of Rat Renal Allografts. *Am J Transplant*. 2011;11(9):1979-1985. doi:10.1111/j.1600-6143.2011.03642.x

37. Chuck NC, Boss A, Wurnig MC, Weiger M, Yamada Y, Jungraithmayr W. Ultra-short echo-time magnetic resonance imaging distinguishes ischemia/reperfusion injury from acute rejection in a mouse lung transplantation model. *Transpl Int*. 2016;29(1):108-118. doi:10.1111/tri.12680

38. Beck WS. A kinetic analysis of the glycolytic rate and certain glycolytic enzymes in normal and leucemic leucocytes. *J Biol Chem*. 1955;216(1):333–350.

39. Borregaard N, Herlin T. Energy Metabolism of Human Neutrophils during Phagocytosis. *J Clin Invest*. 1982;70(3):550-557. doi:10.1172/JCI110647

40. Wahl DR, Byersdorfer CA, Ferrara JLM, Opipari AW, Glick GD. Distinct metabolic programs in activated T cells: opportunities for selective immunomodulation. *Immunol Rev*. 2012;249(1):104-115. doi:10.1111/j.1600-065X.2012.01148.x

41. Priyadharshini B, Turka LA. T-cell energy metabolism as a controller of cell fate in transplantation: *Curr Opin Organ Transplant*. 2015;20(1):21-28. doi:10.1097/MOT.0000000000000149

42. Yap M, Brouard S, Pecqueur C, Degauque N. Targeting CD8 T-Cell Metabolism in Transplantation. *Front Immunol*. 2015;6. doi:10.3389/fimmu.2015.00547

43. Ishii M, Emami K, Kadlecek S, et al. Hyperpolarized13C MRI of the pulmonary vasculature and parenchyma. *Magn Reson Med*. 2007;57(3):459-463. doi:10.1002/mrm.21168

44. Johansson E, Olsson L e., Månsson S, et al. Perfusion assessment with bolus differentiation: A technique applicable to hyperpolarized tracers. *Magn Reson Med*. 2004;52(5):1043-1051. doi:10.1002/mrm.20247

45. Johansson E, Månsson S, Wirestam R, et al. Cerebral perfusion assessment by bolus tracking using hyperpolarized 13C. *Magn Reson Med*. 2004;51(3):464-472. doi:10.1002/mrm.20013

46. Laustsen C, Stokholm Nørlinger T, Christoffer Hansen D, et al. Hyperpolarized ^{13} C urea relaxation mechanism reveals renal changes in diabetic nephropathy: [^{13} C]Urea Apparent Relaxation Contrast Reveals Diabetic Nephropathy. *Magn Reson Med*. 2016;75(2):515-518. doi:10.1002/mrm.26036

47. Wang J, Hesketh RL, Wright AJ, Brindle KM. Hyperpolarized 13C spectroscopic imaging using single-shot 3D sequences with unpaired adiabatic refocusing pulses. *NMR Biomed*. 2018;31(11):e4004. doi:10.1002/nbm.4004

48. Chen DL, Wang X, Yamamoto S, et al. Increased T Cell Glucose Uptake Reflects Acute Rejection in Lung Grafts. *Am J Transplant*. 2013;13(10):2540-2549. doi:10.1111/ajt.12389

49. Stewart S, Fishbein MC, Snell GI, et al. Revision of the 1996 working formulation for the standardization of nomenclature in the diagnosis of lung rejection. *J Heart Lung Transplant Off Publ Int Soc Heart Transplant*. 2007;26(12):1229-1242. doi:10.1016/j.healun.2007.10.017

50. Meyer KC, Raghu G, Verleden GM, et al. An international ISHLT/ATS/ERS clinical practice guideline: diagnosis and management of bronchiolitis obliterans syndrome. *Eur Respir J*. 2014;44(6):1479-1503. doi:10.1183/09031936.00107514

51. Nora JJ, Cooley DA, Johnson BL, Watson SC, Milam JD. Lactate Dehydrogenase Isozymes in Human Cardiac Transplantation. *Science*. 1969;164(3883):1079-1080. doi:10.1126/science.164.3883.1079

52. Tiroke AH, Bewig B, Haverich A. Bronchoalveolar lavage in lung transplantation. *Clin Transplant*. 2001;13(2):131-157. doi:10.1034/j.1399-0012.1999.130201.x

53. Gregson AL, Hoji A, Saggar R, et al. Bronchoalveolar Immunologic Profile of Acute Human Lung Transplant Allograft Rejection. *Transplantation*. 2008;85(7):1056-1059. doi:10.1097/TP.0b013e318169bd85

54. Levine DJ, Glanville AR, Aboyoun C, et al. Antibody-mediated rejection of the lung: A consensus report of the International Society for Heart and Lung Transplantation. *J Heart Lung Transplant*. 2016;35(4):397-406. doi:10.1016/j.healun.2016.01.1223

55. Martinu T, Chen D-F, Palmer SM. Acute Rejection and Humoral Sensitization in Lung Transplant Recipients. *Proc Am Thorac Soc*. 2009;6(1):54-65. doi:10.1513/pats.200808-080GO

56. Keshari KR, Wilson DM. Chemistry and biochemistry of 13C hyperpolarized magnetic resonance using dynamic nuclear polarization. *Chem Soc Rev*. 2014;43(5):1627. doi:10.1039/c3cs60124b

57. Lau AZ, Miller JJ, Robson MD, Tyler DJ. Simultaneous assessment of cardiac metabolism and perfusion using copolarized [1- ^{13} C]pyruvate and ^{13} C-urea: Simultaneous Hyperpolarized Cardiac Perfusion and Metabolic Imaging. *Magn Reson Med*. January 2016:n/a-n/a. doi:10.1002/mrm.26106

Chapter 6: Conclusions and Future Work

6.1. Conclusions

Improving lung transplant outcomes is a vital but imposing endeavor: challenges include the limited availability of donor lungs, the necessity preserving and/or revitalizing lungs before transplant, and high rates of post-transplant graft failure compared to other solid organs. Although a number of novel techniques such as *ex vivo* lung perfusion are currently used to maintain or improve the viability of donated lungs during acquisition and transit, there is no established non-invasive assessment tool for evaluating the health of the tissue before transplantation. In addition, current post-transplant assessment tools—primarily spirometry and X-ray radiography or CT—each have their own inherent limitations. Because spirometry only provides whole-lung measurements, a large number of differential diagnoses must be ruled out by further testing. Both radiography and CT, on the other hand, provide only low sensitivity in the early stages of rejection. We showed that HP carbon-13 magnetic resonance imaging, since it generates contrast due to the metabolism of the tissue or the infiltrating inflammatory cells, is therefore a promising technique for both assessing the viability of lungs before transplantation and predicting post-transplant lung rejection.

In our first set of studies, we used HP [1-^{13}C] pyruvate MRS and ^{31}P MRS to show that the energy status of the lung declines as a function of time during EVLP. The decline in conversion of HP [1-^{13}C] pyruvate to ^{13}C bicarbonate showed that the energy decline was most likely linked to reduction in pyruvate dehydrogenase complex (PDHc) activity and the subsequent decrease in oxidative phosphorylation. As such, we concluded that a part of the energy depletion and loss of viability observed in reperfused ischemic lungs is due to perfusion alone. We also demonstrated that ascorbate upregulates oxidative phosphorylation in the *ex vivo* perfused lung. Although previous studies have postulated that ascorbate's role in minimizing ischemia-reperfusion injury is via its anti-oxidative properties[1,2], our HP [1-^{13}C] pyruvate studies suggest that ascorbate slows the decline in pulmonary mitochondrial activity through an independent interaction with ETC complexes. Based on the observation that lungs experiencing significant decline in energy status are highly prone to edema, it seems clear that maintaining mitochondrial function during EVLP is critical to maintaining organ viability. One of the applicable findings of this set of studies was that the addition of ascorbate to the perfusate during EVLP may be beneficial in prolonging the viability of the lungs being excised, transported and reperfused before transplantation. Furthermore, this study also established that HP [1-^{13}C] pyruvate MRS can be used to assess the response to treatment during EVLP for improving procurement and preservation of lungs for transplantation.

In our second set of studies, we demonstrated that *ex vivo* HP [1-^{13}C] pyruvate spectroscopy can be used to detect pulmonary inflammation and provided histological evidence that infiltrating neutrophils are the most likely source of increased signal compared to heathy tissue. Although the transport and enzymatic processes of HP [1-^{13}C] pyruvate differ than those involved in ^{18}FDG imaging, many features of the techniques appear to be similar, including the several-fold increase of signal in inflammation and the apparent sensitivity to direct metabolism of neutrophils. We also successfully translated these findings into *in vivo* HP [1-^{13}C] pyruvate imaging using a FID-CSI sequence. Due to the inherent problems of imaging lungs *in vivo*—such as the blood-dependent T_1 depolarization, susceptibility due to the air-tissue interface, and the movement of the chest cavity—we see lower metabolite signals than via *ex vivo* spectroscopy; however, we were able to detect a significant increase in the HP lactate-to-pyruvate ratio in inflamed lungs compared to healthy tissue, paving the way for *in vivo* studies for lung transplant rejection.

In our last set of studies, we applied our developed *in vivo* HP [1-^{13}C] pyruvate imaging technique to predict lung graft rejection in an orthotopic left lung transplant model in rats. We showed a significant increase in the HP lactate-to-pyruvate ratio as early as day 3 in the allogenic graft compared to the syngeneic graft. This signal increased further by day 7 and remained much higher than the isograft or native tissue in either cohort at day 14. We also acquired post-transplant microCT imaging at the same timepoints, and found that the HP lactate-to-pyruvate was an earlier predictor of lung rejection compared to CT-derived parameters. Our immunohistochemical staining suggested that the source of this signal was a combination of neutrophils, CD4$^+$, and CD8$^+$ cells, with the largest signal deriving from CD8$^+$ cells on day 7. However, our study leaves a number of unanswered questions, which must be tackled in future studies: how can the role of ischemia-reperfusion injury be separated from that of the tissue rejection process? Can this technique be used to separate differential diagnoses, e.g. aspiration-induced injury or infections? Can the technique be used for long term assessment for predicting bronchitis obliterans syndrome or restrictive allograft dysfunction? Given the broad range of available HP probes, can HP [1-^{13}C] pyruvate potentially be combined with more specific probes to address the shortcomings of this technique? Lastly, can this technique be successfully translated towards imaging humans?

6.2. Planned Future Studies

6.2.1. Post-transplant HP [1-^{13}C] pyruvate MRI of lungs acquired after induction of donor brain-death in a rat model

We have already established the metabolic profile of syngeneic and allogeneic grafts in a rat model. As donor brain death (DBD) has been associated with increased ischemia-reperfusion injury and primary graft dysfunction (PGD), we will transplant lungs obtained after DBD into healthy rats and compare their graft performance with our established transplant model. We will determine whether syngeneic grafts from DBD lungs show a similar metabolic profile compared to our current donor model with normotensive brain death. We will also image allogeneic grafts from DBD lungs to test the hypothesis whether these lungs will show rejection or graft failure earlier than the findings in our current model.

We also plan to use *ex vivo* ^{13}C MR and ^{31}P spectroscopy to measure the tissue energy status in of DBD lungs using EVLP, and we will assess the metabolism as a function of perfusion time, perfusate composition and other factors that have shown to ameliorate or degrade EVLP lungs. Graft performance post-transplantation will be assessed to confirm the success of any therapeutic strategies.

6.2.2. Imaging Post-Transplant Allogeneic Rats with Acquired Immune Tolerance Using Hyperpolarized [1-^{13}C] Pyruvate MRI

Our findings from imaging post-transplant lungs suggest that the lactate-to-pyruvate signal in the allograft originates from both neutrophils and CD3+ lymphocytes. One of the more pressing questions in the field of lung transplantation is the role of inflammation after ischemia-reperfusion injury in the tissue rejection process. In this study (in progress), we plan to image a transplanted allogeneic lung in a recipient rat with acquired immune tolerance to resolve the signal contribution of ischemia-reperfusion injury from that of tissue rejection[3]. Figure 6.1 shows a schematic for generating an adult rat with an acquired immune tolerance for a different rat strain. The first step involves crossing two different strains to produce a crossbred F_1 generation. In our case, inbred Lewis (L) rats were crossed with inbred Wistar-Furth (WF) rats to generate a WFxL (F_1) rats. The bone marrow from the F_1 rats is extracted immediately after birth—before T cells are have matured to identify self and non-self MHC molecules[4,5]—and injected into Lewis neonates (also immediately after birth). This allows the inoculated Lewis (iL) neonates to develop self recognition for both F_1 and Lewis MHC molecules. The F_1 generation is required to avoid graft versus host disease (GVHD) in the inoculated Lewis rat. Once the iL rat is mature, it can be used as a recipient for allogeneic lung transplant.

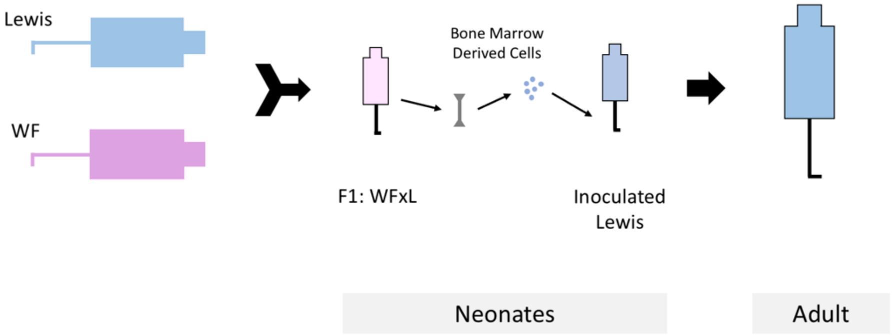

Figure 6.1: Schematic for generating a recipient rat with acquired immune tolerance for an allogeneic graft.

As figure 6.2 shows, the lung transplant is performed similarly to as described in our previous studies (chapter 5). The donated lung is the F_1 rats. The recipient is an iL rat. As the iL rat recognizes the F_1 MHC as self, the lung is not rejected. In our preliminary study, we imaged allogeneic, syngeneic, and the acquired immune tolerant rats on days 3, 7, and 14. On day 3, the average lactate-to-pyruvate ratios of all three transplanted lungs ranged between 0.08 to 0.11 compared to a range of 0.05 to 0.07 for the native lungs. By day 7, the rejected allograft had a lactate-to-pyruvate ratio of 0.3±.04, a 2.7-fold increase compared to the other cohorts, which remained below 0.11. Most importantly, the immune tolerant allograft followed a similar trajectory to the syngeneic graft—showing no signs of rejection. A similar trend is observed on day 14: lactate-to-pyruvate remains elevated in the allograft (0.23±.02), whereas the other transplanted and native lungs remain below 0.08. The immune tolerant cohort was also imaged on day 28 to assess the presence of chronic rejection; the lungs remained viable at this timepoint, based on their low lactate-to-pyruvate ratio (below 0.04). Representative pyruvate and lactate maps acquired on day 7 post-transplantation from our preliminary results can be seen in Figure 6.2. As mentioned, the allograft clearly shows a much greater lactate signal than any of the other lung cohorts, whereas the syngeneic lungs and acquired immune tolerant lungs show similar findings.

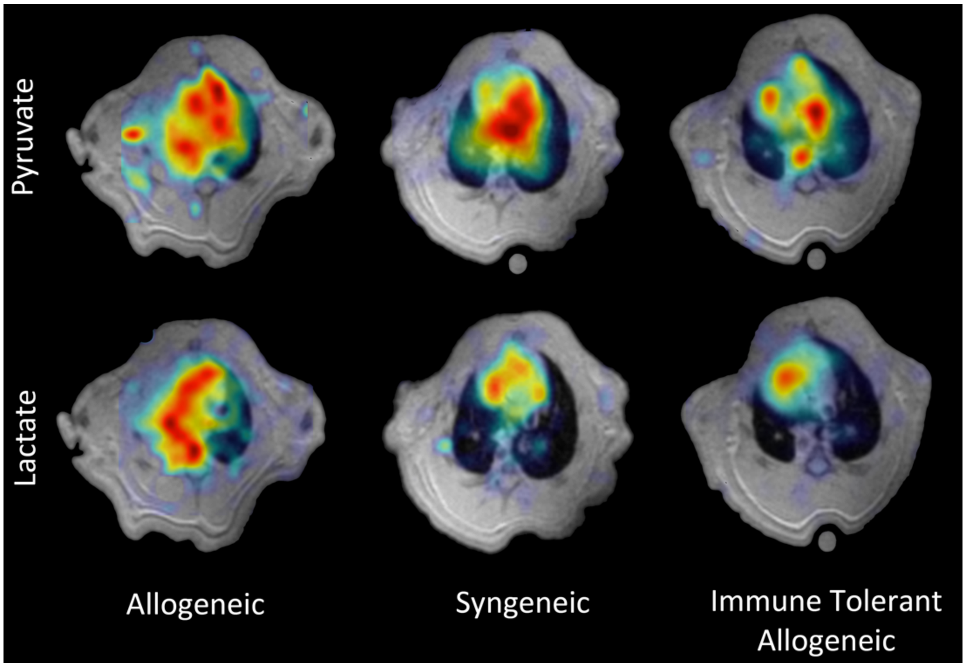

Figure 6.2: Preliminary results from a HP [1-^{13}C] pyruvate MRI study showing the pyruvate and lactate distribution on day 7 post-transplantation in allogeneic (left), syngeneic (middle), and acquired immune tolerant (right) rats.

The next step in this study is to abolish the the acquired immune tolerance by injecting mature T-cells from any inbred Lewis rat (Figure 6.3). As the recipient rat and the injected T-cells are inbred Lewis rats, they will recognize each other as self and no immune response will be triggered in the host tissues.

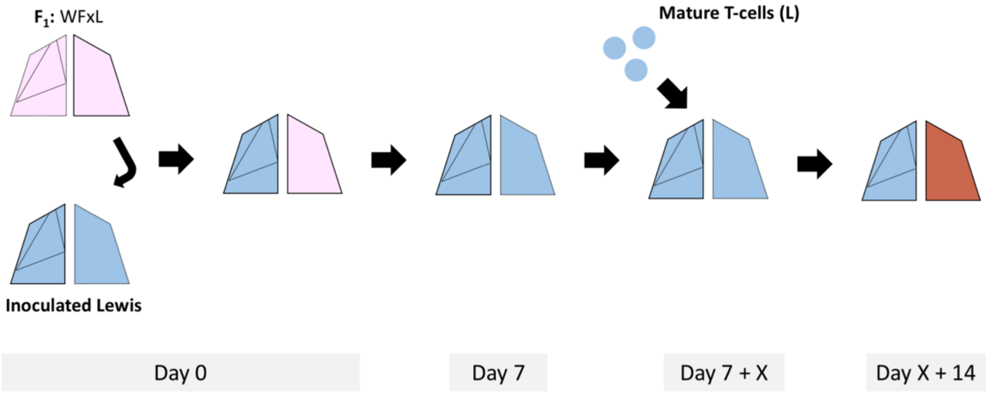

Figure 6.3: Abolishing acquired immune tolerance after lung transplantation by injection of mature T-cells from inbred Lewis rats.

However, the injected mature Lewis T-cells will not recognize the F_1 MHC molecules as self. When CD4+ or CD8+ cells will be presented with the appropriate MHC via various antigen presenting cells (APC), they will recognize the F_1 molecules as foreign antigens and activate an immune response, triggering graft rejection. HP [1-^{13}C] pyruvate MRI acquired after inducing this lung rejection process will allow us to differentiate between the signals emanating from ischemia-reperfusion injury and rejection.

6.3. Further Studies

Once the answers to the questions posed by the above studies are answered, we can add further complexity to our animal models to better mimic the clinical transplantation process. This includes using recipients with models of end-stage progressive diseases, such as radiation-induced or bleomycin-induced fibrosis, or elastase-induced emphysema. Furthermore, we can use a multimodal approach to imaging, combining the findings from HP [1-^{13}C] pyruvate imaging with pre-existing methodologies, as well novel imaging techniques such as HP gas imaging, all for the ultimate goal of improving post-transplant outcomes clinically.

6.4. References

1. Demertzis S, Scherer M, Langer F, Dwenger A, Hausen B, Schäfers H-J. Ascorbic acid for amelioration of reperfusion injury in a lung autotransplantation model in sheep. *Ann Thorac Surg*. 2000;70(5):1684-1689. doi:10.1016/S0003-4975(00)01846-4

2. Baltalarli A, Ozcan V, Ferda B, et al. Ascorbic Acid (Vitamin C) and Iloprost Attenuate the Lung Injury Caused by Ischemia/Reperfusion of the Lower Extremities of Rats. *Ann Vasc Surg*. 2006;20(1):49-55. doi:10.1007/s10016-005-9284-0

3. Billingham RE, Brent L, Medawar PB. Quantitative Studies on Tissue Transplantation Immunity. III. Actively Acquired Tolerance. *Phil Trans R Soc Lond B*. 1956;239(666):357-414. doi:10.1098/rstb.1956.0006

4. Sakaguchi S. Naturally arising CD4+ regulatory T cells for immunologic self-tolerance and negative control of immune responses. *Annu Rev Immunol*. 2004;22(1):531-562. doi:10.1146/annurev.immunol.21.120601.141122

5. Dimichele DM, Hoots WK, Pipe SW, Rivard GE, Santagostino E. International workshop on immune tolerance induction: consensus recommendations1. *Haemophilia*. 2007;13:1-22. doi:10.1111/j.1365-2516.2007.01497.x